Pressure Drop and Recovery in Cases of Cardiovascular Disease: a Computational Study

by

Chrysa Anna Kousera

A thesis submitted as partial fulfilment of the requirements for the degree of Doctor of Philosophy and the Diploma of Imperial College London

April 2014

National Heart and Lung Institute
Imperial College London

Abstract

The presence of disease in the cardiovascular system results in changes in flow and pressure patterns. Increased resistance to the flow observed in cases of aortic valve and coronary artery disease can have as a consequence abnormally high pressure gradients, which may lead to overexertion of the heart muscle, limited tissue perfusion and tissue damage.

In the past, computational fluid dynamics (CFD) methods have been used coupled with medical imaging data to study haemodynamics, and it has been shown that CFD has great potential as a way to study patient-specific cases of cardiovascular disease *in vivo*, non-invasively, in great detail and at low cost. CFD can be particularly useful in evaluating the effectiveness of new diagnostic and treatment techniques, especially at early 'concept' stages.

The main aim of this thesis is to use CFD to investigate the relationship between pressure and flow in cases of disease in the coronary arteries and the aortic valve, with the purpose of helping improve diagnosis and treatment, respectively.

A transitional flow CFD model is used to investigate the phenomenon of pressure recovery in idealised models of aortic valve stenosis. Energy lost as turbulence in the wake of a diseased valve hinders pressure recovery, which occurs naturally when no energy losses are observed. A "concept" study testing the potential of a device that could maximise pressure recovery to reduce the pressure load on the heart muscle was conducted. The results indicate that, under certain conditions, such a device could prove useful.

Fully patient-specific CFD studies of the coronary arteries are fewer than studies in larger vessels, mostly due to past limitations in the imaging and velocity data quality. A new method to reconstruct coronary anatomy from optical coherence tomography (OCT) data is presented in the thesis. The resulting models were combined with invasively acquired pressure and flow velocity data in transient CFD simulations, in order to test the ability of CFD to match the invasively measured pressure drop. A positive correlation and no bias were found between the calculated and measured results. The use of lower resolution reconstruction methods resulted in no correlation between the calculated and measured results, highlighting the importance of anatomical accuracy in the effectiveness of the CFD model. However, it was considered imperative that the limitations of CFD in predicting pressure gradients be further explored. It was found that the CFD-derived pressure drop is sensitive to changes in the volumetric flow rate, while bench-top experiments showed that the estimation of volumetric flow rate from invasively measured velocity data is subject to errors and uncertainties that may have a random effect on the CFD pressure result.

This study demonstrated that the relationship between geometry, pressure and flow can be used to evaluate new diagnostic and treatment methods. In the case of aortic stenosis, further experimental work is required to turn the concept of a pressure recovery device into a potential clinical tool. In the coronary study it was shown that, though CFD has great power as a study tool, its limitations, especially those pertaining to the volumetric flow rate boundary condition, must be further studied and become fully understood before CFD can be reliably used to aid diagnosis in clinical practice.

Acknowledgements

I wish to express gratitude to the people without whose guidance and input this project could not have been possible. First of all, to my principal supervisor Dr Justin Davies, for his excellent guidance and support in all matters, medical or technical.To my co-supervisor Professor Darrel Francis for truly understanding the potential of using the engineering mindset in medical research and allowing me to be part of his multidisciplinary team. To my co-supervisor Professor Yun Xu, who introduced me to biofluid mechanics and has been providing valuable assistance for longer than anyone. And to my co-supervisor Professor Alun Hughes, for contributing some of his incredible knowledge at crucial stages of the project.

On the medical side, I would like to give special thanks to Dr SukhjinderNijjer, who provided the best quality patient data I could hope for and for putting up with my endless questions when trying to understand how to use said data. Great thanks are also accorded to Drs Ricardo Petraco, Sayan Sen, and Christopher Broyd, for patiently enlightening me on all aspects of interventional cardiology. I would also like to thank Dr Nicolas Foin for his insight and advice on the great potential of OCT imaging in CFD applications.

On the engineering side, I would like to express my sincere gratitude to Dr Ryo Torii for almost single-handedly teaching me all technical aspects of CFD, and for coming to my rescue in many a bind, and to Professor Nigel Wood for his continuous support and numerous mind-sharpening conversations on CFD, science and music we've had in the past 5 years. Special thanks also go to Dr Katharine Fraser, for kindly and patiently helping with my bench top experiments.

I would also like to thank all my colleagues in the International Centre for Circulatory Health and Chemical Engineering Departmentfor the fun times we've had together.

Last, but not least, I would like to thank my parents Mrs Eleni and Mr Antonios Kouseras for their loving encouragement and unwavering trust, and my partner Antonios Lampadaridis for his love and support.

Chrysa Kousera

London

April 2014

Declaration of Originality

I hereby declare that this thesis and the work reported herein was composed and originated entirely from me. Information derived from the published and unpublished work of others has been acknowledged in the text and references are given in the list of sources.

Copyright Declaration

Contents

List of Figures

List of Tables

1. Introduction

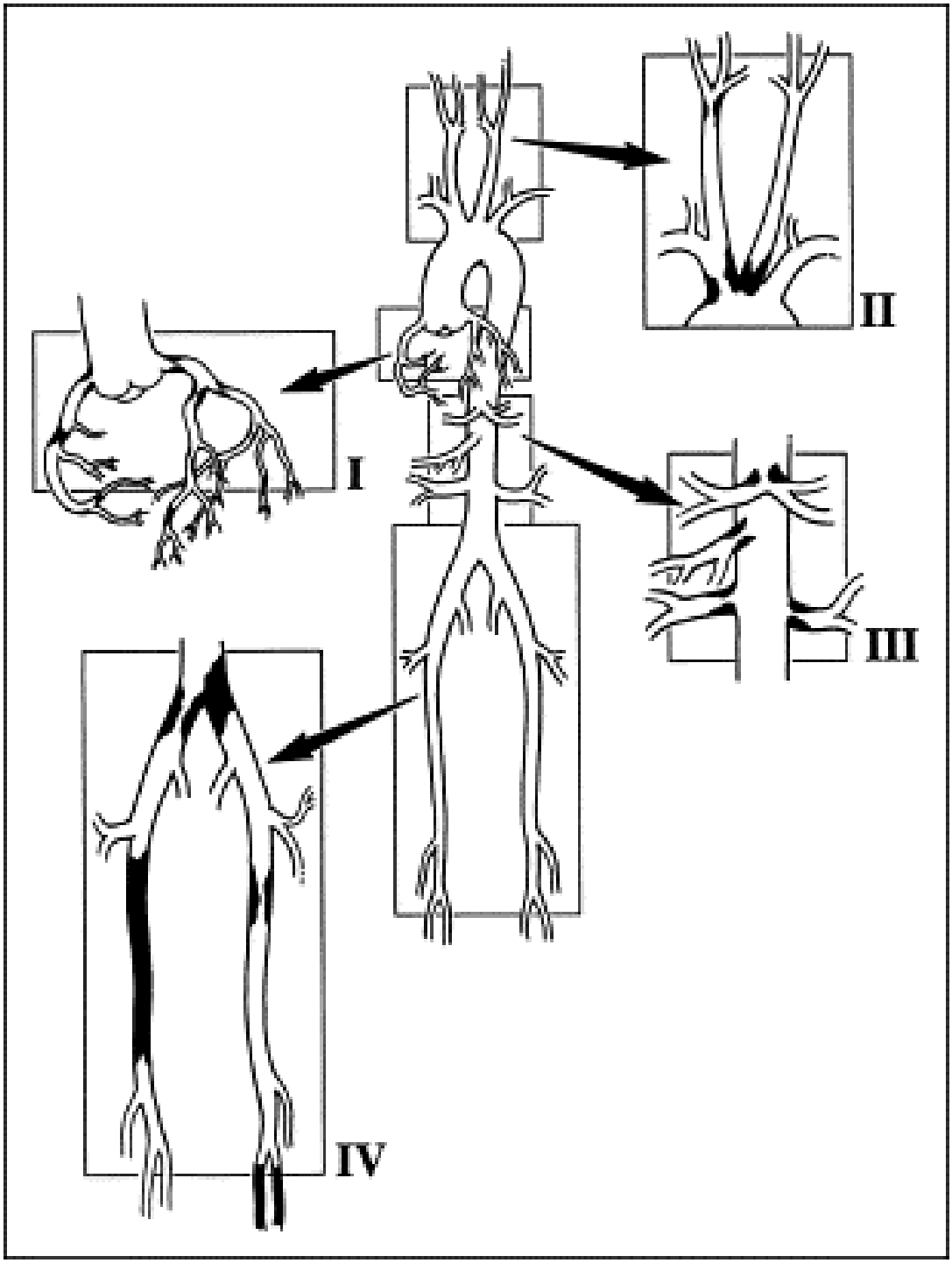

Figure 1-1 Sites with predilection for arterial disease: I: coronaries. II: carotids, III: intercostals, renals, IV: aorto-iliac bifurcation and femoral arteries. It is obvious that bifurcations and curved geometries favour atherosclerosis, because the geometry is determinant of blood-flow patterns.(DeBakey et al., 1985)

1.1 Motivation for the study

Studying the flow of blood through vessels is a worthwhile endeavour, as blood flow plays a significant role in the regulation of vascular health and therefore has a direct connection to vascular pathology (Figure 1-1). The velocity patterns inside vessels determine many physiologically significant parameters, such as wall shear stress, wall tensile stress, energy dissipation and pressure drop.

The importance of flow patterns are nowhere more evident than in the vessels nearer to the heart, such as the aorta and the coronary arteries (Malek et al., 1999, Davies, 2009, Dowd et al., 1999).Their anatomy and physiology makes these parts of the vascular system vulnerable to calcification and atheromatous plaque formation (which leads to aortic stenosis and coronary artery disease, respectively) and their direct interaction with the heart muscle often makes disease there fatal.

1.1.1. The aortic root

Anatomy

The aorta carries oxygen-rich blood from the heart to the rest of the body. It is connected to the left ventricle of the heart via the aortic valve, and the full amount of blood supplied by the heart in each heartbeat passes through it.

The aortic valve is embedded inside the aortic root (Figure 1-2) and consists of (normally) three leaflets, called the cusps, which move passively with the flow; during systole the cusps open to allow blood out of the left ventricle and then close at the start of clinical diastole to prevent blood from flowing backwards into the ventricle following the reversal of the pressure gradient(Underwood et al., 2000, Berdajs et al., 2002).

Pathology

A common disease of the aortic valve is Aortic Stenosis (AS), an abnormal narrowing of the valve opening (orifice) caused by sclerotic change in the valve leaflets resulting from a

process that shares a number of similarities with atherosclerosis in other arteries (Freeman and Otto, 2005). The sclerotic change in the leaflets (Figure 1-3) prevents their free movement and the reduced orifice lead to an acceleration of the flow. If the acceleration of flow is sufficiently large it will result in a large pressure drop. In order to maintain systemic blood pressure and organ perfusion this forces the left ventricle to generate higher intraventricular pressure than normal and eventually fail, if the condition is left untreated (Heinrich et al., 1996).

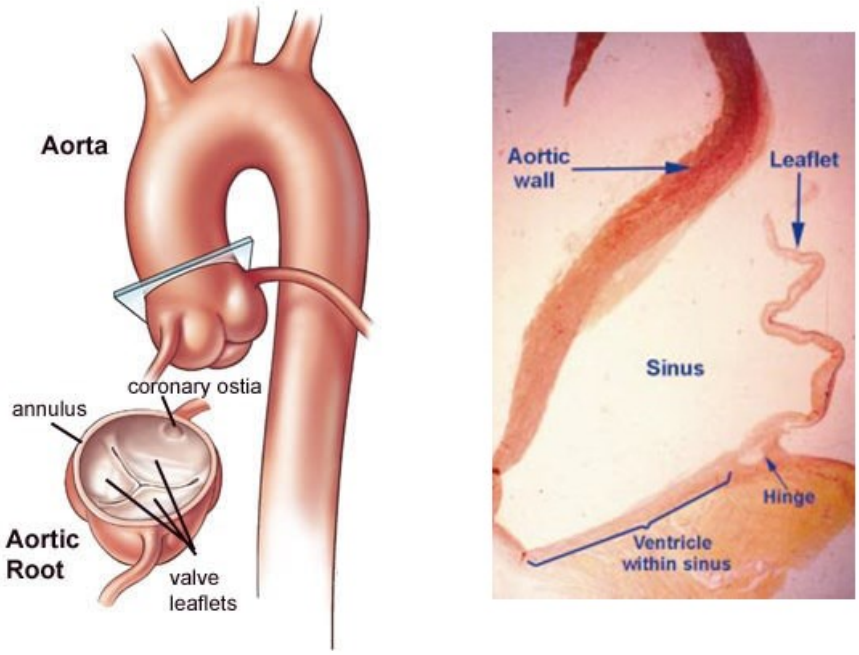

Figure 1-2 Left Schematic representation of the human aortic root and its most important anatomical parts **Right** Aortic root section across one of the coronary sinuses giving a more detailed view of the valve anatomy (Robert H Anderson, *Heart* , 84:670-673, 2000)

According to the American Heart Association (Lloyd-Jones et al., 2009), 29% of participants in the population-based Cardiovascular Health Study (CHS) over 65 years of age who underwent echocardiography had aortic sclerosis (thickening of the leaflets) and 2% had aortic stenosis. The risk of death by cardiovascular disease for those with AS is increased by about 50%. Another study (Otto et al., 1999a) reported that 48% of patients over 85 years of age had asymptomatic aortic sclerosis and 4% of the same age group had aortic stenosis, in keeping with the known increase in prevalence of this condition with increasing age. Unfortunately, the older age group in which AS often happens is also at higher risk of adverse consequences from surgical intervention to replace the valve.

Diagnosis and Treatment

Aortic stenosis is usually diagnosed using a catheter to measure the pressure drop across the stenosis or Doppler ultrasound to measure flow velocities, and from these measurements a value for the restricted area can be calculated (Heinrich et al., 1996). Treatment options include Aortic Valve Replacement open-heart surgery (AVR) and, when the risk of open-heart surgery is too high (i.e. estimated mortality risk is more than 10%), a procedure called Transcatheter Aortic Valve Implantation (TAVI), where a catheter-driven valve replacement takes place inside the beating heart, without the need for the opening of the chest (Vahanian et al., 2008a). Both procedures carry relatively little risk in general, but there are still patients that are considered too high-risk for any of these two procedures.

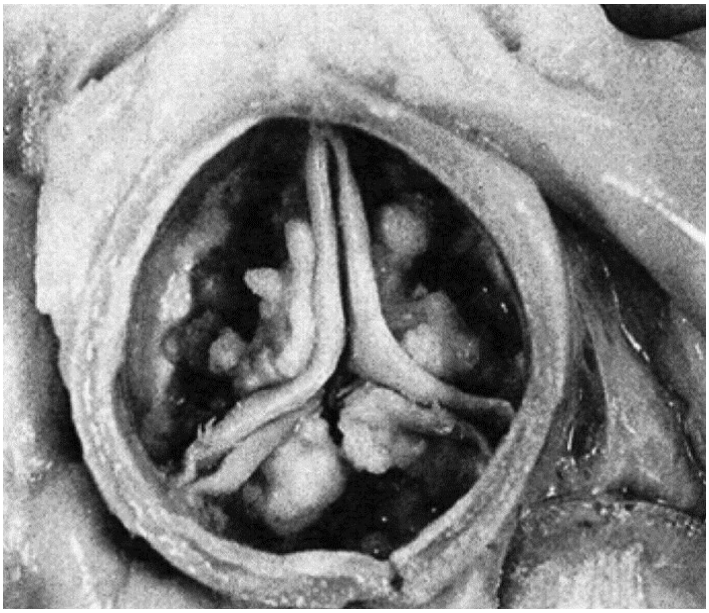

Figure 1-3 Human aortic valve with plaque formed on the leaflets. The leaflets become harder and the plaque prevents them from opening fully, reducing the orifice area.

1.1.2 The coronary arteries

Anatomy

The coronary arteries are the system of arteries that supply blood to the heart muscle. The two main coronary arteries (left and right) stem from above two of the three aortic valve cusps, and then branch out into smaller arteries, arterioles and capillaries that permeate the heart muscle(Ding et al., 2002). It has been shown that blood flow inside the coronary arteries is controlled by forward and backward pressure waves. The majority of coronary blood flow happens during diastole, when the relaxing movement of the heart muscle 'sucks' blood from the aortic root into the coronary ostia (Davies et al., 2008, Davies et al., 2006).

Flow inside the coronary arteries is influenced by their small diameter, branching, intense curvature and tortuosity (Torii et al., 2009d). The complex geometry creates areas of flow separation and low wall shear stress and, combined with disease factors such as high cholesterol levels, this leads to plaque formation in the lumen wall.

Pathology

Atherosclerosis in the coronary arteries is one of the most common causes of death in the Western world. In the United States, 1 in 5 deaths in 2005 were caused by Coronary Artery Disease (CAD), and it is estimated that once every 25 seconds there is a new coronary event and once every minute a CAD-related death. The mortality rate of patients with CAD that present in US hospitals is around 10% (Lloyd-Jones et al., 2009).

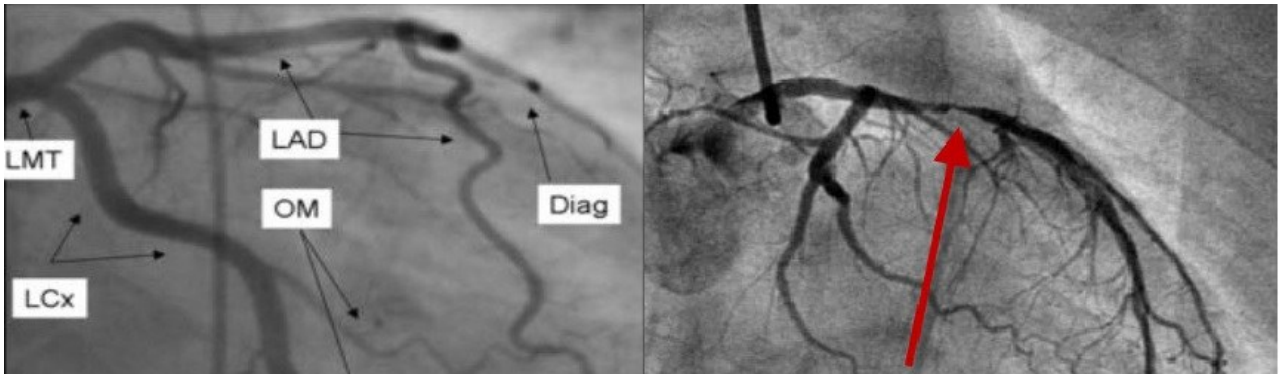

Figure 1-4 Left A normal coronary artery angiogram. The left main (LMT), the left anterior descending (LAD) and the left circumflex (LCx) coronary arteries are visible, among others. **Right** Angiogram of a severely stenosed (95%) left anterior descending coronary artery (stenosis indicated by arrow).

CAD results from the narrowing (stenosis) due to plaque formation and/or occlusion of at least one coronary artery (Figure 1-4). The stenosis increases the resistance to the flow inside the vessel and leads to an observable pressure drop across the stenosis, reducing blood supply. When the resistance becomes too high, or the plaque ruptures and thrombotic occlusion of the vessel ensues the areas downstream of the stenosis are left with limited or no oxygen supply. The protracted lack of oxygen leads to myocardial infarction and heart failure.

Diagnosis and Treatment

There are several methods for the diagnosis of CAD. They can be divided into two categories: anatomical and functional methods. The anatomical methods include angiography, intra-vascular ultrasound (IVUS), CT angiography, and more recently OCT (optical-coherence tomography) scans, and their aim is to assess the cross-sectional area reduction caused by plaque. The most common invasive functional assessment method is called Fractional Flow Reserve (FFR) and involves measuring the ratio of distal to proximal flow rate using a pressure wire (Figure 1-5) under conditions of hyperaemia to calculate the pressure drop across the stenosis. The two categories of methods (anatomical and functional) do not agree on all assessments (Gould and Lipscomb, 1974a). Coronary revascularization decisions guided by fractional flow reserve (FFR) are associated with improved clinical outcomes and reduced healthcare costs, however in the catheter lab fluoroscopy is still the most widely used method of coronary disease assessment (Nam et al., 2010, Tonino et al., 2010, Fearon et al., 2007b).

Treatment options for CAD include medical (drug) treatment, Coronary Artery Bypass Graft surgery (CABG) and angioplasty, usually in the form of Percutaneous Coronary Intervention (PCI). The decision about which method to use depends on the severity assessment of the stenosis. CABG is, as a rule, used in the most severe cases and in emergencies, but deciding on PCI or drug treatment can be more complicated, depending on the overall risk assessment in each individual case. In some cases, the discrepancies between the anatomical and functional assessment methods can prove an obstacle to making the right decision, and could lead to preventable deaths.

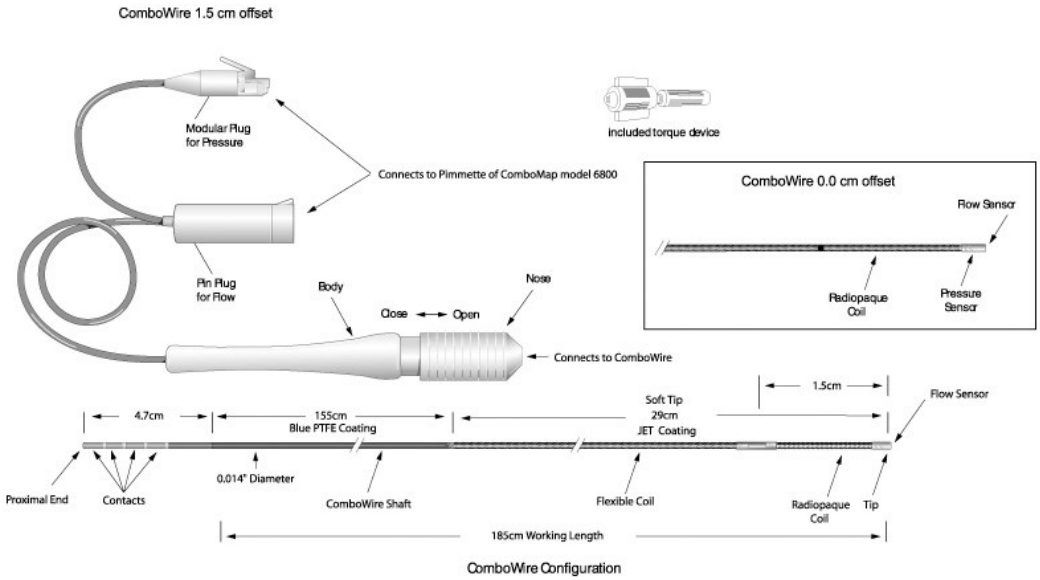

Figure 1-5 ComboWire® XT Guide Wire (Volcano, San Diego California), one of the pressure wires used by the cardiologists of our lab (ICCH) to make Fractional Flow Reserve assessments in patients with Coronary Artery Disease.

1.1.3 Pressure drop as a diagnostic tool

The mechanics of pressure recovery and irreversible pressure loss

In an ideal flow with no constriction or losses, the pressure difference between two points along a streamline is given by the Bernoulli equation when suitably modified for transient flow as discussed by Wood (Wood, 1999):

$$p_0 + \rho g z_0 = p_1 + \rho g z_1 + \frac{\rho q_1^2}{2} + \rho \int_0^1 \frac{\partial q}{\partial t} ds = p_2 + \rho g z_2 + \frac{\rho q_2^2}{2} + \rho \int_0^2 \frac{\partial q}{\partial t} ds \quad (1.1)$$

where p_0 is the total pressure, p_1 and p_2 is the static pressure in two points along one streamline, q_1 and q_2 are the respective velocity values, z_i is the vertical height from the reference pressure, and ρ is the fluid density. The term $\rho g z_i$ indicates the hydrostatic pressure, which for a patient in a lying or supine position (as in most cases of flow and pressure measurements) can be neglected. The term $\rho q_i^2/2$ is the kinetic energy of the fluid at each point and the pressure corresponding to this component is sometimes termed dynamic pressure. Static pressure is the pressure exerted by the fluid when stationary.

According to this equation, the sum of static pressure and kinetic energy in each point along the streamline remains constant and equal to the total pressure of the fluid. If the flow

accelerates, for example passing through a stenosed vessel, static pressure (the pressure measured in medical applications) falls as kinetic energy rises along the streamline. Predictably, when the flow decelerates (for example when coming out of the stenosis) static pressure increases as kinetic energy decreases. This phenomenon is called pressure recovery, and is to some degree present in all cases of vessel stenosis (Heinrich et al., 1996, Clark, 1976b, Clark, 1976a). In Figure 1-6 pressure recovery in the case of flow through the aortic root is presented.

In the lossless case, total pressure remains constant along the streamline (i.e. the sum of 'static pressure plus kinetic energy' remains constant), meaning that it is possible to recover the full amount of static pressure apparently being lost through the narrowing. Of course, in reality no flow is without energy losses, but in the case of healthy blood vessels the energy being lost along a small distance (such as the length of a coronary artery, or of the aortic root) is negligible, in line with the equation of Hagen-Poiseuille for viscous losses:

$$\Delta P = \frac{8\mu LQ}{\pi r^4} \tag{1.2}$$

where ΔP is the pressure drop observed, μ is the viscosity of the fluid, r is the radius of a cylindrical tube, Q is the volumetric flow rate at which the fluid flows and L is the distance between the two measurement locations.

In most physiological flows, L is only a few diameters long, and no significant losses are observed. However, in the presence of a stenosis the flow becomes complicated and disturbed and, in the case of severe aortic stenosis, turbulent. This kind of flow favours a high energy dissipation rate and therefore the amount of energy being lost is no longer negligible. Total pressure is no longer preserved and the sum of static pressure and kinetic energy is smaller distally than proximally (Figure 1-7). This leads to a smaller amount of static energy being recovered, increasing the observed pressure drop. In the case of aortic stenosis, the increased pressure drop forces the left ventricle to pump blood at a higher pressure in order to maintain the required pressure in the ascending aorta, leading to increased myocardial workload, myocardial hypertrophy and heart failure. In the coronary arteries a stenosis increases the impedance to flow and, when the stenosis is severe enough, the flow that passes through it is reduced or stops completely, leading to myocardial infarction and failure.

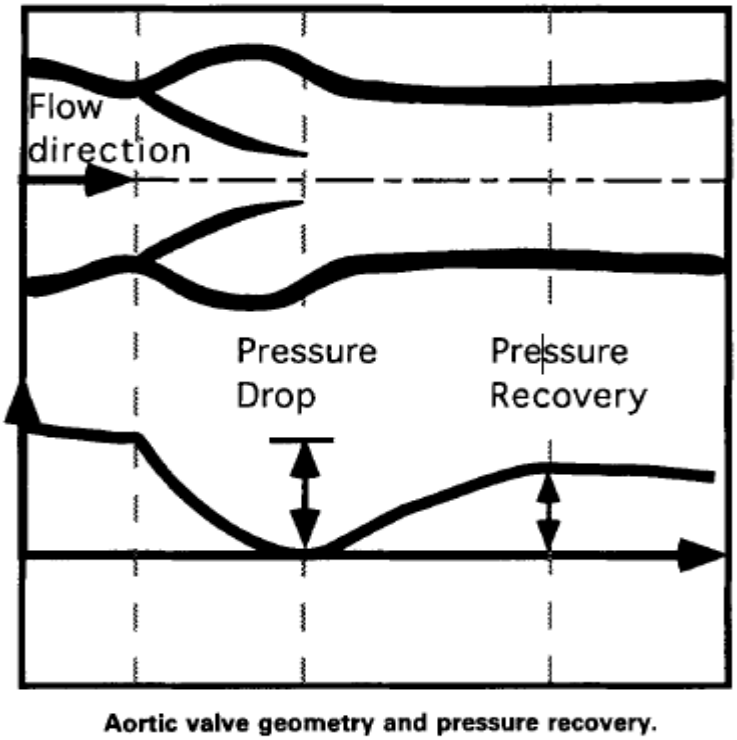

Figure 1-6 The geometry of a normal aortic valve and the respective pressure drop across it. When the flow accelerates through the narrower valve area, static pressure drops considerably, but most of the pressure is recovered downstream as the aorta widens and the velocity decreases, following the Bernoulli principle. Image from (Heinrich et al., 1996).

The above analysis demonstrates the importance of the concepts of pressure drop and pressure recovery in cardiovascular disease. Pressure drop measurement in particular is a reliable indicator of the functional impairment caused by the presence of stenosis, and consequently invasive or non-invasive pressure difference measurement is part of the guidelines for the management of various cases of cardiovascular disease.

Overview of pressure drop in clinical use

Methods to measure the pressure drop across arterial stenosis were being developed even before Cournand, Forssman and Richards developed cardiac catheterisation in the 1940s to investigate pulmonary artery disease (Bloomfield et al., 1946). Catheterisation allowed for simultaneous invasive pressure measurements inside the left ventricle and the ascending aorta. The surplus of pressure in the left ventricle is an indication of aortic stenosis. An example of the pressure traces in a case of severe aortic stenosis is shown in Figure 1-9.

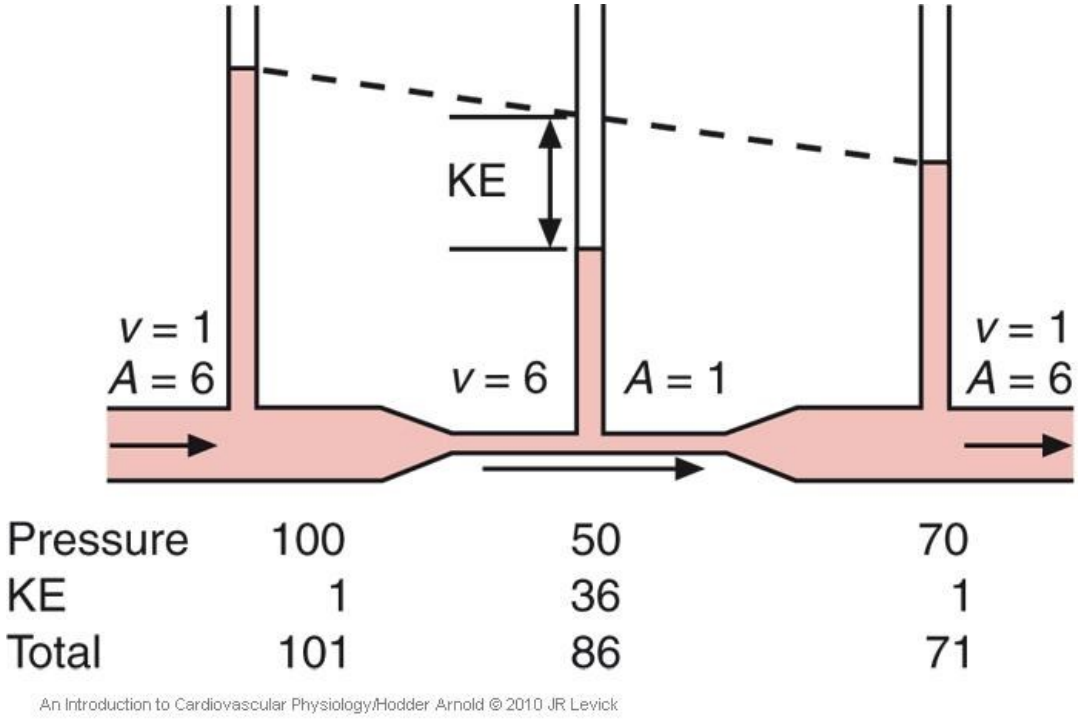

Figure 1-7 Representation of the pressure and kinetic energy (KE) of the flow through a stenosis with significant energy losses. For a given volume flow, velocity *v* increases where the cross-sectional area *A* narrows, for example in a stenosis. Pressure energy is converted into kinetic energy KE at this point. Where the tube widens, i.e. distal to the stenosis, KE is reconverted to the original pressure minus the amount of pressure energy lost inside the stenosis. The overall pressure deficiency is indicated by the broken line. (Image from J. Rodney Levick, "An introduction to Cardiovascular Physiology")

By the mid-70s, the development of percutaneous catheterisation of the coronary arteries was introduced (Judkins, 1967, Dotter et al., 1967, Gruentzig and Meier, 1983) and visualisations of the coronary arteries led to better assessment and treatment of coronary artery disease. In the mid-90's, functional assessment of coronary lesions was established, with the introduction of FFR (Pijls et al., 1991, Pijls et al., 1995). Building on the idea that more severe stenoses incur greater pressure drop under the same flow conditions compared to less severe ones, presented by Gould et al in 1974 (Gould et al., 1974b, Gould and Lipscomb, 1974a), FFR consists of simultaneously measuring aortic (proximal) pressure Pa and pressure at a location distal to the diseased area, Pd, with the help of a pressure wire like the one shown in Figure 1-5 and calculating the ratio of distal to aortic pressure (Pd/Pa). The measurements are made under conditions of drug-induced hyperaemia, when resistance to the flow is considered to become minimal and remains near constant over several cardiac cycle (Pijls et al., 1997) (Figure 1-9). Under these conditions, the pressure ratio becomes a surrogate for the volumetric flow rate ratio at the same locations, a measure of functional severity which is far more difficult to measure than pressure.

The effect of volumetric flow rate on coronary pressure drop

Currently, with the rise of the use of Computational Fluid Dynamics (CFD) in clinical applications, many efforts are underway to use non-invasive diagnostic tools in conjunction with CFD to estimate the likely pressure drop in coronary arteries, without the need for catheterisation (Min and Kochar, 2012, Morris et al., 2013). One parameter that can significantly affect the estimate of the pressure drop, but whose importance is often underestimated, is the volumetric flow rate at the time of measurement. In the presence of stenosis, the relationship between flow rate and pressure is not linear, but is best described by a quadratic relationship (Figure 1-8), where the linear term is believed to correspond to viscous losses and the square term to the energy loss due to disturbances in the flow structure at the exit of a stenosis (Gould, 1978b). Thus, for flow limiting stenoses, a small change in flow rate will result a great change in pressure drop. For this reason, knowing the vessel-specific volumetric flow rate with a satisfactory level of accuracy is important for the mathematical modelling of coronary flow.

Furthermore, in the case of intracoronary flow velocity measurement, the presence of the wire inside the artery may cause discernible changes to the flow measurement (Rajabi-Jaghargh et al., 2011, Dash et al., 1999, Torii et al., 2007). Finally, volumetric flow rate is estimated from measurements of flow velocity with little information on the spatial velocity profile, or the actual cross-sectional area of the measurement location.

In summary, pressure drop is very sensitive to changes in volumetric flow rate, the measurement of which is very difficult non-invasively and subject to errors when measured invasively. Consequently, when considering the numerical modelling of coronary pressure drop, all limitations arising from the errors in estimation of volumetric flow rate need to be taken into account.

The mechanics of blood flow and the effect of disease on flow and pressure distribution in the aortic root and the coronary arteries will be presented in more detail in the following chapter.

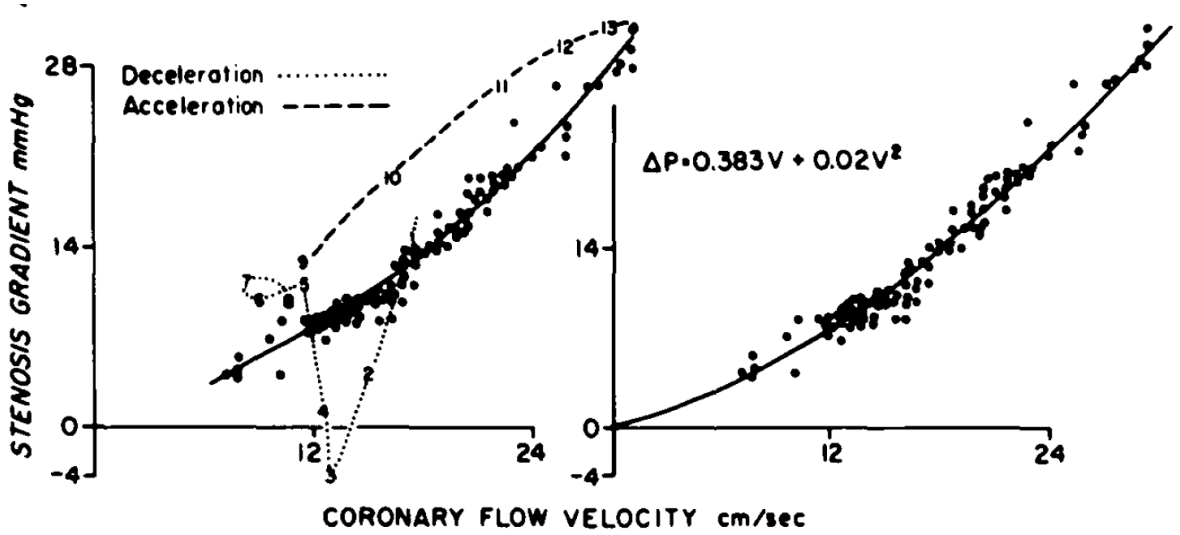

Figure 1-8 Relation between coronary flow velocity and pressure gradient due to a stenosis under resting control conditions.**Left** The pressure drop – flow velocity plot throughout one cardiac cycle. The effects of acceleration and deceleration of the flow are marked by the dashed and dotted lines respectively. **Right** The same plot after the effects of acceleration and deceleration, unrelated to stenosis severity, have been discarded. The relationship between pressure drop and flow velocity is quadratic. Figure adapted from Gould *Circ Res 1978* 43(2): 242-253.

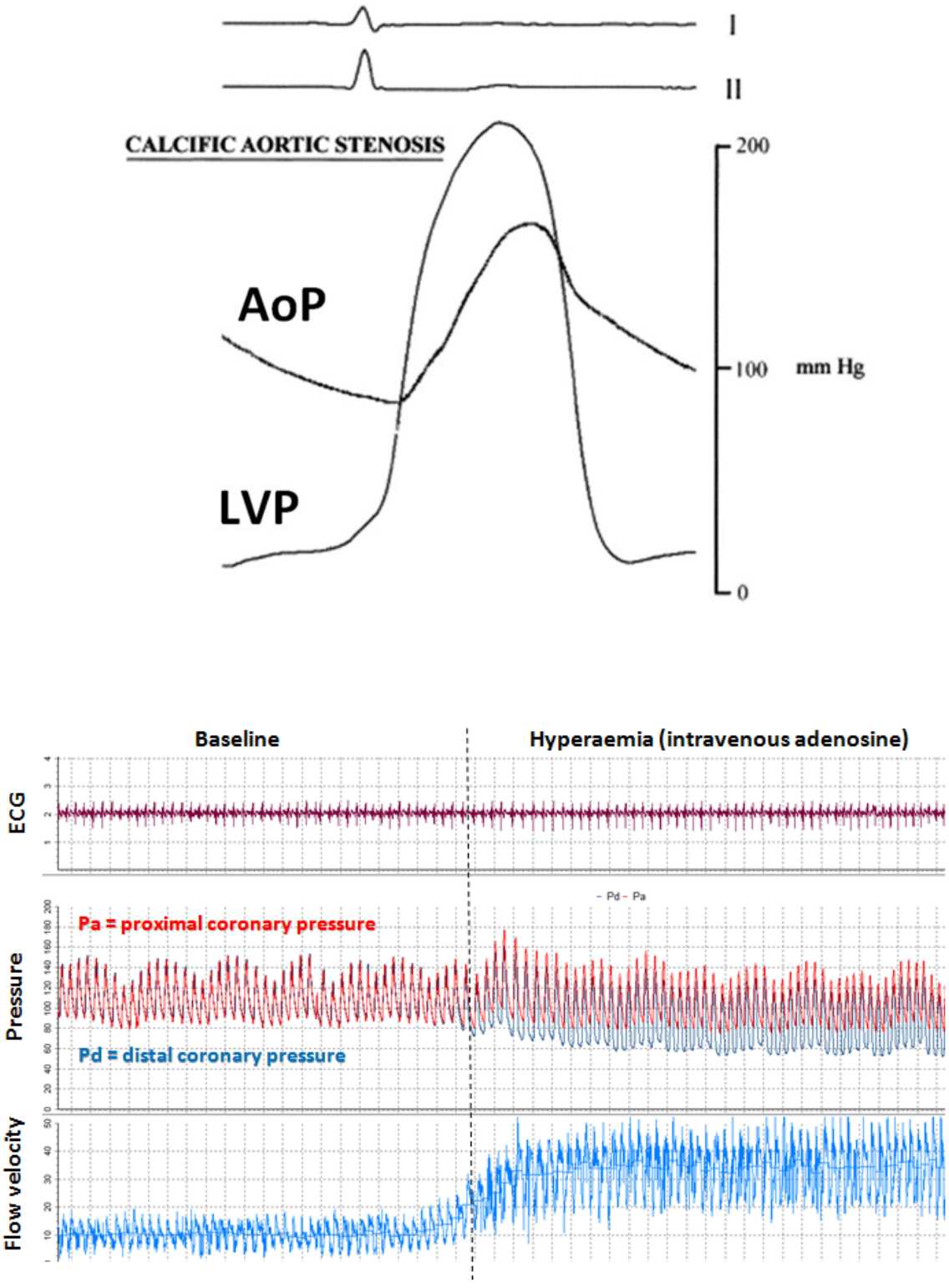

Figure 1-9 Top. Left ventricular pressure (LVP) and aortic pressure measured simultaneously in a patient with severe aortic stenosis. At peak systole the ventricle pressure exceeds aortic pressure by more than 50mmHg. Image adapted from(Rahimtoola, 2006). **Bottom.** Example of a FFR measurement trace. Measurements of proximal and distal pressure are done simultaneously under conditions of drug-induced hyperaemia. The great difference between the proximal (red) and distal (blue) pressure trace indicates the presence of disease. The effect of the hyperaemic drug can be seen in the sudden increase of flow velocity, measured using intracoronary Doppler ultrasound. Image courtesy of Dr Ricardo Petraco and Dr Sukh Nijjer, Hammersmith Hospital, London.

1.2 Objectives of the study and research plan

The aim of this thesis is to explore the role of pressure drop and pressure recovery in cases of aortic valve and coronary artery disease, with the hope of contributing to the better understanding of the underlying scientific mechanisms of cardiovascular disease. It is hoped that a new insight into pressure recovery can be used to relieve the symptoms of aortic valve stenosis in people that are too high-risk to receive the current treatment methods and that the in-depth study of the interaction between pressure and flow in coronary arteries will facilitate the transition to non-invasive estimations of pressure drop across a diseased vessel.

The use of Computational Fluid Dynamics (CFD) to model aortic and coronary haemodynamics has been widespread in the past 15 years. Starting from simple models of idealised geometries and steady laminar flow, CFD has progressed into fully patient-specific studies incorporating complicated anatomy, pulsatile and turbulent flow conditions and other features which bring CFD models ever closer to realistic cardiovascular flows. This powerful tool, however, is subject to the limitations posed by the imaging and functional data necessary for CFD. Therefore, the main objective of the project is to make use of CFD to further increase our understanding of the behaviour of pressure in diseased vessels and find applications for the new knowledge, but also identify the limitations of CFD in the case of coronary artery disease assessment, and propose ways to minimise or overcome them.

The overall objective of the work in this thesis has been broken down into smaller, specific objectives and a research strategy has been outlined. The specific objectives are:

1. To identify the anatomical features which incur the highest energy losses in numerical models of aortic stenosis and coronary artery disease.
2. To conduct a proof-of-concept study showing that it is possible to improve the haemodynamics of aortic stenosis by modifying the anatomy in such a way as to take full advantage of pressure recovery, making use of a validated numerical model that can predict transition to turbulence.
3. To develop a new algorithm for the 3D reconstruction of coronary artery anatomy based on highly accurate imaging data (Optical Coherence Tomography).
4. To use the reconstructed models in numerical simulations, both steady-state and pulsatile, combining the anatomies with the most accurate pressure and flow velocity

measurement data available in fully patient-specific CFD studies with the aim of assessing the ability of CFD to reproduce the measured pressure waveforms.

5. To investigate the effect of parameters such as anatomical model accuracy and flow rate estimation on the accuracy of the CFD-derived pressure drop in models of coronary artery.
6. To compare the volumetric flow rate estimation based on invasive flow velocity data with a gold standard in pulsatile phantom experiments, to identify the extent of the limitations introduced to CFD analysis by the uncertainties involved in the estimation of flow rate.

1.3 Thesis Outline

The thesis starts with Chapters 1 and 2, providing the background and literature review relating to the subject at hand. This is followed by Chapters 3 to 7 where the applications specifically developed during this project are presented.

Chapter 2 includes a detailed description of the medical and engineering background of the project. The medical background section includes a brief presentation of the human circulatory system and its complicated haemodynamics. The nature of cardiovascular disease and one of its main causes, atherosclerosis, are also discussed in this chapter. The effect that atherosclerosis has on blood flow and pressure is discussed with respect to the particular complex haemodynamic conditions observed in the aortic root and the coronary arteries. An overview of the diagnostic (imaging and functional) methods and tools currently available in clinical practice concludes the medical section. The engineering background focuses on the mathematical description of haemodynamics. A review of the mathematical models that have been used in the past to describe blood flow is included in this section. Finally, a literature review of the various experimental, analytical and numerical studies that have attempted to tackle the technical challenges posed by the complicated nature of blood and vessel anatomy are presented, leading to the second section of the thesis where the results of the current project are being presented.

Chapter 3 contains the description of a proof-of-concept study, where it is shown that a minimal modification of the aortic root and proximal ascending aorta anatomy can lead to smaller pressure drop observed across aortic valve stenoses. This CFD study explores the

potential pressure recovery that can be achieved at the presence of modifications, while documenting the technical challenges that the designing of such modifications would incur.

The study of flow and pressure in the coronary arteries is described in Chapters 4 and 5. The custom-developed algorithm that can produce accurate reconstructions of diseased coronary vessels based on OCT images and angiography is described in detail, along with a description of the method's validation in a phantom. Chapter 4 includes the application of the reconstruction method in a group of patients for which there are also pressure and flow velocity data. The results of the pulsatile, fully patient-specific CFD simulations are presented and discussed. In Chapter 6,a sensitivity analysis of the CFD-predicted pressure drop to parameters such as anatomical accuracy and flow rate is conducted. Other possible limitations to CFD as a tool to assess ischaemia due to coronary lesions are also presented and discussed. Chapter 7 comprises of a detailed description of phantom flow experiments conducted in order to assess the error incurred when estimating the volumetric flow rate from flow velocity data.

Chapter 8 concludes the thesis with recommendations on the use of pressure recovery and pressure drop in diagnosis or treatment of cardiovascular disease. The assumptions and limitations of the methodology presented are discussed, and future work suggested in hope that the study presented in this thesis is a step in the right direction to achieve better clinical decision making and new treatment methods in aortic valve and coronary artery disease.

2. Literature Review

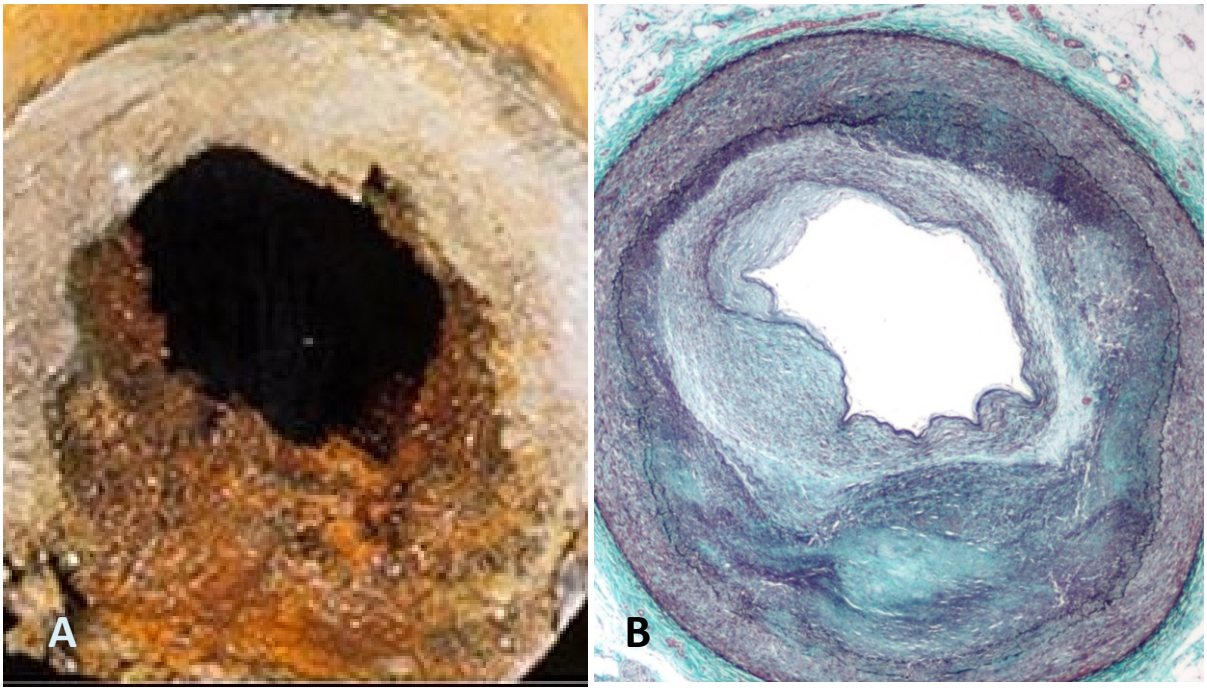

Figure 2-1 A Wax deposits in an oil pipeline and **B** Microscopic view of atherosclerotic plaque build-up in a coronary artery: different scientific fields, same engineering problem.(Image A from http://www.balmsenergy.com/flow_assurance.html)

2.1 Introduction

In this chapter, the engineering and medical background of the research presented in this thesis is explored. The challenges of developing mathematical models for blood flow are discussed, while an overview of the human circulatory system is also given, with a focus on the mechanics of flow and a brief description of atherosclerosis and how accumulation of atherosclerotic plaque in the cardiovascular system can lead to disease. The haemodynamics of the aortic root and the coronary arteries in health and disease are then presented, together with a brief overview of the diagnostic methods used in clinical practice to assess disease severity and the previous computational studies performed in the aortic root and coronary arterial system.

2.2 The basis of computational modelling for cardiovascular flows

2.2.1 The Navier-Stokes equations

When trying to describe a flow mathematically, the starting point is the Navier-Stokes (N-S) equations. They express Newton's second law of the conservation of momentum in a fluid flowing through a "control volume" (Wood, 2006) and, coupled with the equation of continuity, or conservation of mass, they can fully describe the flow field. The N-S equations can be written in several forms. The most useful form of the continuity and conservation of momentum equations when applying a finite volume computational method (FVM) for an incompressible fluid is given by Wood and Xu (2006) as:

$$\rho \frac{\partial}{\partial t} \int_V dV + \rho \int_S (U - U_S) n dS = 0 \tag{2.1}$$

$$\rho \frac{\partial}{\partial t} \int_V U dV + \rho \int_S U(U - U_S) n dS = \int_S [-p + \mu \nabla U + \mu (\nabla U)^T] n dS \tag{2.2}$$

where U is a vector of the instantaneous fluid velocity at time t, p is the static pressure relative to a datum level, n is the unit vector orthogonal to and directed outward from a surface S of the volume, ρ is the fluid density which is assumed constant and μ the fluid viscosity, which in most simulations is also considered constant, as blood is assumed to behave like a Newtonian fluid. U_S is the velocity of the surface S.

The system of equations (2.1) and (2.2) has an exact solution only for laminar flows of simple fluids. For more complex problems, the equations' many non-linearities make obtaining analytical solutions very difficult, therefore approximations and numerical methods are used to solve most problems of practical interest.

Turbulent flows, in particular, are subject to closure problem of turbulence, whereby the number of equations in the model (four, mass conservation and the three components of equation 2.2) are fewer than the number of unknowns in the model (ten: pressure, the three velocity components and the six Reynolds-stress components). Different turbulence models use different approximations in order to define the six Reynolds-stress components and close the system.

2.2.2 Challenges of using computational modelling in cardiovascular flows

Describing blood flow mathematically presents a number of challenges. Blood flow is pulsatile, depending on the frequency at which the heart pumps blood into the aorta. Assuming that a normal person at rest experiences 60 cardiac cycles per minute, one heart beat is around 1 second in duration. In the case of aortic flow, the Reynolds parameters observed place it in the transitional region between laminar and turbulent flow (Figure 2-2). In the case of flow in large arteries, turbulence and transitional models have shown better agreement with experimental data throughout the cycle, whereas the laminar flow assumption presented discrepancies in the velocity profile of the idealized stenosis during mid-acceleration, the phase where turbulence appears (Tan et al., 2008).

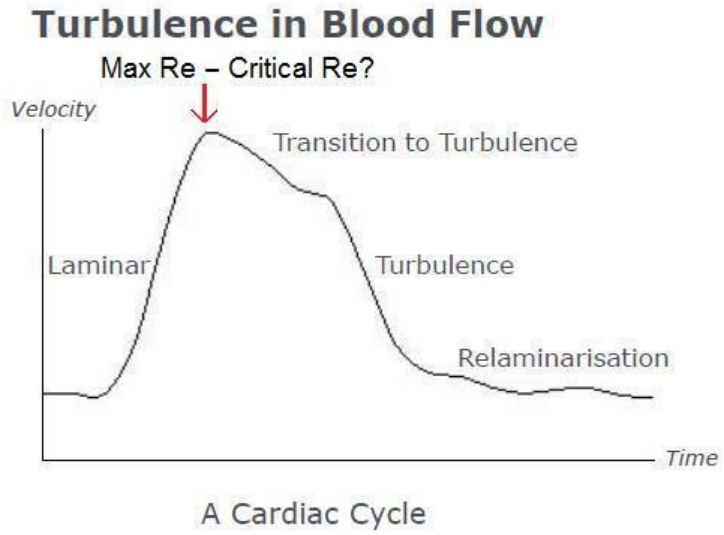

Figure 2-2 A typical cardiac cycle (Velocity vs. Time). For blood flow, the maximum Reynolds number appearing at peak systole can be either above or below the critical Reynolds number for the particular flow (Image courtesy of Dr Felicia P.P. Tan).

Another important factor that hinders the development of a mathematical model is the fact that blood flows through vessels of great geometric complexity (Figure 2-3). Furthermore, haemodynamic forces act on the elastic wall of the vessel, causing it to expand and relax during different phases of the cycle, resulting in the need for models which incorporate fluid-structure interaction (FSI). All these affect the velocity profiles and the shear stress values, and it has been shown that using anatomically accurate models greatly increases the ability of computational modelling to quantitatively match measured data (Tan et al., 2009a).

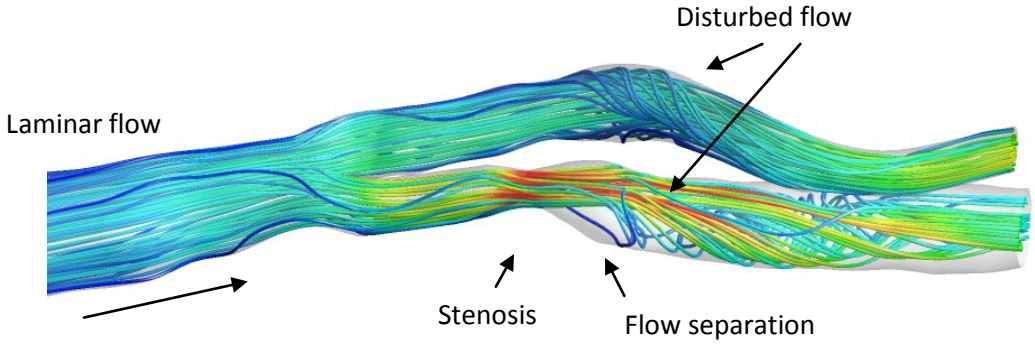

Figure 2-3 Diagram of a vessel containing a bifurcation, showing the effect of geometric complexity on velocity patterns (Image courtesy of Dr Felicia P.P. Tan).

Finally, blood is a non-Newtonian fluid, meaning that its viscosity varies with shear-rate γ (du_i/dx_j), as shown in Figure 2-4. Blood is a shear-thinning fluid, meaning that its viscosity decreases as shear-rate increases (Merrill et al., 1963). In the limit where the value of γ is sufficiently large to ignore the change of viscosity with respect to it, but not large enough to cause damage to particles, fluid flow can be approximately assumed to be Newtonian.

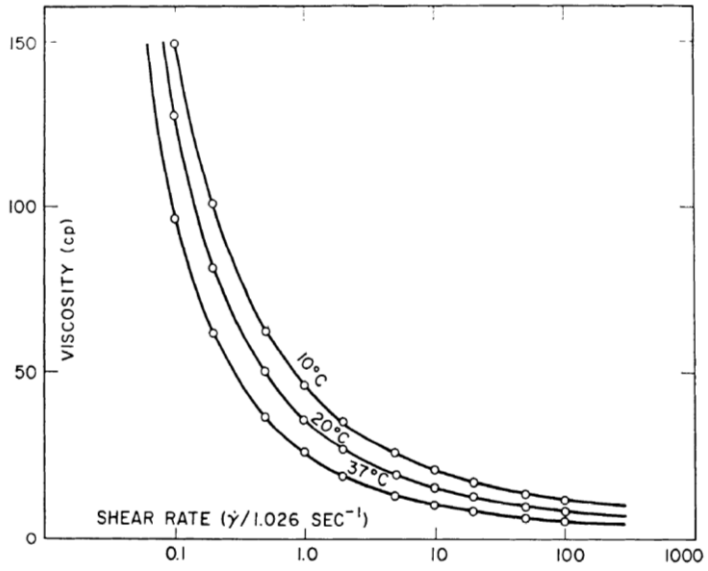

Figure 2-4 Blood viscosity vs. shear rate γ for different temperatures. Blood is a shear-thinning fluid until shear rate reaches about $100s^{-1}$, when viscosity becomes independent of shear rate. Figure adapted from Merill, *J Appl Physiol* 1963 18: 255-260.(Clark, 1976c)

It is still debatable if blood can be accurately modelled as a Newtonian fluid inside large arteries. The average value of shear-rate in the boundary layer of large arteries exceeds $100\ s^{-1}$, which is the minimum value at which blood viscosity is independent of γ. However, this value changes with time, and as the flow is pulsatile and wall shear stress becomes zero at points of flow reversal, it cannot be said for certain that γ is constantly above this value

(Pedley1980). Most models either use Newtonian fluids in their *in vitro* simulations of blood flow (Bluestein and Einav 1994), or make the assumption that the non-Newtonian behaviour of blood can be neglected. In the latter case blood is assumed to have a constant viscosity throughout, usually a value 4 times that of the viscosity of water (4.0 against 1.0 mPas) (Nakamura et al 2006, Kagadis et al 2007, Tan et al 2008 and 2009 among others).

2.3 The mechanics of the human circulatory system

> *"...I found the task so truly arduous... that I was almost tempted to think... that the movement of the heart was only to be comprehended by God. For I could neither rightly perceive at first when the systole and when the diastole took place by reason of the rapidity of the movement..."*
>
> William Harvey, "*De Motu Cordis*", 1628

The circulatory system is an organ system whose primary role is to transfer and deliver oxygen and nutrients to the cells, whilst carrying carbon dioxide and other waste away from the cells.

Blood vessels have different characteristics, depending on their role (Pedley, 1980). Bigger arteries allow blood to travel at high velocities and at a small energy cost from the heart to the various organs; once there, vessel diameters become smaller as they keep branching out and become arterioles and then capillaries. At the capillary level flow is particularly slow, since the vessel diameter is comparable to the size of red blood cells, which often need to deform in order to pass through the vessel (Boryczko et al., 2003).

The increase in total vessel area combined with the increased resistance posed to the flow results in a big drop in both velocity and pressure at the arteriolar level, as shown in Figure 2-5.

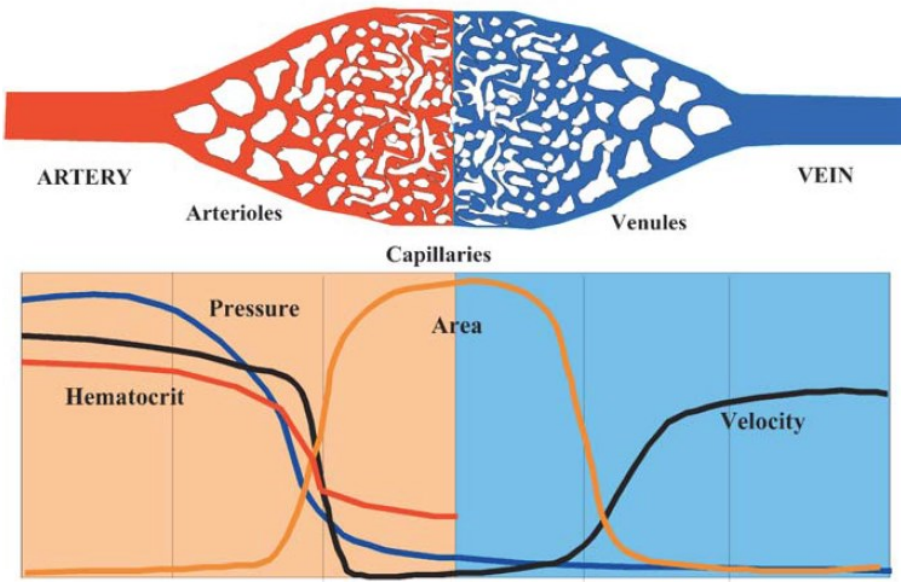

Figure 2-5 Pressure and velocity drop in the circulatory system as a function of total area. Image from (Boryczko et al., 2003).

2.3.1 The main cause of cardiovascular disease: atherosclerosis

Atherosclerosis is the principal source of cerebral and myocardial infarction (stroke and heart attack respectively), the leading cause of death in the US and Europe and a prominent cause of death around the world (Truelsen et al., 2003, Lloyd-Jones et al., 2009). The atheromatous plaque results from the accumulation of lipoproteins which undergo oxidative modification (e.g. oxidised low-density lipoprotein, oxLDL) under the endothelial innermost lining of the luminal wall. This process is accompanied by an inflammatory response involving white blood cells such as monocytes and T-cells which pass from the bloodstream into the sub-endothelium. Monocyte/macrophages try to engulf the lipoproteins, forming lipid-laden foam cells, while proliferation of dedifferentiated smooth muscle cells and the presence of calcium deposits are also commonly observed (Ross, 1993). This process begins as a fatty streak in early life but subsequently results in the formation of a composite material called *atherosclerotic* plaque, or atheroma, Different examples of atherosclerotic plaque are shown in Figure 2-6.

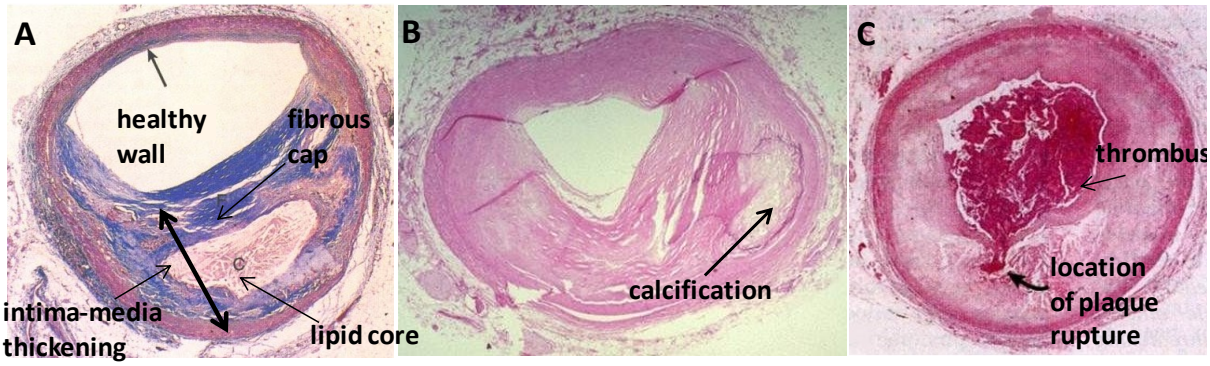

Figure 2-6 Examples of coronary atheromatous plaque under microscopy and staining..A. Lipid core with fibrous cap lesions are more likely to rupture.**B**. Lesions with calcification are considered stable. **C**. Thrombus formed after plaque rupture. (Images from http://library.med.utah.edu/WebPath/)

The mechanism of atherosclerosis formation and progress is very complex and has been studied extensively, but still the interactions between the cells and molecules involved is not entirely clear (Lusis, 2000). Epidemiological studies have shown a multitude of risk factors associated with the formation of atherosclerosis, and they can be divided into two large categories, systemic risk factors and localised risk factors.

The systemic risk factors include elevated cholesterol levels in the plasma (Glass and Witztum, 2001), hypertension (Sun et al., 2000), diabetes (Li and Chen, 2005, Glowinska et al., 2003, Fukuhara et al., 2013), smoking (Kim et al., 2013, Minor et al., 2013), genetic predisposition (Rodrigues et al., 2013, Incalcaterra et al., 2013), age (Nozue et al., 2013) and the male gender (Martini, 2004, Gao and Geng, 2013).

The localised risk factors are mostly associated with abnormal wall shear stress patterns, with studies showing that areas with low (Caro et al., 1969), oscillating (Ku et al., 1985) or both (Malek et al., 1999) wall shear stress patterns correlate with the accumulation of atherosclerotic plaque. There is also suggestion that the high wall shear stress flow conditions resulting from increased flow velocities at vessel narrowings can become harmful, as it can promote the degeneration of the fibrous cap covering the plaque, thus facilitating plaque rapture (Dolan et al., 2013). More recently, the suggestion was made that the multidirectionality of the wall shear stress vector can have an effect in the plaque formation mechanism, with experiments in rabbit aortas indicating that a transverse wall shear stress index incorporating multidirectionality has good correlation with atherosclerosis development sites (Peiffer et al., 2013).

2.3 Aortic Stenosis

2.3.1 The haemodynamics of the aortic valve in health and disease

The aortic valve is situated inside the aortic root and connects the left ventricle with the aorta. It consists of (usually) three leaflets which move passively with the flow to allow the ejection of blood into the aorta during systole, and then prevent the reversal of flow during diastole when the pressure is lower in the relaxing ventricle than in the aorta. Impaired function of the aortic valve can result in smaller opening during systole or insufficient closing of the valve leaflets during diastole, resulting in abnormal flow patterns.

Aortic flow can become intermittently turbulent under certain conditions, which largely depend on an individual's cardiac output and pulse frequency (Nerem and Seed, 1972, Kousera et al., 2013, Bogren and Buonocore, 1999). When cardiac output is high, systolic flow velocity is also high and thus transition to turbulence is more likely. Due to the characteristic geometry of the aortic arch, flow tends to form helical structures during deceleration and diastole, as shown in Figure 2-7.

It is widely thought that the presence of turbulence in the aorta is in itself benign and fairly common, especially during exercise when cardiac output increases (Kilner et al., 1997, Stein and Sabbah, 1976), and poses no danger to an individual's health. In normal aortas, the pressure drop observed across the aortic valve is less than 25 mmHg, and it has been shown (Yacoub et al., 1999) that the recirculation observed just above the aortic valve during closure facilitates flow into the coronary ostia during diastole.

As discussed in the introductory chapter, the most common type of aortic valve disease is aortic stenosis, brought about by the degeneration of the valve leaflets (cusps) (Akerstrom et al., 2013). The degeneration (or aortic valve sclerosis) involves the progressive accumulation of lipids, followed by inflammation and calcification, a process very similar to the formation of atherosclerosis (but with no smooth muscle cell proliferation), which can be present for many years before symptoms appear. Aortic stenosis is more common in elderly patients, who are also likely to have comorbidities, such as coronary artery disease (Stefanini et al., 2013). The presence of aortic stenosis can result in ischaemia even when coronary atherosclerotic lesions are not present (Davies et al., 2011, Broyd et al., 2013, Camuglia et al., 2013). Untreated aortic stenosis has a 3-year mortality rate of more than 50% (Ross and Braunwald, 1968), which increases to more than 80% in cases of severe cardiac comorbidities (Iung et al., 2003).

The presence of stenosis results in stiffer valve leaflets, which cannot open or close fully, resulting in problems both during systole and during diastole. During systole, the limited cross-sectional area of the valve causes an increase in the pressure drop observed (Yap et al., 2010). In order to compensate for the loss of pressure, systolic pressure inside the left ventricle increases, resulting in overexertion of the heart muscle. If left untreated, the increased pressure can result in hypertrophic cardiomyopathy (Smith and Squiers, 2013), which can then cause symptoms such as angina, syncope or dyspnoea (Fallen et al., 1967), due to the fact that the coronary circulation can no longer provide enough oxygen to the hypertrophic heart muscle, leading to ischaemia in the subendocardium (Davies et al., 2011).

During diastole, a valve which is not fully closed will result in aortic regurgitation and results in reduced forward flow, compensated for by an increase in both the systolic and diastolic pressures and a shortened R-R interval. A schematic representation of aortic valve stenosis is shown in Figure 2-8A, while an image of the resulting hypertrophy is shown in Figure 2-8B.

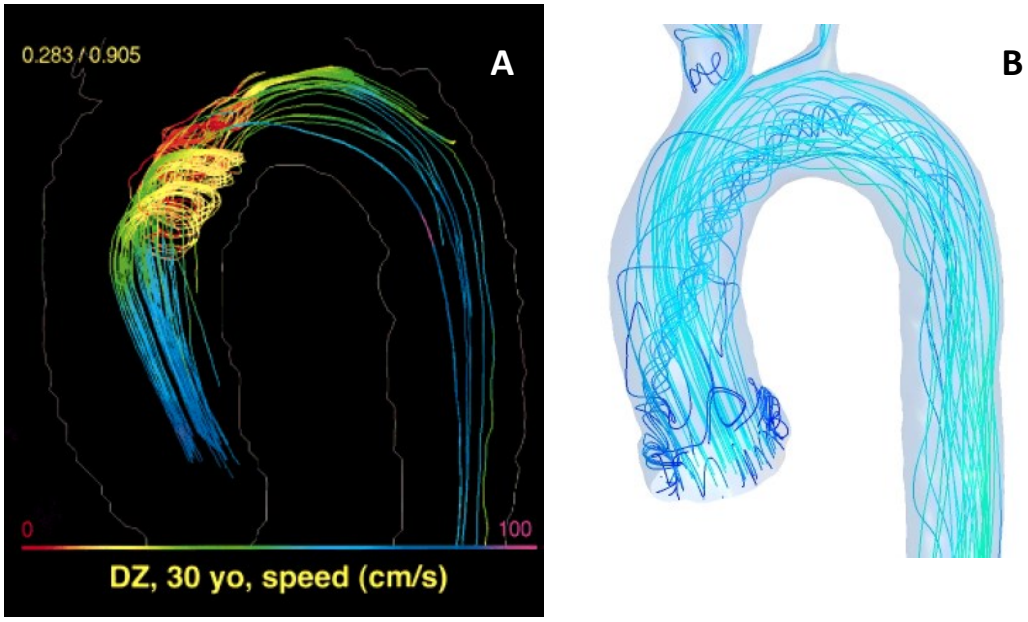

Figure 2-7 Helical flow structures in healthy human aortas during flow deceleration after valve closure (**A**) visualised in 4D MRI (Bogren and Buonocore, 1999) and (**B**) observed in numerical studies (Kousera et al., 2013). The presence of intermittent turbulence in the aorta is considered benign.

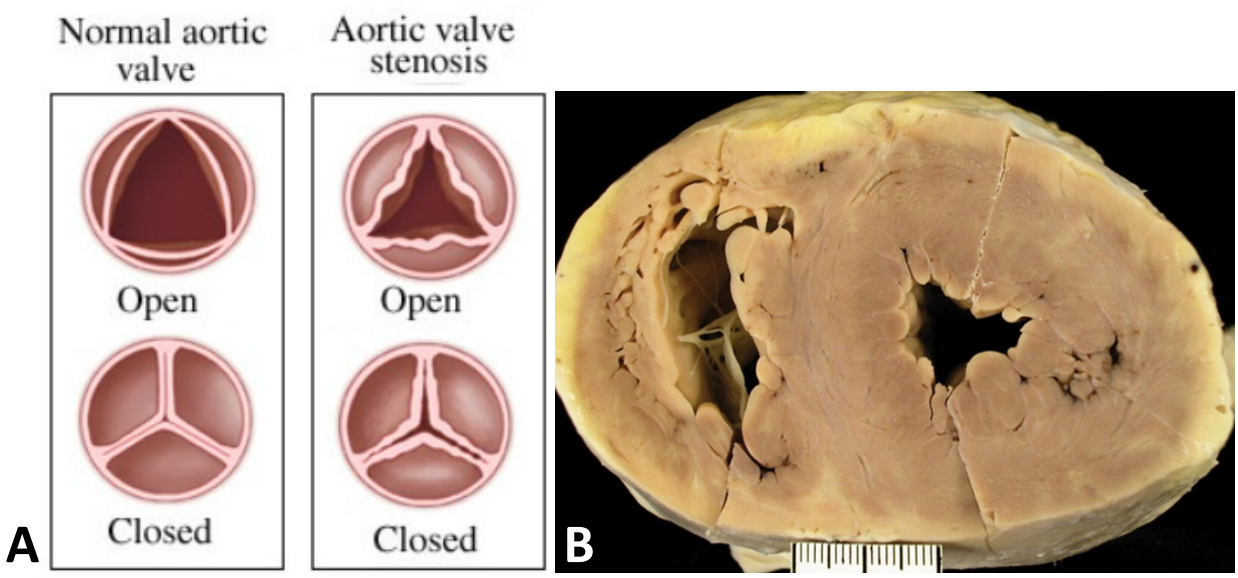

Figure 2-8 A Schematic representation of aortic stenosis.**B**Left ventricular cavity reduced by hypertrophic muscle. (Image adapted from (Ho, 2009))

2.3.2 Treatment options for aortic stenosis

It has been shown that, unlike atherosclerosis, the progress of aortic valve disease cannot be stopped or reversed using current medical therapy, and so the only viable treatment options are those that can help reduce the pressure drop through the valve, whilst preventing regurgitation (Wong et al., 2013, Cowell et al., 2005). This most commonly involves the surgical replacement of the valve (aortic valve replacement surgery, or AVR, shown in Figure 2-9A). AVR is a very invasive process, which is often too high-risk for the elderly population, or population with comorbidities, that forms a large percentage of aortic stenosis patients (Bonow et al., 2006).

A milder, less invasive procedure called Transcatheter Aortic Valve Implantation (TAVI) was developed in the previous decade (Cribier et al., 2002).In TAVI, a replacement (typically bovine) valve is placed inside a crumpled metal frame, and is then delivered via catheter and expanded into place, pushing the original valve against the aortic wall (Figure 2-9B).

The procedure can be very similar to coronary balloon stenting, but an important difference is the need for external pacing at high heart rates in order to maintain the original valve orifice open for as long as possible to place and expand the new valve. The TAVI

procedure is currently considered the best available option for those who are too high-risk to get conventional, surgical AVR, as evidenced mainly from the results of the randomised clinical PARTNER trial (Svensson et al., 2014, Leon et al., 2010) and research into specific types of valves such as the Core Valve Revalving System (Piazza et al., 2008).

However, TAVI is not without complications. There is a 30-day mortality rate of 5-15%, usually due to stroke or vascular complications, which can occur in up to 20% of TAVI patients. The increased mortality risk can be attributed to the fact that TAVI is recommended only for high-risk patients in the ESC guidelines (Vahanian et al., 2012) who have more severe forms of disease and/or comorbidities. In a study comparing TAVI and AVR in patients with similar disease severity (Smith et al., 2011) it was found that the two procedures result in comparable mortality at 1 year, but the patients who received TAVI were more likely to have cerebrovascular events, vascular complications and paravalvular leaks compared to the AVR group. Furthermore, the presence of coronary artery disease results in increased negative procedural and late outcomes compared to combined AVR and coronary artery by-pass surgery (Dewey et al., 2010), while the two-year follow-up of the PARTNER trial shows that increased paravalvular leak in the TAVI group is associated with increased late mortality compared to the AVR group (Kodali et al., 2012).

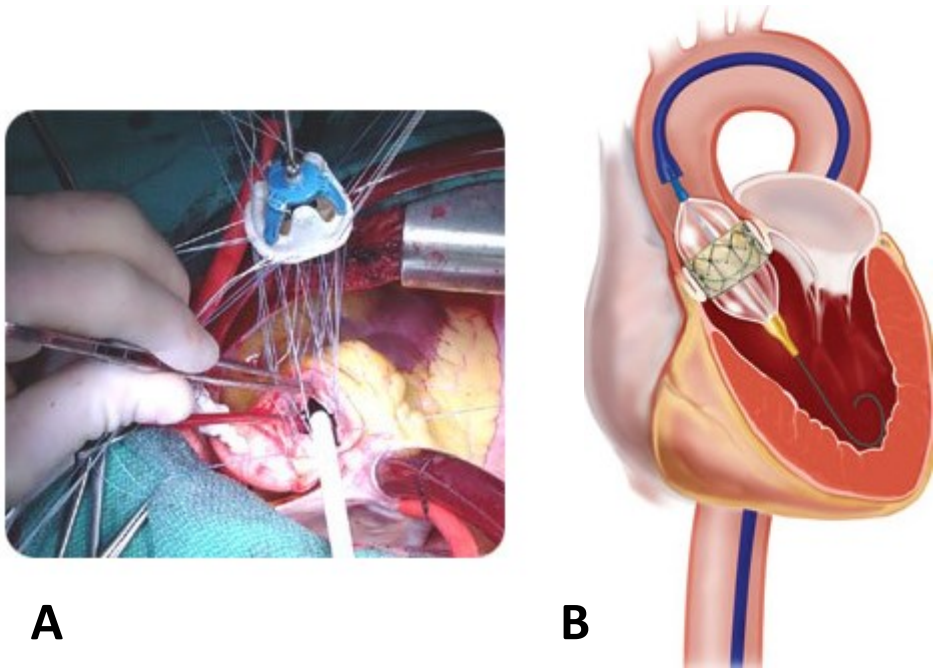

Figure 2-9 Treatment options for aortic stenosis involve the replacement of the diseased valve. **A** Surgical aortic valve implantation.**B** Graph of atranscatheter aortic valve implantation (TAVI) device delivered using a femoral approach (Edwards Lifesciences).

A proof-of-concept study using computational fluid dynamics to explore the potential of a TAVI-like device that would not require aggressive balloon expansion is presented in Chapter 3.

2.3.3 Diagnostic techniques for aortic stenosis

Transthoracic echocardiography is the most common imaging technique used in the diagnosis of aortic sclerosis and stenosis. Echocardiography is quick, cheap and easy to perform at the bedside, with the ability to image large portions of the heart in a very short time, allowing quick evaluation of a patient's heart movement in real time. The aortic valve cusps are best visible in the parasternal short axis and long axis and apical views (Bilen et al., 2014). Echocardiography can provide information on the degree of valve calcification, left ventricular function and wall thickness (Baumgartner et al., 2009). Exercise test and pharmacological (dobutamine) stress echocardiography can be used to assess the presence of ischaemia (Picano, 1992, Lancellotti and Magne, 2013). However, measuring the aortic orifice area from echocardiography is subject to errors and inconsistencies caused by the low image resolution and poor contrast, resulting in operator-dependent and therefore less robust assessment.

CT has also been used to evaluate the valve orifice area with greater accuracy than echocardiography (Bouvier et al., 2006), as well as the size and orientation of the aortic annulus to determine the size of the prosthetic valve required in potential valve replacement surgery (Samin et al., 2014). It is also used to detect calcification, which is visible on CT images as bright white patches. Assessing the degree of calcification (calcium score) can be helpful in assessing the potential for treatment with TAVI, as the presence of calcification poses increased risk of embolization (Tops et al., 2008).

Echocardiography used in conjunction with Doppler ultrasound velocity measurements is the preferred technique to assess aortic stenosis in clinical practice (Baumgartner et al., 2009). Doppler echocardiography can be used to indirectly estimate the valve orifice area, using the continuity equation (derived from the law of conservation of mass) as shown in Figure 2-10. The pressure differential between the proximal (left ventricular) and distal (aortic) side of the valve can also be calculated by applying the Bernoulli equation (Wood, 1999) using the measured velocity at the aortic valve level.

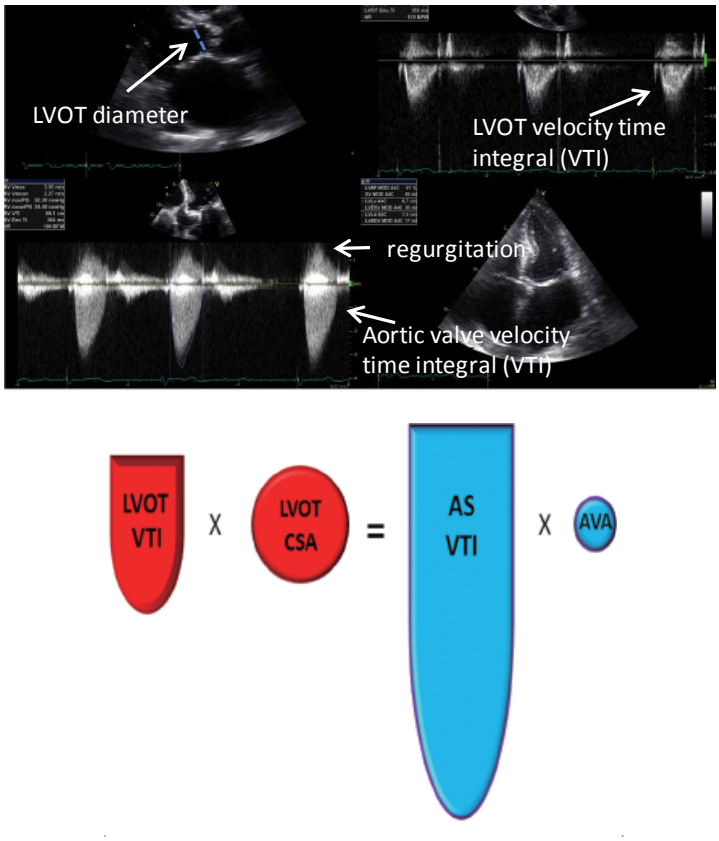

Figure 2-10 Estimation of aortic valve area (AVA) using Doppler echocardiography. The velocity time integral (VTI) is the most accurate way of estimating the mean velocity on the cross-section, and is measured at both the LVOT and the aortic valve level. The continuity equation (schematically represented in the bottom panel) can then be applied to estimate the aortic valve area. Images adapted from (Ozkan, 2012).

The multiple available diagnostic criteria result in a set of guidelines for severity assessment. An aortic valve area of less than 1 cm^2 , a velocity ratio (LVOT level /aortic valve level) of less than 0.25, a peak velocity through the valve of more than 4m/s or mean pressure gradient through the valve of > 40 mmHg are all considered indications of disease (Vahanian et al., 2013, Baumgartner et al., 2009).

2.3.4 Computational modelling of laminar-turbulent transition in the aorta

The Shear Stress Transport turbulence model

One of the most commonly used group of models for turbulent flow simulations is the Reynolds-Averaged Navier-Stokes models (RANS). In this approach, Reynolds decomposition of the flow variables into mean and fluctuating parts is used (Dewan, 2011)(Wilcox 2006). Two-equation RANS models are the simplest complete (closed) models of turbulence, which means that they can be used to "predict properties of a given flow with no prior knowledge of the turbulence structure" (Wilcox 1993), as they do not need to relate the turbulence length scale to some typical flow dimension.

The k-ε (Jones and Launder, 1972) and k-ω (Wilcox, 2006) models are the most commonly used two-equation RANS models. The k-ε model cannot give satisfactory results inside the boundary layer, and generally wall functions have to be used; the k-ω model, though it can simulate flow near the wall, is too sensitive to the entry conditions and it can be more complicated than is needed to describe the bulk flow. In general, these two models give acceptable results for fully turbulent flows, but they do not adapt to transitional flow equally well.

Menter (Menter, 1994b) combined k-ε and k-ω models to form the Shear Stress Transport (SST) model. Blending functions that enable the model to switch from the k-ε model in the core flow and outer zone of the boundary layer to the k-ω model in the inner zones are used, thus combining the advantages of the component models to create a model more accurate and more widely applicable than the previous two.

For the derivation of the model, the k-ε transport equations for turbulence kinetic energy k and dissipation ε are expressed in terms of ω (root-mean-square fluctuating vorticity). (Note that all equations in this paragraph have been multiplied by density, and therefore are expressed in terms of dynamic viscosity. Also, D/Dt is the Lagrangian derivative = $\partial/\partial t + u_i\partial/\partial x_i$):

Original k-ω model (Wilcox, 1993, Menter, 1994a) :

$$\frac{D\rho k}{Dt} = \tau_{ij}\frac{\partial U_i}{\partial x_j} - \beta^*\rho k\omega + \frac{\partial}{\partial x_j}\left[(\mu + \sigma_{k1}\mu_T)\frac{\partial k}{\partial x_j}\right] \tag{2.3}$$

$$\frac{D\rho\omega}{Dt} = \frac{\gamma_1}{\nu_T}\tau_{ij}\frac{\partial U_i}{\partial x_j} - \beta_1\rho\omega^2 + \frac{2\rho\sigma_{\omega 1}}{\omega}\frac{\partial k}{\partial x_j}\frac{\partial \omega}{\partial x_j} + \frac{\partial}{\partial x_j}\left[(\mu + \sigma_{\omega 1}\mu_T)\frac{\partial \omega}{\partial x_j}\right] \tag{2.4}$$

Modified k-ε model (Menter, 1994a):

$$\frac{D\rho k}{Dt} = \tau_{ij}\frac{\partial U_i}{\partial x_j} - \beta^*\rho k\omega + \frac{\partial}{\partial x_j}\left[(\mu + \sigma_{k2}\mu_T)\frac{\partial k}{\partial x_j}\right] \quad (2.5)$$

$$\frac{D\rho\omega}{Dt} = \frac{\gamma_2}{\nu_T}\tau_{ij}\frac{\partial U_i}{\partial x_j} - \beta_2\rho\omega^2 + \frac{2\rho\sigma_{\omega 2}}{\omega}\frac{\partial k}{\partial x_j}\frac{\partial \omega}{\partial x_j} + \frac{\partial}{\partial x_j}\left[(\mu + \sigma_{\omega 2}\mu_T)\frac{\partial \omega}{\partial x_j}\right] \quad (2.6)$$

where:

U_i: mean velocity

$\tau_{ij} = -\rho\overline{u_j' u_i'}$, where u' is the fluctuation of the velocity, Reynolds-stress tensor

$k = \frac{1}{2}\overline{u_i' u_i'}$, turbulence kinetic energy

μ: dynamic viscosity

μ_T: dynamic eddy viscosity

ν_T : kinematic eddy viscosity

Auxiliary relations and closure coefficients:

$$\sigma_{k1} = 0.5, \sigma_{\omega 1} = 0.5, \beta_1 = 0.0750, \beta^* = 0.09, \kappa = 0.41, \gamma_1 = \frac{\beta_1}{\beta^*} - \frac{\sigma_{\omega 1}\kappa^2}{\sqrt{\beta^*}}$$

$$\sigma_{k2} = 1, \gamma_2 = \frac{\beta_2}{\beta^*} - \frac{\sigma_{\omega 2}\kappa^2}{\sqrt{\beta^*}}, \sigma_{\omega 2} = 0.856\ \beta_2 = 0.0828,$$

$$\beta = \beta_0 f_\beta, \beta_0 = 0.0708, f_\beta = \frac{1+85\chi_\omega}{1+100\chi_\omega}, \chi_\omega \equiv \left|\frac{\Omega_{ij}\Omega_{jk}S_{ki}}{(\beta^*\omega)^3}\right|$$

The Ω_{ij} and S_{ij} terms appearing in the definition of χ_ω are called the mean-rotation and mean-strain-rate tensors respectively, and are functions of the velocity gradients.

The procedure followed is to take the two transport equations from the k-ω model and multiply them by a blending function F_1, while the transformed k-ε equations shown above are multiplied by (1 - F_1). Then, the corresponding equations of each model are added together to give the new model:

$$\frac{D\rho k}{Dt} = \tau_{ij}\frac{\partial U_i}{\partial x_j} - \beta^*\rho k\omega + \frac{\partial}{\partial x_j}\left[(\mu + \sigma_k\mu_T)\frac{\partial k}{\partial x_j}\right] \quad (2.7)$$

$$\frac{D\rho\omega}{Dt} = \frac{\gamma}{\nu_T}\tau_{ij}\frac{\partial U_i}{\partial x_j} - \beta\rho\omega^2 + \frac{\partial}{\partial x_j}\left[(\mu + \sigma_\omega\mu_T)\frac{\partial \omega}{\partial x_j}\right] + 2\rho(1 - F_1)\sigma_{\omega 2}\frac{1}{\omega}\frac{\partial k}{\partial x_j}\frac{\partial \omega}{\partial x_j} \quad (2.8)$$

where the constants σ_k and σ_ω of the new model were calculated according to the formula:

$$\varphi = \varphi_1 F_1 + (1 - F_1)\, \varphi_2,\ \varphi = model\ constant \tag{2.9}$$

The function F_1 has been designed to be one near the wall region, thus activating the original k-ω model, zero away from the surface, and the blending takes place in the outer parts of the boundary layer.

A limiter in the kinematic eddy-viscosity is incorporated in the SST model, which enables it to solve accurately for flows where adverse pressure gradients appear. This is because in adverse pressure gradient flows, the ratio of production to dissipation may be higher than one, something that the k-ε and k-ω models could not capture. In those cases Bradshaw's assumption that the turbulent shear stress is proportional to the turbulence kinetic energy is not satisfied, which could end in overprediction of the turbulence-viscosity (Tan et al., 2008). The new kinematic viscosity equation, which satisfies Bradshaw's assumption at all times, is:

$$\nu_T = \frac{\alpha_1 k}{\max(\alpha_1 \omega; \Omega F_2)} \tag{2.10}$$

where F_2 is another blending function that is one for the flow inside the boundary layer and zero for regions of free shear flow.

The blending functions are:

$$F_1 = \tanh({arg_1}^4) \tag{2.11}$$

where $arg_1 = \min(\max\left(\frac{\sqrt{k}}{0.09\omega y}, \frac{500\nu}{y^2\omega}\right), \frac{4\rho\sigma_{\omega 2} k}{CD_{kw} y^2})$ (2.12)

y is the distance to the closest wall and CD_{kw} is defined as:

$$CD_{kw} = \max(2\rho\sigma_{\omega 2} \frac{1}{\omega} \frac{\partial k}{\partial x_j} \frac{\partial \omega}{\partial x_j}, 10^{-10}) \tag{2.13}$$

$$F_2 = \tanh({arg_2}^2) \tag{2.14}$$

where: $arg_2 = \max\left(\frac{\sqrt{k}}{0.09\omega y}, \frac{500\nu}{y^2\omega}\right)$ (2.15)

The model constants are: $\alpha = 5/9$, $\beta = 0.075$, $\sigma_\omega = 0.5$, $\alpha_1 = 0.31$

Transition modelling

Laminar-turbulent transition is a complex phenomenon, but it's not out of the range of RANS methods. With the addition of proper correlations that are taking transition into account, RANS-based transitional models have been developed, which satisfy almost all the requirements for a reliable and robust transitional model (Menter et al., 2006b).

The Shear Stress Transport model with transitional correlations

The SST model has been improved to describe transitional flows, by coupling transport equations for the intermittency γ, and transition momentum thickness Re, informed by empirical correlations, with the SST hybrid k-ε/k-ω model. Additionally, a separated shear layer transition treatment is incorporated.

The intermittency factor γ quantifies the intermittent behaviour that is exhibited by flows during transition. It is defined as the relative fraction of time during which the flow is turbulent at a certain position. It ranges from zero at the transition point to 100 percent at the end of transition when the flow is fully turbulent (Steelant and Dick, 2001).The transport equation for the intermittency γ needs to be added to the model, in order to turn on the production term of the turbulence kinetic energy downstream of the transition point in the boundary layer (Menter et al., 2006):

$$\frac{\partial \rho\gamma}{\partial t} + \frac{\partial \rho U_j \gamma}{\partial x_j} = P_\gamma - E_\gamma + \frac{\partial}{\partial x_j}\left[\left(\mu + \mu_T/\sigma_f\right)\frac{\partial \gamma}{\partial x_j}\right] \quad (2.16)$$

The transition source term is:

$$P_\gamma = F_{length} c_{a1} \rho S [\gamma F_{onset}]^{0.5} (1 - \gamma) \quad (2.17)$$

where S is the absolute value of the strain rate. The function F_{onset} is there to make this term zero in the laminar boundary layer upstream of the transition and activate it when the local strain-rate Reynolds number exceeds the local transition criteria. The function of F_{onset} is such that its value switches rapidly from zero in a laminar boundary layer to one downstream of a transition onset. It's a function of the strain-rate (or vorticity) Reynolds number, Re_V and the turbulent Reynolds number R_T:

$$\mathrm{Re_V} = \frac{\rho \mathrm{y}^2}{\mu} \mathrm{S},\ R_T = \frac{\rho k}{\mu \omega} \tag{2.18}$$

$$F_{onset1} = \frac{\mathrm{Re_V}}{2.193 \mathrm{Re}_{\theta \mathrm{c}}} \tag{2.19}$$

$$F_{onset2} = \min(\max(F_{onset1}, F_{onset1}^4), 2.0) \tag{2.20}$$

$$F_{onset3} = \max(1 - \left(\frac{\mathrm{R_T}}{2.5}\right)^3, 0) \tag{2.21}$$

$$F_{onset} = \max(F_{onset2} - F_{onset3}, 0) \tag{2.22}$$

$Re_{\theta c}$ that appears in equation 2.19 is the critical Reynolds number where the intermittency starts to increase in the boundary layer, and is therefore thought as the location where turbulence starts to grow, as opposed to $Re_{\theta t}$ which is the location where the velocity profile starts to deviate from the laminar profile. The relation between the two is given by an empirical correlation. F_{length} that appears in equation 2.17 is also a function of $Re_{\theta t}$.

The destruction/relaminarisation source is defined as:

$$E_\gamma = c_{a2} \rho \Omega \gamma F_{turb} (c_{e2} \gamma - 1) \tag{2.23}$$

where Ω is the vorticity magnitude. This term is used in two ways: it ensures that the intermittency is close to zero in the laminar boundary layer and it provides a means for the intermittency to return to zero when relaminarisation occurs. F_{turb} is a function used to deactivate the destruction/relaminarisation source when the flow is fully turbulent:

$$F_{turb} = e^{-\frac{{R_T}^4}{4}} \tag{2.24}$$

The constants for the intermittency equation and the related functions are:

$c_{a1} = 2.0$, $c_{e2} = 50, c_{a2} = 0.06$, $\sigma_f = 1.0$

In order to capture the non-local influence of turbulence intensity an equation for the momentum thickness Reynolds number $\overline{Re_{\theta t}}$ is needed. This is defined as:

$$\frac{\partial \rho \overline{Re_{\theta t}}}{\partial t} + \frac{\partial \rho U_j \overline{Re_{\theta t}}}{\partial x_j} = P_{\theta t} + \frac{\partial}{\partial x_j}\left[\sigma_{\theta t}(\mu + \mu_T)\frac{\partial \overline{Re_{\theta t}}}{\partial x_j}\right] \quad (2.25)$$

The role of the source term $P_{\theta t}$is to force the transported scalar $\overline{Re_{\theta t}}$ to match the local value of $\overline{Re_{\theta t}}$ and is given by:

$$P_{\theta t} = c_{\theta t}\frac{\rho}{t}(Re_{\theta t} - \overline{Re_{\theta t}})(1.0 - F_{\theta t}) \text{ , } t = \frac{500\mu}{\rho U^2} \quad (2.26)$$

t is a timescale introduced for dimensional reasons. $F_{\theta t}$is a blending function that is zero in the free stream and one in the boundary layer and it is used in order to deactivate the source term and allow the value of $\overline{Re_{\theta t}}$ in the free stream to diffuse into the boundary layer.

$$F_{\theta t} = \min(\max\left(F_{wake}e^{-\left(\frac{y}{\delta}\right)^4}, 1.0 - \left(\frac{\gamma - \frac{1}{c_{e2}}}{1.0 - \frac{1}{c_{e2}}}\right)^2\right), 1.0) \quad (2.27)$$

$$\theta_{BL} = \frac{\overline{Re_{\theta t}}\mu}{\rho U}, \quad \delta_{BL} = \frac{15}{2}\theta_{BL} \text{ ,} \delta = \frac{50\Omega y}{U}\delta_{BL} \quad (2.28)$$

$$Re_\omega = \frac{\rho \omega y^2}{\mu}, \; F_{wake} = e^{-\left(\frac{Re_\omega}{10^5}\right)^2} \quad (2.29)$$

The constants for this equation are $c_{\theta t} = 0.03$and $\sigma_{\theta t} = 2.0$.

The model as described above made inaccurate predictions of the turbulent reattachment location, placing the reattachment point fat too downstream. This was attributed to the fact that for low free stream turbulence intensity, the turbulence kinetic energy takes longer to grow to a large enough value that will cause the boundary layer to reattach.

To correct this deficiency a modification was introduced to the model, allowing the intermittency to take values larger than one whenever the laminar boundary layer separates. This was achieved using the ratio of the strain-rate Reynolds number Re_V to the momentum thickness Reynolds number Re_θ. For laminar separation the value of the former exceeds the

value of the latter, whereas for all other flows the values are similar. Therefore this ratio is a measure of the size of the laminar separation and is used to increase the production of turbulence kinetic energy. The modifications for separation induced transition are therefore:

$$\gamma_{sep} = \min(s_1 \max\left(\left[0, \left(\frac{Re_V}{3.235 Re_{\theta c}}\right) - 1\right] F_{reattachment}, 2\right) F_{\theta t} \tag{2.30}$$

$$F_{reattachment} = e^{-\left(\frac{R_T}{20}\right)^4} \ , \ \gamma_{eff} = \max\left(\gamma, \gamma_{sep}\right) \ , s_1 = 2 \tag{2.31}$$

The model uses three empirical correlations:

$$Re_{\theta t} = f(Tu, \lambda_\theta), \ \ F_{length} = f(\overline{\mathrm{Re}_{\theta \mathrm{t}}}) \ , Re_{\theta c} = f(\overline{\mathrm{Re}_{\theta \mathrm{t}}}) \tag{2.32}$$

where *Tu* is the turbulence intensity and λ_θ is Thwaites pressure gradient coefficient:

$$Tu = 100 \frac{\sqrt{2k/3}}{U} \ , \qquad \lambda_\theta = \frac{\rho \theta^2}{\mu} \frac{dU}{ds} \tag{2.33}$$

The above model can be coupled with a modified version of the SST model presented previously. The modified equations of the SST are:

Equation for the eddy viscosity:

$$\mu_{\mathrm{T}} = \min\left[\frac{\rho \mathrm{k}}{\omega}, \frac{\alpha_1 \rho \mathrm{k}}{\mathrm{SF}_2}\right] \tag{2.34}$$

Equation for the turbulence kinetic energy:

$$\frac{\partial \rho k}{\partial t} + \frac{\partial \rho U_j k}{\partial x_j} = \widetilde{P_k} - \widetilde{D_k} + \frac{\partial}{\partial x_j}\left[(\mu + \sigma_k \mu_T) \frac{\partial k}{\partial x_j}\right] \tag{2.35}$$

Equation for the specific dissipation rate:

$$\frac{\partial \rho \omega}{\partial t} + \frac{\partial \rho U_j \omega}{\partial x_j} = \alpha \frac{P_k}{\nu_T} - D_\omega + CD_\omega + \frac{\partial}{\partial x_j}\left[(\mu + \sigma_k \mu_T) \frac{\partial \omega}{\partial x_j}\right] \tag{2.36}$$

where $\widetilde{P_k} = \gamma_{eff} P_k$, $\widetilde{D_k} = \min(\max(\gamma_{eff}, 0.1), 1.0) D_k$ (2.37)

The only difference between this and the original SST model is the appearance of the effective intermittency γ_{eff}.

One last modification had to be made in the original SST model and that involved the blending function F_1 that switches between the k-ω and the k-ε model. In the centre of the laminar boundary layer F_1 could potentially switch from one to zero, which is not desirable, as the k-ω model must be active in both the laminar and turbulent boundary layer. The modified blending function is shown below:

$$R_y = \frac{\rho y\sqrt{k}}{\mu},\ F_3 = e^{-\left(\frac{R_y}{120}\right)^8},\ F_1 = \max(F_{1orig}, F_3) \tag{2.38}$$

where F_{1orig} is the original blending function from the SST model.

2.3.5 Computational aorta and aortic root studies

Aortic flow was one of the first applications of CFD in physiological studies. Already in 1985 two studies investigating flow through normal and prosthetic aortic valves were published (Idelsohn et al., 1985, Stevenson and Yoganathan, 1985). Most CFD studies in the 80s and early 90s were done on idealised geometries, usually straight, cylindrical tubes of diameter corresponding to the studied vessel, using simple, steady-state or sinusoidal boundary conditions. Symmetric or eccentric stenoses were added to simulate the effects of disease (Sud and Sekhon, 1990, Wong et al., 1991, Yamaguchi, 1993).

Improvements in the imaging resolution of diagnostic techniques such as MRI and CT made the creation of computational models based on patient anatomical data possible (Moore et al., 1999, Taylor et al., 1998, Long et al., 2000, Milner et al., 1998), while the combination of computational and *in vitro* models allowed for the validation of the mathematical codes used (Weston et al., 1998).

The refinement of computational turbulence models allowed for further study into which models can best describe each type of flow. Two-equation RANS models found application in turbulence modelling in the larger arteries(Kagadis et al., 2008),(Tan et al., 2008).(Tan et al., 2009a) used an SST model with transitional correlations (SST Tran) coupled with fluid-structure interaction (FSI) to simulate a patient specific model of an aortic aneurysm, reconstructed using MRI data, and acquired data for time averaged wall shear stress (TAWSS) and wall displacement that could be valuable for predicting and preventing the rupture of the

aneurysm. The predicted flow structure at the distal end of the aneurysm agreed well with the flow structure measured by PC-MRI, giving validation of the method in this application. Following the validation of the transitional model, (Kousera et al., 2013) investigated the most suitable inflow turbulence intensity levels for applications in the human aorta, studying two different levels of turbulence intensity, 1% and 1.5% (values that arise from precious *in vitro* validation experiments on models of the carotid), and found that an inflow level of 1% provides the best agreement with *in vivo* hot film velocity measurements presented in (Stein and Sabbah, 1976).

The aortic root has been of particular interest to CFD researchers, being one of the first applications of CFD in the study of blood flow. The relatively easy access to anatomical and functional data, and the clinical relevance of the flow conditions means a large number of computational aortic valve studies exist, investigating nearly all aspects of aortic root flow including jet symmetry (Ge et al., 2003), diagnosis (DeGroff et al., 1998), effect on device design (Schoenhagen et al., 2011), and comparison of pre-post procedure flow patterns (Tan, 2011).

2.4 Coronary artery disease

2.4.1 The haemodynamics of the coronary artery tree in health and disease

The movement of the heart muscle is a complicated series of coordinated contractions and relaxations, which are triggered and controlled by electric signals and are repeated in every heartbeat, as illustrated in Figure 2-11. Due to the high amount of work performed by the heart muscle cells and the need for these complicated movements, the perfusion of the heart muscle presents challenges which are unique to the heart. It is therefore common to study the system of arteries providing blood to the heart muscle as a separate circulation "loop", the coronary circulation, which provides blood to the myocardium.

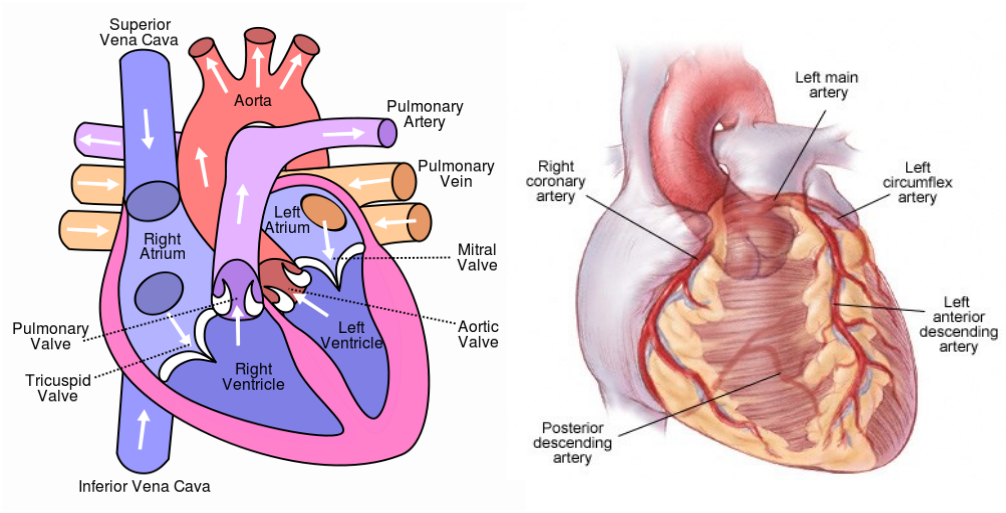

Figure 2-11 Left. Diagram of the human heart and the main vessels through which blood flows in and out of the heart's four chambers. **Right.** Illustration of the epicardial coronary arteries.

The coronary microvasculature and backward-travelling waves

The amount of flow going into the epicardial arteries is controlled by the resistance to the flow posed by the microvasculature, which is located deep inside the heart muscle and is directly affected by the contraction and relaxation of the cardiac muscle (Figure 2-12).

The effect of the heart muscle contracting and relaxing on coronary flow is visible in the relationship between the pressure and flow velocity waveforms (Figure 2-13). Whilst in the aorta the velocity waveform peaks at around the same time as the pressure waveform, in the left coronary artery peak flow occurs during diastole, and in the right coronary artery two

distinct peaks can be seen, one in systole and one in diastole. These actions can be seen in the wave intensity analysis of the coronary circulation (Sen et al., 2013b). A cluster of forward and backward-travelling waves appear during systole and early diastole. During later diastole, however, there are no evident waves in either the coronary or aortic circulation, and the pressure and velocity waveform appear to be falling at the same rate, suggesting quasi-constant resistance at this part of the cycle, which is called the diastolic wave-free period (Sen et al., 2012).

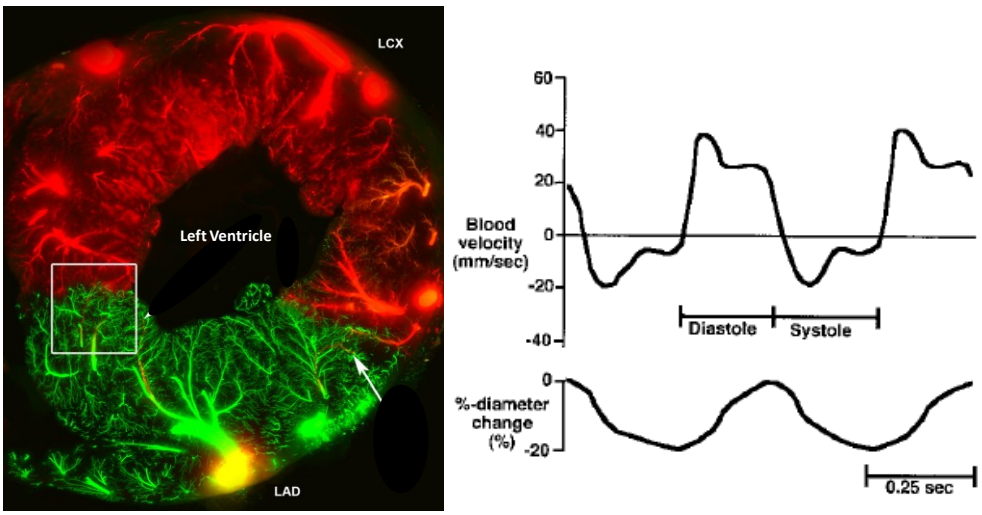

Figure 2-12 Left An image of the intramural microvasculature of a porcine heart taken using imaging microtome. Image adapted from (van den Wijngaard et al., 2011).**Right** Variation of microvessel diameter and its effect on coronary flow. Image adapted from (Kajiya and Goto, 1999).

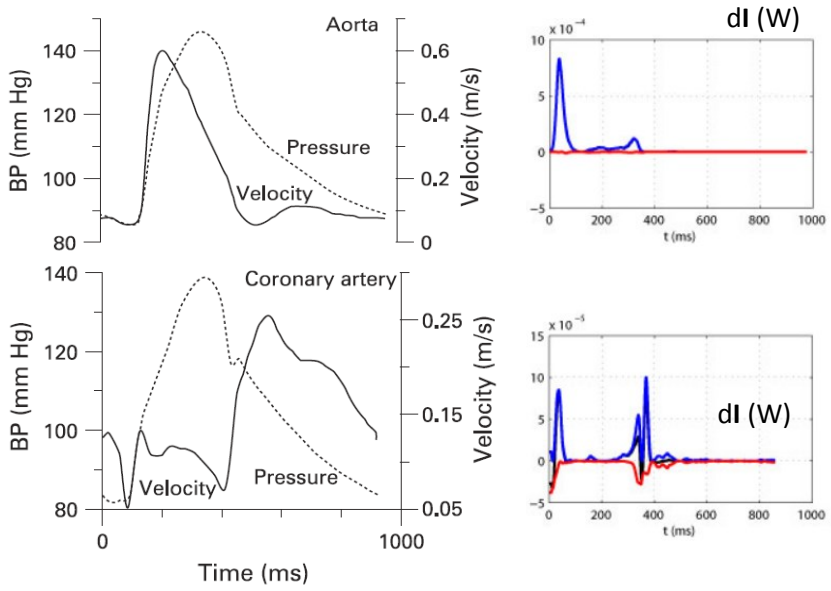

Figure 2-13 Top row. Pressure and velocity waveforms (left) in the human aorta. **Bottom row.** Pressure and velocity waveforms in the left coronary artery (left). Coronary flow during systole is minimal, while peak flow occurs during diastole. Backward travelling expansion waves (red) generating at the microcirculation result in increased diastolic flow. Waveform images adapted from (Davies et al., 2008), wave intensity analysis images adapted from (Parker, 2013).

Autoregulation of coronary flow

In a normal individual, the diameter of the intramyocardial microvessels can be, to an extent, controlled by the vessels. For example, microvessels can widen in case of increased oxygen demand, such as during exercise, and then narrow down again when oxygen demand returns to normal (resting conditions). This means that microvascular resistance can vary considerably in the same person from beat to beat, thus ensuring a sufficient amount of flow is present in the coronary circulation at all times. This effect is called autoregulation of coronary flow.

The autoregulation mechanism can help the coronary circulation maintain the required flow in the presence of disease. The increase in flow resistance posed by the presence of lumen-obstructing atherosclerotic plaque can be almost completely offset by the widening of the microvessels for a wide range of anatomical obstruction, as can be seen in Figure (2-10). However, when the degree of anatomical obstruction becomes very high (for example more than 70% of the lumen area is obstructed by plaque) then the autoregulation system can no longer maintain flow and the disease becomes flow-limiting and intervention may be required.

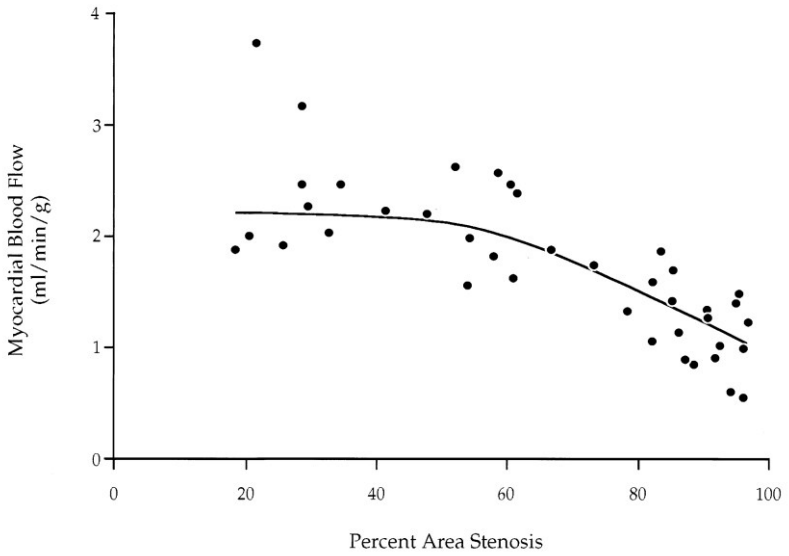

Figure 2-14 Scatterplot indicating the coronary blood flow reserve in the presence of anatomical obstruction Image adapted from (Dicarli et al., 1995).

The haemodynamics of diseased coronary arteries

The presence of atherosclerosis in coronary arteries is the main cause of cardiac death in the world (Lloyd-Jones et al., 2009), as coronary lesions are more likely to be the rupture-prone type, resulting in acute infarction. More stable coronary lesions can also become dangerous, however, as the presence of lesions, sometimes multiple in the same vessel (Figure 2-15), can impair perfusion.

Flow in the coronary arteries is laminar. In the case of healthy vessels, the presence of bends, bifurcations and other complicated geometrical features means that a skewed Poiseuille spatial profile can be expected, with higher velocities observed at the outer side of bends and slower flow at the inner side. In the case of bifurcations, the amount of flow going into each branch can be reasonably estimated by using Murray's law (Murray, 1926) which suggests that the division of flow at bifurcations is directly proportional to the cube of the radius of the daughter vessels, or:

$$f = kr^3 \tag{2.39}$$

where f is the volumetric flowrate going into a given daughter branch of radius r, and k is a constant depending on the fluid's inherent properties and the principle of minimum work exerted by the heart to pump blood into the vessel. More recently, it has been shown that the power of 3 does not provide the best agreement in the case of human coronary vessels, and that other values for the exponent, such as 7/3, have been shown to perform better (Huo and Kassab, 2009).

The pressure drop along a healthy epicardial coronary vessel can be calculated from Hagen-Poiseuille's law that can estimate the pressure drop occurring due to the flow of a fluid with viscosity μ along a pipe of length L and constant radius r, with a flow rate Q, given by the equation 2.40:

$$\Delta P = \frac{8\mu LQ}{\pi r^4} \tag{2.40}$$

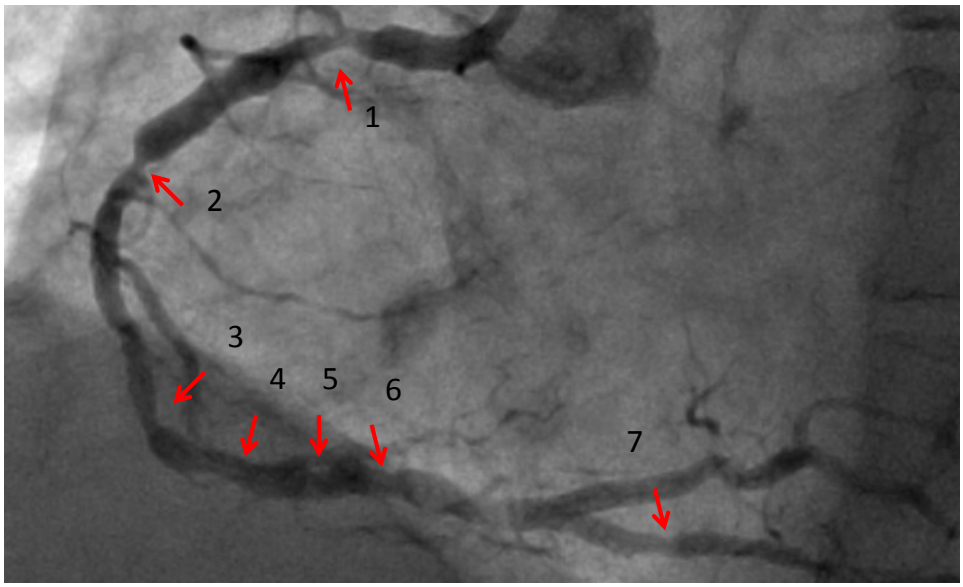

Figure 2-15 Example of how localised risk factors drive the formation of atherosclerosis in a right coronary artery (angiographic image). At least seven lesions can be identified in a single vessel, most of which are located in areas of complicated flow where abnormal wall shear stress can be expected, such as bifurcations (1,4,5) or highly tortuous segments (2,3,6).

Three important assumptions are involved in this equation: a. that flow is laminar b. that the pipe length is considerably larger than its diameter and c. that the pipe has a constant circular radius. In the case of smooth healthy coronary arteries the first two assumptions hold true, and, even though the arteries taper as they are branching out, the change in radius can be considered negligible at the level of epicardial coronary arteries. Applying equation 2.40 for typical coronary flow conditions, a pressure drop of less than 1 mmHg is estimated, indicating that the pressure drop in healthy epicardial coronary arteries is negligible.

In the case of stenosis, Poiseuille's equation for pressure drop does not apply, as the radius can change dramatically in the stenosis, and the length of the stenosis itself is not much larger than the stenosis diameter. Flow is predicted to still be laminar, but the spatial profile inside a stenosis tends to present a flat "inviscid" centre, deviating from a typical Poiseuille flow profile, and disturbances in the form of recirculation appear downstream of the stenosis region due to the sudden spatial expansion. Attempts have been made to develop analytical models which will predict the pressure drop caused by the presence of a stenotic lesion based on geometrical characteristics such as length, degree of stenosis and parameters such as energy/pressure lost to sudden expansion and recirculation, but they appear so far to only work on lesions with particular characteristics (single-vessel lesion, high degree of stenosis) which are not representative of all lesions, and are not applicable to diffuse lesions (Huo et al., 2012, Seeley and Young, 1976, Guagliumi et al., 2013). Therefore, no analytical model exists yet that

can robustly and sufficiently describe the pressure profile in a realistic stenosed epicardial vessel.

As discussed above, the pressure-flow relationship in the coronary arteries is complicated, and is influenced by a sequence of waves generated at both ends of the circulation. When a resistance to the flow is added in the form of a stenosis, coronary autoregulation will lower the overall resistance by dilating the microvessels, which have the ability to adjust their diameter so that flow will increase or decrease according to the needs of the muscle tissue (Feigl, 1983, Deussen et al., 2012). Therefore, despite proximal (aortic) pressure remaining largely constant, and pressure loss in the epicardial vessel becoming non-negligible due to the presence of a stenosis, the supply of flow to the tissue can be maintained at high levels for a wide range of anatomical obstruction. This ability to maintain flow in the presence of disease is called **coronary flow reserve** (Knoebel et al., 1972, Gould et al., 1974a).

As disease progresses, the accumulation of plaque can result in stenoses that pose a high enough resistance to flow that the intrinsic regulating system is overcome: microvessels become maximally dilated and the pressure distal to a stenosis becomes lower than required for sufficient tissue perfusion; a condition called ischaemia (Gould and Lipscomb, 1974a). That is usually when stable coronary stenoses become symptomatic, via a mechanism called "the ischaemic cascade"(Gerdts, 2011). Common symptoms of stable, flow-obstructing stenoses are chest pain, called angina pectoris, either intermittent (for example occurring during periods of exercise) or constant, fatigue and breathlessness. Flow-obstructing stenoses are considered to have lost their ability to maintain a flow reserve, meaning that intervention is required to alleviate the symptoms and restore flow to normal levels (van de Hoef et al., 2013).

2.4.2 Treatment options for stable coronary artery stenoses

While the more severe or acute cases of coronary artery disease (such as left main stem disease, or plaque rupture, respectively) need urgent surgical intervention such as Coronary Artery Bypass Graft surgery or PCI, cases of stable CAD may not require such invasive treatment, or may require no treatment at all. Lowering the level of cholesterol in the blood via medication and/or dietary changes has been proven to prevent, and sometimes reverse the accumulation of atheroma (Ross, 1993, Falk, 2006). In cases where the presence of stenosis is considered to cause ischaemia, percutaneous coronary intervention (PCI) is an option. In PCI, a catheter-delivered balloon is used to break up the plaque to "open" the vessel lumen to reduce

the narrowing (balloon angioplasty). Nowadays it is more common to place a drug-eluting stent during angioplasty (Figure 2-16), because it has been shown that stenting reduces the reoccurrence of stenosis (Violaris et al., 1997).

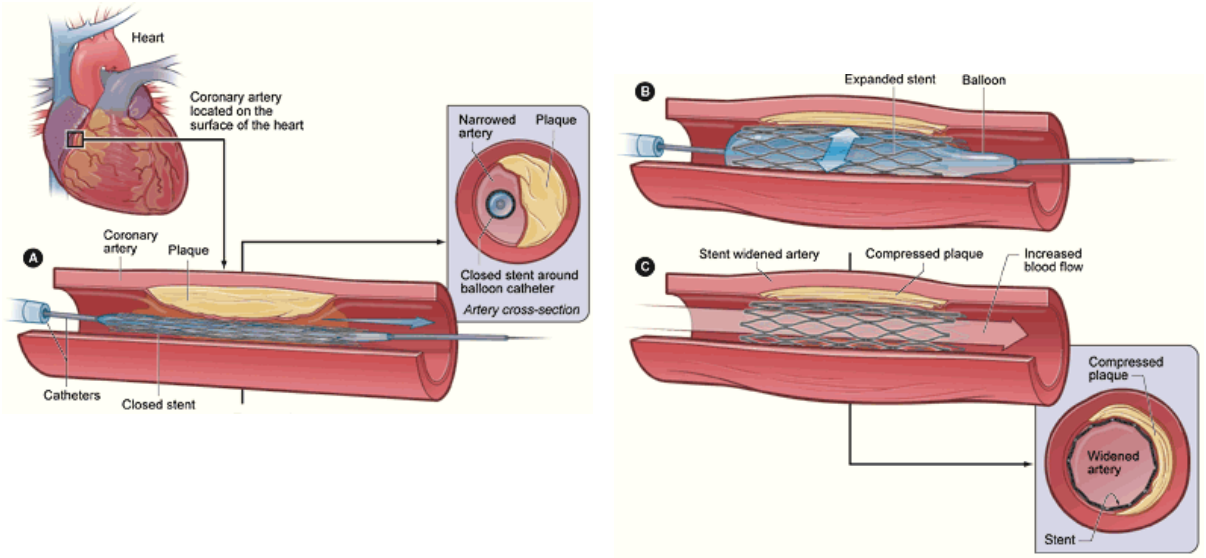

Figure 2-16 Diagram of percutaneous coronary intervention (PCI) to place a stent to "open" a lesion. The stent consists of a meshed metal structure which is delivered to the lesion via catheter on an uninflated balloon (**A**). The balloon is then inflated, allowing the stent structure to push against the wall, compressing the plaque and increasing the lumen area (**B**). The balloon is then deflated and removed, leaving the stent in place (**C**). Drug-eluting stents will then help reduce the plaque burden or prevent further plaque from forming in the immediate area, thus reducing the risk for restenosis.

2.4.3 Diagnostic techniques for coronary artery disease

Coronary artery lesions are often diagnosed before they cause any symptoms, but it is still not possible to accurately evaluate *in vivo* the possibility of a lesion to rupture, or predict its progress (Wentzel et al., 2003a, Schaar et al., 2007). A summary of available diagnostic tools for coronary artery disease is given below.

Invasive coronary angiography

Visualisation of the coronary arteries is more commonly done using techniques that involve patient catheterisation. The oldest and most common is coronary angiography. The in-plane resolution achieved is in the range of 0.12 to 0.2 mm, and it has been used for quantitative coronary anatomical assessment. However, due to the 2D nature of angiography, multiple views are required to avoid pitfalls such as foreshortening (a phenomenon where

objects appear "shorter" due to perspective) and to avoid errors in assessment of oblong, asymmetric stenoses, which are common (Meerkin et al., 2010a). Angiography can only visualise the vessel lumen, and, despite the relatively good resolution achieved, no information on plaque composition can be derived, except for the appearance of calcification as a hazy structure around the lumen. Angiography can be used in conjunction with several other techniques for both anatomical and functional assessment, is commonly used as a guide for intravascular procedures performed in the catheterisation lab, and currently has a Class I recommendation for diagnosis of coronary artery disease in the ESC guidelines.

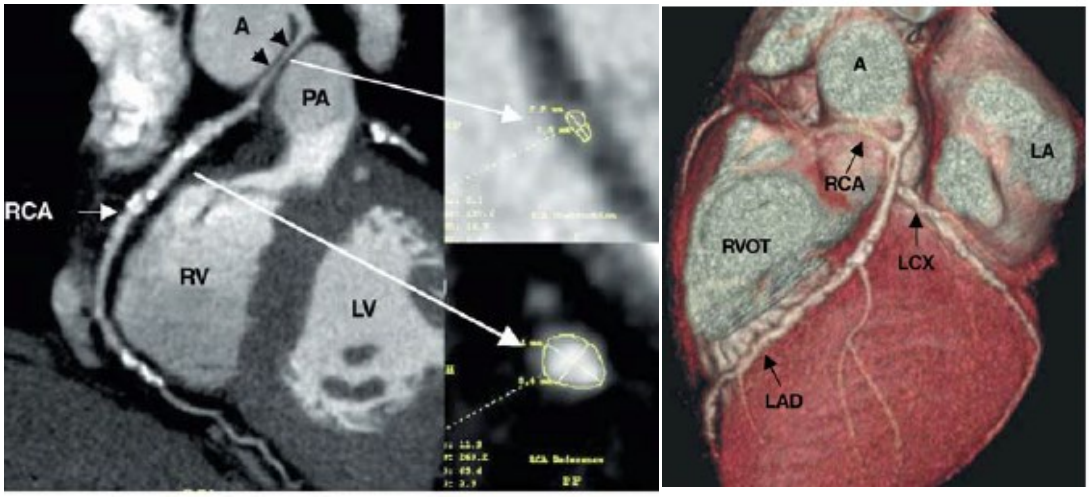

Figure 2-17 A CT angiogram showing a heavily calcified right coronary artery (**left**) and the 3D angiogram resulting from the volume rendering of the CT slices (**right**). The epicardial coronary arteries can be clearly visualised and stenoses identified (black arrows) on the 3D structure. The 3D coronary artery reconstruction from CT can be used in computational fluid dynamics (CFD) applications. Images adapted from (Shi et al., 2004).

Non-invasive techniques: CT and MRI

The field of computed tomography angiography (CTA) is gaining in popularity in recent years (Rubinshtein et al., 2014, Muhlenbruch et al., 2007), boosted by great improvement of image resolution in the past decade with the 64-slice scan MD-CT achieving an in-plane resolution of 0.4-0.5mm (Halon et al., 2006, Schlosser et al., 2008). This allows the quantitative assessment of anatomical obstruction in coronary artery disease with reasonable accuracy, and is considered reliable for ruling out significant coronary artery disease (Windecker et al., 2014). CTA also allows a 3D visualisation of the entire epicardial coronary tree (Figure2-21), which finds application in computational studies (Taylor et al., 2013). The drawbacks of the use of CT for coronary artery disease assessment include the radiation dose

(though that is steadily declining as the method's technology progresses (Goitein et al., 2011)), the lack of real-time images (CT images are averaged over several beats) and the fact that there is no way to measure functional parameters such as pressure and flow velocity concurrently with the imaging. CTA is a Class IIa recommended procedure for the diagnosis of coronary artery disease in the ESC guidelines for the management of stable disease (Montalescot et al., 2013).

Magnetic resonance imaging (MRI) is an imaging method which allows the measurement of velocity in the same imaging session (using phase-contrast, PC- MR) with reasonable spatial resolution, but the imaging resolution of MRI can be too low for visualising the coronary arteries. Even though it can be done (Torii et al., 2009a, Wu et al., 2013) it is not standard in clinical practice.

Intravascular ultrasound

Ultrasound technology can be used to assess coronary arteries invasively. Intracoronary ultrasound (IVUS) has several advantages, including higher in-plane resolution (80-150 μm, as reported by (Raber and Windecker, 2013)) than angiography, and the ability to penetrate deep inside the vessel wall to help visualise plaque composition (Wentzel et al., 2008), making it the established standard for accurate measurements of plaque burden. With IVUS, information about cross-sectional diameter and area, % area or diameter reduction and stenosis length can be derived with great accuracy. However, because the coordinates of the 2D cross-sectional images provided by IVUS in this way are local to each image, no information on the 3D structure, that is the relative position of each cross-section to the others in 3D space, can be derived, meaning that IVUS cannot provide information on vessel curvature and tortuosity, which is important from a fluid dynamics point of view, but also in the study of plaque structure.

The idea of pairing IVUS with angiography to create a complete picture of coronary vessels was first proposed two decades ago (Laban et al., 1995). Several commercial software packages currently available can produce 3D coronary reconstructions based on bi-plane angiographic views (Ramcharitar et al., 2008) in a rapid manner that can be used online for diagnostic purposes. Mapping IVUS-derived lumen contours onto the angiographic reconstructions using a co-registration method helped increase the fidelity of the

reconstructions, allowing for better mapping of plaque formation and allowing patient-specific numerical flow studies (Prause et al., 1997, Slager et al., 2000).

Examples of reconstruction using CTA, angiography and angiography-IVUS co-registration are shown in Figure 2-19.

Optical Coherence Tomography

Optical coherence tomography (OCT) is an imaging method originally developed for application in opthalmology, but also currently in clinical use for the intravascular imaging of coronary vessels (Tsimikas and DeMaria, 2012). An OCT probe uses low-coherence interferometry to record 2-dimensional images of the lumen cross-sections. The image acquisition process in the catheterisation laboratory is similar to that of IVUS, but OCT can achieve in-plane resolutions of less than 10 μm in the axial direction (20-40 μm in the lateral direction) (Suter et al., 2011). However, due to high attenuation of the signal in the tissue, the penetration depth of OCT is considerably smaller than that of IVUS, achieving a range from 0.1 - 2 mm depending on the type of tissue (Huang et al., 1991, Tearney et al., 1997). This means that the assessment of plaque structure and composition is limited to the innermost areas of the wall. Also, due to the high attenuation of the OCT signal in blood, occlusion or flushing of the vessel with OCT-transparent agent is required before an OCT scan.

The early methodology for OCT scanning, time-domain OCT (TDOCT), involves acquisition times which are long enough to require balloon occlusion to expel blood from the area of interest. The occlusion often results in intermittent chest pain or ECG changes (Tearney et al., 2012). Furthermore, the use of a photodetector at the receiving end of the reflected light results in signal-to-noise ratio (SNR) which can be below the minimum accepted SNR of 80 dB (Yaqoob et al., 2005). The newer methodology of spectral-domain OCT (SDOCT) utilises a spectrometer instead of a photometer, resulting in deeper tissue penetration, faster acquisition times and 20-30 dB higher SNR on average compared to TDOCT (Choma et al., 2003). This ensures that occlusive bloodflushing is not required (non-occlusive methods used instead), and the SNR has been shown to remain above 80 dB even at low light acquisitions (Leitgeb et al., 2003). Two types of SDOCT are commonly used: Fourier-domain OCT (FDOCT), which employs a wide-spectrum light source and a low-loss spectrometer for detection, and swept-source SDOCT, or optical frequency domain imaging (OFDI), which makes use of a narrow

bandwidth light source that can be tuned to measure spectral oscillations at evenly spaced wavelengths (Yaqoob et al., 2005). FDOCT is a method commonly seen in coronary imaging.

OCT has been shown to accurately measure fibrous cap thickness and detect minor cap disruptions (Girassolli et al., 2013, Kubo et al., 2013), while it can also visualise intraluminal structures, including plaque composition, lipid pools, intraluminal thrombi and intimal vessels (Tearney et al., 2012) with excellent reproducibility (Gonzalo et al., 2009). There is also evidence that OCT can be used to identify signs of cardiac allograft vasculopathy which cannot be detected with IVUS (Cassar et al., 2013). The very high resolution of OCT images has also been used in the assessment of stent failure and optimisation of stent implantation (Tyczynski et al., 2010) (Class IIa and IIb respectively in the ESC guidelines for myocardial revascularisation), post-ACS (acute coronary syndrome) assessment (Kume et al., 2006), and the study of the development of neointimal tissue around stent struts (Feng et al., 2013, Foin et al., 2014).

The use of OCT in a 3D reconstruction algorithm similar to that developed for use with IVUS for use in patient-specific computational fluid dynamics applications is presented in Chapter 4.

Near-infrared spectroscopy and multi-modality intravascular techniques

Another intravascular technique used mainly for research purposes is near-infrared spectroscopy (NIRS). The NIRS probe can detect the presence of lipids inside the vessel wall, and maps of the vessel wall showing the extent of lipid presence can be produced (Waxman et al., 2009). However, NIRS gives no information on lumen anatomy and provides only binary results on the presence or not of lipids (Goldstein et al., 2011, Jaguszewski et al., 2013), making the potential benefit from its use alone unclear (Groves et al., 2014). This limitation of NIRS can be overcome by pairing it with other intravascular imaging techniques to provide a more complete description of the disease.

The idea of using multiple imaging modalities to help interpret data is not new, and is being commonly used in non-invasive imaging techniques, such as pairing PET with MRI, or CT with SPECT (van der Hoeven et al., 2012). A multimodality catheter acquiring IVUS and NIRS data simultaneously was developed (Schultz et al., 2010), and in the five years since the first application in man it has been used in multiple studies (Mallas et al., 2011, Wentzel et al., 2010, Pu et al., 2012, Madder et al., 2013, Dohi et al., 2014), which suggest that the

combination of the two methods results in better identification of vulnerable plaque (Figure 2-18B). Recently, NIRS has been used in conjunction with OCT, either as part of an NIRS-IVUS multimodality catheter (Roleder et al., 2014) or as a combined NIRS-OCT catheter (Fard et al., 2013).

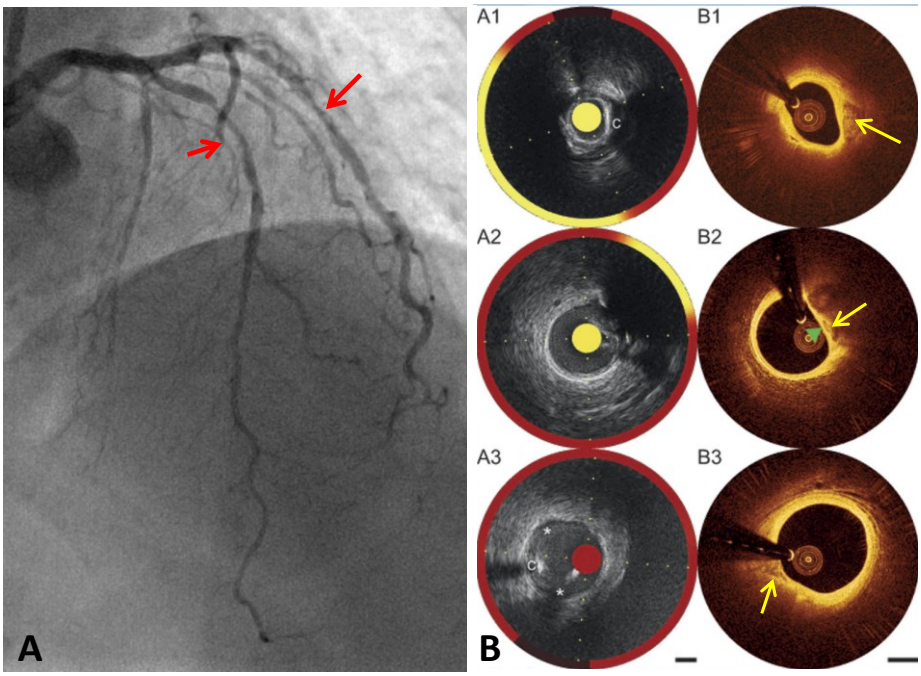

Figure 2-18 A Angiographic view of the left side of the coronary artery tree (cranial view, 33^{o} angle tilt) showing a lesionsin the left anterior descending and circumflex arteries (red arrows). Image courtesy of Dr SukhNijjer, Hammersmith hospital, London.**B** Matched images of vessel lumen cross-sections usingIVUS co-registered with NIRS (column A) and OCT (column B) at three different locations (1-3). Image adapted from (Regar et al., 2013).

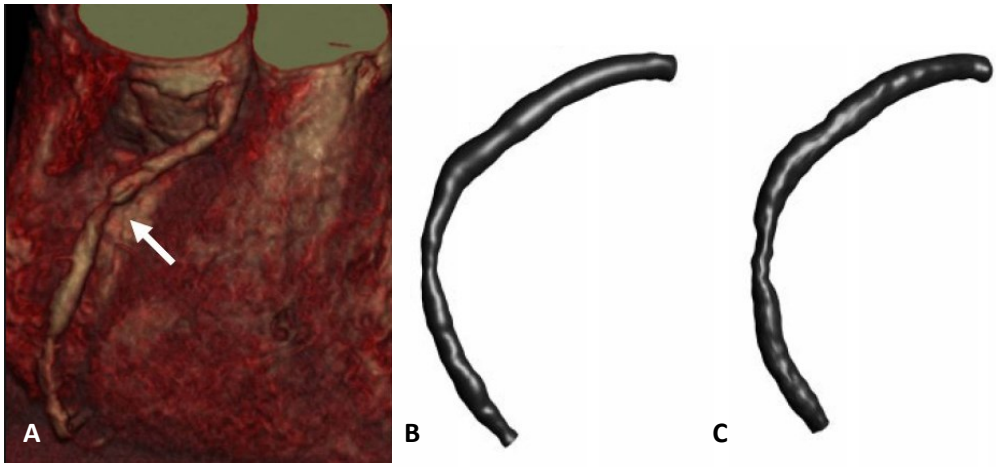

Figure 2-19 3D reconstruction of coronary artery stenosed segment (white arrow) using 16-slice CT angiography (**A**), bi-plane angiography (**B**) and IVUS-angiography co-registration. Images B and C represent the same vessel segmentNote the smoother appearance as well as the artefact stenosis appearing at the distal end of image B, which was not visualised using IVUS, indicating error in the angiographic reconstruction. Image A adapted from (Rodriguez-Palomares et al., 2011), images B and C adapted from (Wentzel et al., 2008).

Coronary artery disease assessment: anatomy vs. function

Myocardial muscle perfusion can be assessed using non-invasive methods such as positron-emission tomography (PET) and single-photon emission computed tomography (SPECT) which can highlight areas of ischaemia by tracing blood perfusion with the use of tracing particles such as Thallium and Rubidium (Case and Bateman, 2013, Mullani and Gould, 1984). However, these methods cannot provide information on individual lesion anatomy or severity, and questions have been raised on the cost-effectiveness of the methods (Iwata and Ogasawara, 2013). PET and SPECT are often used as a gold standard in detecting ischaemia and is used as validation for other methods (De Bruyne et al., 1994a).

The vast majority of functional assessment of coronary stenosis is performed non-invasively with the use of exercise testing and pharmacological stress-testing. However, the use of intravascular Doppler ultrasound in conjunction with angiography and pressure measurements to estimate coronary flow reserve is on the rise and catheters incorporating both pressure and flow velocity transducers are commercially available.

The use of pressure drop for the functional assessment of coronary artery stenosis severity is based in a series of experiments in dogs by Gould (Gould et al., 1974a, Gould and Lipscomb, 1974b, Gould, 1978a) in the 1970s exploring the pressure-velocity relationship in the coronary arteries, under resting and hyperaemic conditions under maximal vasodilation. The main conclusions from those studies were that, in the presence of a stenosis a. the ability of the vessels to respond to increased flow demand (i.e. coronary flow reserve) becomes smaller as the resistance to the flow posed by the stenosis increases and b. pressure drop across a stenosis increases with increasing flow velocity, but the change is sharper (i.e. happens at lower velocities) for severe stenoses (Figure 2-20). Furthermore, it was demonstrated that the correlation between pressure and flow velocity, or resistance and flow reserve are not linear, but quadratic, possibly an indication of the combined viscous and flow separation energy losses occurring (Gould and Kelley, 1982).

As discussed previously, the autoregulatory mechanism for adapting to increased oxygen demand is to dilate the subendocardial microvascular bed to reduce resistance to the flow. The amount by which flow velocity increases in vasodilator-induced maximal hyperaemia is an indication of the coronary flow reserve. In the case of severe stenosis, microvascular dilation is necessary even at resting conditions, to compensate for the added

resistance posed by the presence of disease, thus reducing the vessel's flow reserve. With increasing stenosis severity the degree of microvascular dilation at rest increases until maximum dilation is reached. At this point there is no coronary reserve and any further increase in oxygen demand will result in ischaemia during periods of increased flow demand (such as during exercise). Therefore, measuring the coronary flow reserve is a way to assess the functional impairment caused by a stenosis before a stenosis becomes ischaemic at rest (Lipscomb and Gould, 1975), allowing for earlier diagnosis with potentially better clinical outcomes.

It was suggested by (Pijls et al., 1993) that, under conditions of hyperaemia, resistance to flow is minimised and presumably constant, indicating a linear relation between flow rate and pressure. They argued therefore, that by measuring the pressure drop across a stenosis under maximal vasodilation, an assessment of stenosis severity could be made without the need for flow measurements, which were at the time unavailable in clinical use, and that a functional assessment of stenosis could be more accurate than anatomical assessments (De Bruyne et al., 1994b).

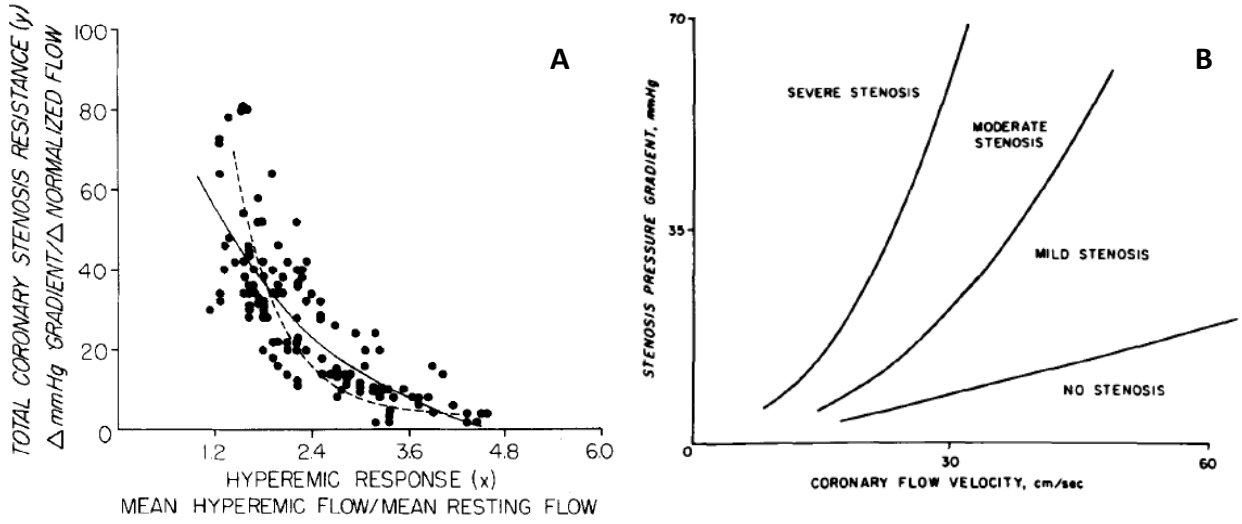

Figure 2-20 A Relationship between stenosis resistance and hyparemic response in dogs (Gould and Lipscomb, 1974a). When resistance becomes too high, hyperaemic response approaches unity **B** The pressure gradient – flow velocity relationship for varying degrees of stenosis. Pressure drop increases faster in severe stenosis (Gould, 1978a).

Fractional flow reserve, or FFR, is defined as the ratio of maximum flow in the presence of a stenosis to what maximum flow in the coronary artery would be if there was no

stenosis. Under conditions of hyperaemia, the myocardial FFR, FFR_{myo} , can be calculated by the equation (2.41):

$$FFR_{myo} = \frac{(Pd-Pv)}{(Pa-Pv)} \quad (2.41)$$

Pa, *Pd* and *Pv* are mean aortic pressure (proximal to the stenosis), pressure distal to the stenosis and right atrial pressure respectively, all measured at maximal vasodilation. The ability of FFR to assess myocardial ischaemia was validated against PET (De Bruyne et al., 1994a). Subsequently, *Pv* was eliminated from the equation and FFR became simply the ratio of mean distal to proximal pressure under conditions of hyperaemia *Pd/Pa* (Pijls et al., 1996). The maximum FFR value of 1 indicates no pressure drop across the stenosis; stenosis severity increases with decreasing FFR, and the cut-off point for the best clinical outcome was originally set at 0.75 (Kern et al., 1997), but then revised upwards to 0.80 before the first clinical study was performed (Fearon et al., 2007a).

Studies were conducted comparing the new method with anatomical assessment. It was suggested that FFR can detect ischaemic lesions with greater accuracy than anatomy-based assessment methods such as angiography (Sant'Anna et al., 2008), and that this may lead to better management of disease and better clinical outcomes when using FFR over angiography to guide percutaneous coronary intervention (PCI) decisions (Siebert et al., 2008, Sant'Anna et al., 2007). The DEFER and FAME clinical trials (Pijls et al., 2010, Pijls et al., 2007) indicated that there is no benefit in performing PCI in functionally non-significant stenoses, and that FFR-guided PCI decisions result in better clinical outcomes (Nam et al., 2011). In the FAME 2 trial (De Bruyne et al., 2012) it was shown that PCI results in significantly fewer instances of the primary endpoint (a composite of death from any cause, non-fatal myocardial infarction or urgent revascularisation) compared to medical therapy, in lesions assessed based on FFR and not angiography. The study was in fact halted due to the large difference of primary end point instances between the two groups (4.3% in the PCI group vs.12.7% in the medical therapy group), which was mostly driven by the high rate of urgent revascularisation in the medical therapy group. The hazard ratio between the two groups increased from 0.32 to 0.39 in the two-year follow-up (8.1% vs. 19.5% incidence of primary end point)(De Bruyne et al., 2014), and the PCI group results are consistently comparable to the registry of patients with non-ischaemic lesions. The results of the FAME 2 study suggest that FFR can discriminate between ischaemic and non-ischaemic lesions better than angiography, resulting in the revascularisation of only functionally impaired lesions.

FFR currently holds a Class I recommendation by the ESC for assessing the ischaemically-relevant coronary lesions when evidence of ischaemia is not otherwise available (Montalescot et al., 2013), a better classification than intracoronary imaging methods IVUS and OCT (Class IIa).

Given the increasing evidence that functional assessment works better than anatomical assessment, summarised in a meta-analysis study by (Christou et al., 2007), ways to improve on the FFR concept have been made. FFR is limited by the fact that there is no guarantee microvascular resistance is indeed constant during maximal hyperaemia, and there is no way to assess if maximal vasodilation has been achieved (Pijls and Tonino, 2011), indicating that incorporating flow velocity in functional assessment may be necessary. The ability to measure intracoronary flow velocity using Doppler wires enabled a more detailed study of the pressure-flow relationship *in vivo* in the catheterisation lab, allowing the direct measurement of microvascular resistance (Chamuleau et al., 2003). Though direct measurements of coronary flow reserve and resistance were initially dismissed (de Bruyne et al., 1996), a new type of functional index was developed, which took into account both hyperaemic pressure drop and hyperaemic resistance to assess stenosis(Meuwissen et al., 2002b). The most well-known index of this type is the hyperaemic stenosis resistance index (HSR), which is the ratio of mean hyperaemic pressure drop to mean hyperaemic flow velocity for a given stenosis (Meuwissen et al., 2002a) and is arguably an index closer to the original experiments than FFR. HSR is associated with better prediction of ischaemia compared to either FFR or CFR when using a cut-off point of 0.8 mmHg/cm (Kern et al., 2006).

Despite the better clinical outcomes associated with functional assessment, the need for administration of a vasodilator to achieve hyperaemia adds costs and time to the process, and the uncertainty over achieving maximal hyperaemia has led to poor adoption of functional indices in clinical practice. Only about 6-8% of medical centres throughout the world are regularly using functional assessment to guide PCI (Kleiman, 2011). Also, it has recently been shown that in cases of severe stenoses hyperaemic flow is not significantly different to resting flow, due to the inability of the microvasculature to achieve further dilation (Tarkin et al., 2013) suggesting potential alterations in the FFR lesion classification. In fact, the variability in hyperaemic response can result in uncertainty and confusion in cases of intermediate coronary stenoses, which are cases where functional assessment is close to the FFR cut-off point. It has been shown that, even though the FFR reproducibility across the entire range of FFR values is higher than 95%, in the intermediate area ±0.05 from the FFR cut-off of 0.80, diagnostic

accuracy of a single FFR measurements drops to about 50%, as shown in Figure 2-21 (Petraco et al., 2013c).

In the initial experiments it was argued that hyperaemia was necessary, as the true pressure gradient was considered to be "masked" by the varying microvascular resistance in resting conditions. The evidence from more recent literature, however, suggests that the hyperaemia requirement may be problematic.

Sen *et al.* (Sen et al., 2012), based on the wave intensity analysis study of the aorta and coronary arteries, suggested that during the cardiac cycle at rest there is a period of constant microvascular resistance, when pressure and velocity are proportional to each other, and the pressure drop during that period could be used to assess stenosis severity without the need for hyperaemic measurements.

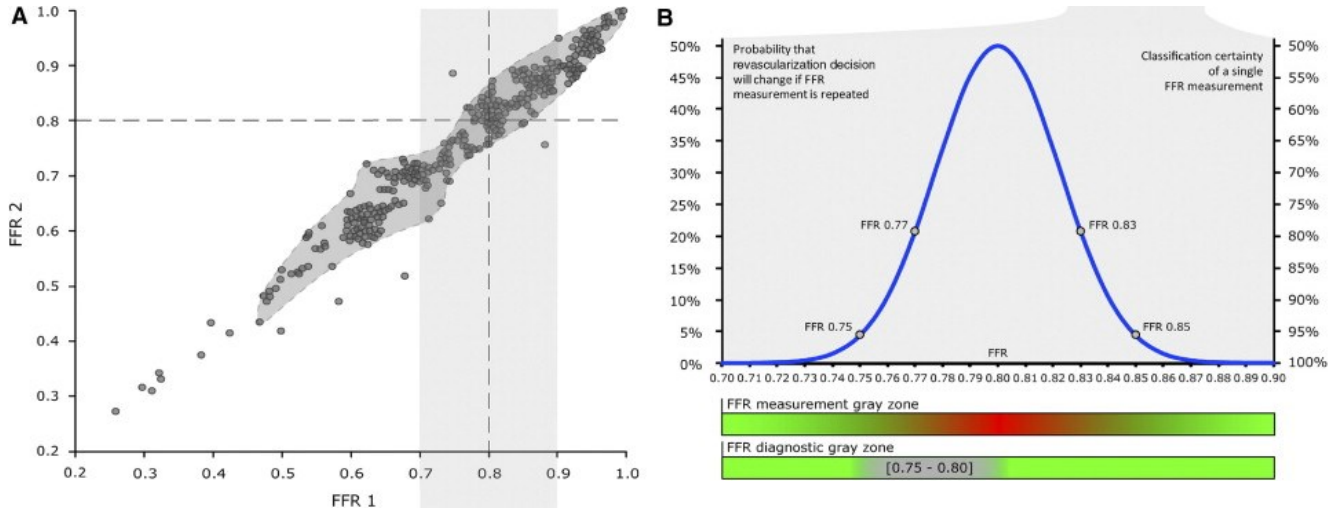

Figure 2-21 A Test-restest reproducibility of FFR. The dotted lines indicate the 0.80 cut-off point, while the vertiocal grey shaded area shows the intermediate lesions that have a FFR of 0.7 to 0.9. **B.** Diagnostic uncertainty (probability that revascularisation decision will change if a FFR measurement is repeated) plotted across the FFR range from 0.70 to 0.90Image adapted from (Petraco et al., 2013c).

Their study suggests that the masking effect occurring during resting flow can be attributed to the presence of waves generated at the distal end of the circulation, making the measurement of the distal to proximal pressure ratio (*Pd/Pa*) an unreliable tool for assessing stenosis severity. However, during a major part of diastole, no waves, backward or forward travelling are detected, and resistance during this "wave-free" period is constant and low (Sen et al., 2013b), ensuring high flow velocities which can help differentiate between ischaemic and non-ischaemic stenoses (Figure 2-22). The study resulted in the development of the

instantaneous wave-free ratio (iFR) index with a cut-off point of 0.90, which has been shown to be at least just as good as FFR at guiding PCI (Petraco et al., 2013a, Sen et al., 2013a) with the added benefit of not requiring hyperaemia to measure.

There have been unfavourable comparisons of iFR with FFR (Johnson et al., 2013, Rudzinski et al., 2012, Pijls et al., 2012) but the comparison of any method to FFR is limited by the uncertainties and poor test-retest reproducibility of FFR in the clinically relevant intermediate lesion severity range. As stressed by (van de Hoef et al., 2012b), FFR can be a clinically useful tool, but its scientific basis is not strong enough to suggest it should be used as gold standard against which other methods should be compared, while (Claessens et al., 2004) highlighted the importance of incorporating zero flow pressure, which is the pressure at the zero-flow intercept in a flow-pressure diagram (Nanto et al., 2001),in the FFR calculations, which is not commonly done in clinical practice. A hybrid iFR-FFR approach has been suggested, in which only stenoses that fall within an iFR range of 0.86 to 0.93 would get an FFR to clarify the diagnosis, thus greatly reducing the use of vasodilators and potentially enhancing the adoption of functional assessment (Petraco et al., 2013b).

Despite the critique on the use of resting conditions to assess stenosis severity, the attractiveness of the idea of functional assessment without the need of vasodilator drugs has led to the development of other non-hyperaemic indexes, such as baseline stenosis resistance, or BSR (van de Hoef et al., 2012a), which, like HSR, is the ratio of mean pressure drop to mean velocity, but at rest.

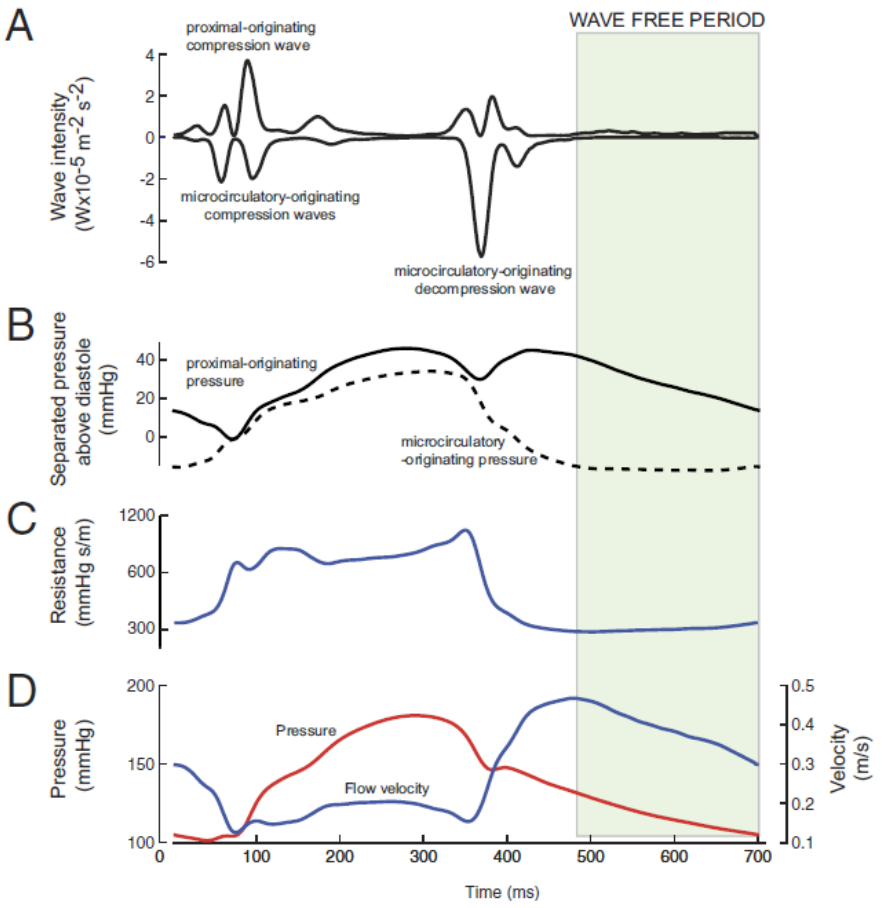

Figure 2-22 Wave-intensity analysis in the coronary arteries indicates there is a period during diastole where no waves are generated (**A,** shaded green area), during that time the suction pressure generated in the microcirculation (**B**, dashed line) is at its highest and constant, meaning that resistance, too, is minimum and constant during that period (**C**). This is reflected in the way that the pressure and velocity appear to be changing at the same rate (**D**, appearing as parallel lines in the wave-free period) suggesting that, during the wave-free period at rest, pressure can be used as a surrogate for flow. Image from (Sen et al., 2012).

Limited understanding of coronary pressure-flow relationship can result in less-than-optimum diagnosis

While in the case of aortic stenosis anatomical obstruction can be used as a surrogate assessment method for functional impairment, this is not possible in the case of coronary artery disease. This is because the pressure-velocity relationship in the coronary arteries is complicated by the presence of compression and decompression waves originating in the microcirculation, as discussed in section 2.2.3. The diameter of the microvasculature changes throughout the cycle and from beat to beat, resulting in large variations in downstream resistance to the flow. The pressure waves generated at the distal end result in variations in

velocity which can be independent of the anatomical obstruction at hand. For this reason, there is poorer than expected correlation between anatomical-based and function-based assessment of coronary artery disease, with function-based assessment shown to result in better clinical outcomes (Pijls et al., 2010).

The fact that so many different functional indices exist which propose to measure the same thing (ischaemia) but appear not to be in agreement with each other, or have poor test-retest reproducibility, is a clear indication that the complexity of the pressure-flow relationship in the coronary arteries means that great care should be taken when attempting to interpret the results as a reliable assessment of function. Though the concept of coronary flow reserve is widely accepted, attempts at measuring and/or estimating it can be fraught with practical issues which could cast uncertainty over the reliability of the measurement (Hoffman, 2000).

However, the clinical studies suggesting that functional assessment can be better than anatomical assessment indicate that the development of a globally accurate functional method of evaluating ischaemia is worth pursuing. It is considered that the discrepancy between the anatomical and functional tests can be attributed to the fact that the two method types are looking into different aspects of coronary artery disease, and it is thought that these aspects may be complementary. For this reason studies have attempted to develop new assessment methods which combine anatomical and functional methods, which are often performed together, in an attempt to improve assessment (Sinha Roy et al., 2008, Matsumoto et al., 2013, Zafar et al., 2013), but so far no clinical data exist to test the accuracy of these methods in a clinical setting.

An attempt at understanding the pressure-flow relationship in the coronary arteries using computational fluid dynamics modelling is presented in Chapters 4-6.

2.4.4 Computational modelling of coronary arteries

Computational modelling in the coronary artery tree developed later than modelling of the larger arteries. The smaller size, the location of the coronary arteries on the heart muscle and the complicated flow conditions resulted in delays in the development of patient-specific models, which only started appearing less than a decade ago. (Banerjee et al., 1999) and (Torii et al., 2007) studied the effect of pressure and flow wires used in invasive assessment on the velocity spatial profiles in idealised models of curved tubes. (Banerjee et al., 2000) used measurements of coronary flow reserve from patients who underwent angioplasty to study

residual stenoses, while (Torii et al., 2009b) used patient-specific anatomical models taken from MRI images of one patient pre and post angioplasty to study the change in haemodynamics. A non-Newtonian approach to coronary flow allowed researchers to establish the locations of particulate buildup in curved arteries (Jung et al., 2006). More complicated approaches incorporate the movement of the epicardial coronary vessels on the beating heart muscle, but there is no indication that the temporal change in curvature and torsion have significant effects in the flow patterns (Torii et al., 2010, Hayashi and Yamaguchi, 2002). (Wentzel et al., 2003b) and (Gijsen et al., 2014) have been using CFD investigating the links of flow and wall shear stress patterns in the coronary arteries and bifurcations to the probability of vulnerable plaque rupture.

Computational modelling of coronary flow reserve

Given the increasing interest in the studies of coronary flow reserve, and the development of functional assessment of coronary artery disease, it is not surprising that CFD studies have tried to come up with ways to replicate the invasive functional tests with equally reliable, non-invasive ones. The concept of using a non-invasive or mildly invasive imaging techniques to obtain anatomical data which can then be used in CFD simulation to provide virtual CFR or FFR data is a very attractive one, but the actual implementation of this is proving to be quite challenging. The most famous use of CFD to help evaluate FFR non-invasively is the concept of FFR_{CT}(Zarins et al., 2013), where computed tomography angiography (CTA) images are used to reconstruct the coronary artery tree (at the level of epicardial vessels). Murray's law and assumptions on volumetric flow rate based on a patient's myocardial mass and brachial pressure are used as boundary conditions in steady-state flow simulations to produce the FFR profile of the entire structure, arguably helping to identify ischaemic lesions (Taylor et al., 2013). Clinical trials (Min et al., 2012a, Min et al., 2012b) report accuracy levels of 70-80% when compared to invasive FFR measurements, while negative predictive value is higher than positive predictive value (which has been shown to be as low as 67%). The limitations of the method may be attributed to the use of non patient-specific flow data as boundary conditions, and in particular in the use of a single value for coronary flow reserve (~4) across an entire range of stenoses, when by definition flow reserve declines with stenosis severity.

Few other attempts at testing the ability of CFD to predict ischaemia exist. The two existing studies have used angiographic data to create anatomical reconstructions in steady-state CFD simulations. (Siogkas et al., 2013) used flow data at rest averaged over the wave-free period, therefore modelling iFR. A good correlation with measured FFR was observed, though the study was limited by the small number of patients (n=7) and the stenosis range which was skewed towards non-ischaemic lesions. The other study (Morris et al., 2013)used flow velocity and pressure boundary conditions averaged over the entire cohort to also achieve a good correlation with measured data. However, similar limitations apply to this study too. Though it had a larger number of patients (n = 35), a small fraction of those (9 stenoses or 25%) belonged in the clinically relevant intermediate lesion severity range, while many of the geometries represented post-PCI anatomies, meaning that the majority of lesions (21, or 60%) were in the non-ischaemic range.

The CFD studies published so far indicate that CFD may be better at modelling non-ischaemic lesions than ischaemic, which is potentially useful, but further investigation is required to try and understand the reason behind the discrepancy.

3. Pressure Recovery in an idealised model of aortic stenosis

Figure 3-1 Echocardiography-based stereolithography model of the aortic valve of an aortic stenosis patient.Stenosed orifice to the right of the picture. Image adapted from(Gilon et al., 2002)

3.1 Introduction

In this chapter, the aim is to test the hypothesis that recovery of pressure in cases of aortic stenosis is possible by remodelling the aortic root and ascending aorta. CFD is used in a proof-of-concept study to show whether implanting a device designed to maximise pressure recovery will lead to significant reduction of pressure loss in cases of severe aortic valve stenosis. The device is tested for three different valve orifice anatomies, ranging from completely idealised to patient-specific, to observe the effects of anatomy irregularities on its effectiveness. Such a device could potentially be useful as an alternative treatment option for patients who are not fit for valve replacement surgery.

On a previous study of flow in the ascending aorta (Kousera et al., 2013) it was determined transition to turbulence for part of the cycle is common in healthy subjects, making it a certainty that flow will undergo transition to turbulence in cases of aortic stenosis too. Therefore, the γ-Re_θ Transition Model (SST Tran), which has been validated for arterial flow as described in Chapter 2, is used in steady state simulations representing the moment of peak systole when maximum flow through the valve (and therefore maximum pressure drop) occurs.

The results presented consist of comparisons between flow simulation with and without the original device design for the three different valve orifice shapes. The parameters investigated were the velocity field, the pressure distribution and the turbulence kinetic energy. Further investigation of the differences in the flow patterns near the valve orifice was necessary to assess the limitations of the original device design, and to provide information about possible future improvements.

The chapter concludes with a summary of the work presented, and suggestions on what the next steps in the development of this device could be.

3.2 Methodology

3.2.1 Idealised model geometry

An idealised virtual 3D model of the left ventricular outflow tract (LVOT), aortic root with a domed, unmoving valve inside (fully open) and proximal ascending aorta was built in ANSYS ICEM CFD 13 (ANSYS Inc., Cannonsburg, PA) software. An example model and the dimensions used are shown in Figure 3-2**.** In order to study only the effect of valve shape on flow and pressure patterns, a simple idealised geometry was created, and so the LVOT was assumed to have a circular cross-section (its shape is normally elliptic), the ascending aorta was designed as a straight tube with no curvature and the coronary ostia were omitted. The ascending aorta section was created longer than real life (100 mm compared to a normal length of around 50 mm), in order to minimise the effect of the outlet on the numerical results, and also to allow enough space for the flow to develop completely after boundary layer reattachment. The LVOT, however, was kept at a typical length of 30 mm, in order to simulate the undeveloped nature of flow coming out of the left ventricle and through the valve.

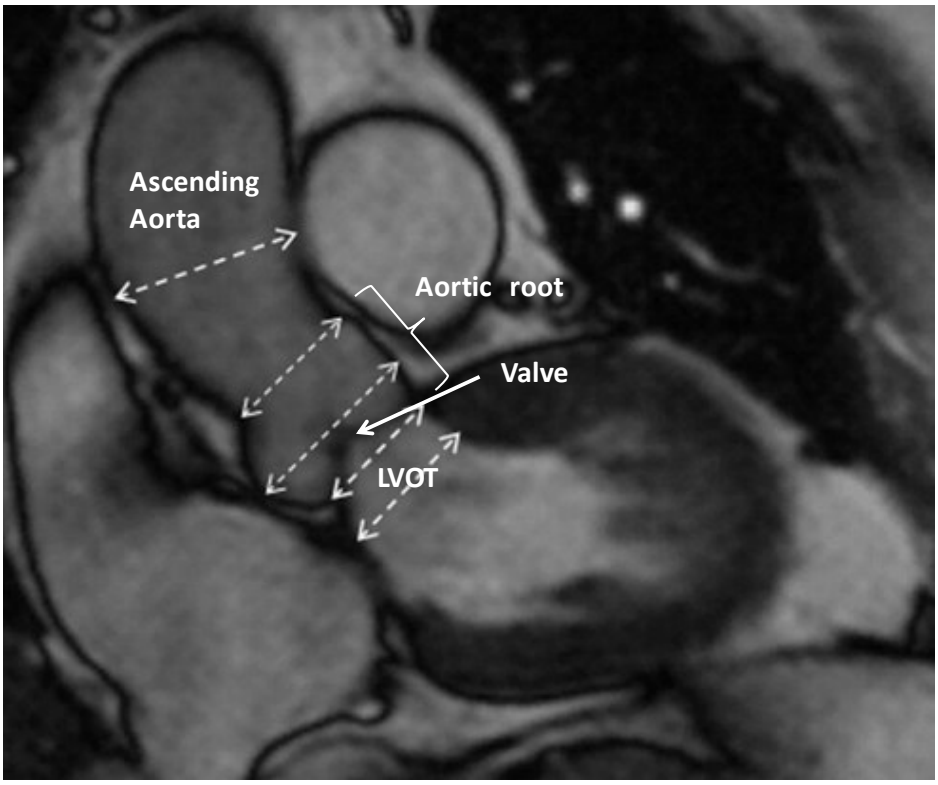

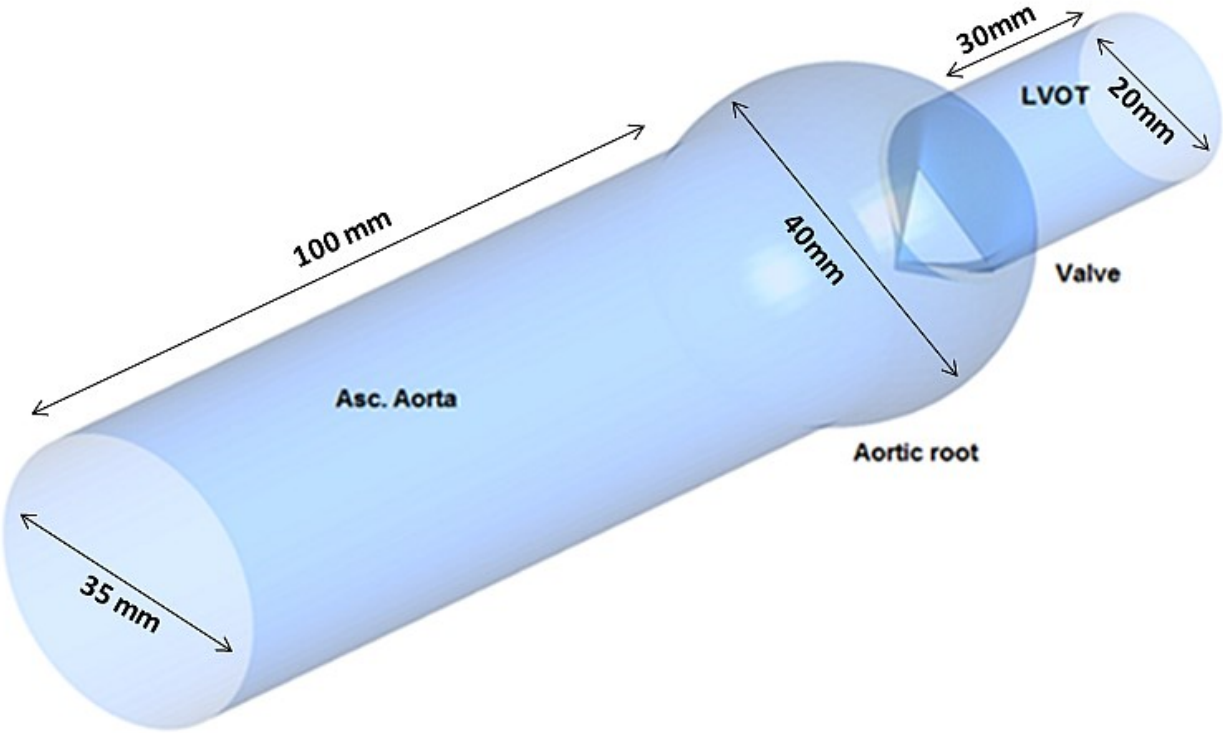

Figure 3-2 Top. MRI scan of the left ventricular outflow tract (LVOT), aortic root and valve and ascending aorta, image adapted from (Paelinck et al., 2011). **Bottom.** Example of the idealised LVOT, aortic root and ascending aorta geometry used in the CFD simulations. The diameters and lengths were chosen based on characteristic values commonly found in patients with aortic stenosis. The idealised geometry comprises a longer than real life ascending aorta section and does not include curvature.

3.2.2 Valve shape

Three different valve shapes were tested: a circular disk, a triangular disk with rounded edges, and a highly irregular valve shape taken from a patient's CT scan as seen in Bouvier et al (Bouvier et al., 2006). The valve geometries are shown in Figure 3-3**.** Since there would be no quantitative comparison among the three valve geometries, emphasis was given on creating characteristic shape differences, progressing from completely ideal to entirely realistic anatomies, so achieving the same orifice cross-sectional area was considered of lesser importance. The cross-sectional area of the circular disk was the largest at around 100 mm^2, while the triangular shaped orifice had a cross-sectional area of 70 mm^2. The cross-sectional area of the patient-specific valve orifice was calculated based on the CT image as 64.4 mm^2. Because of the differences in cross-sectional area, quantitative comparison of pressure drop was only made between the same orifice shapes, with or without the device, and not among different valve shapes.

The whole geometry, including the valve dome was modelled as rigid. Though healthy aortic valve leaflets are subject to considerable movement during a cardiac cycle, opening and closing fully, the calcified plaque that has formed on the leaflets of stenosed valves reduces their mobility considerably, making them almost rigid in more severe cases. Furthermore, in this study the valves were studied at just one part of the cycle, peak systole, where the valve is open at the maximum. The assumption of a rigid valve dome is, therefore, justified.

3.2.3 Device design

The shape of a calcified aortic valve, especially a domed one, resembles a nozzle, as indicated in Figure 3-1 (Gilon et al., 2002). Flow through nozzle-shaped openings accelerates rapidly within a small distance, becomes disturbed and separates from the wall downstream. The flow jet created is subject to high shear that leads to substantial energy losses. Therefore, the shape of a calcified valve is very unfavourable when it comes to recovering lost pressure.

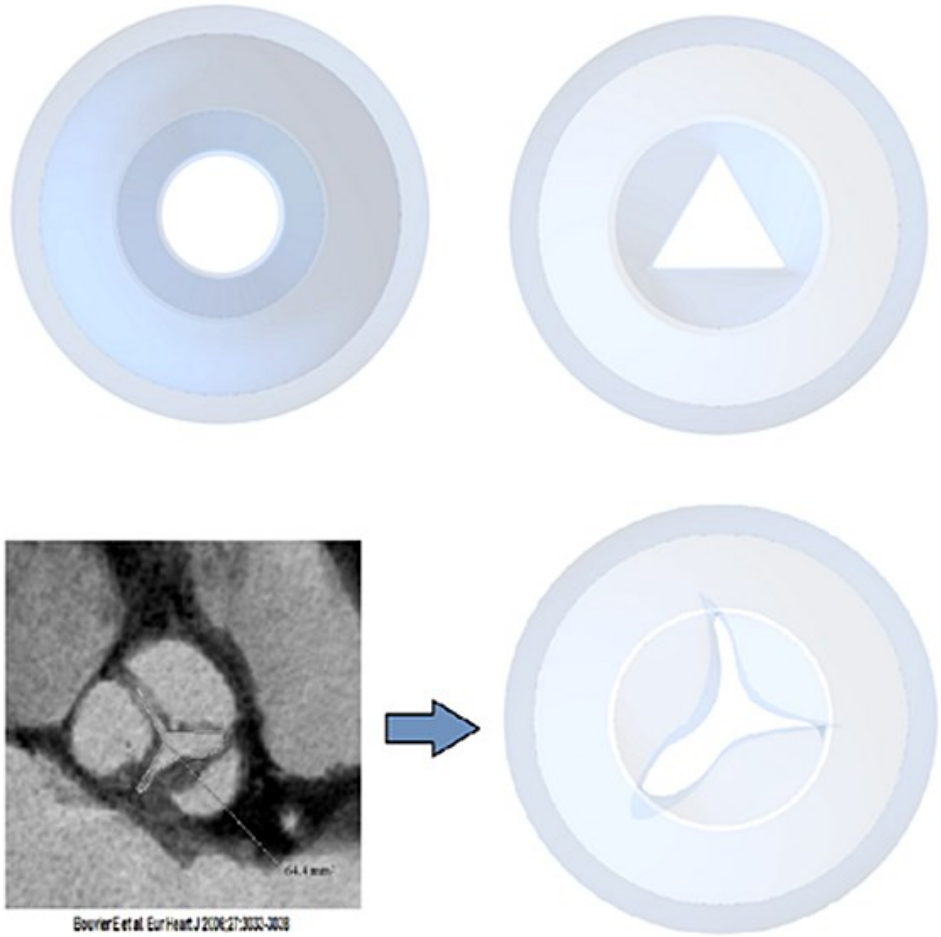

Figure 3-3 The three different valve orifice shapes used in the simulations, circular, triangular, and patient-specific based on a CT scan as shown in (Bouvier et al., 2006)

The design of the device used was chosen to have particular characteristics that favour pressure recovery, namely reshape the flow downstream of the valve in such a way as to maximise pressure recovery and minimise energy losses. In order for this to be achieved, the device must induce quick reattachment of the separated flow jet. A Venturi-like diffuser shape like the one shown in Figure 3-5 was decided on, given the use of similar designs in applications that have similar goals (Xu and Huang, 2011, Meakhail et al., 2008). The walls of the device are tapering out in a way that captures the jet coming from the orifice along the region where high shear is expected, and in this way the desired flow reattachment is induced within a few millimetres.

It is clear that the device would have maximum effect if it could be placed exactly on the orifice, but doing so would block coronary flow and so the device was originally placed 10 mm away from the orifice opening. This was done in an attempt to test the concept of

pressure recovery on a simple geometry, before considering more complicated device structure which would accommodate the coronary arteries and other issues that may arise.

The distal side of the device has the same diameter as the ascending aorta at that point, enabling a smooth transition from the device to the vessel lumen downstream, and a potential tethering point.

3.2.4 Computational mesh generation

The resulting six geometries (two for each valve shape: one without the device implanted, and one with the device implanted) were meshed using tetrahedral elements. The size of the domain, the complexities created by the presence of an internal wall (the valve dome inside the aortic annulus) and the expected presence of high velocity gradients required a large number of elements to ensure detailed and accurate results, resulting in grids of upwards of 1.2 million nodes and more than 4 million elements. A prism layer was placed near the domain wall in order to achieve better element size control. Because of the use of a turbulence mathematical model, the size of the elements adjacent to the wall was chosen so that the parameter y+ had a value of less than two (Kim et al., 1971). By doing this, an important modelling condition is satisfied: the first layer of elements near the wall is entirely contained in the viscous sublayer of the boundary layer, consequently enhancing convergence and ensuring accurate solution near the walls. A cross-section of the mesh along the central axis of the domain is shown in Figure 3-5.

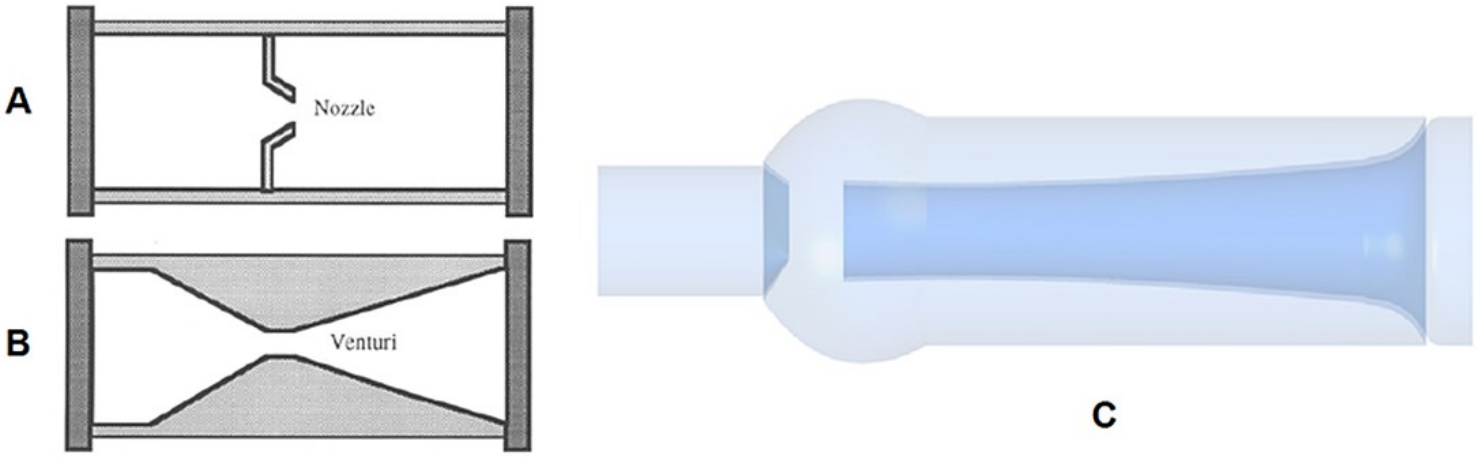

Figure 3-4 A The calcified aortic valve resembles a nozzle, a configuration which leads to high energy losses due to sudden cross section expansion. **B**. The Venturi shape, where the cross-sectional area increases gradually, preventing flow separation and minimising energy losses. **C**. The device model placed inside the idealised model. The device resembles a Venturi, following the lines of high shear patterns in order to prevent energy losses.

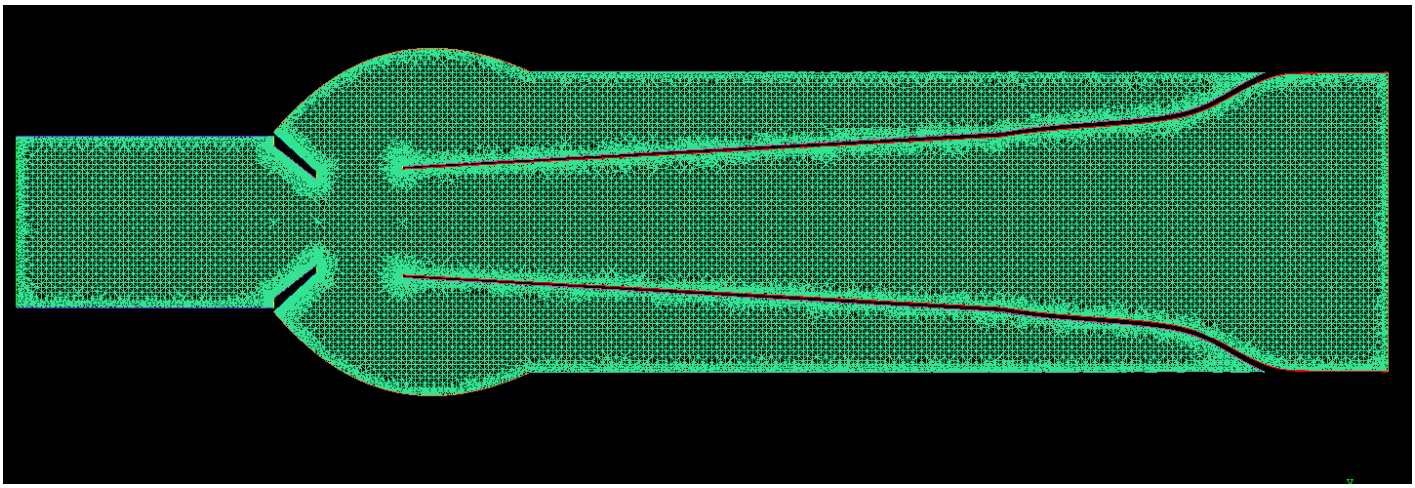

Figure 3-5 A cross-section of the mesh of the geometry shown in Figure 3-4 C. Due to the complicated geometry and flow conditions, a very fine mesh was used, comprising of 1.2 million nodes, or upwards of 4million elements.

3.2.5 Boundary conditions and simulation set up

The same flow parameters and boundary conditions were used in all simulations so that the results would be comparable. The simulations were run under the assumption of rigid walls and blood was modelled as Newtonian and incompressible, with dynamic viscosity set to 0.00334 Pa.s and density to 1060 kg/m^3. These assumptions have been shown to be acceptable for studies in large arteries such as the aorta (as discussed in Chapter 2). Steady-state simulations were set up, using boundary conditions likely to be observed in a stenotic aortic

valve region at peak systole. Specifically, the inlet volumetric flow rate was chosen such that velocity at the orifice with a typical cross-sectional area of 70mm^2 would be around 4m/s (Figure 3-6). A flat inlet velocity profile was chosen, in order to reflect the fact that the flow going into the aortic valve is not fully developed. A turbulence intensity level is required at the inlet, and based on previous work this level was set to 1% (Kousera et al., 2013). The solution satisfies the no-slip condition at the walls, while the outlet boundary condition was left as an opening (fluid is allowed to flow both into and out of the domain) with zero relative pressure. The solution convergence target was set to a strict root-mean square velocity residual of 10^{-6}, which was achieved in all cases between 100 and 200 iterations.

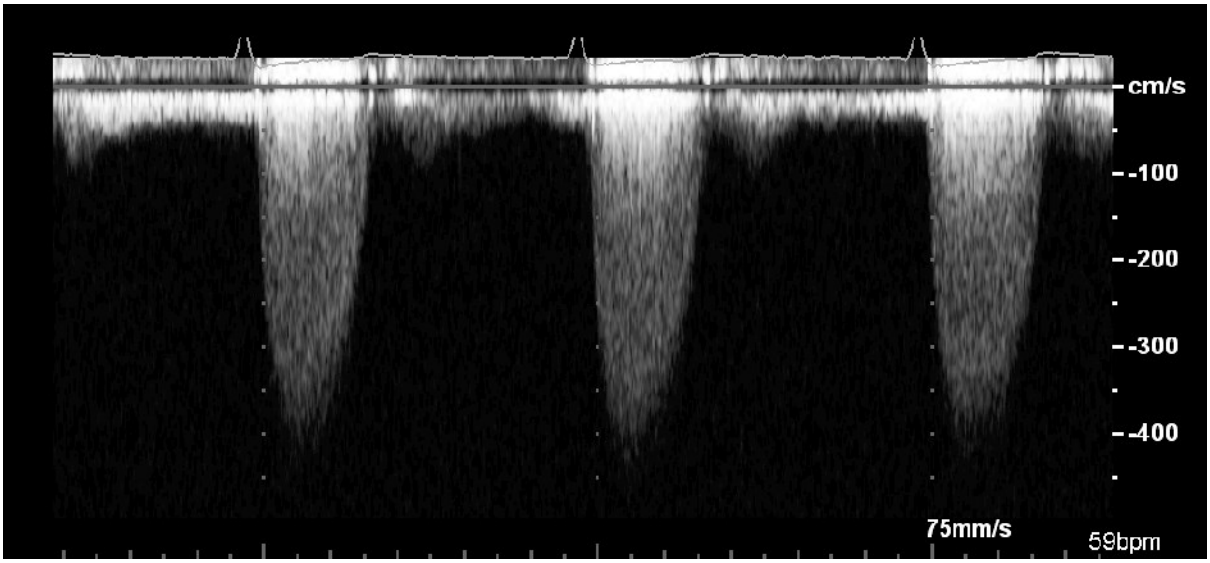

Figure 3-6 Velocity through a stenosed aorta, measured using echocardiography. Peak velocity reaches 400cm/s, or 4m/s. Image courtesy of Dr Matthew Shun-Shin, St Mary's Hospital, Imperial College London.

The choice of the zero pressure condition combined with the rigid wall assumption means that the pressure values obtained are not those observed by measuring brachial artery blood pressure, but since the focus of this study is on pressure differences between different locations in the domain and not absolute pressures, the results reported are not affected by the choice of outlet pressure level.

3.2.6 Transitional turbulence model

The mathematical model used for these simulations was the Shear Stress Transport model for turbulence, enhanced with correlations for intermittency γ and momentum thickness Reynolds number Re_θ that allow it to detect transition from laminar to turbulent flow, otherwise known as the γ-Re_θ Transition Model (Langtry and Menter, 2009). It has been shown (Nerem and Seed, 1972, Kousera et al., 2013) that Reynolds numbers observed in the human aorta vary throughout the cycle in such a way that flow can change from laminar to turbulent and back, and turbulence may exist only in parts of the anatomy, therefore a mathematical model capturing this transitional state would be better suited for the present study than a fully turbulent or laminar model. The γ-Re_θ Transition Model is a RANS (Alfonsi, 2009) model that has successfully been used in the past (Tan et al., 2009b) to describe this type of physiological flow, and has been shown to be particularly adept at matching experimental data in cases where spatial retardation of the flow occurs, such as the sudden flow expansion from the stenosed valve orifice to the ascending aorta. A full description of this model and why it was chosen as the most suitable for this application can be found in the engineering background section of Chapter 2.

3.3 Results

3.3.1 Flow patterns, turbulence kinetic energy and pressure drop

The results for the simulations on the circular, triangular and patient-specific orifice in the original state and with the device implanted are shown in Figures 3-7, 3-8 and 3-9 respectively. Velocity vectors and turbulence kinetic energy (TKE) were plotted on a characteristic two-dimensional plane passing through the centre of the geometry in the longitudinal direction. In this view, the progress of the jet as it moves away from the orifice and into the ascending aorta can be seen plainly, and the differences between the valve orifice shapes can be distinguished best. A pressure plot along the vessel centreline indicates the amount of pressure drop observed as flow passes through the orifice, and the potential pressure recovery achieved by the presence of the device.

The jet coming out of the circular orifice is symmetrical, and it expands in a similar way in all directions while decelerating, before reattaching to the walls (Figure 3-7). There is an area of low velocity recirculation inside the sinuses and almost stationary flow at the side of the ascending aorta before flow reattachment. The symmetry of the flow pattern is reflected in the TKE plot; TKE is high in areas of high fluid shear, near the edges of the expanding flow jet. TKE is energy that is transported from the main flow to the turbulent, high-shear regions; this energy is irreversibly lost to the main flow, and thus TKE is a suspected major contributor to the high observed pressure drop across the orifice. The small pressure recovery observed in the pressure plot confirms the irreversible nature of the lost energy.

With the device in, the jet coming out of the orifice is captured immediately and flow reattachment happens very quickly inside the device lumen. Flow again expands and decelerates gradually, but this time attached to the walls, avoiding the development of high shear. The TKE plot indicates a significant reduction of energy loss, meaning that, as the flow decelerates, pressure is recovered downstream. Comparing the pressure plots with and without the device it is clear that, though the pressure drop at the orifice is the same in both cases, a significant proportion (57%) of energy and pressure are recovered downstream in the presence of the device.

Similar observations can be made in the case of the triangular orifice with rounded edges (Figure 3-8). The out flowing jet is not symmetrical and flow reattaches mostly to one side of the lumen resulting in an asymmetric TKE pattern, but with the device in place the jet is captured before it deviates far from symmetry. Even so, the different angle of impact with the device leads to a small but distinct area of high TKE resulting in a smaller, but still significant proportion of pressure being recovered (50%).

In the case of the patient-specific lumen there is no symmetry in the jet coming out of the orifice, and in fact the highest velocities are observed near the corners of the orifice, forming three separate jets (Figure 3-9). This behaviour leads to chaotic flow downstream, and high TKE values very near the orifice itself. For this reason, the device used in this case was slightly modified to include a funnel-like proximal end that would ensure that all three high-velocity jets were captured and channelled through the device. Even with this modification, the pressure recovery observed (14%) is considerably lower than in the previous two idealised cases.

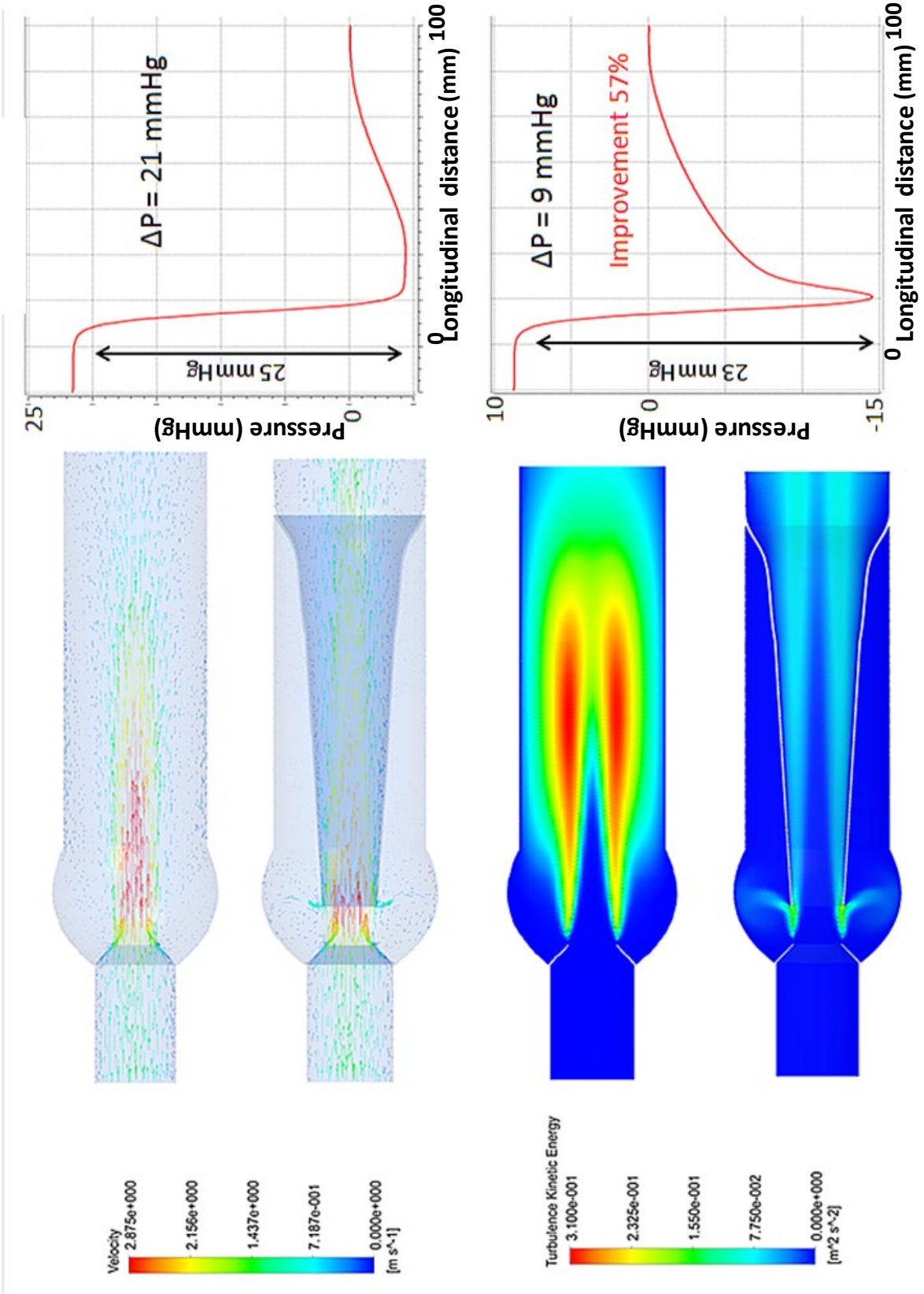

Figure 3-7 Velocity vectors and turbulence kinetic energy pattern on the longitudinal mid-plane for the circular orifice, without and with the device. The pressure plot along the geometry centreline suggests that 57% of the pressure is recovered in the presence of the device.

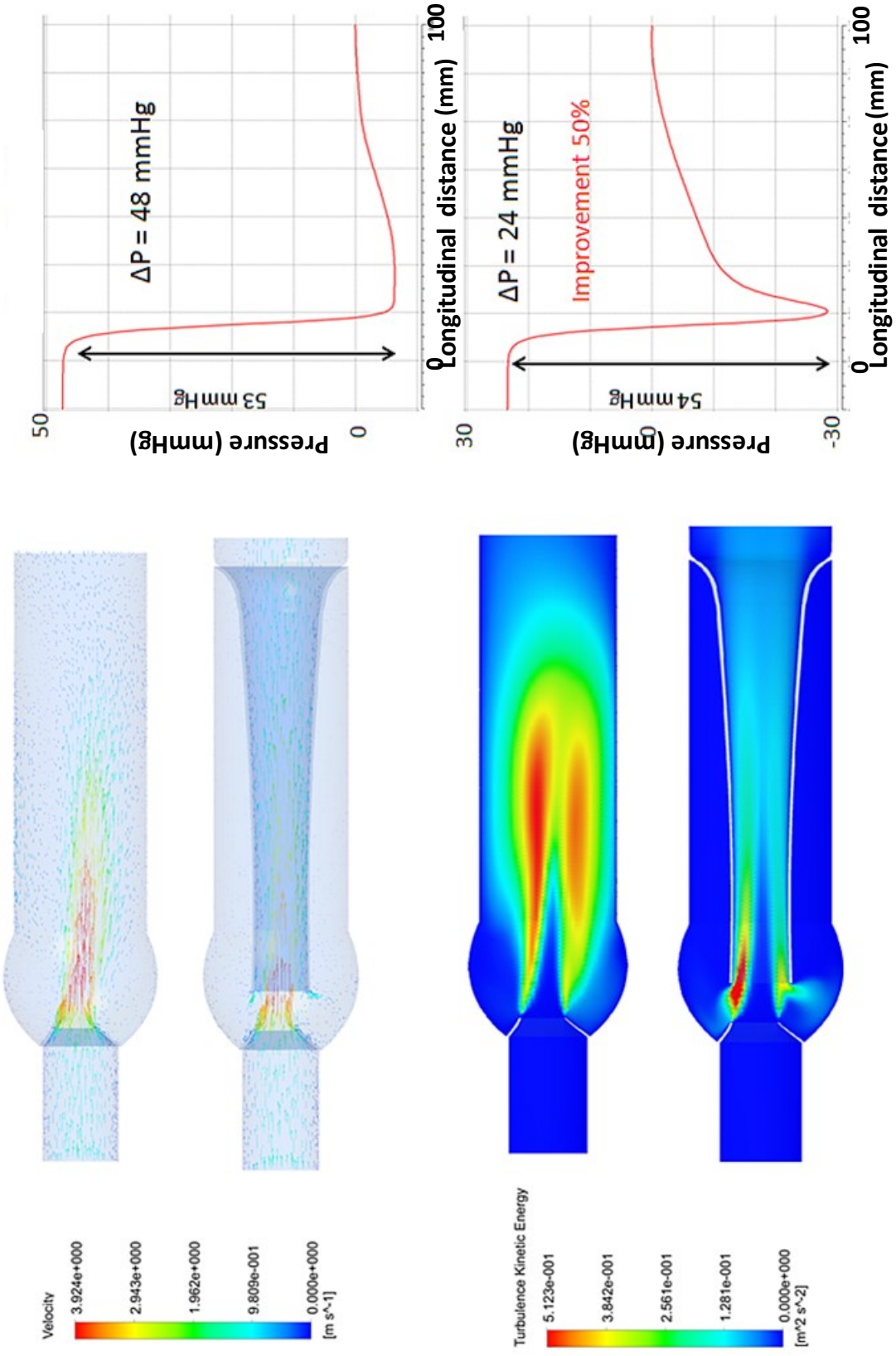

Figure 3-8 Velocity vectors and turbulence kinetic energy pattern on the longitudinal mid-plane for the triangular orifice, without and with the device. The pressure plot along the geometry centreline suggests that 50% of the pressure is recovered in the presence of the device, despite the asymmetric nature of the incoming jet.

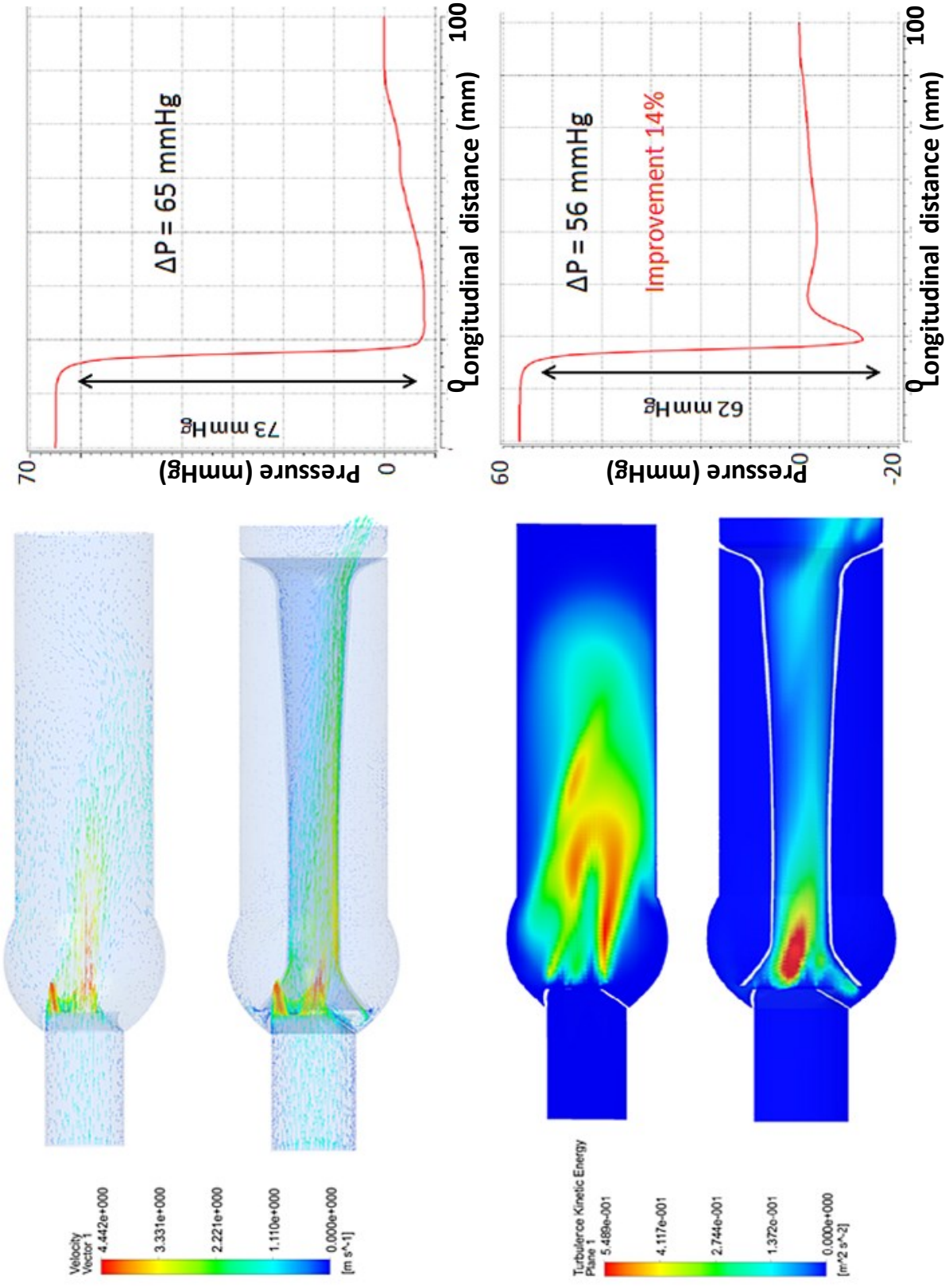

Figure 3-9 Velocity vectors and turbulence kinetic energy pattern on the longitudinal mid-plane for the patient-specific orifice shape, without and with the device.The device was modified to include a funnel-shaped proximal end in order to capture the irregular jets coming out of the orifice. The pressure plot along the geometry centreline suggests that 14% of the pressure is recovered in the presence of the device, a considerably lower amount than in the idealised cases. This suggests that in the patient-specific case the reduction in the level of TKE is not enough to achieve useful pressure recovery.

3.3.2 Effect of valve orifice shape on flow patterns and pressure drop

From the TKE plots it is quite clear that the presence of the device greatly reduces the amount of turbulence kinetic energy in the ascending aorta. Therefore, we hypothesized that the discrepancy between the pressure recovery achieved in the idealised cases and that achieved in the realistic case is because in the realistic case another source of irreversible energy losses is present that is not related to the TKE levels in the ascending aorta. A plot of velocity streamlines near the valve orifice is shown in Figure 3-10. It is obvious that in the case of a circular orifice flow through the stenosis is very structured and laminar, with a flat spatial profile and no high-shear edges to cause energy loss. In the triangular orifice some secondary motion caused by the edges and the domed structure is observed. In the irregular orifice, however, the flow structure has already completely broken down at the orifice, with secondary motion, backward flow and three high-velocity jets coming out in different directions from the pointed edges of the orifice. This means that a high amount of energy has already been lost at the orifice that the tested device design cannot recover.

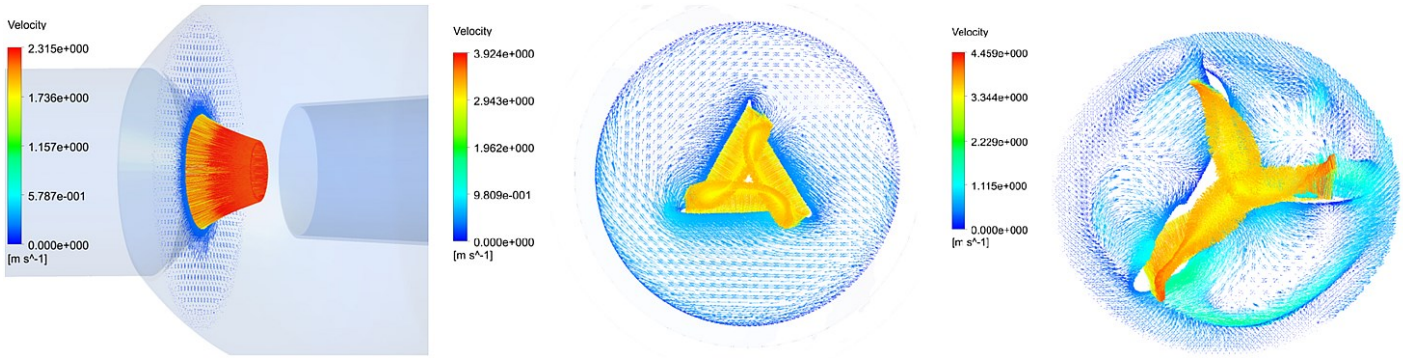

Figure 3-10 Velocity vectors indicating flow patterns on the valve orifice for the three difference rifice shapes. In the circular orifice case the flow jet coming out of the valve is very structured, whilst secondary motion is observed in the triangular orifice shape. In the case of the patient-specific orifice, however, flow is irregular, with no central jet, but just smaller jets coming out in different directions, and large areas of recirculation. The marked difference in flow patterns around the orifice could be the reason why the device cannot achieve high pressure recovery in the patient-specific case.

To test this hypothesis further, another simulation was conducted, where the device was designed so as to be a complete extension of the patient-specific valve orifice. The results are shown in Figure 3-11. The results indicate that a device attached to and completely matching the orifice geometry can produce a similar amount of pressure recovery (56%) as the non-

attached device can in the symmetric circular and triangular geometries. This strongly suggests that there is a significant amount of energy being lost on the orifice that cannot easily be recovered downstream.

3.4 Discussion

This study aimed to prove that maximising pressure recovery inside the ascending aorta can help decrease the pressure drop across the valve by a clinically significant margin. That margin was predicted to be up to 57% for the chosen inlet Tu level.

This result demonstrates that the geometry of a stenosed aortic valve and the anatomy downstream favour high shear flow that results in increased energy and pressure losses, but modifying the geometry of the valve and/or the anatomy distal to it using a properly shaped device could help reduce energy losses and result in higher pressure recovery. However, highly irregular orifice shapes that are a common occurrence in diseased valves result in a large amount of energy irreversibly lost on the orifice, lowering the efficiency of the device to the point where only an exact extension of the orifice will provide significant benefit.

Designing such a device that covers the orifice presents challenges, since without modifications this design results in the blocking of the coronary ostia. Further study is required to overcome this problem.

3.4.1 Patients who would benefit from a pressure recovery device

According to the American Heart Association (Lloyd-Jones et al., 2009), 29% of Community Health System patients over 65 years of age who underwent echocardiography had aortic sclerosis (thickening of the leaflets) and 2% had aortic stenosis. The risk of death by cardiovascular disease for those with aortic stenosis is increased by about 50%. In another study (Otto et al., 1999b) it is stated that 48% of patients over 85 years of age have asymptomatic aortic sclerosis and 4% of the same age group have aortic stenosis, in keeping with the known increase in prevalence of this condition with increasing age. The older age group in which aortic stenosis often happens is also at higher risk of adverse consequences from surgical intervention to replace the valve.

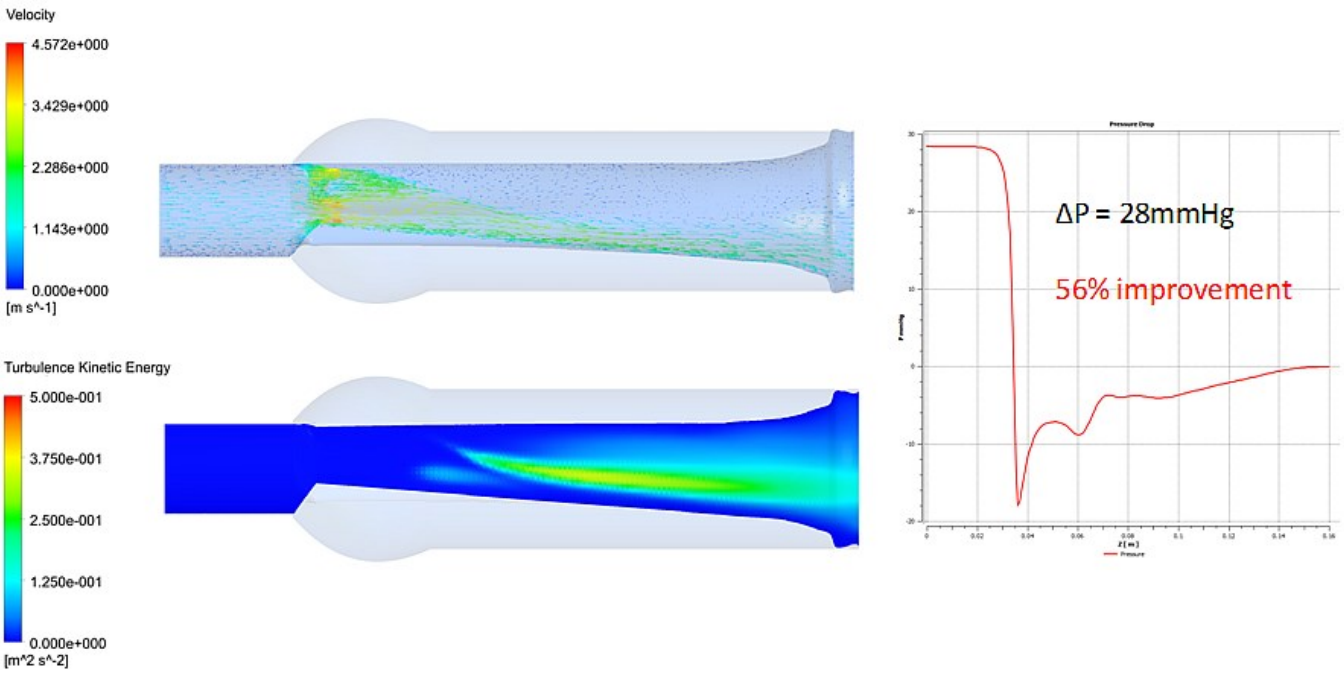

Figure 3-11 Velocity vectors and turbulence kinetic energy pattern on the longitudinal mid-plane for the patient-specific orifice shape, with a device modified to fit the orifice shape exactly. The pressure recovery achieved in this case indicates that significant energy losses occur on the irregular patient-specific orifice, necessitating a device redesign that will address the issue.

Current treatment options for aortic valve stenosis include Aortic Valve Replacement open-heart surgery (AVR) and, when the risk of open-heart surgery is too high (i.e. estimated mortality risk is more than 10%), a procedure called Transcatheter Aortic Valve Implantation (TAVI), where a catheter-driven valve replacement takes place inside the beating heart, without the need for the opening of the chest (Vahanian et al., 2008b). Both procedures carry little risk in general, but there are still patients that are considered too high-risk for any of these two procedures.

Given the previously stated prevalence of the disease in older individuals who are more likely to have medical comorbidities, there is a considerable percentage of patients who would benefit from a procedure that is less demanding than the currently available options.

3.4.2 Device effectiveness in realistic vs. idealised valve geometries

This preliminary study showed that, though in an idealised geometry it is possible to recover pressure downstream of aortic stenosis by implanting a simple device that minimises irreversible turbulence kinetic energy losses, when trying to apply the principle in a realistic

valve shape, many challenges arise, as the original device cannot recover energy losses at the orifice, but only downstream from it. This result demonstrates the perils of using over-simplified idealised geometries to simulate flow in the human vessels, and shows that important features of the geometry that have a measurable effect on the flow, such as the valve shape irregularities, would need to be identified and incorporated into virtual models before drawing conclusions relevant to clinical practice.

3.4.3 Limitations of the study

The study on the aortic stenosis is a preliminary, proof-of-concept study. For this reason, an idealised geometry was used to represent the left ventricular outflow tract, aortic sinuses and proximal ascending aorta, while omitting important anatomical features such as the coronary ostia. The geometry consisted of circular, straight tubes, while the sinuses were represented as a symmetric, spherical shape. All simulations were steady-state, modelling blood as Newtonian and incompressible. The simplified, idealised design was chosen so that the study could better focus on the effect of the valve orifice shape in the efficiency of the device tested. Clearly, pulsatile studies in more realistic anatomies are required to further test the viability of the concept.

3.4.4 Potential applications of the device

The potential issues concerning the practical implementation of a relatively large device inside the ascending aorta have not been considered in this study. These would include challenges regarding the percutaneous implantation of the device and the potential need for anticoagulant therapy to prevent clotting. Further development would be necessary to miniaturise, and further assess the thrombogenic properties of the valve. Based on the analysis presented, it is also clear that in order to be effective, a Venturi device would be required to cross the valve, thus excluding the coronary ostia from aortic flow.

The above analysis suggests that the device would not be suitable for development into a clinical application as is. It is likely that the modifications required to make this device

clinically useful would present similar challenges to those involved in the current TAVI procedure. Therefore, the main advantage of a potential Venturi device would be that the valve does not have to be returned to its original, pre-stenosis cross-sectional area to achieve significant decrease in pressure drop, avoiding the aggressive balloon stent inflation required in TAVI. Stroke is the most common adverse effect for TAVI, with a 20% likelihood of stroke within 30 days of a TAVI procedure (Smith et al., 2011). It is difficult to know if the incidents of stoke at 30 days could be reduced by not aggressively expanding the aortic valve. Further testing would be necessary to assess this.

3.5 Summary and Conclusion

In this chapter, the aim was to investigate the use of the phenomenon of pressure recovery in a device design that could reduce the pressure drop observed across stenosed aortic valves. The device was tested in three virtual models of valve orifice anatomy in a proof-of-concept study.

Steady-state CFD simulations were set up using an idealised model of the left ventricular outflow tract, aortic root and ascending aorta. A rigid, domed valve was placed inside the root, testing three different valve orifice shapes: a completely idealised circular disk shape, a triangular shaped disk with rounded edges and a valve shape based on the CT scan of an actual aortic stenosis patient. For each orifice shape the original geometry and a geometry incorporating the device were produced. The flow conditions were chosen to represent peak systole, when maximum flow, and therefore maximum pressure drop, is observed. The flow velocity and turbulence kinetic energy patterns were compared between the original and device-implanted geometries and their effect on the behaviour of pressure throughout the geometry was examined.

It was found that the proposed device can recover more than 50% of the pressure lost on an idealised circular or triangular orifice, but its effectiveness is greatly diminished when applied to a realistically irregular patient-specific orifice. Observing the velocity and TKE patterns suggests that, in the case of the patient-specific orifice, recovering the energy lost as shear in the proximal ascending aorta is not enough to achieve a level of pressure recovery that could become useful in clinical practice. Studying the flow patterns on the orifice revealed that flow patterns in the patient-specific case are markedly more irregular than those in the circular

and triangular idealised cases, indicating a large amount of energy loss occurs on the orifice itself.

Modifying the device to place it across the orifice increased its effectiveness to the levels observed in the idealised models, suggesting further modifications are required in the device to ensure energy lost on the orifice will be recovered too, the most likely of which is to create a device that will cross the valve, starting from the LVOT and ending in the ascending aorta. This would result in remodelling of the aortic root, adding challenges to the device design, including the need for a new valve inside the remodelled aortic root, and provision for flow into the coronary arteries. In conclusion, this device, with the modifications required to make it clinically applicable, would likely not present an advantage compared to existing procedures.

4. A new algorithm for accurate 3D coronary artery reconstruction based on Optical Coherence Tomography and angiography

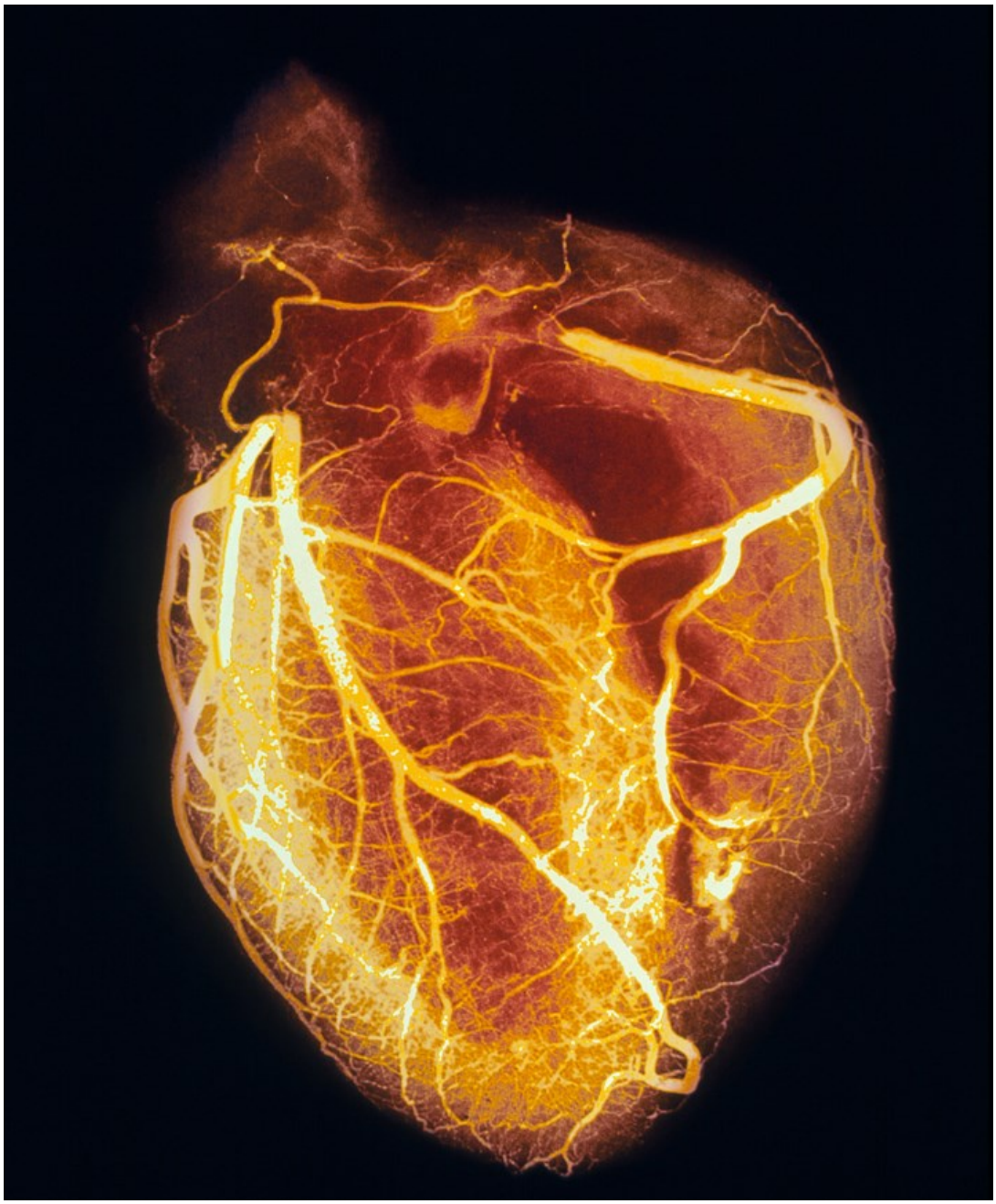

Figure 4-1 A 3D image of the healthy human heart, epicardial coronary arteries visible. Image copyright National Geographic, 2007.

4.1 Introduction

In the previous chapter, the role that pressure drop can play in the treatment of aortic valve disease was explored. In this chapter the role of pressure drop in the diagnostics of coronary artery disease is investigated. The coronary arteries are one order of magnitude smaller than the aorta, which presents challenges to both imaging the vessels and measuring flow rate. For this reason, fully patient-specific numerical (CFD) studies of human coronary arteries are fewer than other, larger arteries, and there is still considerable room for improvement.

In this chapter, a novel method for the 3D reconstruction of human coronary artery anatomy is presented, making use of the high resolution and contrast of Optical Coherence Tomography (OCT), combined with angiography data to create one of the most accurate coronary artery reconstructions to date. The chapter begins with a description of the custom algorithm developed to achieve the reconstruction, followed by the presentation of the reconstruction method's validation using a phantom model of idealized artery geometry. The use of this method in fully patient-specific, pulsatile CFD simulations is then presented in the next Chapter. An overview of the reconstruction and CFD process is shown in Figure 4-2.

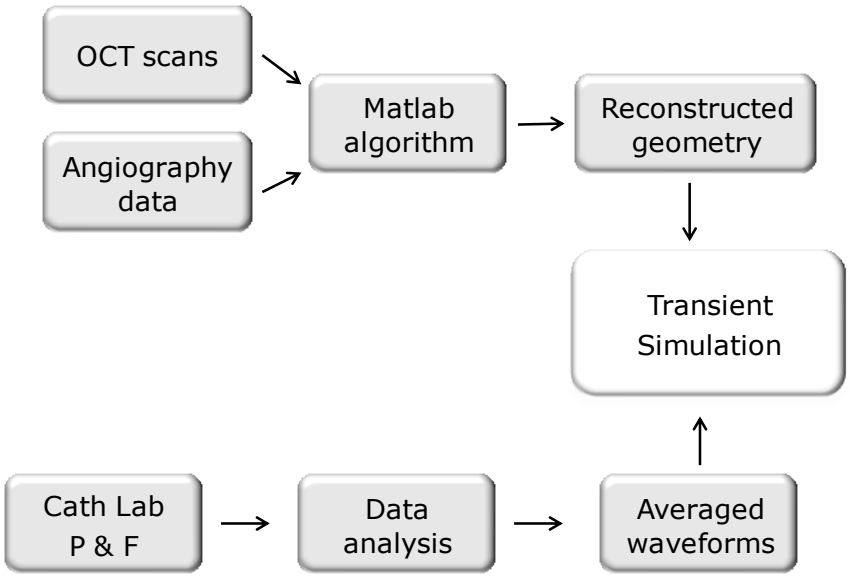

Figure 4-2 Overview of the reconstruction and CFD simulation set up process for the patient-specific study of human coronary arteries.

4.2 Patient Demographics

Nineteen patients (age 65.9±10.8; 14 (73.7) male) with 21 stenoses (of which 13 located at the left anterior descending artery, 5 at the right coronary artery and 3 at the left circumflex artery) scheduled for invasive coronary angiography and pressure wire assessment were formally enrolled into the study. Patients with significant aortic stenosis and mitral regurgitation were excluded to avoid confounding coronary flow velocity patterns. Patients with significant renal impairment limiting angiographic dye use were also excluded since OCT imaging was a prerequisite of the study. Table 4-1 provides the demographic data for the patients.

Table 4-1 Demographic data for patient group (n = 19)

Mean age in yrs (range)	65.9 (44-81)
Male (%)	14 (73)
Mean BMI (range)	30.17 (21.63-41.82)
Risk factors (n, (%))	
hypertension	13 (68.4)
hypercholesterolemia	14 (73.7)
diabetes	8 (42.1)
current smoker	4 (21)
prior MI	4 (21)
peripheral vascular disease	1 (5.3)

4.3 Imaging data acquisition

4.3.1 Angiography

Angiographic images were acquired using a 6 F guiding catheter via a 6 F sheath engaged into the left main stem for left coronary system stenoses or the ostial right coronary artery. Fluoroscopic angiography was performed using a Toshiba system (Infinix) and archived into a McKesson Medcon system (McKesson, San Francisco).

Angiograms were obtained in serial monoplane using an isocentred table. Two unobstructed views of the vessel segment of interest with at least 45 degrees angle of separation between views were taken. Table panning was prohibited during data acquisition. Electrocardiographic data determining the cardiac phase was stored simultaneously with the angiographic data. The coronary artery images for the reconstruction were selected during diastole.

DICOM files were imported into CAAS QCA3D (Pie Medical Imaging BV, Maastricht, The Netherlands) and the centreline of the vessel was traced manually in both views. An anatomical feature evident on both views was used as a fiducial point to aid the reconstruction (Figure 4-3). The reconstructed vessel was stored in the stl file format (Chua et al., 1997).

4.3.2 Optical Coherence Tomography (OCT)

Optical coherence tomography (OCT) was performed using the C7 Dragonfly intravascular imaging catheter and Ilumien console (St Jude Medical, Minnesota). The 2.7 F OCT imaging catheter was advanced over an intracoronary angioplasty wire across the coronary stenosis and image acquisition was performed after automated injection of contrast media given at the rate of 4 ml/s for 4 seconds. Contrast media replaces intracoronary blood and allows light based imaging of the vessel lumen at high resolution. Care was taken to ensure stenosis and vessel were imaged with good quality. Data was archived upon the Ilumien and exported as DICOM and TIFF format for offline analysis.

The presence of imaging artefacts such as non-uniform rotational distortion, saturation or motion required a second scan. However, since the data acquisition was complex, requiring post-PCI assessment, it was not clinically safe to perform further runs, as the amount of contrast used would reach dangerous levels.

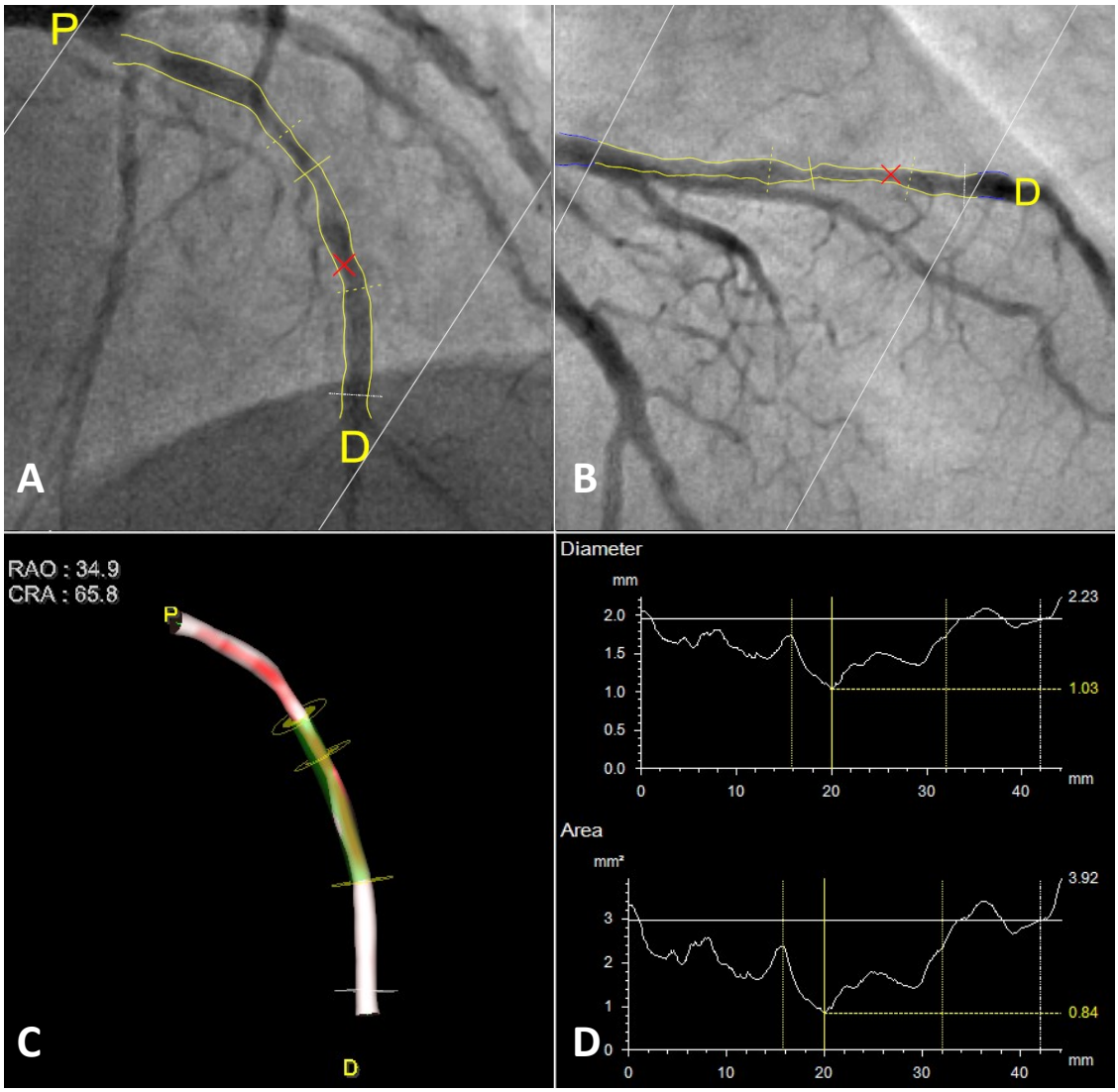

Figure 4-3 A-B. Two angiographic views used for the reconstruction. The yellow lines indicate the traced lumen while the red cross represents the fiducial point as seen in both pictures. **C.** The 3D reconstruction based on the images A and B, using software CAAS QCA3D. Areas of disease are shown in red, while green indicates the suggested path of the original normal vessel, providing estimation for % anatomical obstruction. The lumen contours are represented by circles and ellipses. **D.**Diameter and cross-sectional area plots along the reconstructed vessel, providing the location of the minimal luminal area.

271 images of the vessel segment were acquired for each OCT acquisition (a typical OCT slice shown in Figure 4-4) with a slice interval of 0.2 mm (i.e. 54.2 mm length). In six cases, incomplete expulsion of blood by contrast led to a swirling pattern reducing the quality of the images, resulting in the necessity to exclude slices from the analysis, typically 50 slices

(10 mm) at the end of the pullback run where the lumen could not be reliably estimated. The smallest vessel segment reconstructed was 29 mm long. In one case, two overlapping OCT scans were performed in an attempt to image a longer vessel segment where diffuse disease was present, and so the longest vessel reconstruction in this dataset was 65 mm long.

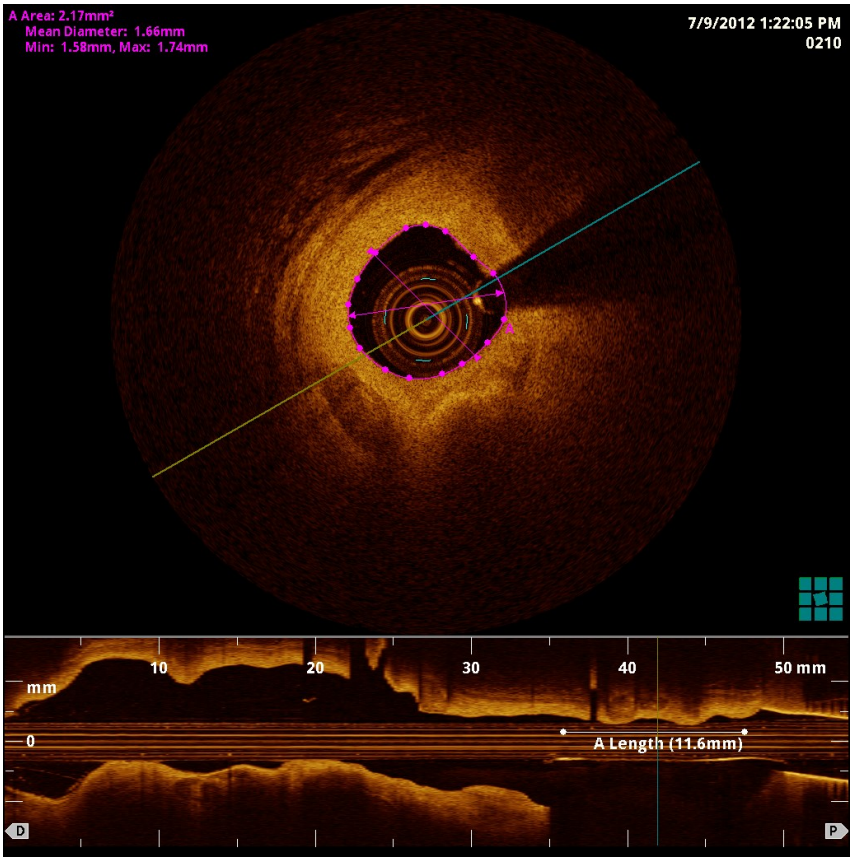

Figure 4-4 A typical OCT slice, showing the minimal luminal area (MLA) of a proximal right coronary artery stenosis. The lumen wall is coloured bright orange, while the lumen appears black, the contrast between the light and dark areas is very high, facilitating contour tracing. The image resolution is 10μm. A longitudinal cross-section of the vessel segment imaged can be seen at the bottom.

Reference points for the matching of the two methods were provided by visual identification of the OCT catheter on the coronary angiogram at its distal-most location in the vessel (when the pullback begins). The location of branches and other geometrical features, such as the catheter or the lesion itself were also used to assist matching. Since the starting point and the length of the pullback were clearly defined, it is easy to locate the proximal end of the segment to be reconstructed (Figure 4-5). Changes to the OCT catheter tip position or vessel diameter following contrast injection were not considered in this study.

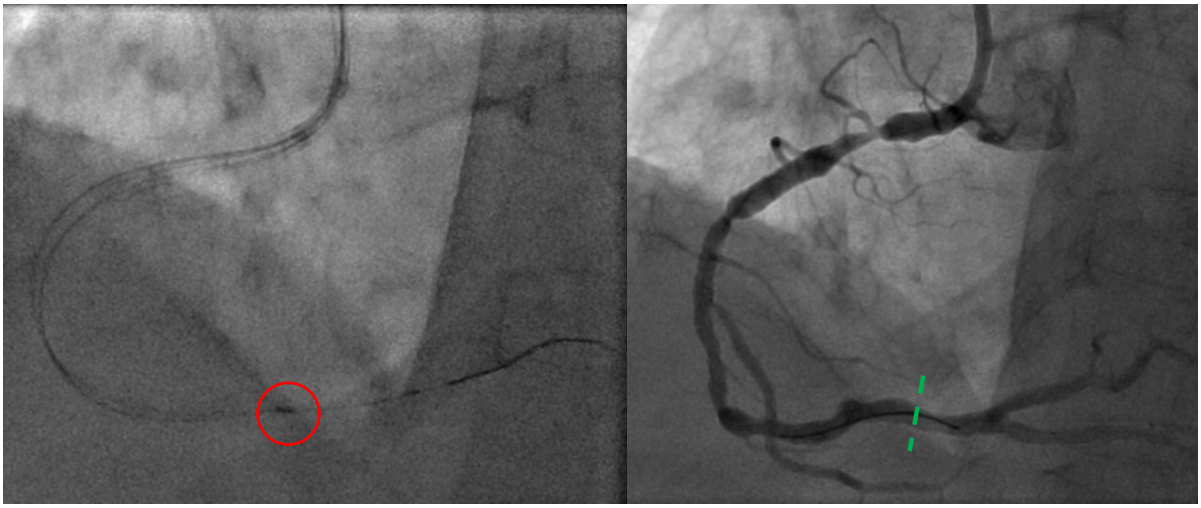

Figure 4-5 Left. Anangiograohic view of the OCT catheter inside the vessel at its most distal location. The catheter can be seen as two black dots on the wire. The pullback begins at the location of the most proximal of the two dots (red circle). **Right.** The corresponding location of the pullback beginning on the vessel using the same view (19 degrees left anterior oblique, 19 degrees cranial). The green line indicates the beginning of the centreline tracing. Knowing the pullback start point and length, it is easy to determine the end point.

4.4 3D Reconstruction Algorithm

The data collected were analysed off-line using a custom software package designed in a Matlab environment (MathworksInc, Natick, Mass). The reconstruction process is described below:

4.4.1 Segmenting the lumen contours from the OCT slices

The OCT scan slices (1024x1024 pixels, resolution 10μm/pixel) were imported into Matlab R2012a (Fig 4-6A). The guide wire and OCT catheter were masked automatically prior to segmentation, to avoid errors in the algorithm. The algorithm scans each prepared slice radially for the points of maximum brightness, as shown in Figure 4-6B. Points lying outside 1.5 standard deviations either side of the mean distance from the cluster centroid were removed and the remaining points were smoothed using a moving average filter with a span of 11 points either side (Fig 4-6C). Thresholding was used to aid the algorithm. The brightness threshold used was optimised for each slice such that noise and other undesirable features (such as minor swirling) were removed automatically. The lumen contours were then traced using an active contour algorithm, a process (Matlab, function Snake2D, copyright

2010, Dirk-Jan Kroon) utilising a deformable spline which outlines object contours using gradient vector flow (Xu and Prince, 1997, Xu and Prince, 1998). The initial spline in each frame was defined as a circle around the centroid of the cluster points (Fig 4-6C). Once the contours were traced they were located on the XY (Z=0) plane of Cartesian coordinates, with the centroid placed on the origin. The normal unit vector for the surface defined by the contour was therefore $\hat{z}$ = (0, 0, 1) (Fig 4-8).

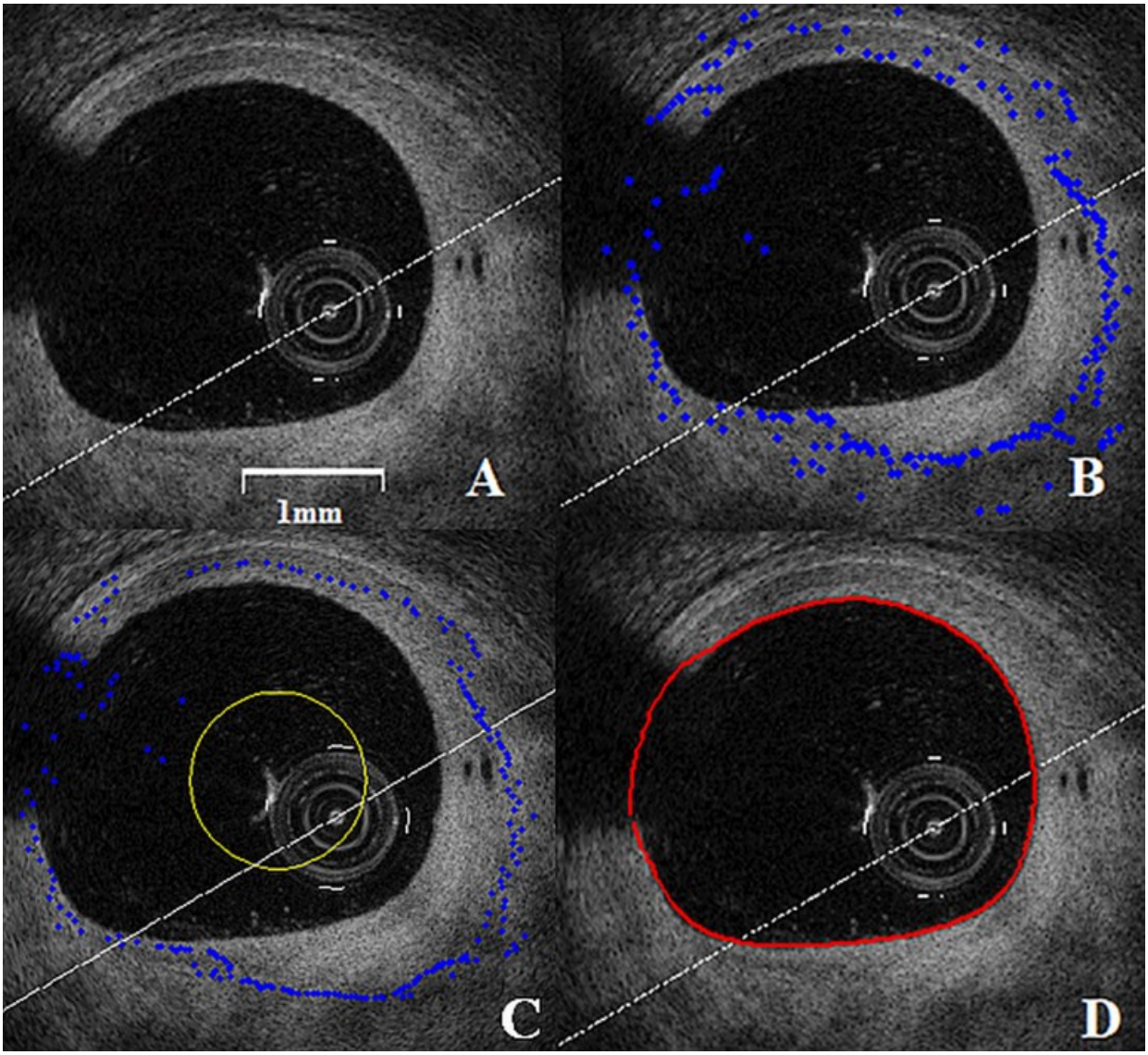

Figure 4-6 A. Original OCT scan imported as a greyscale image into Matlab software **B.** Same image with dots indicating the points of maximum brightness as found in the first stage of the algorithm. **C.** The dots represent the same points after deleting outliers and smoothing. The circle near the centre is drawn around the centroid of the points cluster and serves as the initial spline of the active contour algorithm. **D.** Segmentation of the lumen (bold line) is achieved using an active contour algorithm.

The lumen tracing algorithm is semi-automatic, with very few minor adjustments required as input. Most of the input required is related to the parameters of the active contour

algorithm, which include the expansion (balloon) factor and stiffness and sensitivity to noise. These parameters need to be adjusted to the image quality and vessel caliber that can vary considerably from patient to patient.

4.4.2 Calculating the centreline of the vessel from angiography

The anatomy reconstruction provided by QCA3D was imported into Matlab as a set of vertices in Cartesian coordinates (Figure 4-7). For each few millimeter segment of vessel which typically contains 3 to 4 vertices in the longitudinal direction, vertex coordinates were averaged to obtain the coordinate of the segment's centroid. The spline formed by the calculated centroids was then smoothed using a least squares interpolation method. The smoothing parameter was set to 0.9, close to the neutral value of 1, so that the smoothed spline points remained close to the original data.

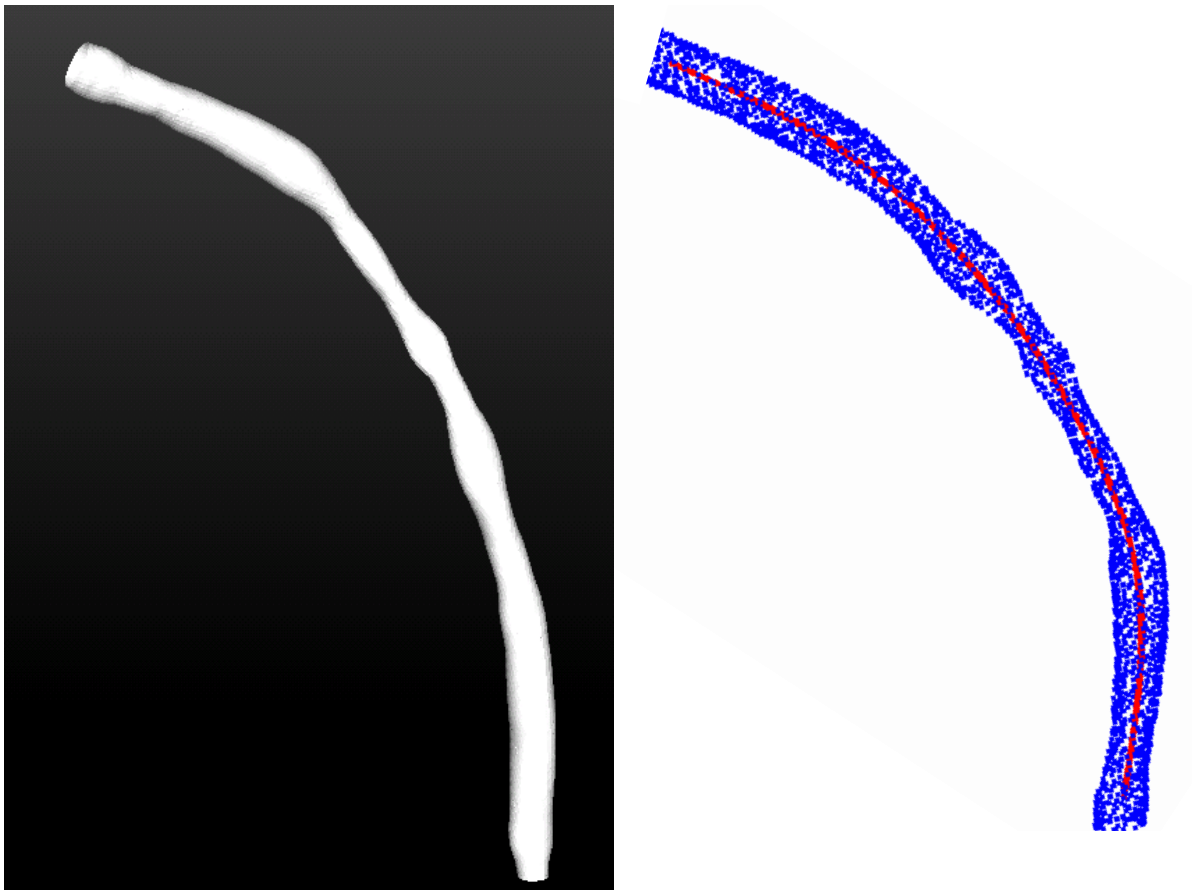

Figure 4-7 Left. The vessel reconstructed using CAAS QCA3D software based on the data from shown in Figure 4-3. **Right**. The surface points (blue) are imported into Matlab and the centreline (red) is calculated and smoothed.

4.4.3 Combining contour and centreline data to obtain reconstructed geometry

The calculated centreline provides the 'spine' onto which the lumen contours will be mapped. It is first divided into vectors 0.2 mm in length, equal to the slice thickness; these vectors form the surface normal vectors of the plane onto which each lumen contour will be placed. The angle, ϑ, between the normal vector of the XY plane and the centreline vectors is calculated as in equation (4-1):

$$\vartheta = \arccos\left(\frac{\hat{z} \cdot (destination\_surface\_normal)}{|\hat{z}||destination\_surface\_normal|}\right) \tag{4.1}$$

Angle ϑ is the angle of rotation, while the unit vector corresponding to the cross product of the vectors forms the axis of rotation; the x, y and z components of the unit vector are noted as v_x, v_y and v_z respectively. These parameters are used in a 3D rotation matrix (Table 4-2) which is applied to each contour. The process is schematically represented in Figure 4-8.

Table 4-2 The rotation matrix used on the contour slices so that they become aligned with the centreline. The inputs required are the angle of rotation ϑ, and v_x, v_y and v_z, which are the x, y and z components respectively of the unit normal vector of the cross product between the two vectors, which forms the axis of rotation

$$\begin{bmatrix} X' \\ Y' \\ Z' \end{bmatrix} = \begin{bmatrix} \cos\vartheta + v_x^2(1-\cos\vartheta) & -v_z\sin\vartheta + (1-\cos\vartheta)v_x v_y & v_y\sin\vartheta + (1-\cos\vartheta)v_x v_z \\ v_z\sin\vartheta + (1-\cos\vartheta)v_x v_y & \cos\vartheta + v_y^2(1-\cos\vartheta) & -v_x\sin\vartheta + (1-\cos\vartheta)v_y v_z \\ -v_y\sin\vartheta + (1-\cos\vartheta)v_x v_z & v_x\sin\vartheta + (1-\cos\vartheta)v_y v_z & \cos\vartheta + v_z^2(1-\cos\vartheta) \end{bmatrix} * \begin{bmatrix} X \\ Y \\ Z \end{bmatrix}$$

Once the contours have been rotated to the desired orientation, the distance between their current and intended location is calculated, and a translation is applied, placing the contours in their final location.

The final step is to apply in-plane rotation of each contour. Due to lack of catheter path information, a uniform rotation was applied throughout the vessel. The information needed for this step is provided by the angiographic images. A characteristic geometrical feature (like a branch) is identified in both the angiogram and the OCT scan. Then the vectors d_0 and d_1 are drawn from the centre of the vessel to the common point in the OCT slice and

angiogram respectively (Figure 4-8). The characteristic point from the OCT scan is traced through the initial rotation and translation, and the new vector d'_0 is traced on the final contour plane. The angle between d'_0 and d_1 is the in-plane rotation angle. All contours are then rotated by the same angle. This method works under the assumption that the OCT catheter does not rotate around its axis during the scan. Given the fact that an OCT catheter is protected by a stiff sheath and the lengths scanned are relatively small (54.2 mm), this is a reasonable assumption, which has been shown to result in credible reconstruction, as shown in the validation section 4.5 of this chapter.

The reconstruction is complete when the contours are exported in the form of 3D Cartesian coordinates into a custom-developed FORTRAN routine which combines the data into a stereolithography file. The resulting 21 geometries are presented in Figure 4-11.

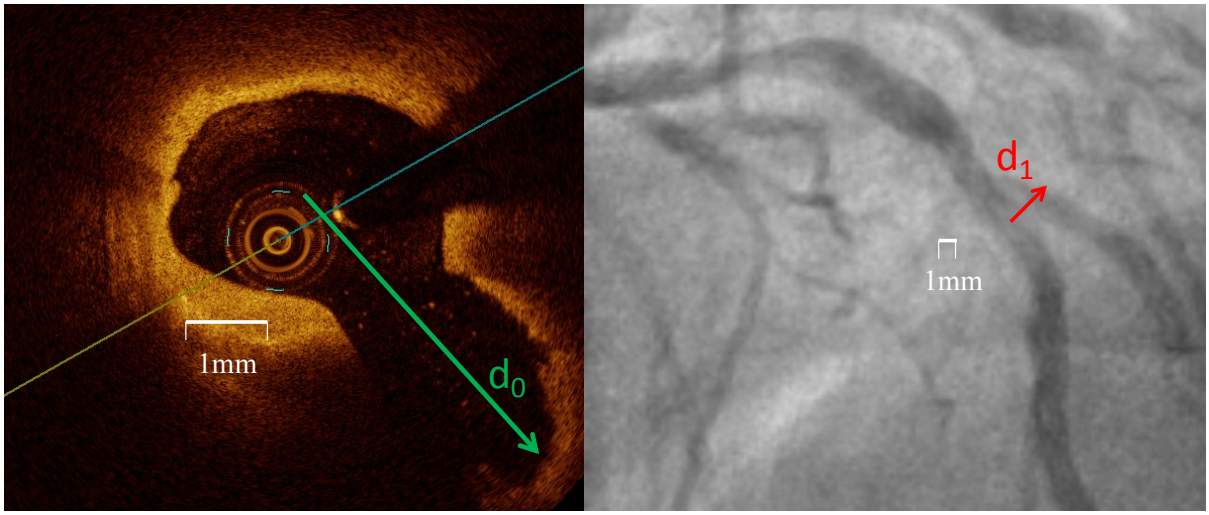

Figure 4-8 Determination of in-plane rotation angle **Left.** The vector d_0 connecting the centroid of the vessel cross-section to the fiducial point (in this case a branch) in the OCT slice is shown in green. **Right.** The same distance traced on the angiogram, shown in the red vector d_1. The vector d_0 is traced throughout the initial translation-rotation process, to form the vector d'_0 when the lumen contour is placed in the final plane. The angle between d'_0 and d_1 is the angle of in-plane rotation.

Each vessel is reconstructed using the 3D angiography-based reconstruction technique before adding the OCT contours. The results of the two different methods applied to the same vessel segment are compared in Figure 4-10, where the added fidelity from the OCT images over the more smoothed 3D angiography images is apparent. The OCT-based reconstruction appears considerably more irregular as would be expected in vivo, while the shape of the lesion also looks considerably different, though the calculated minimal luminal area (MLA) is similar. These differences are due to the QCA3D software representing the vessel contours as ellipses, whereas the OCT based methodology more closely represents the true lumen

contours segmented from the OCT scans. This results in realistic reconstruction that requires no smoothing of the contour shape and minimal smoothing of the centreline.

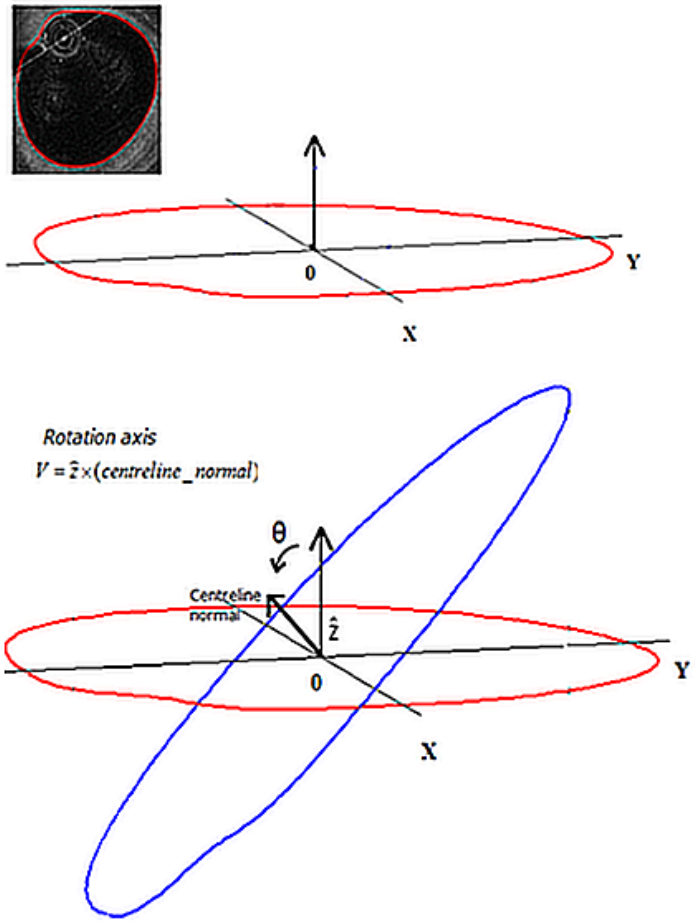

Figure 4-9 Schematic representation of the 3D rotation of the lumen contours. **Top.** The contours originally lie on the XY plane, with $\hat{z}$ as plane normal. **Bottom.** The vessel centreline provides the unit vector which becomes the rotation axis. Applying the rotation matrix on the original contour coordinates, the coordinates of the rotated geometry can be calculated. Finally, the oriented contours are translated into position.

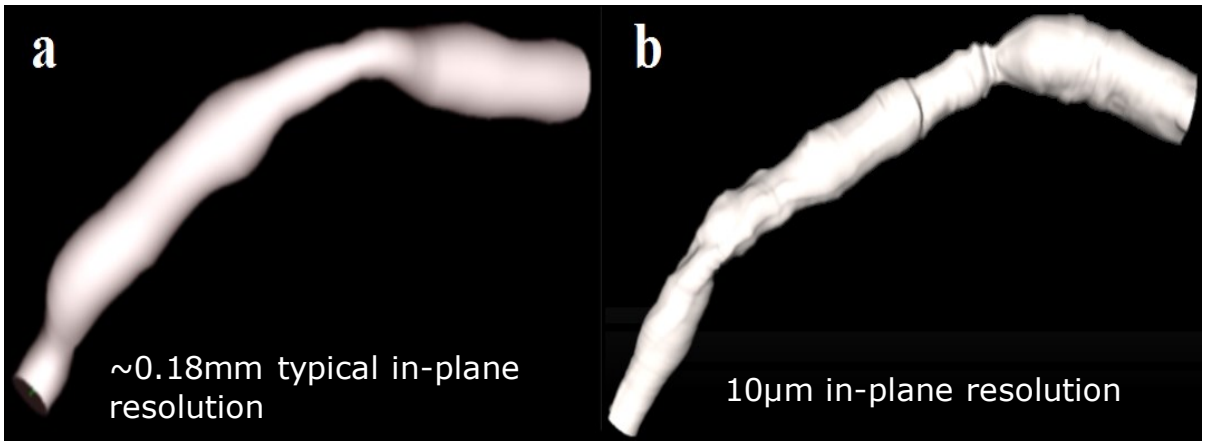

Figure 4-10 Comparison of the angiography-based QCA3D reconstruction **(a)** and the angiography with OCT reconstruction **(b)** methods applied to the same vessel segment. In the QCA3D method lumen contours are represented as ellipsoids giving a smoothed appearance. Whereas the lumen contours from the OCT images provide a much closer representation of the vessel characteristics, including, surface irregularities and the lesion shape.

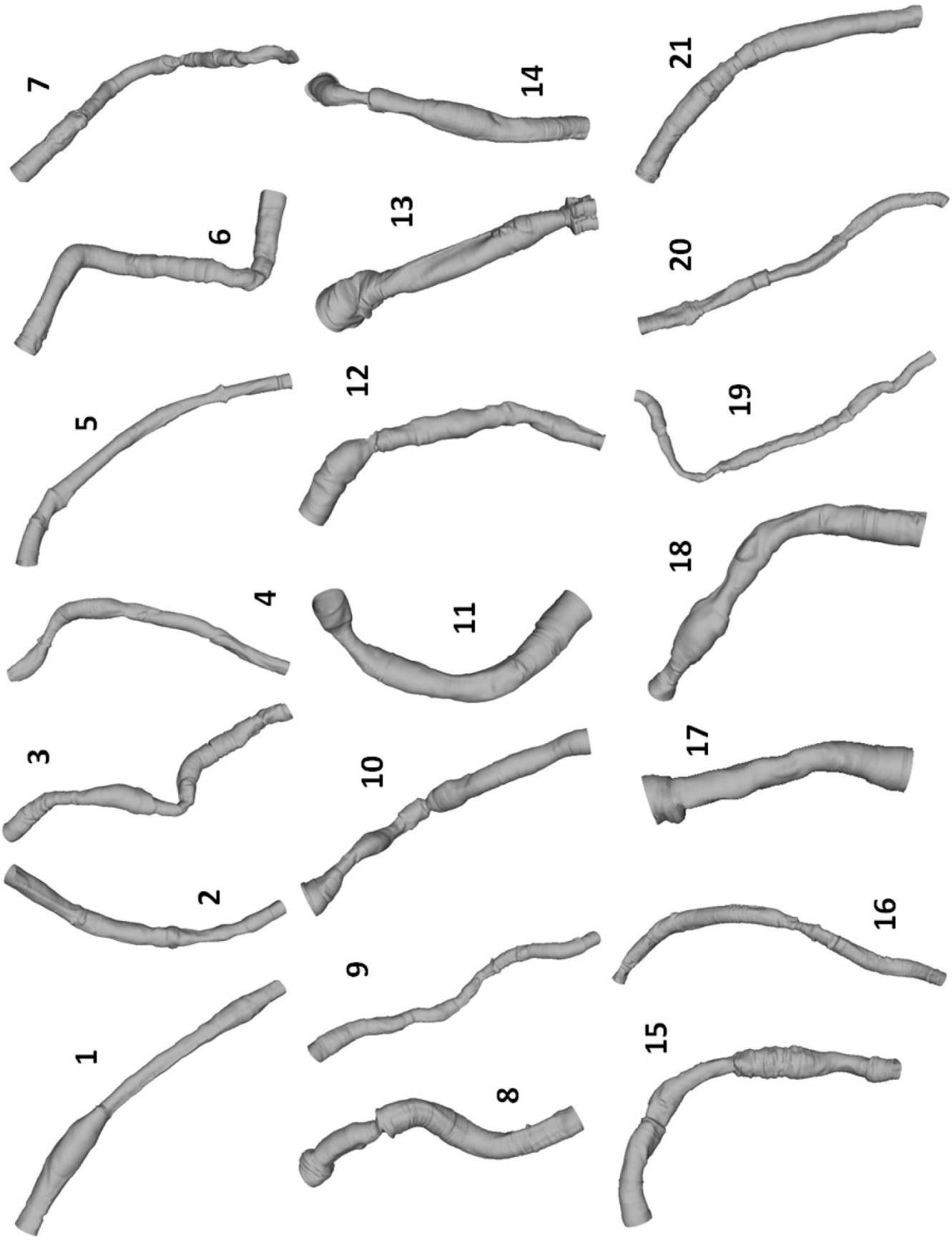

Figure 4-11 Examples of reconstructed coronary artery anatomies using the method described in this chapter.

4.5 Validation of the reconstruction method

As with all computer-based modelling, testing of the new method was required to ensure that the reconstructed geometry represents the real vessel anatomy. For this reason, a virtual 3D model of idealised coronary anatomy, including branching, curvature, and the presence of stenosis was built, and with the aid of rapid prototyping a phantom model was made, which was then imaged using the same protocol applied to the human vessels presented above. A virtual reconstruction was produced and then compared to the original virtual model, in an attempt to evaluate how close the reconstruction method can get to the real anatomy. The final result was found to be satisfactory. The full methodology used for the validation is described below.

4.5.1 Virtual 3D model of an idealised coronary stenosis

A model of idealised stenosed coronary anatomy was built in ANSYS ICEM CFD 13 (ANSYS Inc., Cannonsburg, PA). The geometry is 52 mm long with a diameter ranging from 3.5 mm at the proximal end to 2.5 mm at the distal end, mimicking the normal tapering of the vessel as it branches out. It consists of a main vessel and a bifurcation branching out at an angle of 45 degrees. An eccentric, 50% diameter (75% cross-sectional area) stenosis was included in the model, placed near the bifurcation region, a common occurrence in cases of coronary artery disease. Care was taken to include features that would pose challenges to the reconstruction algorithm, such as the presence of a branch, which creates large areas of shadow, and of a stenosis placed exactly on the bifurcation which has also been a challenge for the reconstruction algorithm to capture, so that model presented a true challenge for the algorithm. The model is, however, lacking curvature in the longitudinal direction, which limits the model's ability to validate the centreline assumption.

A cross-section of the model is shown in Figure 4-12. The geometry was converted to a stereolithography (stl) file and a wall thickness of 1mm was added to the model to facilitate the rapid prototyping process that followed.

4.5.2 Rapid prototyping to produce phantom model

The virtual 3D model was then used as a model for rapid prototyping (Sirris, Brussels, Belgium). The Polyjet printing method was used. Polyjet is a 3D printing method which was developed in 2001 as a very promising technique, improving on the accuracy of other methods, whilst achieving lower surface roughness for smoother models (Pilipovic et al., 2009, Salmi, 2013). The method consists of printing very thin (0.16μm) layers of photopolymer material using a technique similar to ink-jet 2D printers. The CAD-guided layers of photopolymer build up to create the 3D geometry whilst being simultaneously cured under an ultra-violet light to maintain structure. The final spatial resolution of the structure is about 0.016 mm (Ibrahim et al., 2009) , comparable to the OCT slice thickness of 0.2 mm.

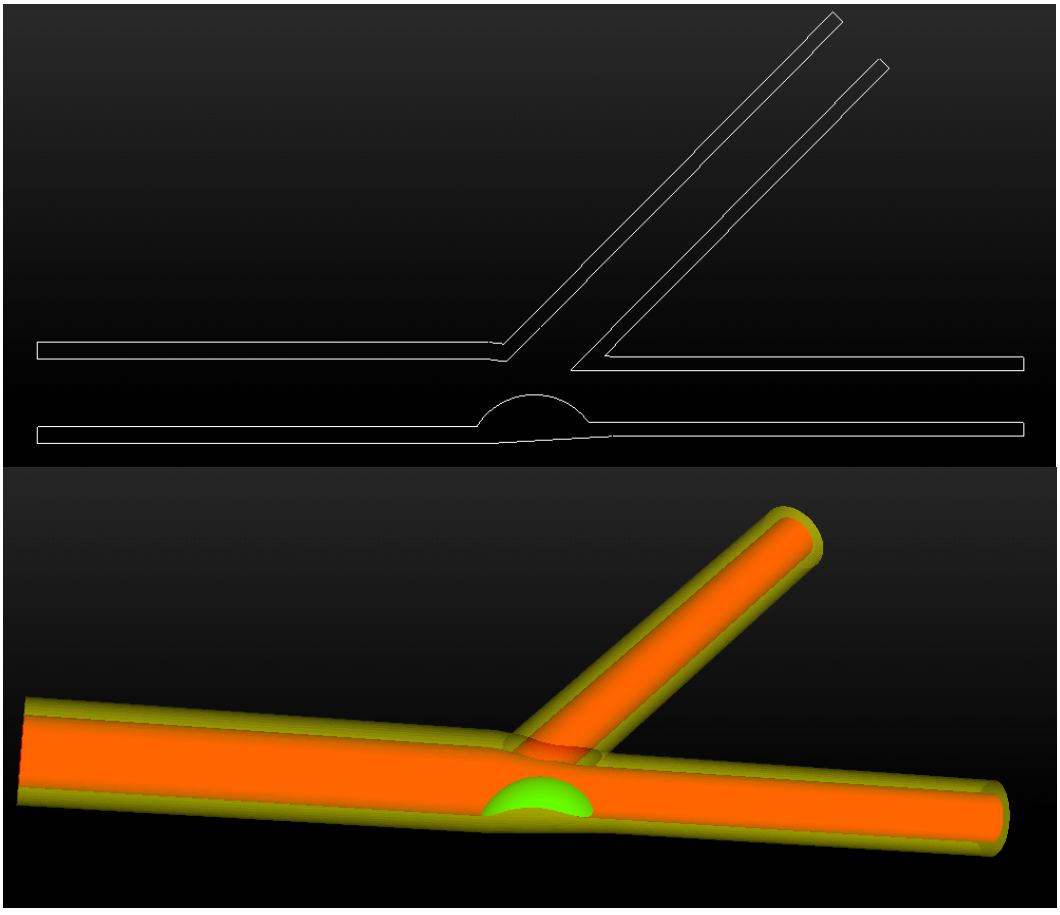

Figure 4-12 Top A two-dimensional sketch of the proposed model geometry. The addition of a branch and a stenosis very near the bifurcation were designed to pose a realistic challenge to the algorithm. **Bottom** The final 3D model, the lumen to be imaged is shown in orange and the stenosis is highlighted in green. A 1mm-thickness wall was added (transparent yellow) to aid the rapid prototyping process.

Initially Polyjet was limited by the lack of variety of compatible materials (Durham, 2003), but with the development of new materials it has become the preferred method of producing phantom models, especially in cardiovascular and other medical applications (Murugesan et al., 2012, Salmi et al., 2013b, Salmi et al., 2013a, Lambrecht et al., 2009).

The material chosen for this application was TangoPlus FullCure W (Objet ltd, Rehovot, Israel), a rubber-like, commercially available material. The material has a combination of properties that make it attractive for use in a phantom model of coronary artery, as it is compliant, durable, is unaffected by water and can be transparent below a certain thickness, allowing for easier control of the OCT catheter. The mechanical properties of the material as used in arterial phantoms, an application similar to the one presented in this chapter were investigated by (Biglino et al., 2013) who showed that TangoPlus is a material suitable for use in *in vitro* testing of arterial models, achieving a distensibility that is within the physiological range, as shown in Figure 4-13. A picture of the final model is shown in Figure 4-14. As there would be no modelling using human blood, or modelling of the arterial wall structure and properties, the interaction of the TangoPlus material with blood was not investigated.

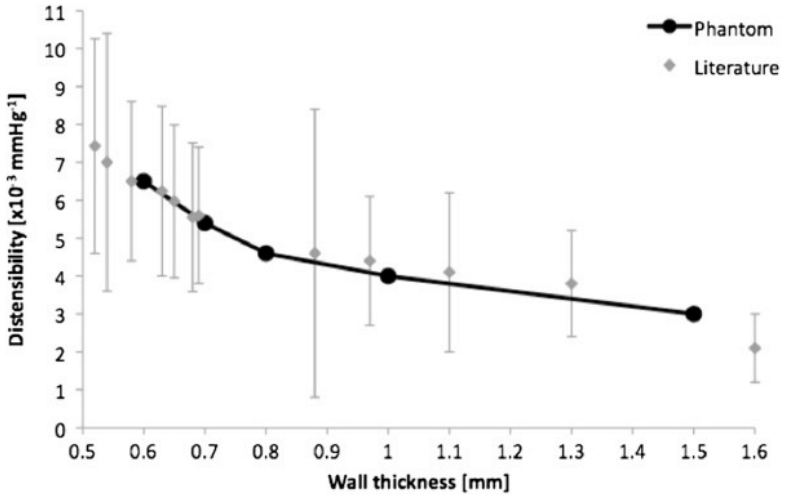

Figure 4-13 A plot of wall distensibility vs. wall thickness for a TangoPlus phantom arterial model (black circles) compared to the physiological range (grey diamonds). Image reproduced from (Biglino et al., 2013)

4.5.3 Imaging of phantom model

A known limitation of the OCT method is that it can only visualize one branch at a time. For this reason, only the model's side branch was imaged using OCT. The reason that the side branch was chosen was because it would provide a bigger challenge to the model, because it has a curving centerline and provides a dimmer view of the stenosis (the stenosis being located on the main vessel). It should also be noted that the rapid prototyping process resulted in a rough model 'lumen' (Figure 4-15 and 4-19), adding another challenge to the model, as roughness was not included in the original virtual model.

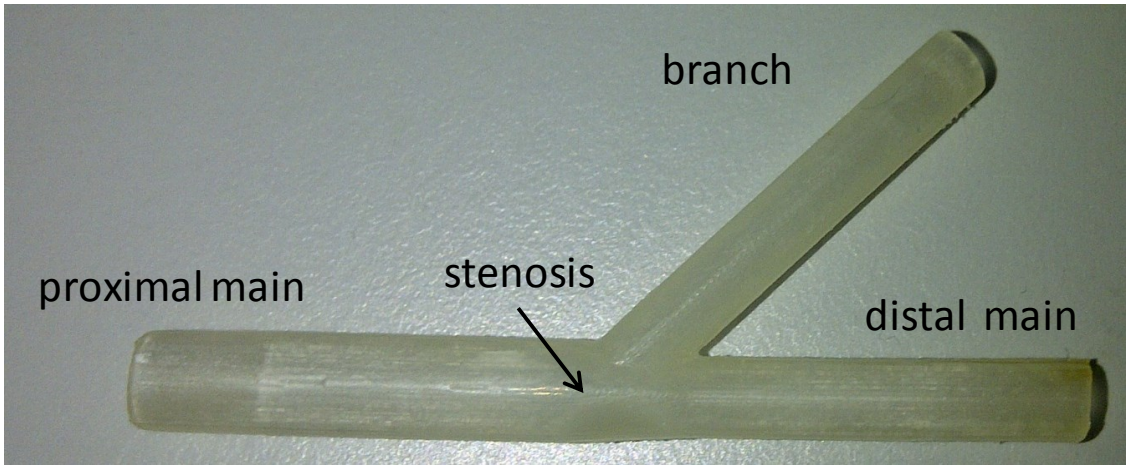

Figure 4-14 The final phantom model that was created using rapid prototyping from the virtual model shown in Figure 4-12. The material (Tangoplus) is distensible and partially transparent allowing for easy visualisation of the OCT catheter during imaging. The rapid prototyping process resulted in a smaller lumen compared to the one created in the virtual model, due to the presence of roughness which was difficult to remove.

The imaging protocol followed was the same as described in sections 4.3.1 and 4.3.2. For the OCT imaging 271 images of the model segment were acquired with a slice interval of 0.2mm, (i.e. 54.2mm length). A slice showing the presence of stenosis and the branching is shown in Figure 4-15. For the angiography data acquisition angiograms were obtained so that there were at least two unobstructed views of the model with a sufficient angle between the views to allow for good quality reconstruction, as shown in Figure 4-16.

4.5.4 3D Reconstruction and comparison to virtual model

The reconstruction method was the same as described in section 4.4. The angiography images and angiography-based reconstruction are shown in Figure 4-17, while the completed reconstruction compared to the original model is shown in Figure 4-18.

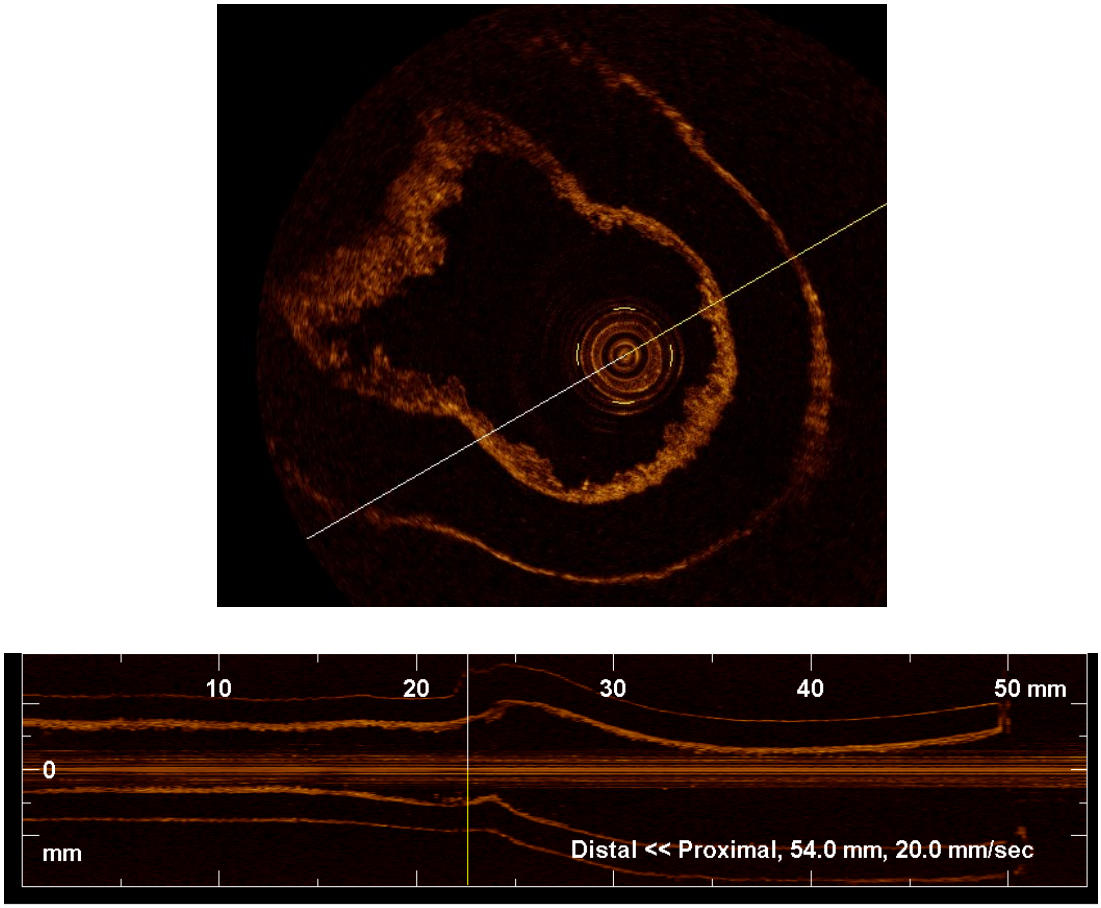

Figure 4-15 Top. An OCT scan slice of the phantom model, showing both the stenosis (top left) and the bifurcation. The roughness seen on the lumen surface is a result of the rapid prototyping process, and was not present in the virtual model. Since the stenosis was in the main vessel and not in the branch, it was visualised at a distance, which has affected the contrast of the stenosis images. This was deliberately chosen to test the algorithm's effectiveness at low contrast **Bottom.** A longitudinal view of the scanned model. The parameters were kept the same as in the patient protocol to facilitate comparison.

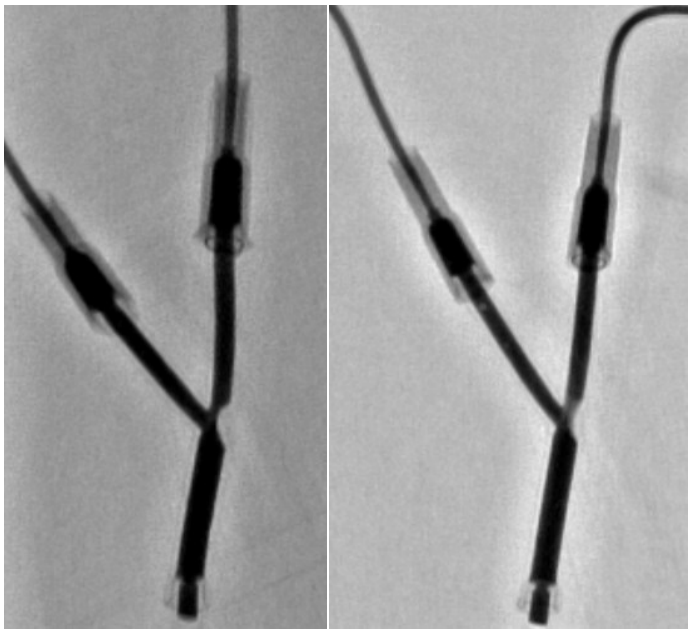

Figure 4-16 Two angiographic views of the phantom model, injected with contrast agent. The stenosis is clearly visible in both views. The two views form an angle of ~50 degrees, enough to provide an initial 3D reconstruction. Care was taken to include views that are routine in the cath lab.

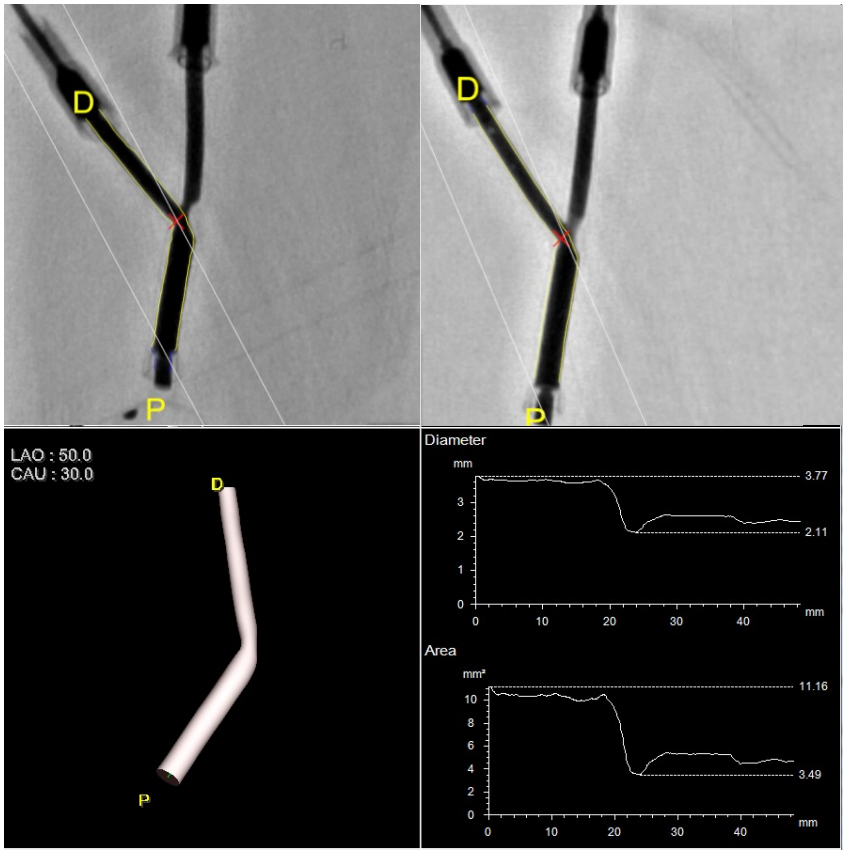

Figure 4-17 **Top row.** The two angiographic views shown in Figure 4-16 were used for the initial reconstruction. The process is the same as shown in Figure 4-2. **Bottom row.** The reconstruction result (shown left) and the diameter and area plots as calculated from that. The sudden dip in diameter and area near the halfway point indicates the presence of the stenosis.

Qualitatively, from the image of the two models (original and reconstructed) superimposed it can be clearly seen that the reconstruction is in good agreement with the original geometry. Using the new reconstruction method it was possible to capture the bifurcation angle, and also trace the contour and eccentric location of the stenosis very well, despite the reduced contrast created by the dimmer view of the stenosis (Figure 4-15).

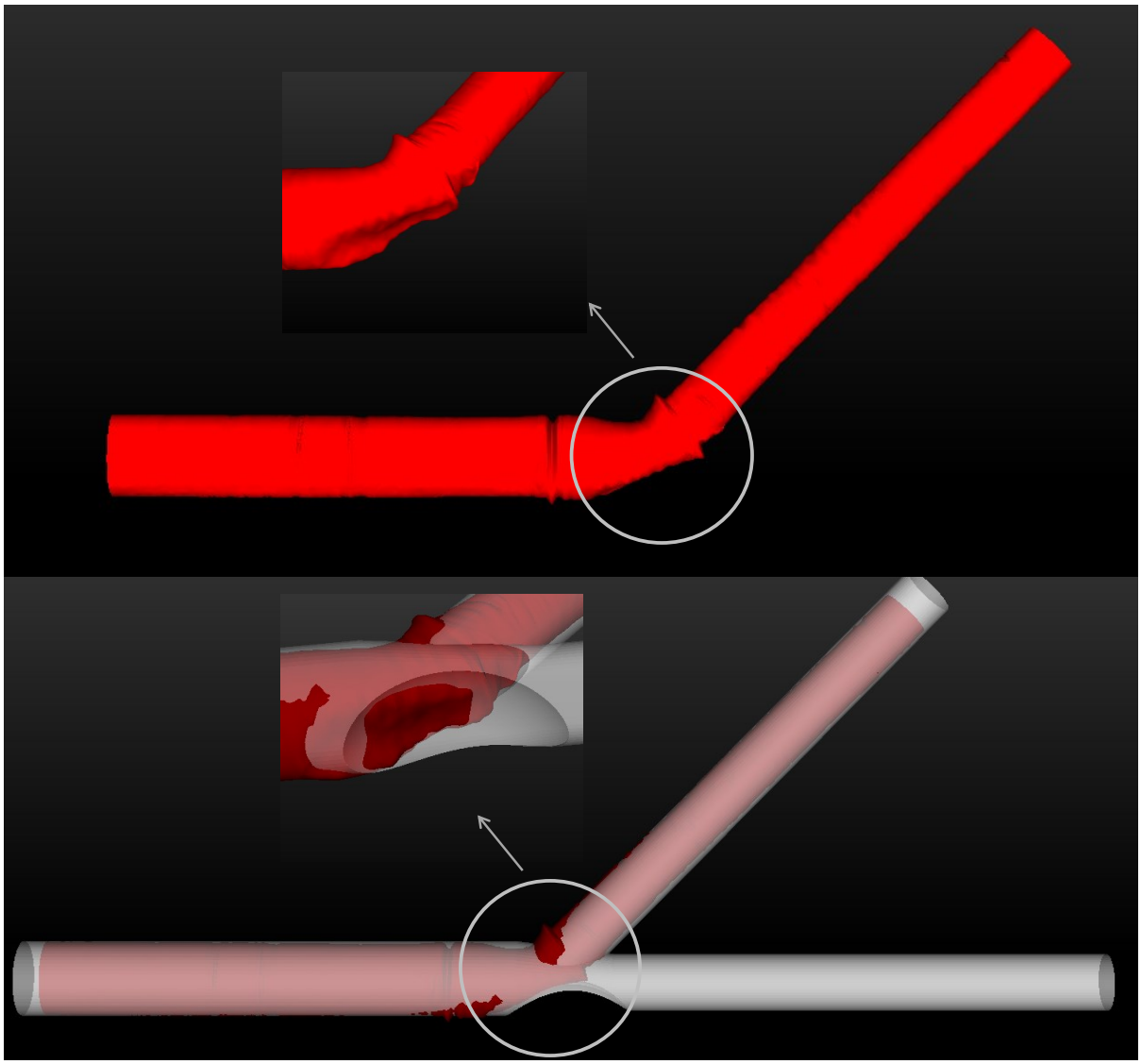

Figure 4-18 Top. The first attempt at reconstruction of the model branch.An misstep of the algorithm is visible just proximal to the stenosis. Modifying the algorithm parameters can easily fix this. The stenosis area is shown enlarged at the inset. **Bottom.** Same as the top figure, but with the original virtual model design superimposed in grey. Visual assessment indicates that the two models (original and reconstructed) are quite close, with good agreement on the bifurcation angle and the tracing of the stenosis.

Two tests were carried out to assess quantitatively the level of agreement of the reconstructed geometry to the original one. In preparation for the tests, the 3D geometries (original and reconstructed) were divided into 2D planes parallel to the x axis (which coincides with the longitudinal axis of the main vessel) 0.2 mm apart. This simplified the 3D

geometry into a set of 2D planes of constant x, enabling us to determine the error in the estimation of y and z coordinates only.

The first test consisted of calculating the error in the y and z direction of the reconstructed geometry's centreline. The mean of differences between the reconstructed and original geometries was calculated for the y and z direction, respectively, and was then normalised by the diameter of the vessel. It was found that the reconstruction was accurate within 0.60% of the vessel diameter in the y direction and within 0.36% of the vessel diameter in the z direction, indicating a very high level of accuracy.

The second test consisted of calculating the correlation between the area of the reconstructed and the original cross-sections. The reconstructed cross-sectional areas were found to be 18% less than the original cross-sectional areas. This consistent underestimation is attributed to the presence of roughness in the phantom model imaged for the reconstruction, which made the effective lumen contour smaller than the originally designed one. The extent of the presence of roughness can be seen in Figure 4-19. This is a limitation of the method that was used to test the model's accuracy. The underestimation of the cross-sectional areas is consistent with the presence of roughness in the model, suggesting that in the application of the reconstruction method on human vessels, where the interest is in detecting the true lumen, the cross-sectional areas calculated will be closer to the clinically real value.

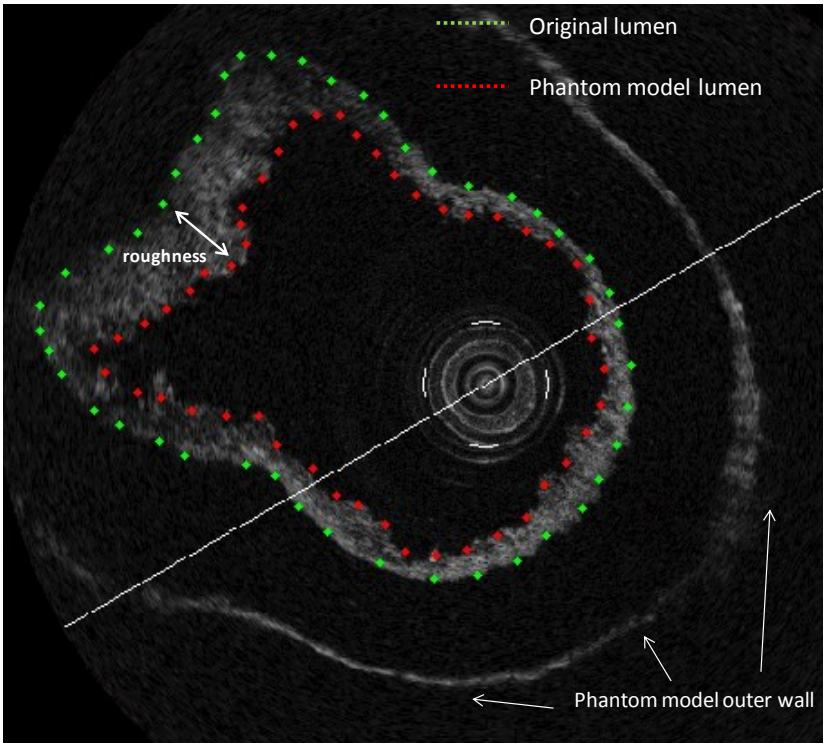

Figure 4-19 The OCT slice of Figure 4-15 showing the difference between the original model lumen (green marking) and the phantom model lumen (red marking). It is obvious that the lumen of the phantom model is smaller than the model it was based on, and this is due to limitations in the rapid prototyping method resulting in a marked level of surface roughness. The reconstruction algorithm is tuned to detect the inner lumen contour (shown in red) and so resulted in a 18% underestimation of the cross-sectional area. This issue is not expected to affect application of the reconstruction method on patients.

4.5.5 Conclusion

Testing of the method on a phantom model of known geometry provided validation for the reconstruction algorithm presented in this chapter. The reconstructed phantom geometry is in agreement with the original virtual model qualitatively. Quantitatively, the model has been shown that it can follow the vessel centreline very closely with error of less than 1% in all directions. Due to limitations in the rapid prototyping method, the phantom model lumen was smaller than the original model lumen, resulting in 18% underestimation of the cross-sectional area, an error which is attributed to the discrepancy between the phantom model and the original as shown in Figure 4-19, and not to a fault in the algorithm.

4.6 Discussion

4.6.1 Optical coherence tomography provides high resolution

Optical Coherence Tomography is an increasingly utilised imaging tool that offers considerably higher in plane resolution than IVUS (Cilingiroglu et al., 2012, Athanasiou et al., 2012, Tu et al., 2011). It allows the representation of all the geometrical features of the anatomy, including macroscopic roughness and jagged, calcified edges, which contribute to increased wall shear stress and the hemodynamic effects of stenoses, but cannot easily be imaged using other commonly used methods (Bark and Ku, 2010, Park et al., 2012, de Cesare et al., 1993). The centreline-based reconstruction method has been used successfully by (Athanasiou et al., 2012) and (Tu et al., 2011), who also provide validation for the method's accuracy.

4.6.2 Fusion of OCT with angiography overcomes coronary reconstruction challenges

The accurate reconstruction of coronary anatomy has proven a great challenge. MR imaging of coronary arteries is rarely used in clinical practice, involves sophisticated methods (Keegan et al., 2004) and long image acquisition time (Torii et al., 2009a, Cardenes et al., 2011). CT angiography is more promising, achieving a typical slice thickness of 0.75 mm (Hoffmann et al., 2006) but surface smoothing is required, which introduces errors. Quantitative analysis of coronary anatomy (2D QCA) is possible using angiography data (Girasis et al., 2011). The 2D approach based on uniplanar angiography, however, does not account for foreshortening, or for the fact that the same stenosis severity can be graded differently in different angiographic views (Seiler, 2011). This limitation has been addressed by using 3D coronary artery reconstruction based on two orthogonal angiography views. This method, supported by software such as CAAS QCA3D (Gronenschild et al., 1994) or CardioOp-B (Meerkin et al., 2010b) produces a reconstructed vessel volume consisting of circular or elliptical lumen contours, avoiding many of the pitfalls associated with 2D analysis (Schuurbiers et al., 2009, Ramcharitar et al., 2008). Other angiography techniques such as rotational angiography (RoCA), or combinations of CT and angiography have been used to produce reconstructions that are corrected for heart movement and unreliable ECG

gating (Cardenes et al., 2011, Cardenes, 2012). RoCA has been used in a proof-of-concept attempt to computationally predict pressure drop across coronary artery stenosis (Morris et al., 2012). However, in those cases, the lumen contours are still assumed to be circular or elliptic, which offers no information about the real geometry of the lumen.

The fusion of angiography and intra-vascular ultrasound (ANGUS) method (Slager et al., 2000) utilises the actual contour of the lumen from intravascular ultrasound (IVUS) pullback imaging with in plane and longitudinal resolutions of ~0.1 mm (100 μm) and ~0.5 mm respectively. IVUS scans only provide the local coordinates of the lumen contours, and therefore the contours are mapped onto an angiography-based model to obtain the final reconstructed geometry. This requires knowledge of the exact path of the IVUS wire, adding additional time to the patient scan.

This study continues in the same vein as the studies mentioned above, trying to improve our understanding of coronary disease by a) increasing the accuracy of the contour tracing by using OCT and b) calculating and comparing phasic pressure and velocity results using patient-specific data. The proposed method makes use of data collected from routine catheter laboratory procedures as input, with no additional information required and no extra time per scan. The reconstruction algorithm developed is reliable, robust, and requires minimal user input and can be applied to any clinical dataset. The resulting reconstruction inherits the high resolution of OCT, while being equally easy and practical to perform as angiography-based reconstruction.

The pairing of OCT with angiography has been attempted by other groups within the last two years, with most research conducted concurrently with, and published after, the method presented in this chapter. So far the method has proven useful in applications where increased reconstruction fidelity is required. Most studies focus on studying the effect of local haemodynamics on plaque development and rupture (Vergallo et al., 2014, Bourantas et al., 2012b) and the combination of OCT with angiography has been shown to better assess the potential for neointimal thickness development around stents (Bourantas et al., 2014). To the author's knowledge, no studies pairing the new OCT-angiography fusion with CFD to measure FFR have been conducted as of the writing of this document.

4.6.3 Method limitations

A number of limitations have been identified during the development of this reconstruction method.

The angiographic views were acquired using serial monoplane, rather than biplane imaging. This presents challenges regarding matching the timing of the frames used in the angiographic reconstruction from which the centreline was extracted. This is a limitation of the method, which could result in erroneous estimation of the vessel centreline. However, ECG was available, limiting the valid option frames to the diastolic phase of the cycle, while monoplane angiography has also been used in past OCT-angiography fusion with success (Tu et al., 2011). However, performing the reconstruction with biplane angiographic images would likely result in better reconstruction.

OCT imaging is subject to imaging artefacts. Most of these artefacts, such as motion, inefficient expulsion of blood or oversaturation are easily identifiable and a repeat scan is enough to overcome these issues. However, issues relating to elliptical distortion due to skewed catheter position may not be as easy to identify, but can potentially compromise image quality. These issues could be addressed by looking at repeat scans of the same vessel section but due to patient health concerns these were not available for all vessels. Additionally, part of the lumen contours in an OCT scan is hidden by the shadow of the catheter. An interpolation method based on the vessel curvature on either side of the shadow was used to approximate the lumen contour in that section. Therefore, lumen features covered by the shadow could not be viewed and included in the final reconstruction. The same technique was used for side branches.

The results of the OCT lumen tracing were not validated against manual contouring. This constitutes another limitation of the method. However, the high resolution and contrast of OCT imaging results in more accurate imaging and therefore less ambiguous object boundaries compared to other methods, such as IVUS, and therefore the algorithm result was considered reliable. Validation against manual contouring in future is, however, necessary to provide more confidence in the reconstruction result.

Due to the limitation of intravascular imaging techniques such as IVUS and OCT, information on the position of the lumen contours in 3D space must be obtained from another

imaging method, most commonly angiography. Different reconstruction approaches have used either the centerline (Cilingiroglu et al., 2012, Athanasiou et al., 2012, Tu et al., 2011), or the imaging catheter path (Wentzel et al., 2008) as the base for the 3D reconstruction. The use of the catheter path is clearly the more accurate option, as the image contours are obtained perpendicularly to the catheter path, which doesn't coincide with the centerline, especially in curved anatomies. Furthermore, information on the catheter path torsion can be obtained and the lumen contours' in-plane orientation determined using a rotating TNB frame (Wentzel et al., 2003b). Due to lack of torsion information, in a centerline-based reconstruction a uniform in-plane rotation is used.

However, imaging of the catheter pullback using diluted contrast agent without any imaging acquisition is required to enable catheter path-based reconstruction, adding time and effort to the imaging, meaning it is difficult to obtain this information outside of a research setting. The centerline method is less accurate, but has been shown to work when used in OCT-based reconstructions (see references in section 4.6.2 and above), providing useful results with the need for fewer resources.

Changes to the OCT catheter tip position or vessel diameter following contrast injection were not considered in this study. This could affect the accuracy of OCT and would be true of any intravascular approach that attempts to perform fusion with angiography for vessel reconstruction.

A phantom model was used to validate the reconstruction technique. The model included a bifurcation stenosis and branching geometry. However, it lacked curvature in the longitudinal direction, which limits the model's ability to validate the centreline assumption.

Errors introduced by the limitations presented in this model are expected to be low, but they can potentially contribute to sources of error when the model is used in CFD studies. The impact of the reconstruction method limitations on the CFD simulation results are further discussed in Chapters 5 and 6.

4.7 Summary and Conclusion

The aim of this chapter was to present a novel method for creating accurate 3D virtual models of coronary artery anatomy and then use the new models in fully patient-specific CFD simulations to estimate distal pressure and FFR. The use of a high-resolution, high-contrast imaging method (OCT) resulted in reconstructions which capture the real shape of the lumen. The contour-tracing algorithm developed and presented in this chapter is quick (7s per slice) and requires minimal input which mostly consists of minor adjustments to parameters due to the difference in contrast and vessel calibre among patients.

The lumen contours are originally calculated in local 2D coordinates. Their positions in 3D space are determined using angiographic views, which provide information about the vessel centreline. The lumen contours are positioned perpendicular to the centreline, in a departure from the established method of using the catheter path, saving both effort and time, and resulting in contour positioning of equivalent accuracy. The final shape of the reconstructed vessel is determined using a uniform in-plane rotation based on fiducial points in the OCT and angiographic views. The reconstruction method was validated by creating and then imaging a phantom model of known geometry, resulting in small errors (less than 1%) in centreline estimation. An 18% underestimation in luminal area is attributed to the presence of roughness in the phantom model, but not in the original geometry used to compare, and exposes a limitation of the rapid prototyping technique used to create the phantom and not of the algorithm.

The study presented in this chapter demonstrates that it is feasible to combine OCT invasive imaging with conventional coronary angiography to produce credible coronary vessel reconstructions. The process is relatively quick and semi-automated, and has been validated on a phantom model of idealised coronary anatomy. This reconstruction method was combined with patient-specific measured data of flow velocity and pressure in fully patient-specific CFD simulations. The results of the CFD study are described in the next chapter.

5. Application of the new coronary artery reconstruction method in CFD simulations

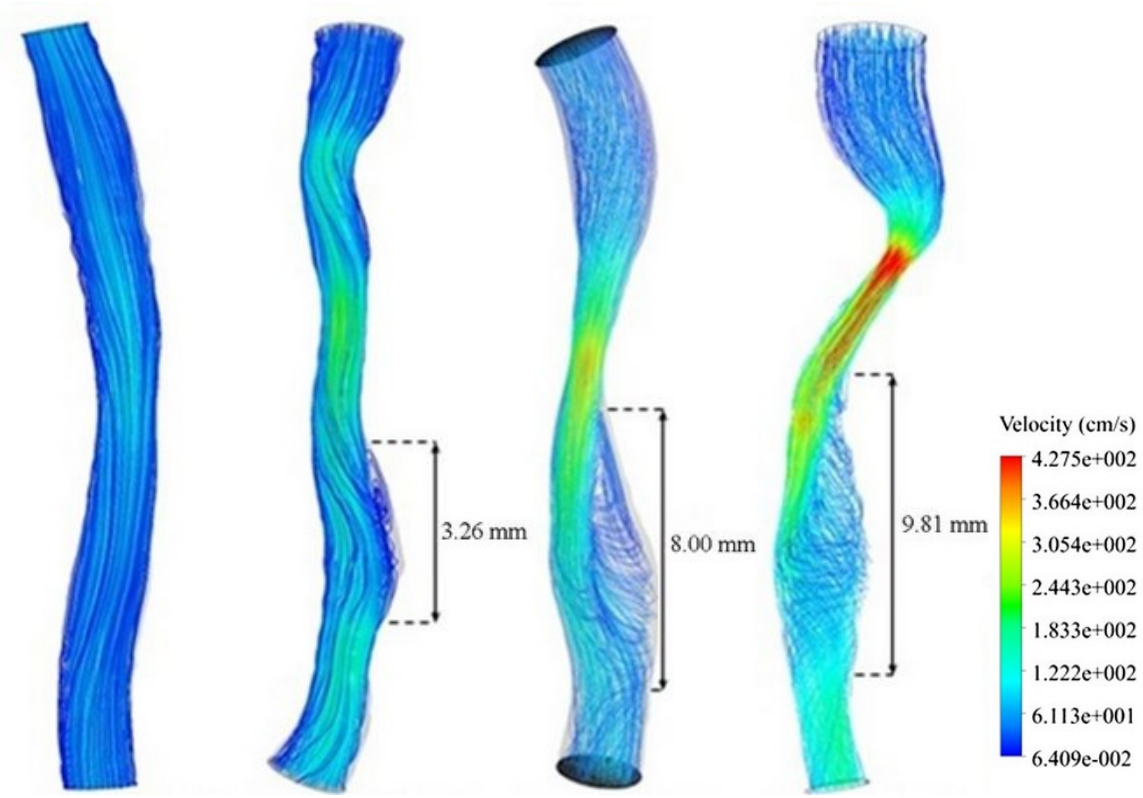

Figure 5-1 CFD flow streamlines simulated in patient-specific models of coronary arteries of increasing (left to right) anatomical obstruction. There is evident change in the flow patterns downstream of the diseased area. Image from (Javadzadegan et al., 2013)

5.1 Introduction

In the previous chapter, a new method of reconstruction of 3D coronary geometry using OCT and angiographic data was described. In this chapter, the setup of CFD simulations using the new reconstruction method combined with patient-specific, invasively measured pressure and flow velocity data is presented. The simulation results are assessed both in qualitative terms (testing that the model can realistically model transient coronary flow) and in quantitative terms (testing if the model can predict distal pressure given proximal pressure and distal flow velocity data). The chapter concludes with a list of the method's limitations leading up to further investigations presented in Chapters 6 and 7.

5.2 Invasive pressure and flow velocity measurement

Simultaneous pressure and Doppler flow velocity measurements were made in the target vessel using a Combowire XT (Volcano Corporation, San Diego USA). Intracoronary nitrates (300 mcg) were administered prior to wire insertion. The Combowire pressure measurement was equalised with the aortic pressure at the coronary ostia. Simultaneous proximal aortic pressure (Pa) and distal coronary pressure (Pd) and flow velocity data were acquired at resting and hyperaemic conditions, the latter was induced by intravenous adenosine infusion (140mcg/kg/min) into the right femoral vein using a 6F sheath.

Initial measurements were made at the ostium, prior to making further measurements proximal and distal to the coronary stenosis. Great care was taken to ensure a high density Doppler envelope was recorded to ensure accurate tracking by the digitisation systems. At the end of each recording, the pressure sensor was returned to the catheter tip to ensure there was no pressure drift. Where drift was identified the measurements were repeated. Electrocardiogram (ECG), pressures and flow velocities were archived in the device console (ComboMap®, Volcano Corporation). An example of the raw data acquisition screen is shown in Figure 5-2. The data were exported from the console into a computer, and analysed further using custom-built software Study Manager (Academic Medical Center, University of Amsterdam, The Netherlands). During the data acquisition detailed notes were taken to time the location of the wire in conjunction with the angiographic images of the wire, to facilitate

offline analysis.

The measured FFR of the lesions is skewed towards non-flow limiting (17/21 lesions are above the 0.80 cutoff). However, two thirds of the lesions studied (14/21) fall within the intermediate lesion range (0.7-0.9). Intermediate lesions can benefit most from FFR-guided clinical decisions (Doh et al., 2014) but are also the most challenging for CFD studies to replicate (Nakazato et al., 2013b). Of the 17 non-flow limiting lesions, nine had a FFR value between 0.81 and 0.85, while two lesions had a FFR of 0.80. 11 of the 17 lesions received PCI despite a negative measured FFR, due to other indications of flow limitation, such as persistent symptoms, or CFR < 2, further confirming that the majority of the lesions studied fall in the clinically relevant intermediate severity category.

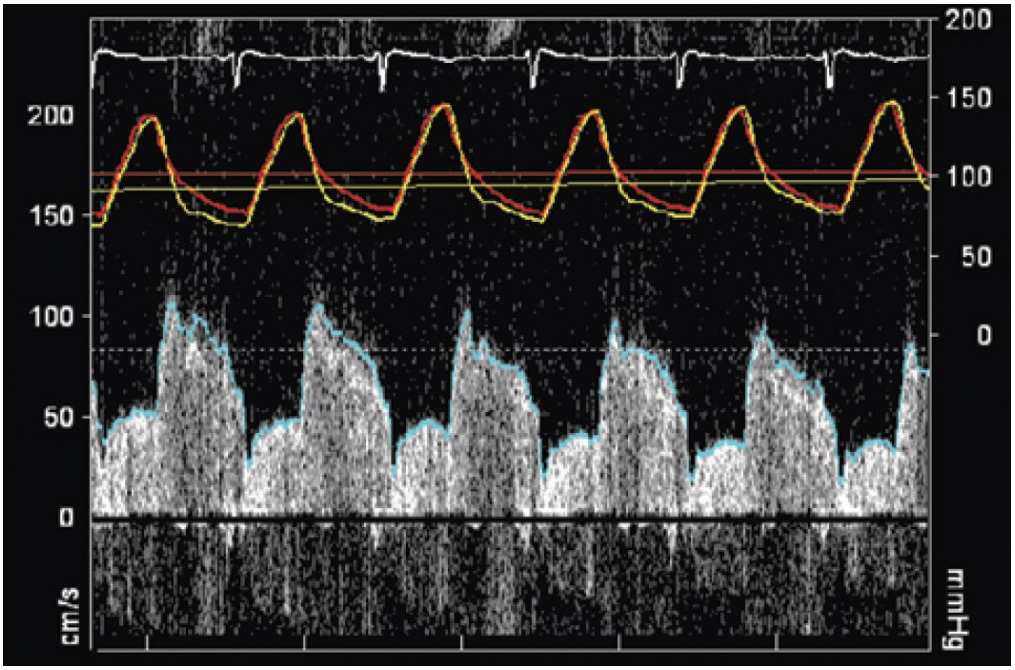

Figure 5-2 A typical screenshot of the Volcano Console during the data acquisition using Combowire XT. Proximal pressure (Pa) is measured at the coronary ostia and is shown in red. The pressure at the location of the wire, usually distal to the stenosis (Pd), is shown in yellow. The bottom section shows the Doppler velocity signal in greyscale, and the automatic tracing of the waveform produced by tracking the maximum velocity in the sample volume at each time point (shown in light blue). The measurements are ECG-gated (ECG trace at the top of the image in white).

5.3 Simulation set-up

The improved reconstructed anatomy described in the first section of this chapter was used in CFD simulations to allow more realistic representation of patient-specific data.

Simulations were carried out using 21 patient-specific cases of reconstructed coronary anatomy combined with the respective patients' pressure and flow velocity. In some cases the location of the stenosis was very proximal, and so proximal extension to the vessel was added by maintaining the same cross-sectional area as the original proximal end, to avoid numerical errors arising from the entrance effect. The patient demographics are the same as in section 4.2.

5.3.1 Volume rendering and meshing

Each of the reconstructed vessel segments represented a luminal surface surrounding the flow domain, which was discretised into an unstructured hexahedral mesh of 120-150,000 elements using ANSYS ICEM CFD 13 (ANSYS Inc., Cannonsburg, PA). The mesh resolution near the wall was locally refined, achieving a thickness of about 0.2% of the vessel diameter for the elements adjacent to the wall. The high resolution near the wall significantly improved convergence of the computation. Images of the mesh used are shown in Figure 5-3.

5.3.2 Patient-specific boundary conditions and simulation parameters

Transient pulsatile simulations were set up using Ansys CFX pre-processing software (ANSYS UK). The boundary conditions were based on the patient-specific pressure and flow velocity waveforms acquired during FFR measurement (Figure 5-4). The proximal pressure, distal pressure and distal velocity waveforms were ensemble averaged over five to seven beats using the peak R wave as a fiducial marker to improve the signal to noise ratio, whilst preserving the characteristic features, such as the anachrotic and dicrotic notch. The averaged waveforms were then decomposed into the first 15 frequency harmonics using Fourier decomposition, and the resulting components were recombined into a series of trigonometric polynomials (Figure 5-5). This process provided a representation of the waveforms in a convenient equation form that could be input directly into the simulation set-up.

The inlet boundary condition was defined as the aortic (proximal) pressure waveform. The distal velocity waveform was imposed at the outlet boundary, together with a flat spatial profile, as this provided the best agreement with normal volumetric flow rate values (Torii et al., 2010).

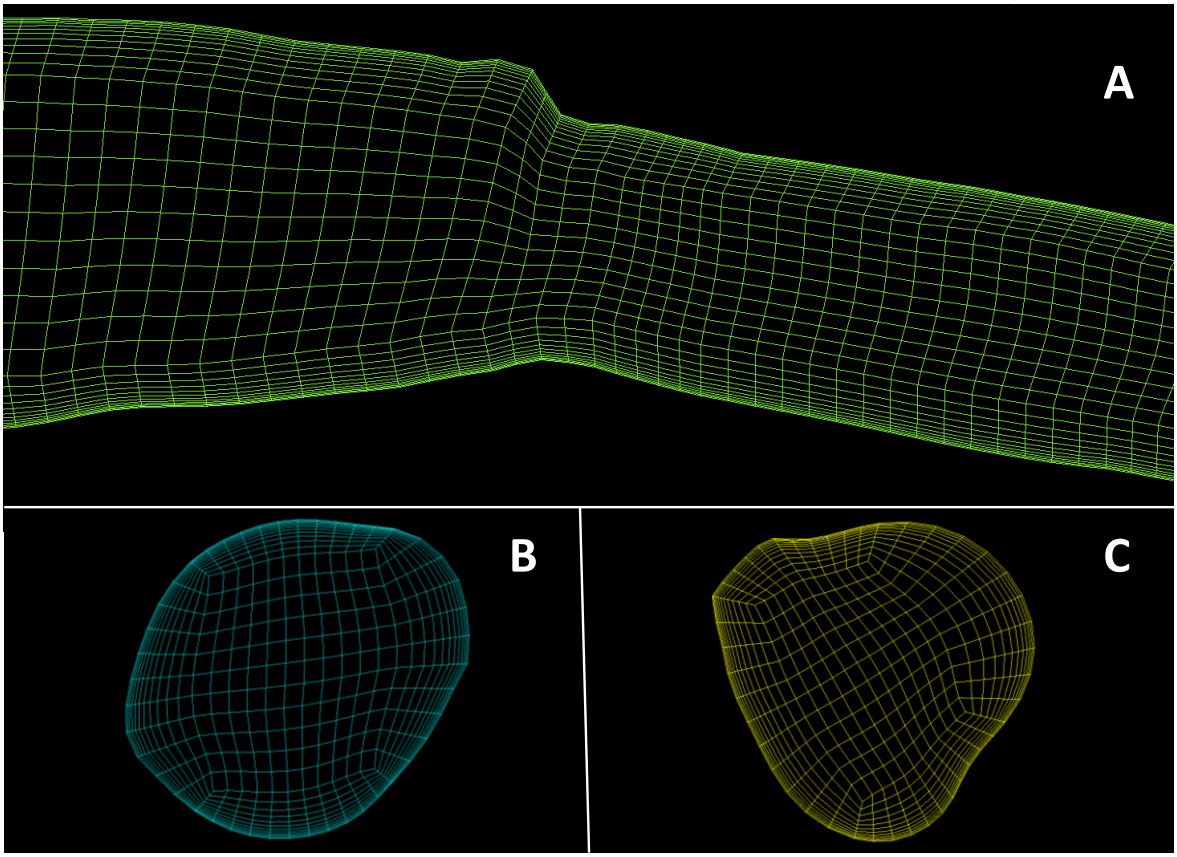

Figure 5-3 Examples of the unstructured, hexahedral mesh with added prism layers usedin the models. **A.** Mesh at the stenosis **B.** Mesh at the inlet cross-section. **C.** Mesh at the outlet cross-section.

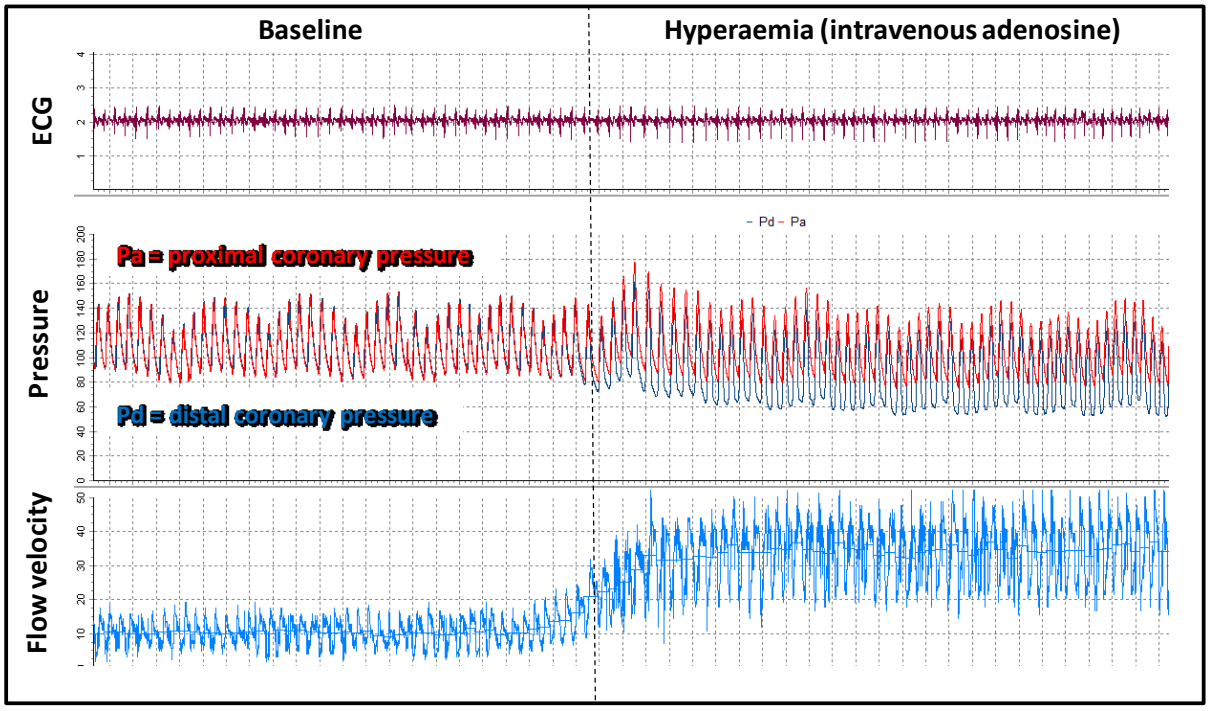

Figure 5-4 Patient pressure and flow velocity measurements just before and after administering the vasodilator adenosine to increase flow. At baseline, when flow is normal, there is little difference in the proximal and distal pressure waveforms. After flow increases the deviation of the Pa and Pd waveforms indicating disease is more pronounced. The data for the CFD simulations were taken by ensemble averaging 5-8 beats from the hyperaemia measurement section.

This combination of pressure and velocity boundary conditions means that peripheral (microvascular) resistance to the flow is implicitly incorporated. The coronary circulation is unique since blood flow is predominantly diastolic rather than systolic. During systolic myocardial contraction, the microvasculature is compressed meaning that microvascular resistance rises significantly. In contrast, during diastole and active myocardial relaxation, the microvascular resistance falls leading to an acceleration of flow. Resistance is not constant during the cardiac cycle but varies dramatically and only phasic analysis allows determination of instantaneous resistance at any given point in the cycle. The fluid dynamics inside the coronaries are greatly affected by this variation (Vignon-Clementel et al., 2010, Sen et al., 2012) and using zero-pressure or other unrealistic boundary conditions results in physiologically unrealistic pressure and wall shear stress values.

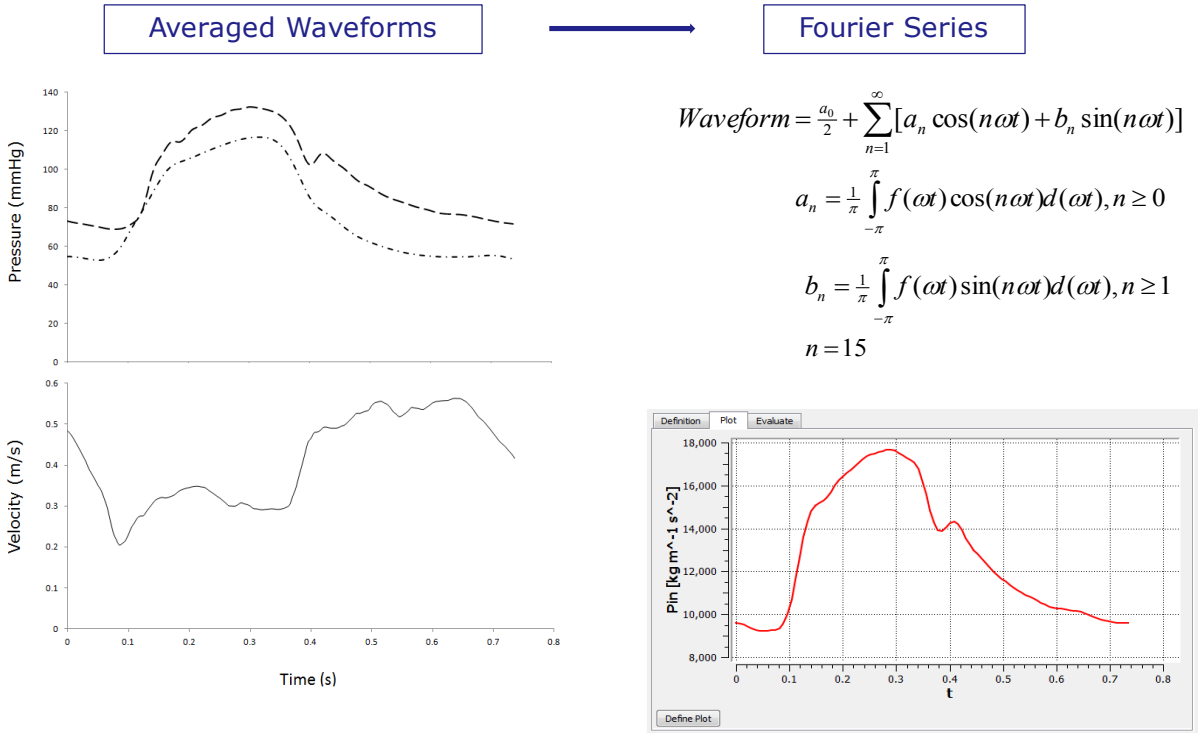

Figure 5-5 The ensemble averaged waveforms for proximal pressure (Pa, top), distal pressure (Pd, just below Pa) and flow velocity (bottom).

The vessel wall was assumed to be rigid and immobile, while blood was modeled as Newtonian (mid-range viscosity of 0.00334 Pa.s) and incompressible (density 1060kg/m^3). Motion of the coronary arteries was neglected for reasons of simplicity, as calculations are not likely to be affected significantly by the domain vessel motion (Torii et al., 2010). Rigid wall has also been shown to be a reasonable assumption for CFD simulations of blood flow in

large arteries; though arteries are compliant and can be modeled so, it has been shown that the increased numerical accuracy provided by fluid-structure interaction (FSI) models is not significant enough to justify the increased computational costs of FSI (Tan et al., 2009b, Torii et al., 2009c). Also, coronary arteries are less compliant than larger arteries, further justifying the rigid wall assumption.

The maximum Reynolds number observed was low (<400), meaning that flow is laminar throughout the cycle, with observed disturbances caused by the presence of geometry irregularities. The system of the continuity and Navier-Stokes equations was solved iteratively for each element of the mesh in ANSYS CFX Solver 13. A root-mean-square error of less than 10^{-6} was specified as the convergence target, and a maximum of 25 iterations per time step was set in order to reach the desired convergence. The time step was chosen at 0.001s, based on previously conducted time-independence tests by (Tan et al., 2008).

5.3.3 Statistical testing

Transient results

The calculated distal pressure waveforms were compared against the measured data. Two statistical tests were performed. First, for each case, the shape of the calculated waveform was compared to that of the measured waveform using Pearson's correlation with the aid of open-source statistical computing software R (http://www.r-project.org/). A correlation coefficient was produced for each patient and also a mean correlation throughout the cohort. This test was considered necessary in order to evaluate the ability of the method to accurately model the time-varying microvascular resistance. Even though patient-specific data of pressure and velocity were applied as boundary conditions, the rigid wall assumption (which means impedance is not modelled) could still have a marked effect on the shape of the resulting waveform.

The second statistical test was to calculate the mean of differences between the calculated and measured pressure waveforms. This was done for all time points throughout the cohort, in order to evaluate the overall ability of the model to quantitatively assess the distal pressure on a given anatomy.

Time-averaged results

The ratio of mean distal to proximal pressure (Pd/Pa) measured under conditions of hyperaemia, otherwise known as FFR is, as discussed in Chapter 2, clinically important as it could improve diagnosis. For this reason the FFR derived from the CFD results was compared to the FFR resulting from the ensemble averaged waveforms of the clinically measured pressure data. A correlation plot and a Bland-Altman (Altman and Bland, 1983) plot were created to assess the model's ability to predict FFR. The results are presented in the section below.

5.4 Results

5.4.1 Flow and pressure patterns

An example of the flow patterns observed in a coronary stenosis can be seen in Figure 5-6, while the corresponding pressure profiles are shown in Figure 5-7. The flow accelerates upon entering the stenosis, then separates from the boundary and forms a high velocity jet which becomes reattached to the vessel wall distally. Due to the presence of curvature and the tortuous nature of the coronary vessels, flow patterns are not symmetrical, but the jet coming out of the stenosis tends to reattach on the outer side of the bend, leaving a long area of recirculation on the inside of the bend.

The increased flow through the stenosis predictably results in a sudden drop in pressure due to the Bernoulli effect. However, as in the case of aortic stenosis described in Chapter 3, viscous losses due to the increased flow combined with the extensive recirculation lead to irreversible pressure losses. Consequently, even though flow velocity distal to the stenosis is on a similar level to the velocity proximally, only a small fraction of pressure is recovered, and a distinct pressure drop is observed in the part of the vessel which is distal to the stenosis. The Reynolds number remains well below 400 at all times for all cases considered, which means that the assumption of laminar flow is justified.

5.4.2 Comparison of calculated and measured distal pressure waveforms

The distal pressure waveform calculated by the CFD simulation was compared to the measured distal pressure waveform and the cross-correlation coefficient test was used as a

measure of similarity between the two. The results are displayed in Figure 5-8. The mean cross-correlation coefficient for the total of 21 cases was 0.898±0.005 ($p<0.01$), whilst the mean of the differences between measured and simulated results was -3.45 mmHg (4.4% of the mean measured pressure), with a mean standard deviation of differences of 8.17 mmHg, as seen in the Bland-Altman plot of Figure 5-9.

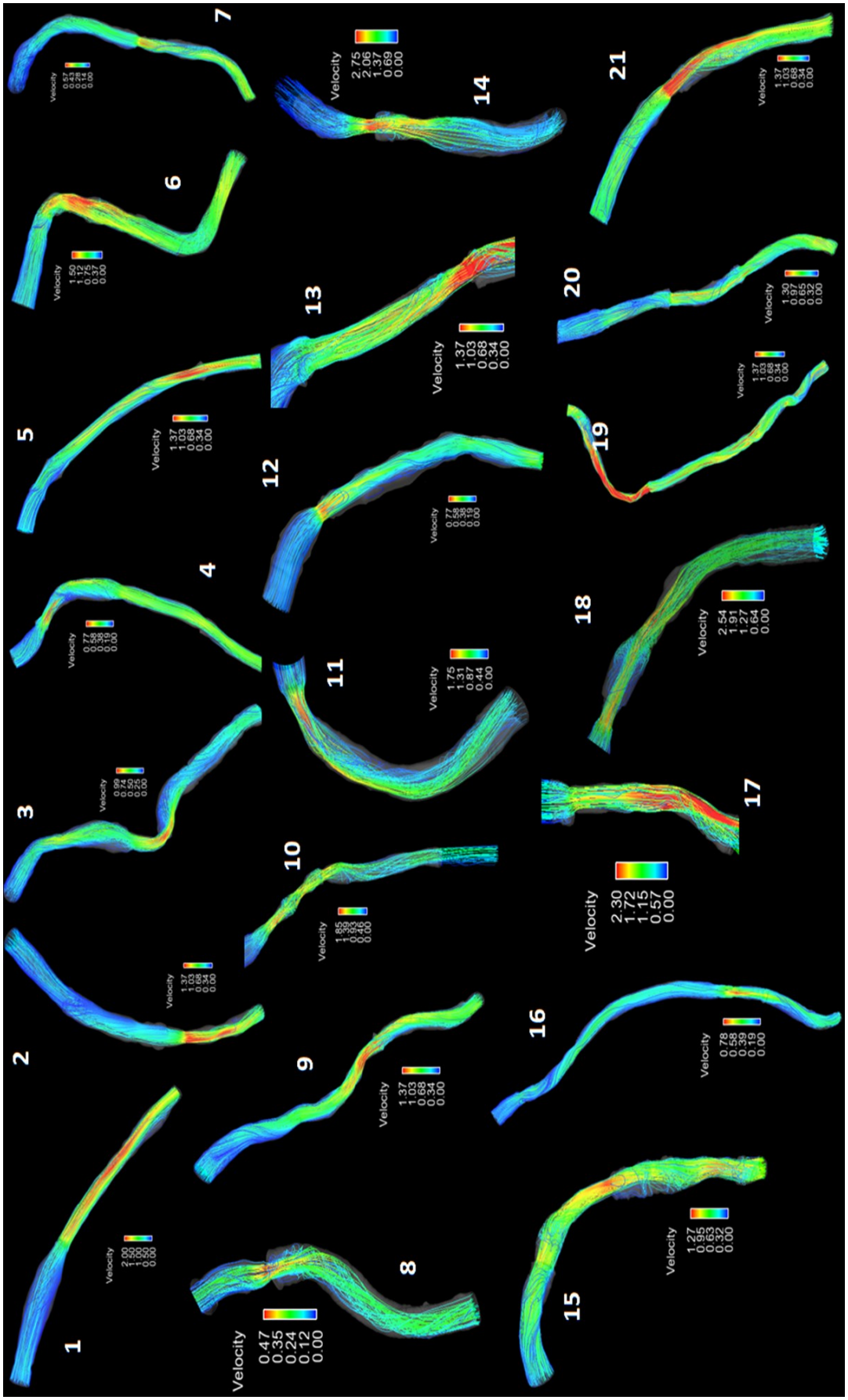

Figure 5-6 Velocity streamlines in the 21 lesion anatomies studied.

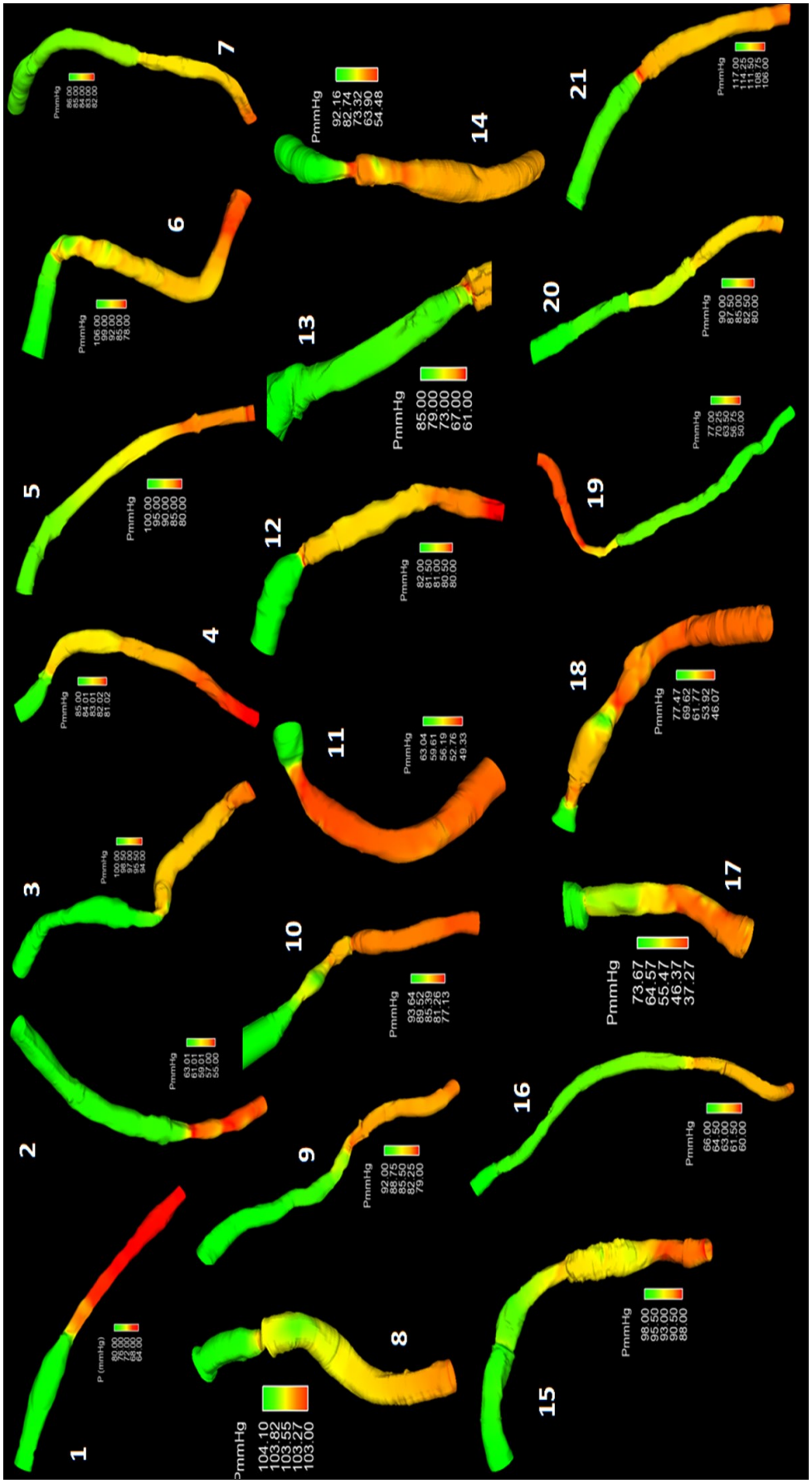

Figure 5-7 Pressure profiles in the 21 lesion anatomies studied. The red colour indicates low pressure.

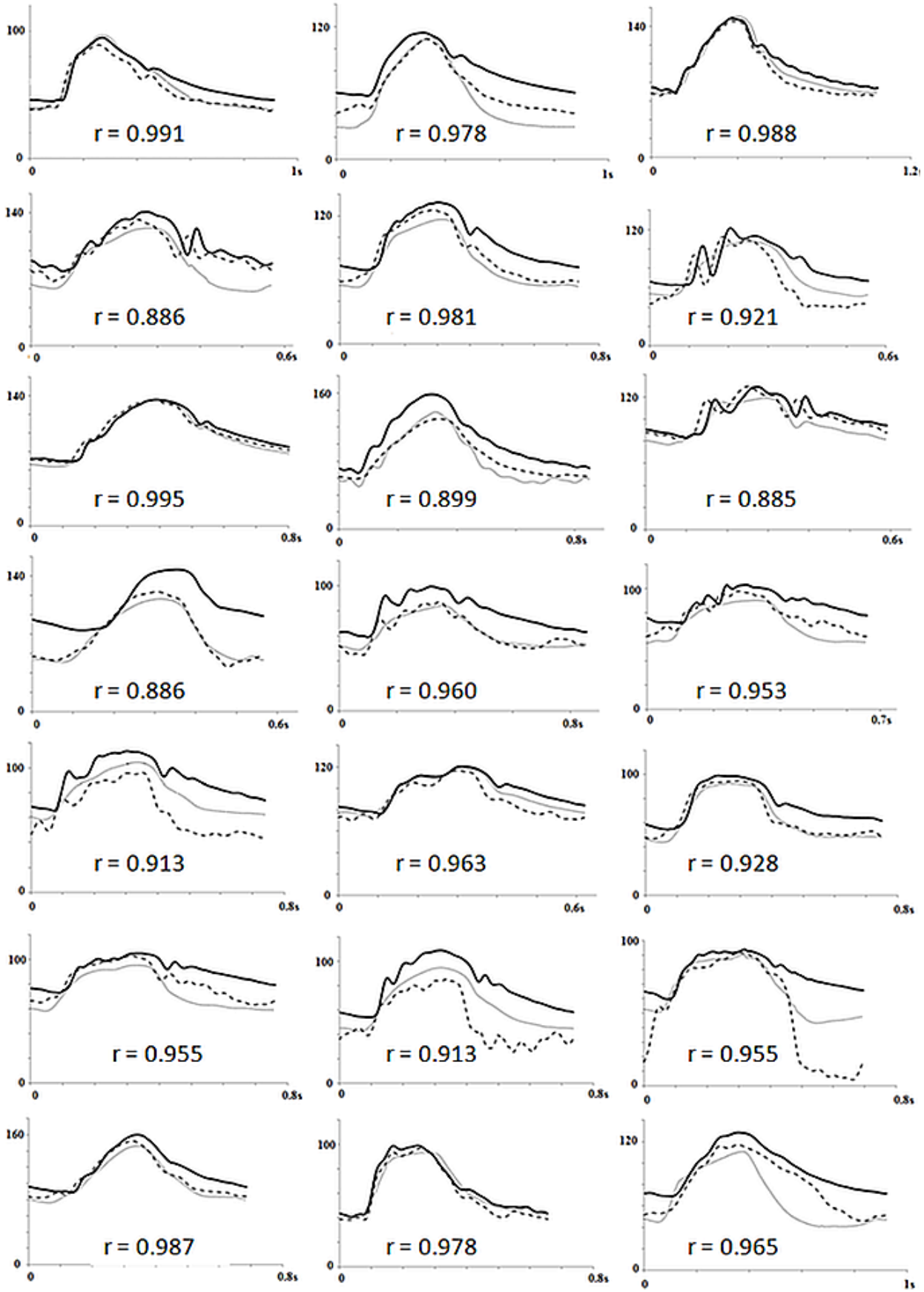

Figure 5-8 Comparison of the measured (grey line) and calculated (dashed line) distal pressure waveforms for all lesions (the proximal pressure is shown in black). The model-predicted distal pressure correlates well with the measured pressure waveform, as indicated by the correlation coefficient being very high for all cases.

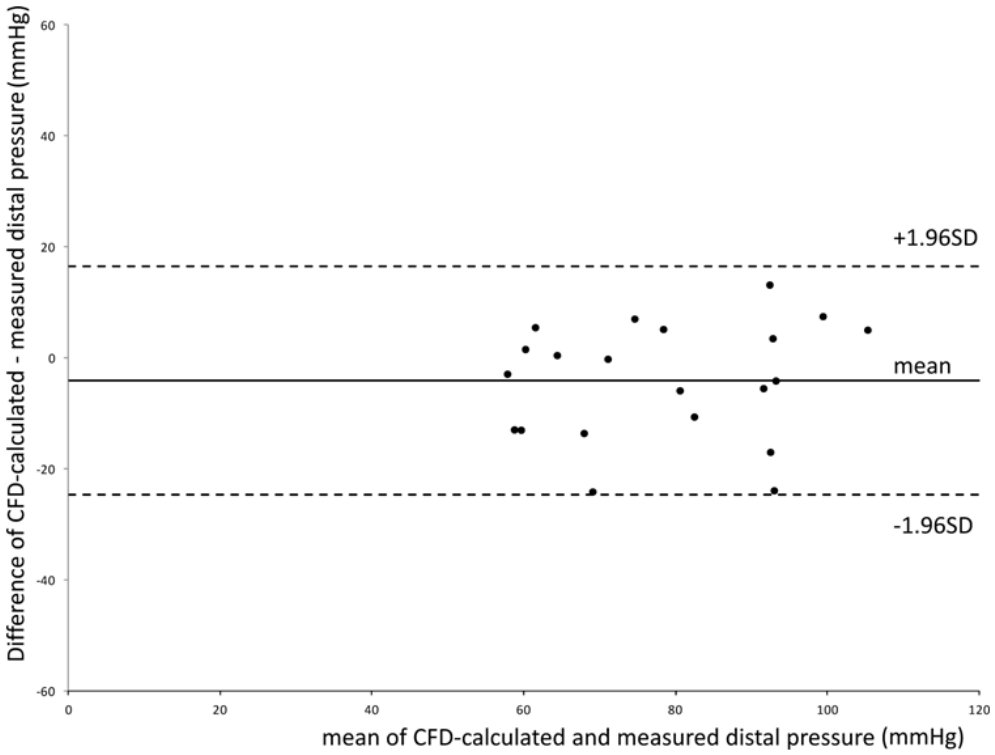

Figure 5-9 Bland-Altman plot of the differences between the mean distal pressure calculated by the CFD model and the measured values. A bias of less than 4 mmHg was found, and the limits of agreement were found to be between -24.6 and 16.4 mmHg.

5.4.3 Comparison of calculated vs. measured FFR

The FFR values calculated by the CFD model were compared to the values of FFR measured by averaging the ensemble-averaged measured aortic and distal pressure waveforms over a cardiac cycle. The correlation plot is shown in Figure 5-10. The correlation coefficient was 0.58, which indicates a positive correlation, but is not as strong as one would expect from fully patient-specific CFD simulations. This result, however, bears resemblance to the result reported in (Morris et al., 2013) where the authors attempted to calculate FFR using steady-state CFD on reconstructions based on rotational angiography.

A Bland-Altman plot of the same data was created and is shown in Figure 5-11. There is no bias in the mean of the two sets of data (calculated and measured), and the standard deviation is 0.08, which is less than 10% of the FFR value range (from 0-1). The limits of agreement are placed at ±1.96 standard deviations. This indicates that nearly all the calculated data points are within ±0.165 of the corresponding measured data points. Given

that the cut-off point for FFR is 0.80, the differences within the limits of agreement could be significant for each individual patient.

The binary cut-off of FFR means that the CFD results can also be evaluated in terms of whether the FFR prediction (significant or non-significant) is in agreement with the measured values. In Figure 5-12 it is shown that in 16 out of 21 vessels the CFD-based FFR prediction would agree with the measured assessment of lesion significance. Of the five lesions where the CFD-based and measured FFR were in disagreement, the FFR significance was overestimated by CFD in three cases and underestimated in two. These results represent a 77% success rate for CFD-based FFR prediction in this cohort.

The combined information from the correlation and Bland-Altman plots suggests that uncertainty over the accuracy of the calculated FFR remains after using patient-specific anatomical, pressure and velocity data. These results are further discussed in the next section.

5.5 Discussion

5.5.1 Patient-specific phasic flow analysis

Patient-specific coronary artery CFD studies are scarce compared to other large vessels, such as the aorta, since high-quality anatomical and velocity data is difficult to acquire. Previous studies have been limited to models based on post-mortem vessel casts with steady flow as boundary conditions (Goubergrits et al., 2009), or generic combinations of idealised or patient geometry and velocity waveforms (LaDisa et al., 2006, Yin et al., 2009, Yakhot et al., 2005). To date there is only a limited number of fully patient-specific simulations of coronary flow in the literature; one involves very long image acquisition time not suitable for clinical applications, whilst another uses aortic pressure and flow data to implicitly calculate flow in the coronary tree by simulating a larger part of the cardiac anatomy (Torii et al., 2010, Hajati et al., 2012).

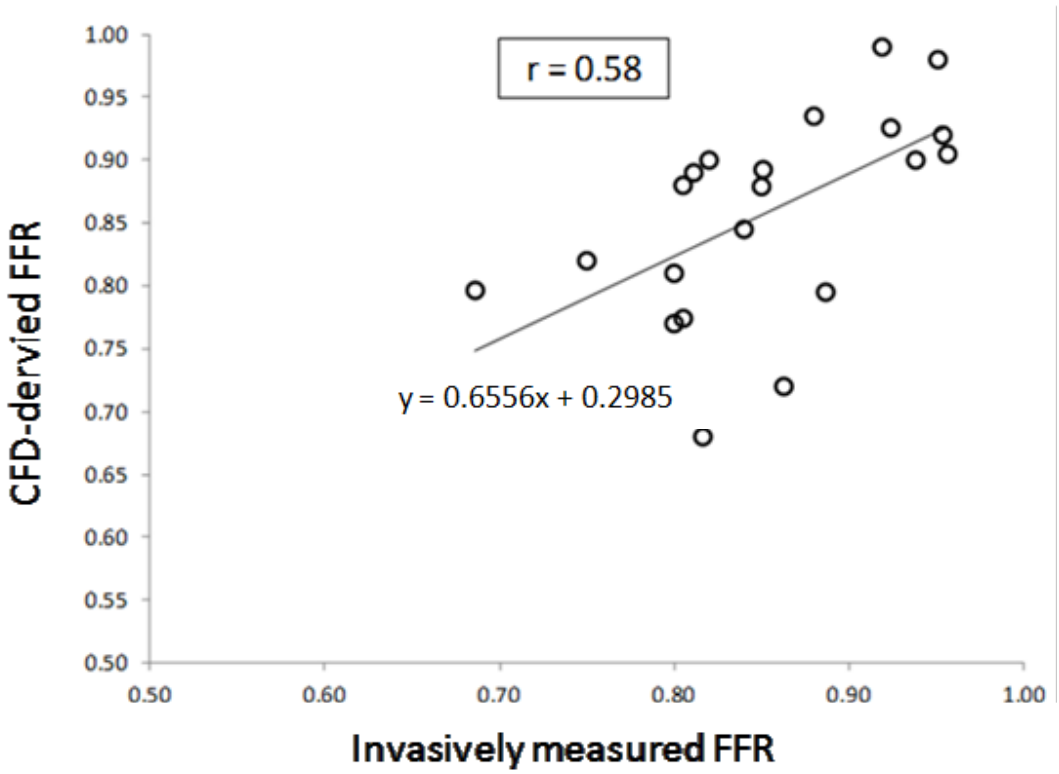

Figure 5-10 Predicted (calculated by CFD) FFR vs. measured FFR for the 21 lesions studied. The correlation coefficient between the two sets of data is 0.58, suggesting a positive correlation, but not as strong as could be expected.

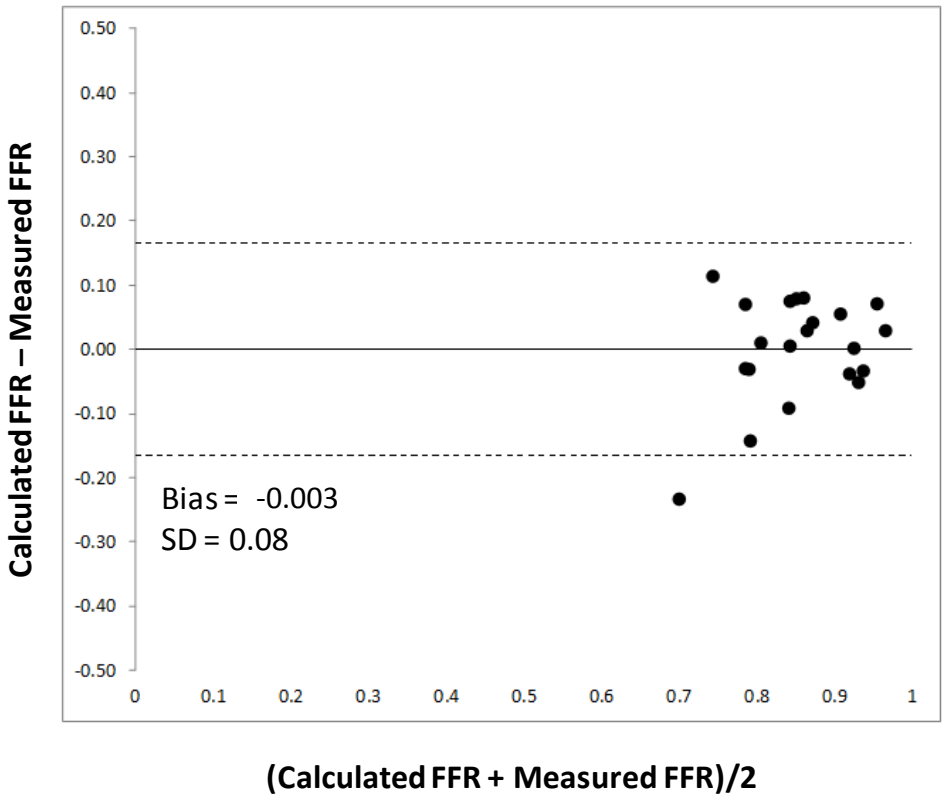

Figure 5-11 Bland-Altman plot of the calculated and measured FFR values for the 21 lesions studied. No bias was detected between the two sets of data, and the standard deviation was small at 0.08.

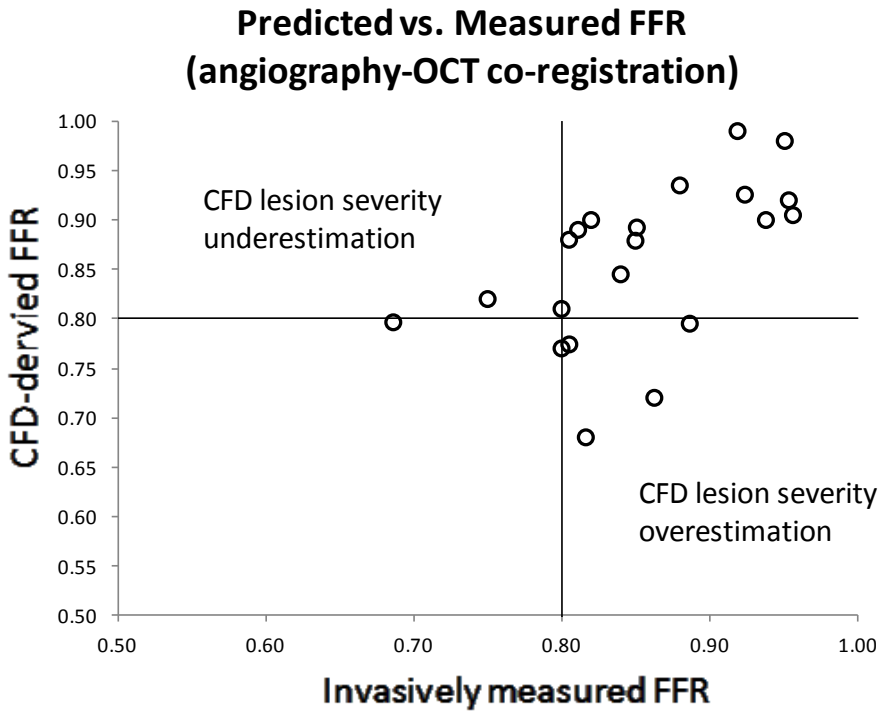

Figure 5-12 Predicted (calculated by CFD) FFR vs. measured FFR for the 21 lesions studied. The vertical and horizontal lines represent the FFR cut-off point of 0.80 for the measured and predicted data respectively. Points lying in the bottom left and top right quarters represent successful prediction of lesion significance from the CFD. A total of five points lie in the top left and bottom right quarters, indicating unsuccessful prediction of lesion significance.

Furthermore, the majority of the literature focuses upon mean pressure and velocity values. However, mean flow is not representative of true phasic flow due to nature of the coronary circulation. Extrinsic compression by the myocardium in systole means that flow velocity is much less during systole, while active relaxation and decompression of the microcirculation lead to greatly accelerated flow in diastole. Therefore, our approach was to model patient-specific conditions for the entire cardiac cycle, calculating phasic pressure waveforms and comparing with measured data.

5.5.2 Limitations of the proposed model

Where algorithmic predictions differ from the measured values, there are several sources of potential errors. These include limitations of the reconstruction algorithm and the measured haemodynamic parameters. These are discussed separately below.

Limitations based on the reconstruction method

As discussed in the limitations section of Chapter 4 (Section 4.6.3), the reconstruction method used to produce the 3D models used in the CFD simulations presented in this chapter is subject to limitations, including the use of monoplane angiography, and the use of the centreline instead of the OCT catheter path, either due to data not being available in a clinical setting, or in order to simplify the data collection and reconstruction process. Though results presented in other publications (Tu et al., 2011, Bourantas et al., 2012a) appear to validate the assumptions made in this study, it is possible that errors introduced by the reconstruction process propagate to the CFD simulations and result in errors and inaccuracies.

Currently, the existing centreline-based reconstructions making use of OCT-angiography or IVUS-angiography fusion have not yet been used to estimate FFR from CFD simulations, so no direct comparison with the results of the current study can be made to compare and identify which reconstruction errors are critical to the CFD result. The centreline-based reconstruction method has, however, been used in CFD studies focusing more on the flow patterns near the wall and the related wall shear stress with reliable results (Bourantas et al., 2014, Bourantas et al., 2012a, Vergallo et al., 2014).

This study's limitations are further explored in Chapter 6, in the context of the results and limitations of similar studies.

Limitations based on data collection and processing

Results obtained from mathematical models based on patient-specific data can be compared directly with *in-vivo* measurements. Whilst this provides an opportunity to test the reliability of the models, it should be recognised that human *in-vivo* measurements using state-of-the-art technology are themselves limited with well-recognised measurement variability (Mynard and Steinman, 2013).

Invasive intracoronary measurements involve simultaneous pressure and Doppler wire assessment. This wire requires training in its use and does not yet behave like a typical angioplasty wire. Therefore for technical reasons it may not be possible to acquire flow velocity data in all vessels and across all lesions. Other researchers have estimated coronary flow by using thermodilution techniques (De Bruyne et al., 2001, Pijls et al., 2002). However, these approaches do not generate a flow waveform which can be co-registered with the electrocardiogram and pressure waveforms. Furthermore, thermodilution techniques can be affected by the volume of the injectant, the length of the vessel and the number of side-branches.

Volumetric flow rate can only be estimated *in vivo* in humans. Open-chested animal models have previously allowed estimation of volumetric flow rate based upon isolated arteries with measuring tools inserted into the vessel with careful measurement of vessel diameter (Gould and Kelley, 1982). This technique is not possible in humans. We chose to estimate volumetric flow rate using measured flow velocity with the assumption of an idealised spatial flow profile and combined this with highly accurate cross-sectional areas measured with OCT. All methods to measure vessel diameter are inherently limited as coronary vessels can show marked changes in size dependent upon endothelial function, the flow volume and the intracoronary pressure generated by flow (Muller et al., 2012). As such, our estimation is not biased to over or under estimation and follows the current state-of –the art in this field.

However, even though our results are not biased when it comes to comparing the mean of differences across the entire 21-lesion cohort (as indicated by the Bland-Altman plot, Figure 5-11), it does lead to a high standard deviation of ~8 mmHg in predicted pressure, which suggests that the difference between the CFD-calculated and the measured pressure difference at a given time-point for a single patient could be over- or under-estimated by as much as 16 mmHg (2 standard deviations). This indicates a level of uncertainty in the CFD calculations that prevent the use of this method as an accurate predictor of pressure drop in the coronary arteries.

A further limitation is that we can only model resistance based upon flow velocity and measured pressure. The true impedance relies upon modeling vessel wall elasticity which

remains a limitation of all CFD approaches to date.

Other practical limitations of the method employed in this study include the approach to imaging the vessel. Simultaneous bi-plane angiographic imaging was not available in all cases, operated multi-view angiography using isocentred imaging equipment was used instead. Theoretically the availability of bi-plane imaging will lead to improved three-dimensional angiographic reconstructions and more accurate modeling, though monoplane angiography has been used in OCT-angiography fusion with success (Tu et al., 2011). Our model also performed well without bi-plane imaging and is expected to produce better results when it becomes available in the future. Whilst bi-plane imaging is increasingly common, it is expensive, not in routine use for all patients; the use of single plane imaging means it is readily applicable to the majority of patients.

OCT contour segmentation and reconstruction are limited by the shadow cast by the intracoronary wire along which the OCT catheter runs. This limitation is inherent to OCT technology and is overcome by the use of specialized interpolation functions in the active contour algorithm. However, the validation work on the reconstruction method presented in section 4.5 suggests that there are few errors in the reconstruction which would not be expected to significantly affect the CFD results.

A key limitation associated with all CFD studies is that this approach is not fully automated and cannot currently produce an output within the time frame of performing a live intra-coronary procedure. The CFD simulation requires an average of 48 hours of computer processing using a conventional desktop workstation and a parallel 4-core run. Increase in computer processing power and optimisation of the algorithms will improve this in the future.

The effects of individual sources of error in the CFD FFR calculations are investigated in Chapter 6.

5.5.3 Potential Applications for future

By modeling the haemodynamics of specific coronary lesions it is possible to assess and predict the impact of shear stress, and physiological pressure gradients imposed by a

given lesion. Treatment using such pressure based techniques (such as FFR) have been shown to improve clinical outcomes. Using a combination of imaging modalities combined with derived pressures and velocities, it may be benefit both current clinical practice, in addition to on-going work attempting to further understand the relations between shear stress and likelihood of stenosis rupture or occlusion. By accurately modeling phasic pressure changes in the distal vessel, this model may allow greater understanding of how a coronary stenosis impacts coronary physiology throughout the cardiac cycle, rather than an averaged across the cycle.

5.6 Summary and Conclusion

In this chapter, geometries reconstructed from OCT and angiographic data as described in the previous chapter were combined with invasively measured proximal pressure and distal flow velocity data in pulsatile CFD simulations, in an attempt to compare the CFD-calculated distal pressure waveform to the clinically measured pressure. The results for a 21-patient cohort indicated a very small mean of differences (4.4%), but with a higher than expected standard deviation of ~8mmHg. This result indicates that uncertainty over the CFD-calculated pressure drop for an individual patient remains significant even when using state-of-the-art imaging, pressure and flow velocity data, which is reflected in the positive, but not as high as expected correlation between the calculated and measured FFR (r=0.58).

The potential sources of error in the CFD simulations and their effect on the CFD results are further investigated in Chapters 6 and 7.

6. Further investigation of the differences between CFD-derived and measured physiological parameters under hyperaemia

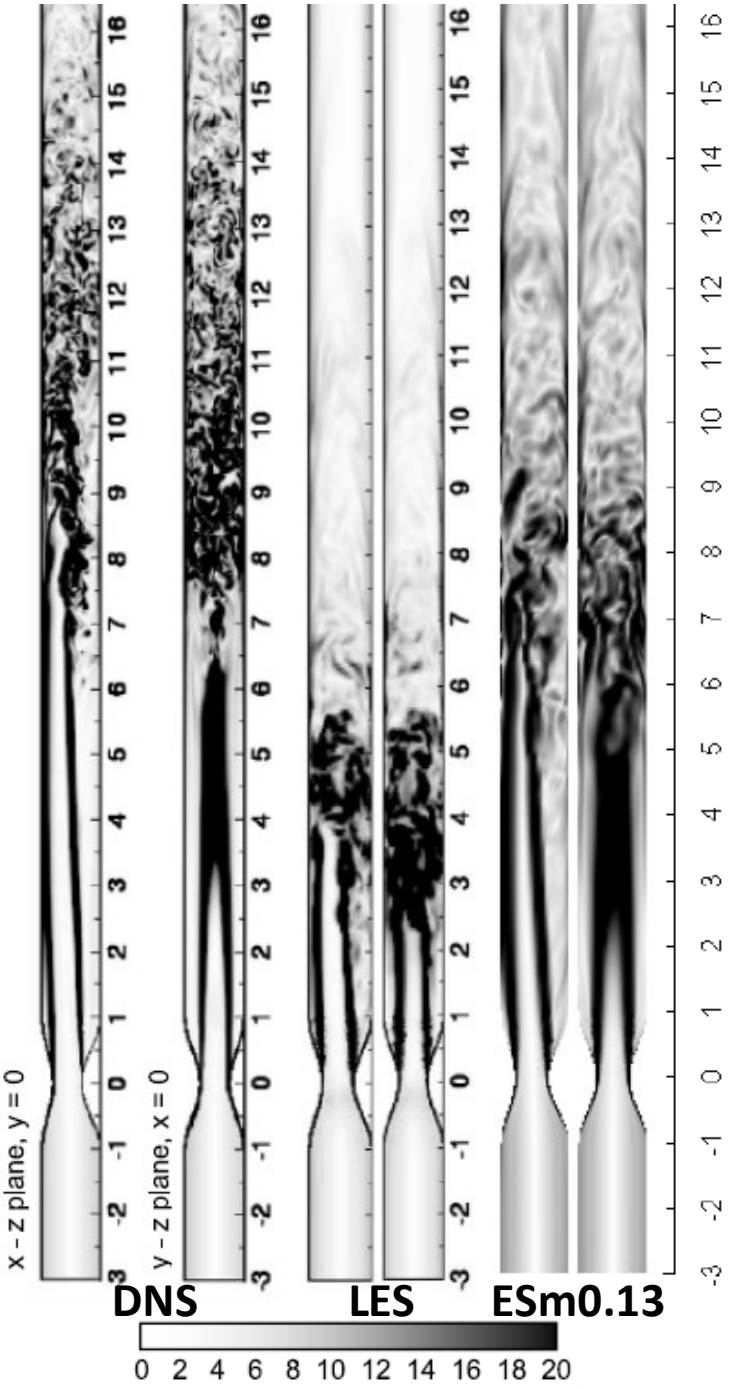

Figure 6-1 Instantaneous vorticity plots in an idealised model of carotid stenosis, using three different CFD models (adapted from (Tan et al., 2011)).The variation in the results suggests that, as impressive as the capabilities of CFD are, validation against a gold standard is always necessary before the results can be considered reliable.

6.1 Introduction

CFD is currently being presented as a non-invasive alternative to estimating FFR in patients with coronary artery disease. In the previous chapter it was shown that, despite being capable of predicting FFR in a 21-vessel cohort, fully patient-specific phasic CFD simulations cannot reliably predict the FFR of all individual vessels within the cohort. The limitations posed to the CFD models were discussed and the conclusion was reached that further investigation is required in order to identify which of the limitations presented can significantly affect the CFD result.

The parameters which are expected to have the biggest influence on the CFD estimations of FFR include misrepresentation of the patient anatomy in the 3D model and errors in the estimation of boundary conditions compared to the actual flow conditions in the vessel. Tests were devised to assess the sensitivity of the CFD result to variations in anatomy and volumetric flow rate, while the effect of the proximal pressure variability on the FFR ratio was also investigated as a potential cause of discrepancy. Three different types of patient-derived anatomy (angiography-based reconstruction, OCT-only reconstruction and the novel OCT-angiography co-registration method described in the previous chapter) were combined with patient-specific flow rates in phasic CFD simulations and the resulting FFR results were compared to the measured values. The effect of volumetric flow rate is investigated in a sensitivity analysis of the effect of flow rate on FFR within the normal hyperaemic range in three stenoses of varying severity.

Other limitations, such as omission of branches or errors associated with velocity measurement, and the effect they may have on the potential of CFD to accurately predict FFR are also discussed at the end of the chapter.

6.2 Effect of anatomy on CFD-based FFR predictions

6.2.1 Model description

The data from the cohort of 21 vessels (19 patients) presented in Chapter 4 were used for this study (patient demographics shown in Table 4-1). For each vessel an angiogram, an OCT scan, and invasive pressure and flow velocity data were available. The pressure and flow were measured for resting and hyperaemic flow. A detailed description of the methods used to acquire these data is shown in chapter 4 sections 4.3 and 4.8.

The angiographic imaging DICOM files were imported into CAAS QCA3D software (Pie Medical Imaging BV, Maastricht, The Netherlands) and the centreline of the vessel was traced manually in two views with a known angle between them. An anatomical feature evident on both views was used as a fiducial point to aid the reconstruction (Figure 4-3 contains a detailed description of the process). The final vessel reconstruction consists of elliptical cross-sections. The short and long axes of the ellipse are determined by the 2D measurements on each of the two views, and so the estimation of cross-sectional area has been shown to be reliable (Schuurbiers et al., 2009, Goubergrits et al., 2009). However, the fixed geometrical shape of the cross sections results in a smooth appearance of the vessel 3D reconstruction, and though the vessel's curvature and tortuosity are captured, it is not a true representation of the lumen shape.

The OCT data were analysed using a custom software package designed in a Matlab environment (MathworksInc, Natick, Mass). The reconstruction process consisted of an algorithm which traces the lumen contours based on the contrast between the wall (light) and lumen (dark) areas of the images. OCT, as all intravascular methods, only provides local, 2D coordinate information, and so, apart from the longitudinal distance (slice thickness), there is no information on the relative position of the resulting lumen contours in 3D space. The 3D reconstruction consists of a tube with the OCT catheter path coinciding with the Z axis and the lumen shaped based on the true lumen contours extracted from OCT, placed on X-Y planes 0.2 mm (slice thickness) apart. The final result contains no vessel curvature or tortuosity information, but is a reliable representation of the lumen shape.

The two imaging methods, angiography and OCT, provide incomplete but complementary information. Therefore, an algorithm combining the two using a co-registration process can result in a more reliable reconstruction. Lumen contours were traced on the OCT scans, and were then rotated and mapped onto the centreline of the angiographic reconstruction, which contains curvature information, with the help of several fiducial points to enable co-registration between the two methods. The reconstruction process is described in detail in chapter 4. The 3D reconstruction achieved by this method is shown along with the other two methods in Figure 6-2.

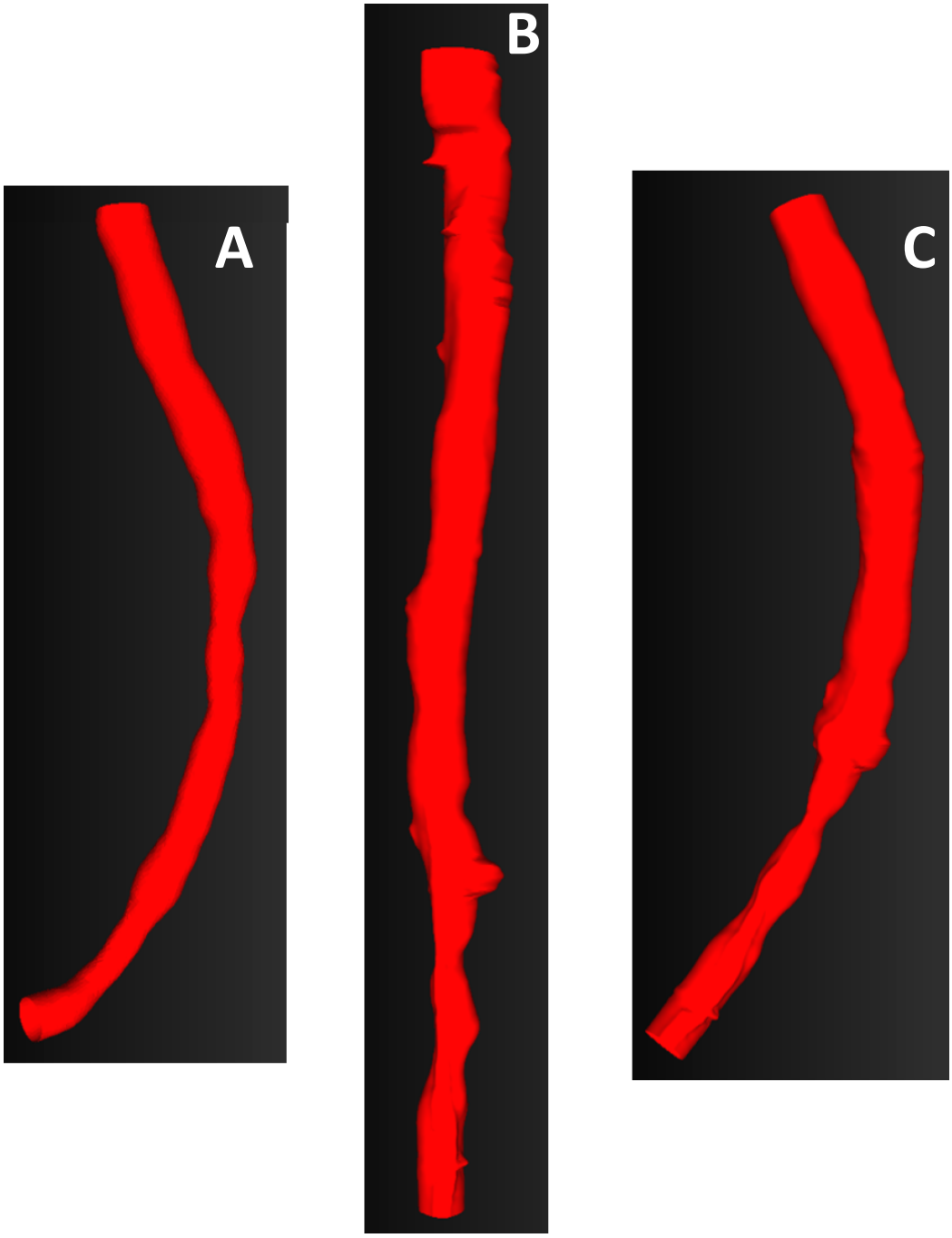

Figure 6-2 A. Angiography-based reconstruction of a lesion in the left circumflex coronary artery. The curvature and tortuosity of the vessel are captured in 3D space by using two angiographic views to create the reconstruction. The lumen contours, however, are represented by elliptical shapes and do not represent the true lumen shape. **B.** OCT-based reconstruction of the same vessel segment. The lumen contours extracted from the OCT images provide important extra information, such as the presence of a tandem lesion at the distal end of the vessel (bottom), that the angiographic reconstruction presents as a single stenosis. However, there is no information on curvature and tortuosity, meaning that some contours are skewed compared to the neighbouring ones, resulting in artefact sharp edges, and the vessel segment appears longer than reality. **C.** The same vessel segment reconstructed by co-registering angiography and OCT. The detailed representation of the lumen contours from OCT combined with curvature information from angiography, contributes to a superior reconstruction.

6.2.2 Simulation set-up

Volume rendering and meshing

Hexahedral meshes of 120-150,000 finite volumes were created for all geometries using the methodology described in paragraph 4.9.1. In the geometries incorporating the OCT-derived lumen contours, the wall roughness was markedly higher than in the geometries created based on angiography only. For this reason, grid refinement near the wall was considered necessary to capture the flow around the rough geometry, but also to improve the simulation convergence.

Boundary conditions and simulation parameters

Pulsatile simulations were set up using Ansys CFX 13.0 pre-processing software (ANSYS UK). The boundary conditions were provided by the patient-specific pressure and flow velocity waveforms acquired during FFR measurement. The proximal pressure and distal velocity waveforms were ensemble averaged over five to seven beats using the peak R wave as a fiducial marker to improve the signal to noise ratio, whilst preserving the characteristic features, such as the anachrotic and dicrotic notch. The boundary conditions were vessel-specific, and so each set of boundary conditions was used three times, one for each reconstruction method. Fourier decomposition of the waveforms was used in order to convert the waveforms in a convenient equation form that could be input directly into the simulation set-up. The CFD model assumptions made in all cases were that flow is laminar (max Re ~ 400), blood is Newtonian and that there is no wall distension or domain motion. Justification of these assumptions is presented in chapter 4.

6.2.3 Results and discussion

The CFD-predicted vs. measured FFR plots for the three different anatomy reconstructions are shown in Figures 6-3 to 6-5. In the case of angiography-based and OCT-based reconstruction, no correlation was found between the predicted and measured FFR (correlation coefficient of 0.048, $p = 0.84$ and 0.12, $p = 0.6$ respectively), while for the

combined OCT and angiography reconstructed models a statistically significant positive correlation (correlation coefficient 0.58, $p = 0.003$) was found.

From the plots presented in Figures 6-3 to 6-5 it is evident that the geometry used to represent the patient anatomy plays an important role in the validity of the simulation outcome. It also appears that the use of angiography-based or the OCT-based reconstructions alone led to failure to estimate the pressure drop inside the vessel, with only the combined angiography-OCT reconstruction method providing a positive correlation with measured FFR data.

This result indicates that in order to provide reliable predictions of FFR, a true representation of both the lumen shape and the curvature and tortuosity of the vessel needs to be included in the model geometry. Curvature and tortuosity information can be easily obtained using imaging methods such as angiography or CT, and sometimes MRI. However, reliably visualising the true shape of the coronary vessel lumen contours can only be achieved with high-resolution, usually intravascular imaging methods, such as OCT or IVUS. 64-slice CT offers high resolution imaging too, but it still only has accuracy comparable to angiography (Sehovic, 2013, Lee et al., 2013).

The correlation between the measured and predicted FFR in the best geometrical representation is not high enough to suggest that geometry is the only important factor in the success of a CFD simulation. In what follows, other possible parameters the CFD-derived FFR may be sensitive to are tested and discussed.

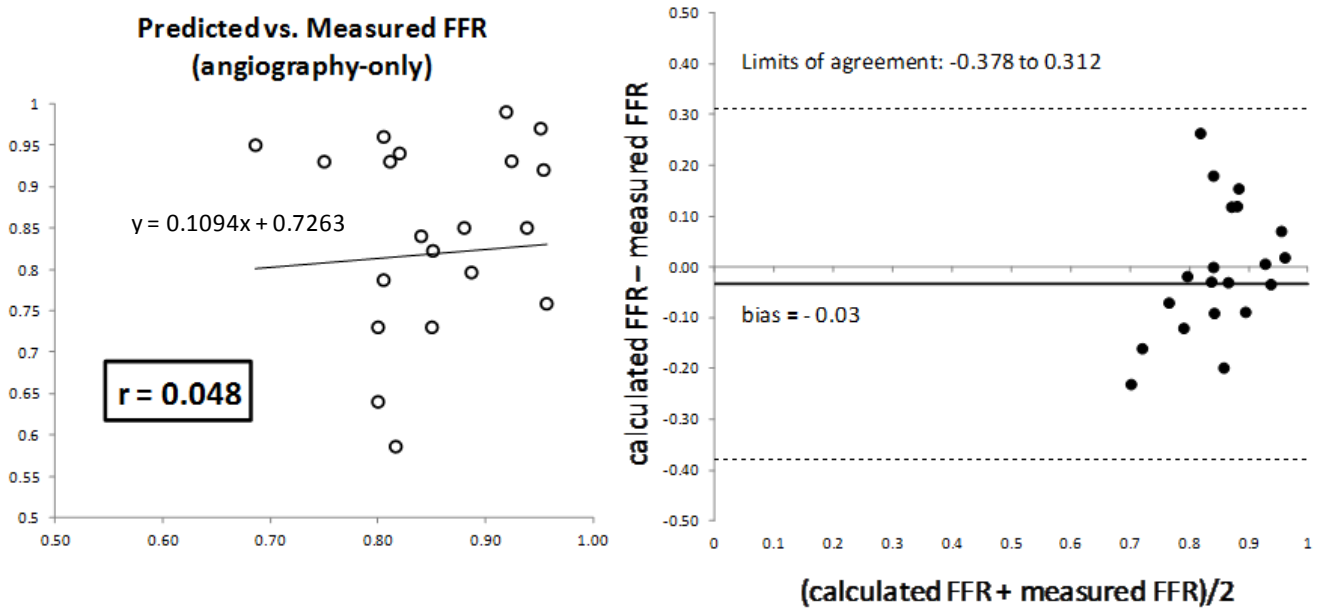

Figure 6-3 CFD-predicted vs. measured FFR plot and corresponding Bland-Altman diagram using angiography-based models. There was no correlation between the two data sets.

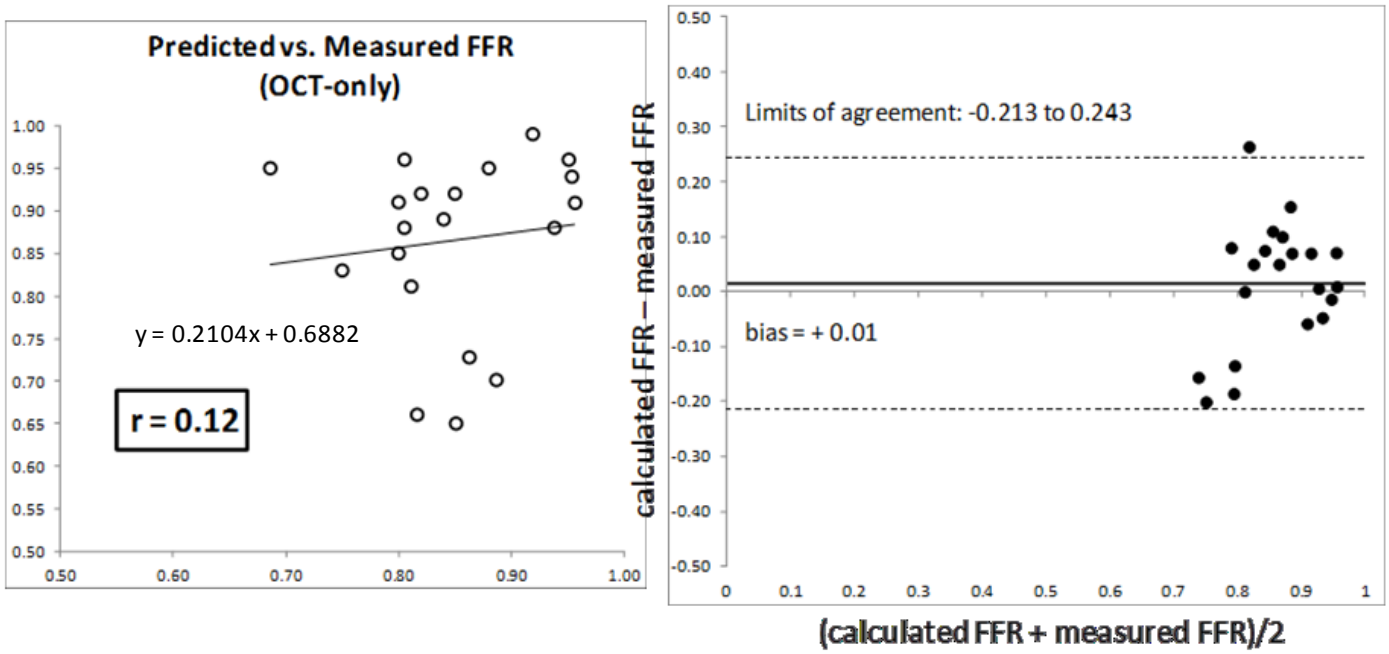

Figure 6-4 CFD-predicted vs. measured FFR plot and corresponding Bland-Altman diagram using OCT-based models. There was no correlation between the two data sets.

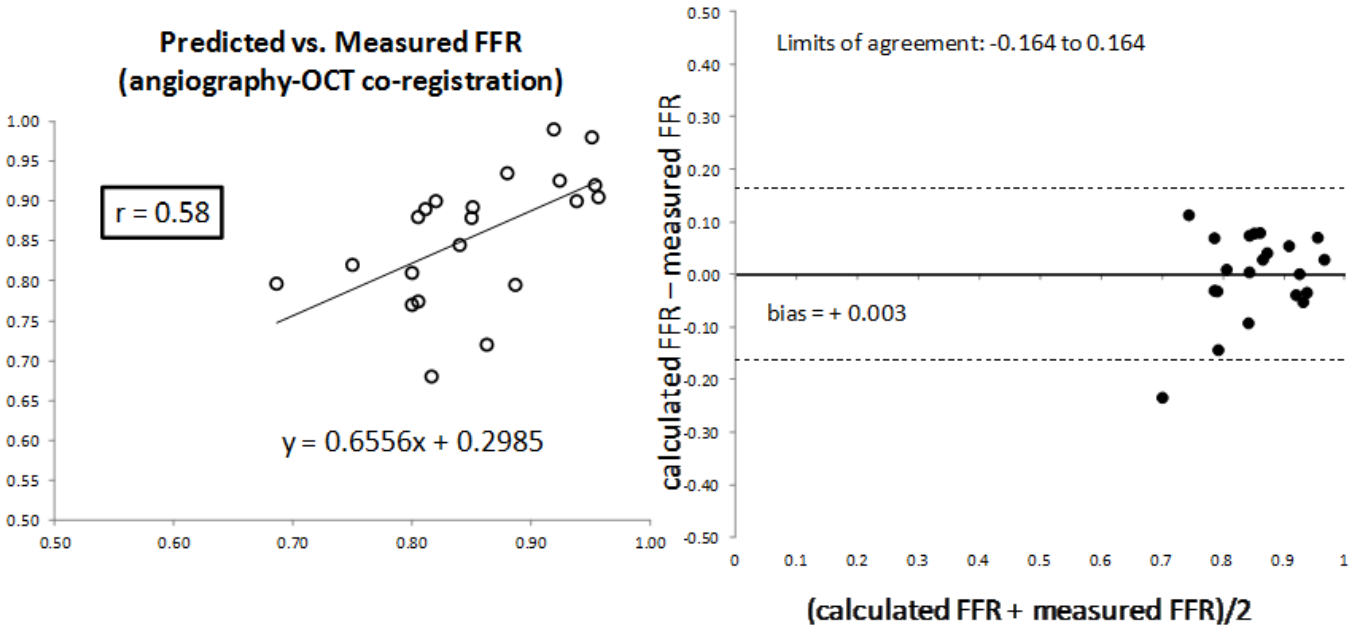

Figure 6-5 CFD-predicted vs. measured FFR plot and corresponding Bland-Altman diagram using fusion of OCT and angiography reconstructed models. There was a positive correlation between the two data sets.

6.3 Effect of hyperaemic proximal pressure (Pa) on the FFR ratio

Fractional flow reserve is defined as the ratio of distal to proximal pressure (Pd/Pa) under maximal vasodilation. It has been established (Tarkin et al., 2013) that the administration of vasodilators like adenosine results in variations in proximal pressure, with commonly lower Pa observed during hyperaemia compared to resting flow conditions (Figure 6-6). Since the proximal pressure is used as the denominator in calculations of FFR, it could be assumed that the lowering of proximal pressure could result in overestimation of lesion severity.

In order to test the effect of Pa in the FFR calculations, the observed pressure drop across the lesions during invasive and CFD-based FFR calculations were compared using absolute differences. The calculations were done in the 21-vessel group studied in Chapter 4, and the pressure drop was calculated as (mean hyperaemic proximal pressure) - (mean hyperaemic distal pressure) in the measured data and the CFD results using the geometries

obtained by the OCT-angiography co-registration algorithm. The results of the comparison are shown in Figure 6-7.

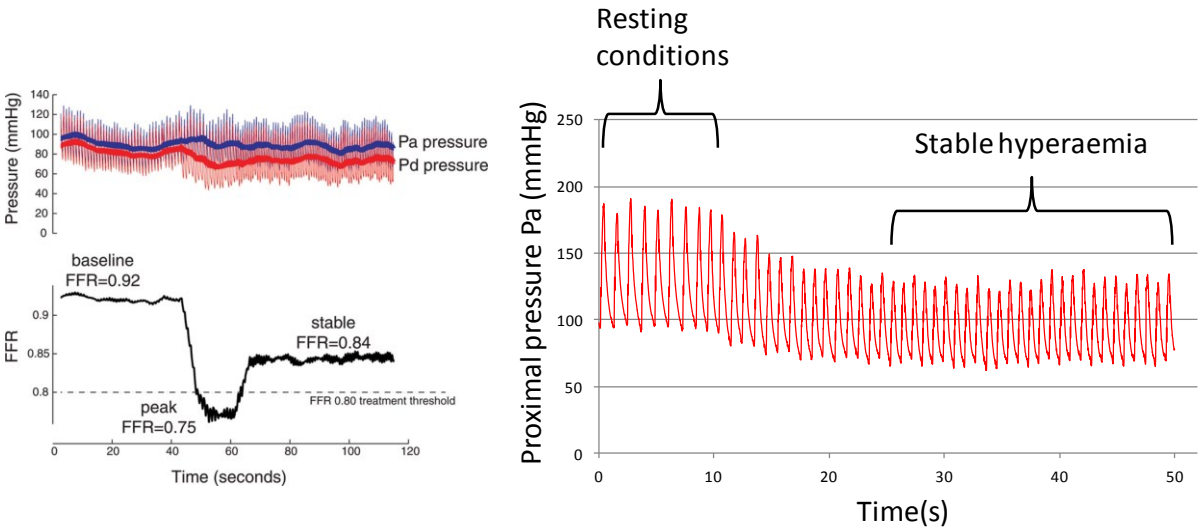

Figure 6-6 Left. An example of change in the FFR classification (severity assessment) during adenosine-induced hyperaemia. Intracoronary proximal (Pa) and distal (Pd) pressure traces are shown at the top, while at the bottom is the respective FFR ratio. It can be seen that, before reaching stable hyperaemia, FFR falls below the threshold, possibly due to simultaneous Pa depression. Image from (Tarkin et al., 2013). **Right.** Example of proximal pressure depression during adenosine-induced hyperaemia in one of the vessels used in the CFD simulations.

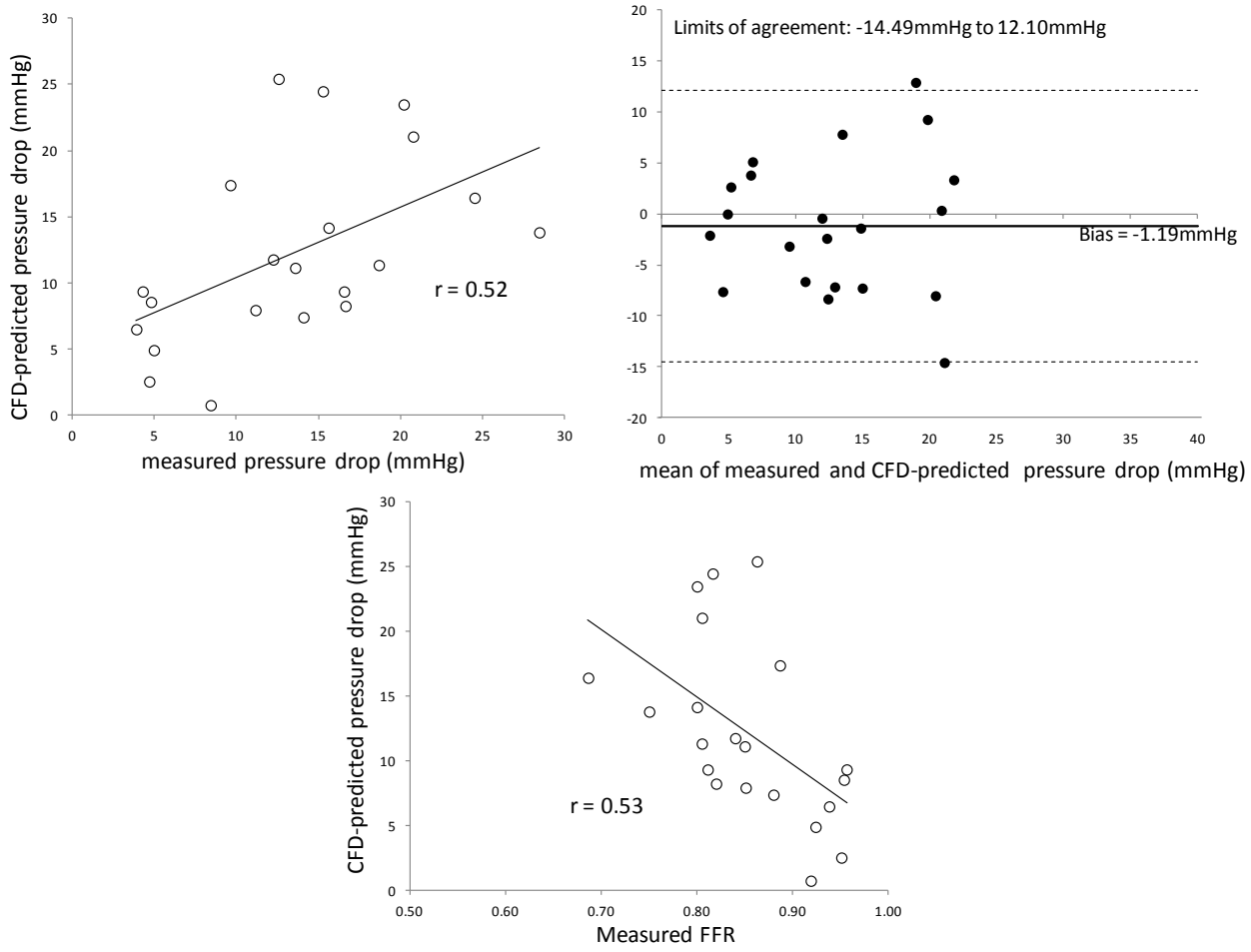

Figure 6-7 CFD-predicted pressure drop vs. measured pressure drop correlation plot (top left) and Bland-Altman plot (top right) show that removing Pa from the calculations does not result in higher correlation. Similar correlation was found when testing CFD-predicted pressure drop against the measured FFR.

The results suggest that removing proximal pressure from the comparison between measured and CFD-predicted pressure drops does not result in improvement in the correlations, or the limits of agreement achieved in a Bland-Altman plot. In fact, the correlation coefficients between CFD-predicted pressure drop vs. measured pressure drop and CFD-predicted pressure drop vs. measured FFR are very similar, suggesting that the magnitude of proximal pressure has little to no effect on the accuracy of the CFD result.

6.4 Sensitivity of CFD-predicted FFR to volumetric flow rate

The results presented in section 6.2 suggest that there is a positive correlation of

predicted and measured FFR when using the most accurately reconstructed coronary anatomy available. However, the correlation was not as strong as one would expect based on the use of state-of-the-art pressure and flow velocity data as boundary conditions. This suggests that more parameters can have marked effects on the accuracy of the CFD-based FFR estimation.

We hypothesized that the error in the estimation of coronary volumetric flow rate from coronary flow velocity provides a large source of measurement variability.

6.4.1 Model description

In order to test this hypothesis, three of the patient-specific coronary anatomies of the original cohort presented in Table 5-1 were selected to perform a sensitivity analysis on. The geometries were chosen based on the stenosis severity as indicated by the measured FFR value; one had a FFR of 0.68, considerably smaller than the 0.80 cutoff, indicating severe stenosis, another had a FFR of 0.95 indicating mild disease, while the third had a FFR of 0.81, indicating moderate disease. The angiography/OCT fusion reconstructed geometries of the three vessels are shown in Figure 6-8.

Steady state CFD simulations were set up. A pressure of 100mmHg, representing a typical mean aortic pressure (Pa) was chosen as inlet boundary condition in all cases. The outlet boundary condition was volumetric flow rate, which varied from 1.2 to 2.8 ml/s in 0.4ml/s increments. All values used are within the physiological range of cycle-averaged volumetric flow rate observed in the coronary arteries during vasodilation (Sakamoto et al., 2013).

6.4.2 Results and discussion

The predicted pressure drop is shown in Figure 6-9. The results are shown as % pressure drop compared to the inlet pressure of 100mmHg, so that a 20% pressure drop indicates a distal pressure measurement of 80mmHg, or a FFR of 0.80, representing the cutoff value.

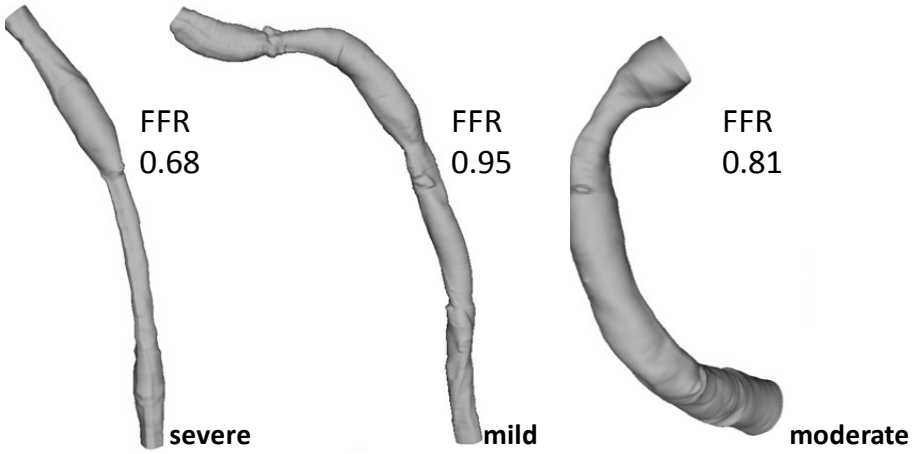

Figure 6-8 Three vessel anatomies taken from the original 19-patient cohort and used in the sensitivity analysis. Measured FFR is shown for each lesion.

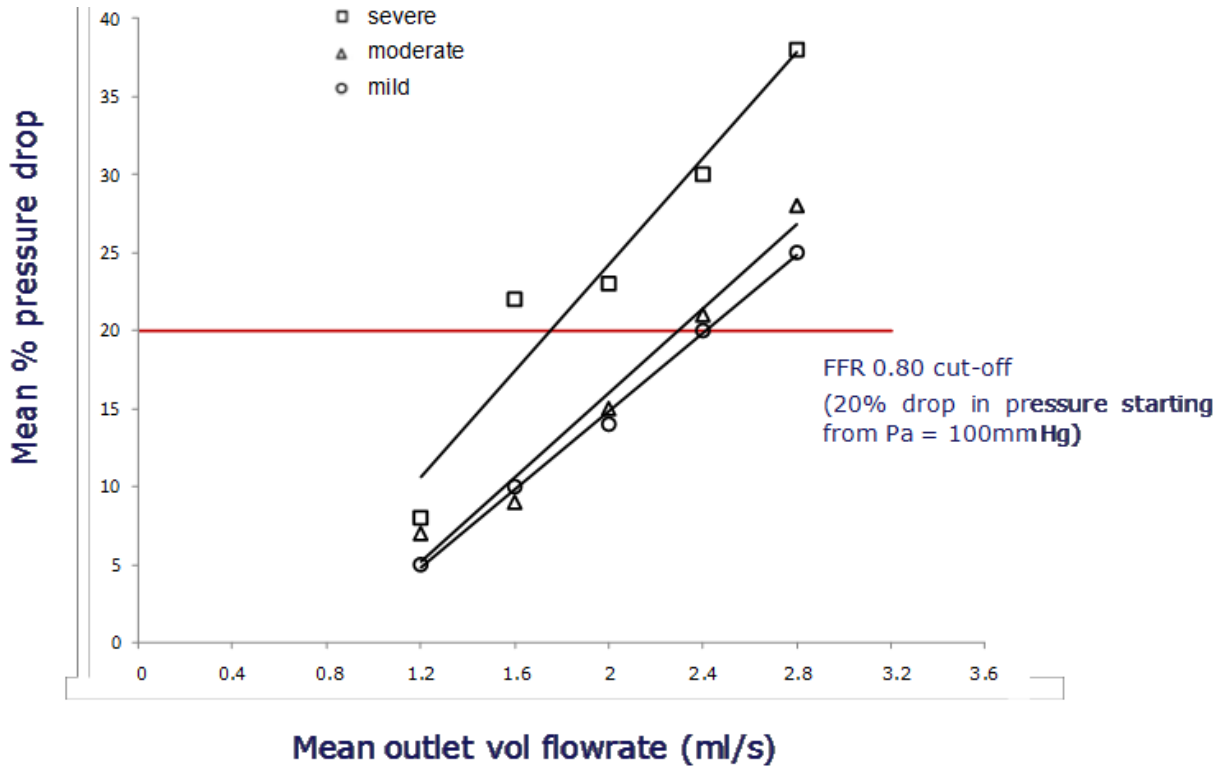

Figure 6-9 Mean % pressure drop vs. volumetric flowrate for three different patient-specific coronary anatomies with varying degrees of disease severity. The red line indicates the FFR cutoff point of 0.80, suggesting that the volumetric flowrate is an important parameter in determining the overall pressure drop. This result is not surprising, but is rarely considered when using pressure drop to assess coronary stenoses in clinical practice.

Several attempts to use CFD for the prediction of FFR can be found in the literature. The imaging techniques used for coronary vessel reconstruction vary from non-invasive 64-slice CT, to invasive rotational coronary angiography, to fusion of angiography with

intravascular ultrasound. In all cases a good correlation between the CFD-estimated and the measured FFR values is shown. However, the agreement is not as high as might be needed to make a clinically satisfactory diagnostic technique. In the VIRTU-1 study (Morris et al., 2013), the overall bias between measured and calculated FFR was low, but the limits of agreement were found to be almost 0.3 either side of the mean.

All of the existing studies have struggled with acquiring reliable patient-specific volumetric flow rate data. The approach taken to overcome this challenge varies from study to study: in the VIRTU-1 study (Morris et al., 2013) a steady-state Windkessel model of microvascular resistance and impedance (Segers et al., 1999) boundary condition was adopted, using one set of parameters averaged over all cases, essentially assuming the same set of boundary conditions for all cases. A complicated system of resistance, impedance and capacitance used in a lumped heart model, combined with a Windkessel resistance model and Murray's law (Murray, 1926) were adopted in the calculation of FFRct (Kim et al., 2010). The parameters of the system were fine-tuned to fit each patient's data, resulting in a positive predictive value of 74%, as presented in the DISCOVER-FLOW study (Koo et al., 2011). The concept of TIMI frame count (Gibson et al., 1996) was used to estimate resting flow rate from angiographic images in a small study of 7 patients (Siogkas et al., 2013). While the agreement with the measurement was quite high, with a correlation coefficient of 0.85, the cases presented had very mild stenoses, all having a FFR measurement >0.85 which is not representative of the general population of CAD patients. Also, as with DISCOVER-FLOW, the flow rate estimations were not validated against the real flow rate at the time of the FFR measurement.

A study by (Papafaklis et al., 2014), published after work on the current study was completed and published, proposed a way to circumvent the uncertainties in the volumetric flow rate estimation which are evident in all attempts to incorporate volumetric flow, measured or estimated, into CFD simulations for FFR. Steady-state CFD simulations of models built using angiography are run, setting a constant mean proximal pressure and calculating the mean distal pressure for a range of flow rates which range from 1 – 4 ml/s, values which correspond to the normal range for hyperaemic flow. The area under the pressure drop-flow curve (a measure they call vFAI) is used as a measure of function. The method achieves good correlation with measured data, however the study is limited by a small cohort.

Looking at Figure 6-9 it is clear that pressure drop rises proportionally to the rising volumetric flow rate. A 1.6ml/s increase in flow rate can result in a CFD-FFR variability ranging from 20%-30% depending on the lesion severity. This result is important in that it shows a variation in volumetric flow rate which is within the range observed in coronary vessels during hyperaemia can result in the CFD-based FFR "reading" changing from significant to non-significant, when no other change in anatomy or pressure has been made. The linear relationship within this small range appears to be in agreement with Hagen-Poiseuille's law, but the pressure-flow relationship in the presence of stenosis appears to become quadratic when larger ranges are considered.

This result highlights the importance of using reliable estimations of volumetric flow rate as boundary conditions in CFD simulations in order to obtain a reliable FFR reading, indicating that a validation of the methods used in previous studies to estimate volumetric flow rate is necessary before CFD-derived FFR can become a reliable non-invasive assessment of ischaemia-causing coronary lesions. There are many challenges associated with volumetric flow rate estimation both at rest, and especially during hyperaemia, such as errors in the velocity readings and missing information on the spatial distribution of velocity. As a result, a physical experiment was designed in order to test the accuracy of the volumetric flow rate estimation from invasively measured flow velocity against a gold standard flow rate measurement, and the results are presented in the next chapter.

6.5 Other factors that can affect the FFR predictions

6.5.1 Branch omission

One of the primary limitations of OCT, and all intravascular methods, is the inability to visualise more than one vessel at a time. This limits CFD modelling to simulations of a single vessel, omitting the bifurcations, the runoff to branches or the collateral flow from other vessels, which puts into question the assumption of the conservation of mass within the control volume which is inherent to any CFD flow analysis. This can have a marked effect on CFD studies of the wall shear stress distribution (Wellnhofer et al., 2010).

Apart from a study measuring coronary flow distribution in dogs with artificially induced occlusions (Schuhlen et al., 1994), no studies were found that directly measure flow

distribution in the branches of the coronary arterial tree in human owing to limitations posed by the measurement methods. Flow distribution in coronary branches is controlled by downstream resistance to the flow, which is variable among vessels in the presence of progressing disease.

One way to bypass the problem is to simulate the entire coronary arterial tree based on a high-resolution CT-scan, including all the visible branches and determining the outflow conditions based on the radii of the branches and microvascular resistance data(Murray, 1926) and the oxygen demand of the tissue supplied by each vessel. This approach has been shown to work (Taylor et al., 2013, Koo et al., 2011, Nakazato et al., 2013a) but the accuracy of the method is still lower than expected.

The use of Murray's law could provide a way to partially overcome the single-vessel limitation of OCT and other intravascular imaging methods. Knowing the angle of the side branch to the vessel visualised (which can be estimated using angiography) and measuring the length of the branch shadow in the OCT scan, it may be possible to make a reasonable estimate of the branch cross-sectional area and, therefore, make it plausible that flow lost to branches can be calculated. However, using such a method would also require further assumptions, such as assuming a circular branch cross-section. More importantly, parameters likely to affect branch flow such as the potential presence of stenosis in the branches and collateral flow from other vessels, would still not be taken into account. No CFD studies incorporating side branchesin their calculations of FFR exist to date.

6.5.2 Errors in the imaging data and reconstruction method

A number of limitations have been identified during the development of the reconstruction method, which are discussed in detail in sections 4.6.3 and 5.5.2. These limitations pertain to either the way the data was collected (e.g. the use of monoplane angiography, use of data from one OCT run per vessel in most cases), or in the reconstruction process itself (e.g. use of centreline instead of the catheter path). It is possible that these assumptions or potential sources of error in the imaging and reconstruction processes can propagate and affect the CFD results, though there are currently no data to quantify the effect these would have in the CFD-based estimation of FFR.

One surprising result presented in this chapter was the low correlation between FFR derived from angiography-only based reconstruction and the measured values. Studies have shown positive correlations of CFD-derived FFR with measured values using either angiography (Siogkas et al., 2013, Papafaklis et al., 2014), or imaging techniques with lower imaging resolution than angiography, such as CTA (Min et al., 2012b). We hypothesize that the reason behind the apparent discrepancy lies in the method of reconstruction. Specifically, the studies mentioned above make use of algorithms which trace the true lumen shape on the angiogram or CT scan. Contrary to that, the use of the QCA 3D software only provides elliptical lumen sections which approximate the vessel cross-sectional area, but not the actual lumen shape. The addition of the OCT-derived lumen contours results in a major improvement and a positive correlation, suggesting that the lumen shape is required as well as an accurate estimate of the cross-sectional area in order for the CFD model to achieve good agreement with the measured FFR. The correlation of the OCT-angiography fusion derived FFR is comparable to that of other, similarly-sized studies.

6.5.3 Errors in the pressure and flow velocity data

In this chapter it was shown that the quality of the CFD simulation results depend strongly on the quality of the patient data used in the reconstruction process and as boundary conditions. No imaging or measuring method is without errors. Depending on the equipment used, operator skill and parameters beyond the operator's control, there is marked patient-to-patient variability in the quality of the data.

Errors in the measurement of pressure are usually in the form of drift, which is a consistent over- or under-estimation of the pressure reading that can be easily identified, measured and corrected. Errors in the intravascular measurement of velocity, however, are more complicated to detect and identify, and more challenging to correct.

The Volcano Combowire used in the study contains a Doppler ultrasound probe. The ultrasound beam emitted by the probe detects the particle with the highest velocity within the sample volume and records the component of the velocity at which it travels in the direction of the beam. Two important assumptions are made about the velocity measurements: (a) the velocity recorded is the maximum inside the sample volume and (b) the ultrasound beam

covers enough of a vessel cross-section to record the maximum velocity in that cross-section. These two assumptions combined suggest that all volumetric flow rate estimations made from these measurements should assume the recorded velocity is the maximum on a given cross-section. Whilst the first assumption appears to be valid, based on the mechanism of Doppler ultrasound (Doucette et al., 1992), the second one may not be true at all times, meaning that the maximum velocity on the cross-section may not be recorded if it lies outside of the sample volume. This is possible in clinical practice, as it is common to bend the end of the wire where the probe is located by, typically, ~23 degrees in order to allow easier guidance of the wire through bends and bifurcations. Even though the wire is carefully rotated to record the highest velocity, the common occurrence of high velocity jets attached to the wall may mean that peak velocity is still missed. The effect of the ultrasound beam's change of direction affected by the bending of the wire has not been investigated yet.

The importance of potential erroneous flow velocity measurements is that small errors can have a significant effect on the volumetric flow rate estimation, a parameter that FFR estimation is very sensitive to, as shown previously. Most studies (Doucette et al., 1992, Chou et al., 1994) suggest that the velocity distribution profile inside the coronary arteries comes close to a Poiseuille parabolic distribution, but usually skewed towards the outer side of the vessel curvature. This is supported both by experimental and CFD studies (Manbachi et al., 2011) and also by the fact that the Womersley parameter (a measure of pulsatility) for coronary flow is lower than in the aorta (ranging between 5-10 for most cases), indicating that a Poiseuille parabolic profile may be a better approximation than a Womersley profile in this case (Wood, 1999).

The volumetric flow rate is given by the surface integral of the measured velocity on the cross-section (equation 6.1). An important assumption in equation 6.1 is that the velocity id measured perpendicular to the cross-sectional area. Calculating the volumetric flow rate can be done analytically when the mean velocity over the cross section is known, by multiplying the mean velocity by the cross-sectional area. Given that in a parabolic velocity distribution the mean velocity is known to be half the maximum, volumetric flow rate estimations $Q_{parabolic}$ from Doppler ultrasound-derived maximum velocity v_{DUS} measurements can be calculated using equation 6.1 for $Q_{parabolic}$:

$$Q = \iint_{Cross\ section} v \cdot dA \quad \rightarrow \quad \begin{cases} Q_{flat} = A * v_{DUS} \\ Q_{parabolic} = A * \frac{v_{DUS}}{2} \end{cases} \tag{6.1}$$

where A is the cross-sectional area at the measurement location.

There is, however, evidence from the CFD results (Figures 6-11 and 6-12) that the velocity profile can deviate significantly from the Poiseuille profile in the area downstream of a stenosis. When flow is forced through a stenosis, the spatial profile becomes almost flat, with the mean flow velocity being almost equal to the maximum flow velocity on the cross section. It would result in smaller errors in the estimation of flow rate, if velocity measurement could be made within the stenosis as then the measured velocity could be directly multiplied by the cross-sectional area to provide the instantaneous flow rate (Q_{flat} in equation 6.1). However, high velocities near the stenosis region can result in increased technical challenges in obtaining velocity measurements, as the presence of a jet and recirculation reduces the steerability of the wire, while the presence of stenosis also restricts wire manoeuvring. Assuming a Poiseuille parabolic velocity distribution to estimate flow rate in the area near a stenosis would result in flow rate underestimation. On the other hand, in the area just downstream of a stenosis, especially in the presence of curvature, the high-velocity jet created by the presence of stenosis can separate from the vessel wall, and then reattach on the outer side of a curved region, creating a very high velocity peak near the outer wall, combined with retrograde flow at the inner wall. In the case of such skewed spatial profiles, the peak velocity on the cross-section can be higher than twice the mean, in which case an overestimation of the flow rate would occur. Therefore, assuming a Poiseuille profile to estimate volumetric flow rate in that case can result in random over- or under-estimation of the volumetric flow rate, depending on the location of the wire at the time of measurement.

In the transient flow simulations presented in chapter 4 and in paragraph 5.2 both the assumption of a parabolic and a flat velocity distribution were tested. There was consistent underestimation of the pressure drop measured when the parabolic flow assumption was used, whilst the flat profile assumption appeared to provide the best agreement with the measured data, and therefore it is the only result shown. This would suggest that the velocities measured in this way are closer to the mean velocity on the cross-section, rather than the maximum. This could be explained by the ultrasonic beam missing the maximum velocity on the cross-section, which can, as discussed, be near the edges due to the potentially skewed profile, and thus less likely to be captured by the beam, as shown in Figure 6-10. Though no studies investigating the effect of a skewed velocity profile and/or ultrasonic beam for the coronary arteries, careful positioning of the wire was a major suggestion/limitation reported in the most widely quoted Doppler probe validation paper

(Doucette et al., 1992), while studies in the carotid arteries found the skewness present can affect the Doppler ultrasound measurements (Mynard and Steinman, 2013), indicating that similar errors may be present in intracoronary ultrasound measurements.

The better agreement achieved with the flat profile assumption is problematic when taking into account the deviation of the maximum velocity from the mean in each cross-section evidenced by the CFD results shown in Figures 6-11 and 6-12. The fact that the maximum cross-sectional velocity downstream of a stenosis appears more likely to be at least twice the mean suggests that the flat profile assumption should theoretically overestimate volumetric flow rate (and therefore pressure drop) in most cases. In practice there is an almost equal possibility of over- or under-estimation in the CFD-predicted pressure drop, suggesting the presence of random, rather than systematic, error.

A possible explanation for this could be derived from revisiting the assumption that, because of the low Womersley parameter values, flow in healthy vessels will be close to parabolic at all time points in the cycle. The velocity profiles plotted at near-peak flow in the healthy part of the vessel (either proximal or very distal to the stenosis, when flow is no longer affected by the stenosis) shown in Figures 6-11 and 6-12 suggest a flattening of the profile, compatible with mild flow pulsatility, which results in the maximum cross-sectional velocity being closer to the mean than it would be in a Poiseuille profile. Combining this observation with the concept that the velocity recorded by the Doppler wire probe may not be the maximum in the cross-section (as discussed above), this observation would suggest that the velocity recorded could be closer to the mean value than the maximum -though more likely to be overestimated than underestimated- thus making the option of the flat profile assumption the better choice in flow rate estimations.

This, however, would only be valid in measurements made in a healthy vessel segment (such as shown in Figure 6-12). In the cases of highly skewed flow profiles just distal to stenoses on curved vessel sections (such as in Figure 6-11) the effects of pulsatility are eclipsed by the effects of local geometry, and the possibility of peak flow being outside the probe beam is higher, as illustrated in Figure 6-10, resulting in flow rate underestimation.

The effect of incident angle, a consistent underestimation occurring because the ultrasound beam is not aligned to the direction of flow (therefore measuring velocities that are not perpendicular to the cross-section), which can exceed 20 degrees in many cases,

would also result in underestimation of the maximum cross-sectional velocity, contributing to the errors observed.

The effect that the presence of the wire itself has on the flow profile have been investigated using CFD (Torii et al., 2007). It was shown that the presence of a catheter inside a coronary blood vessel creates an obstruction which results in a modified, M shaped flow profile that results in ~15% reduction of peak velocity within the sample volume compared to a catheter-free vessel. The effect of the presence of the catheter in the change in pressure is not as pronounced as the effect on flow, meaning that this could also suggest that the peak velocity measured by the wire may, in fact, be lower than the actual peak velocity.

The fact that velocity measurements can be made at any part of the vessel and that the type of cross-sectional profile encountered cannot be known at the time of measurement suggest a random nature of the resulting error (over- or underestimation of flow rate) that is supported by near-zero bias of the CFD results as shown in Chapter 5.

Though there are alternatives to measuring coronary flow rate and velocity, they are, in general, more limited than intravascular Doppler ultrasound. Phase-contrast MRI can provide information on flow at the coronary ostia, but the temporal resolution is low, about 10 times less than invasive measurements at best (Markl et al., 2007). Another suggested way is to time the perfusion of contrast in the angiographic imaging. Though this has been shown to result in reliable results (Siogkas et al., 2013), its use would be limited by low contrast of the angiographic views, and the frame rate of the angiographic acquisition.

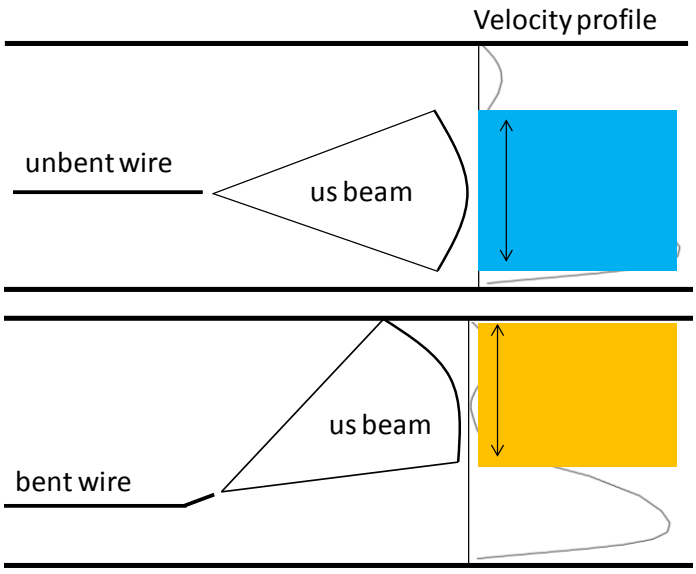

Figure 6-10 Schematic representation of the Doppler ultrasound beam velocity detection. When the wire is unbent the conical beam is pointing straight, capturing the largest part of the cross-section (blue section). Wires are routinely bent in clinical practice to aid manoeuvring. The US probe is at or near the tip of the wire, meaning that in the case of a bent wire the beam is pointing off-centre. This means that it can capture a smaller section of the cross-section (yellow section). When the velocity profile is skewed, as it is often the case in the coronary arteries, the off-centre beam could randomly not capture the maximum velocity on the cross-section.

6.5.4 Effect of measurement location uncertainty

Even though it is possible to angiographically visualise the flow wire as it is making measurements inside a vessel, it is still possible that errors in registering that location with the respective location in the 3D reconstructed model used in CFD simulations can be made. In the case of coronary stenosis, there could be great variation in the lumen's cross-sectional area within just a few millimetres (Figure 6-13), especially in cases of more severe stenosis and/or the presence of diffuse disease, which may not be clearly visible in the angiographic images, but could mean marked differences in area within a small longitudinal distance. Estimating the area of the cross-section where the velocity measurement was made in such cases can prove a challenge, which will have an important influence on the flow rate estimation. In the case of a vessel with a true diameter of 3mm and a measured velocity of 0.3m/s, misestimating the vessel diameter by 0.3mm can result in more than 20% under- or overestimation of the flow rate. Taking into account the results of Figure 6-9, this is a potential problem with Combowire-based flow rate estimates, and one which cannot easily be assessed in *in vitro* experiments with straight, unobstructed tubes, or *in vivo* measurements in healthy vessels.

Another uncertainty related to cross-sectional area estimation is the compliance of the arterial wall and the heart motion. Though in the coronary arteries wall compliance is limited by the fact that coronary vessels are positioned inside grooves on top of the relatively stiff heart muscle, some level of compliance still exists, and combined with the heart muscle movement which may distort the vessel shape, it can be seen that cross-sectional area estimation is subject to several sources of error, which has never been quantified.

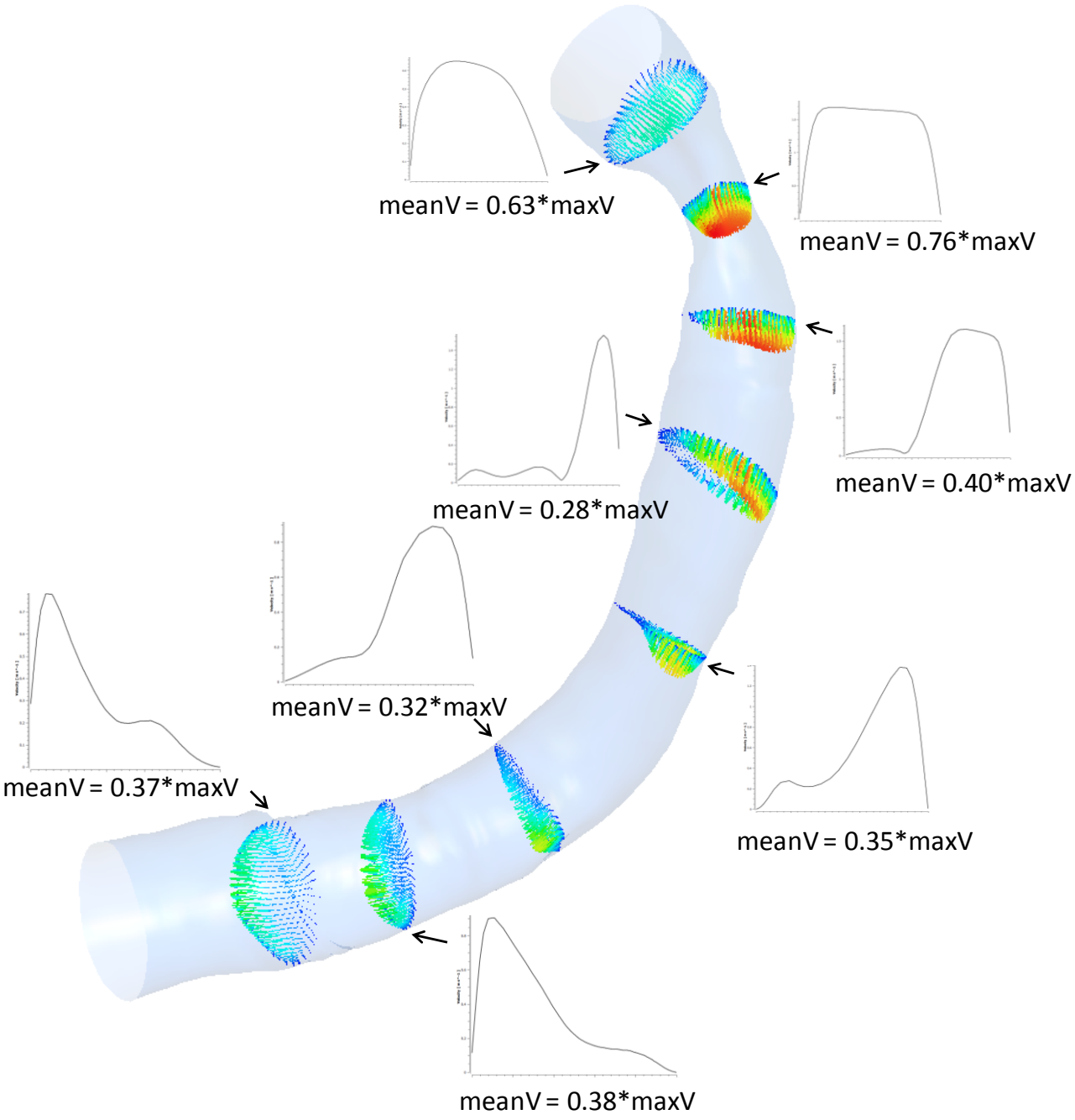

Figure 6-11. CFD-derivedspatial velocity profiles at various locations in a patient-specific model of right coronary artery stenosis. The presence of stenosis combined with curvature results in highly skewed profiles which can affect the ultrasound probe measurements.

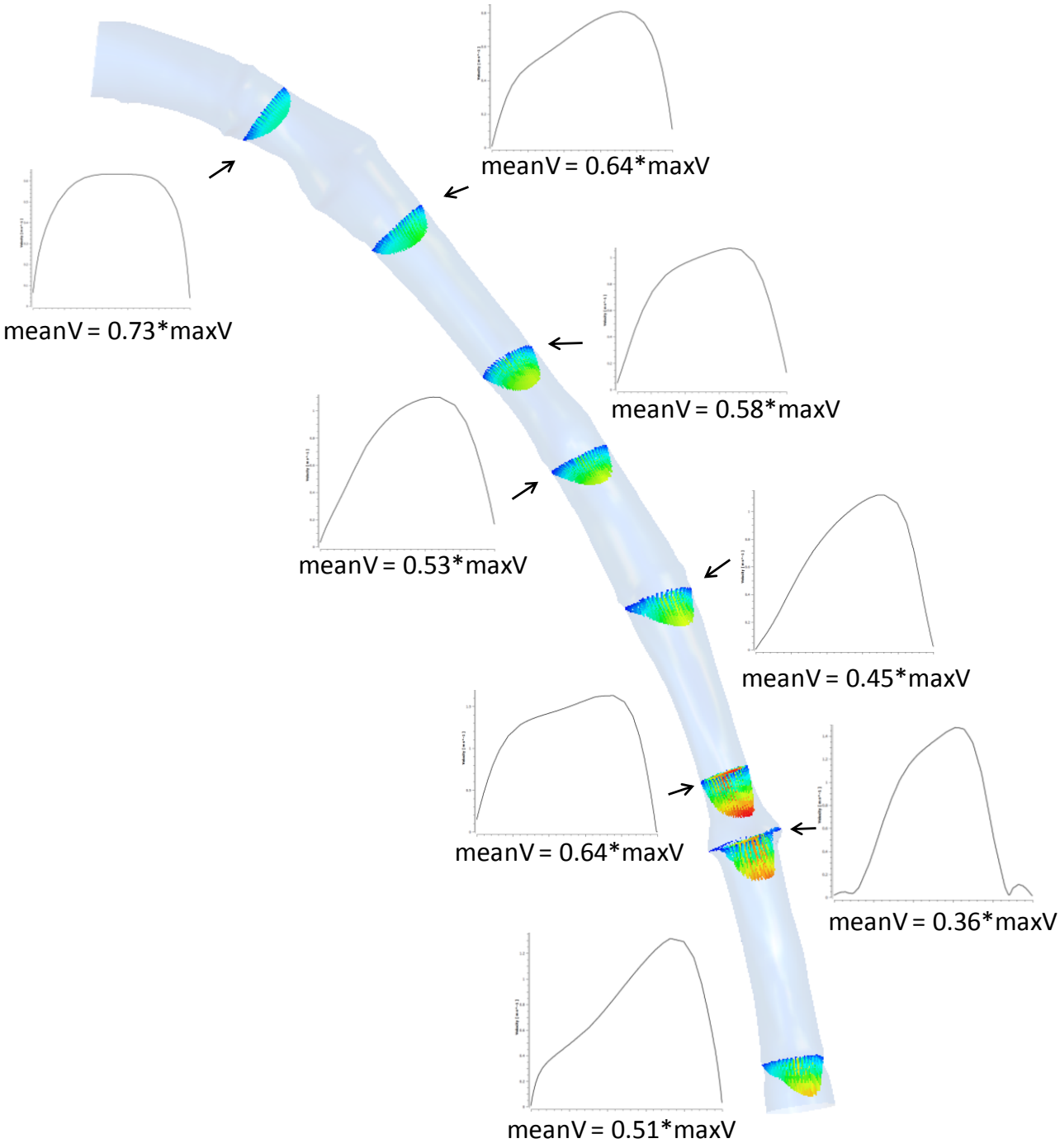

Figure 6-12 CFD-derived spatial velocity profiles at various locations in a patient-specific model of left anterior descending coronary artery stenosis. The milder stenosis and degree of curvature means that the spatial profiles remain close to Womerlsley-type flow for most of the vessel length.

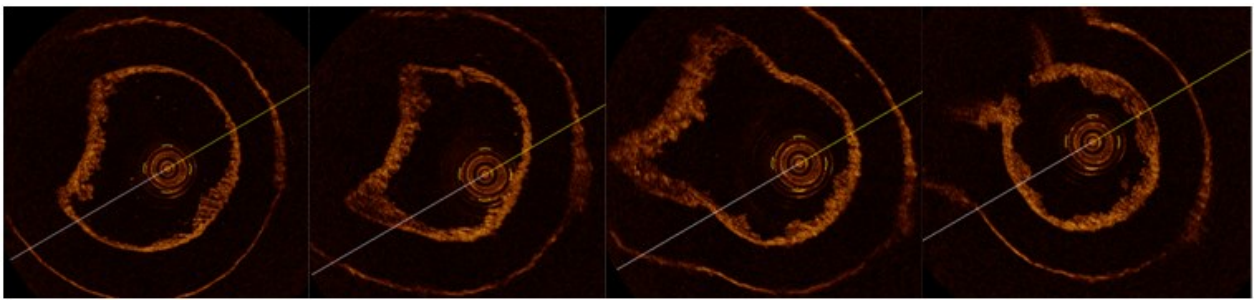

Figure 6-13 (Left to Right) Proximal to distal cross-sections of the phantom model taken 1mm apart at the level of the bifurcation/stenosis area. In the case of stenosis, the cross-sectional area can vary significantly within a few millimetres, introducing another source of uncertainty in the flow wire velocity based estimation of flow rate

6.6 Summary and Conclusion

In this chapter an attempt was made to evaluate the different parameters which could have an effect in the ability of CFD to provide accurate estimation of FFR values.

The first parameter to be tested was the accuracy of the anatomical representation. The results clearly show that a high quality reconstruction of the vessel of interest is necessary in order to obtain reliable FFR values. CFD models using angiography-only or OCT-only anatomy reconstructions resulted in FFR predictions which had no correlation to the measured values. The reconstruction method of angiography-OCT co-registration presented in Chapter 4 did result in a positive correlation of 0.58.

However, it was shown that an accurate geometry representation is not enough, as the CFD-based estimation of FFR was shown to be highly sensitive to the variation in volumetric flow rate, a parameter which is a necessary part of any CFD simulation set-up. A sensitivity analysis was conducted to study the effect that varying the volumetric flow rate within the physiological range would have on the CFD-calculated pressure drop for three given patient-specific anatomies of varying level of severity, based on their measured FFR. It was found that the pressure drop observed is proportional to the volumetric flow rate, and the same lesion anatomy can appear as significant or non-significant depending on the flow rate.

Other potential limitations to achieve an accurate CFD-based FFR calculation were also discussed. The effect of branch omission on the CFD results has been poorly studied and has been shown to have an effect in calculated wall shear stress, meaning that this is an important limitation that needs to be addressed. The use of intravascular Doppler ultrasound

has a set of limitations and caveats which lead to uncertainties over the volumetric flow rate estimation, which in turn has been shown in this chapter to be one of the most important parameters that can affect the CFD result.

The results presented in this chapter suggest that the two main parameters which can affect the CFD-based estimation of FFR in a patient-specific manner are the quality of the anatomical reconstruction, and the estimation of volumetric flow rate. The constant improvement of imaging techniques, both invasive and non-invasive, and the presence of a strong technical background on reconstruction techniques are making accurate anatomy reconstruction progressively better and more widely available. Estimating volumetric flow rate information for currently available data is not as straightforward. Studies that have attempted to use CFD to estimate FFR provide a positive correlation to the measured FFR values, but the correlation is not high enough to warrant the replacement of the current invasive techniques with the use of CFD to estimate FFR. The results shown in this chapter suggest that a better understanding of the way flow velocity data are obtained *in vivo* and a closer inspection of the methods used to estimate the volumetric flow rate from these velocity data is necessary before the use of CFD for non-invasive estimation can be considered as a reliable method to assess coronary lesion severity.

The observations and conclusions reached from the results presented in this chapter indicate that the uncertainty over the volumetric flow rate estimation from invasive Doppler ultrasound measurements can have a significant effect in the CFD results. Based on the conclusions from this chapter physical experiments were considered necessary in order to estimate the actual error in the calculations of volumetric flow rate based on Doppler ultrasound velocity measurements. The results of these experiments are presented in Chapter 7.

7. Phantom testing of flow rate estimation based on invasive flow velocity measurements.

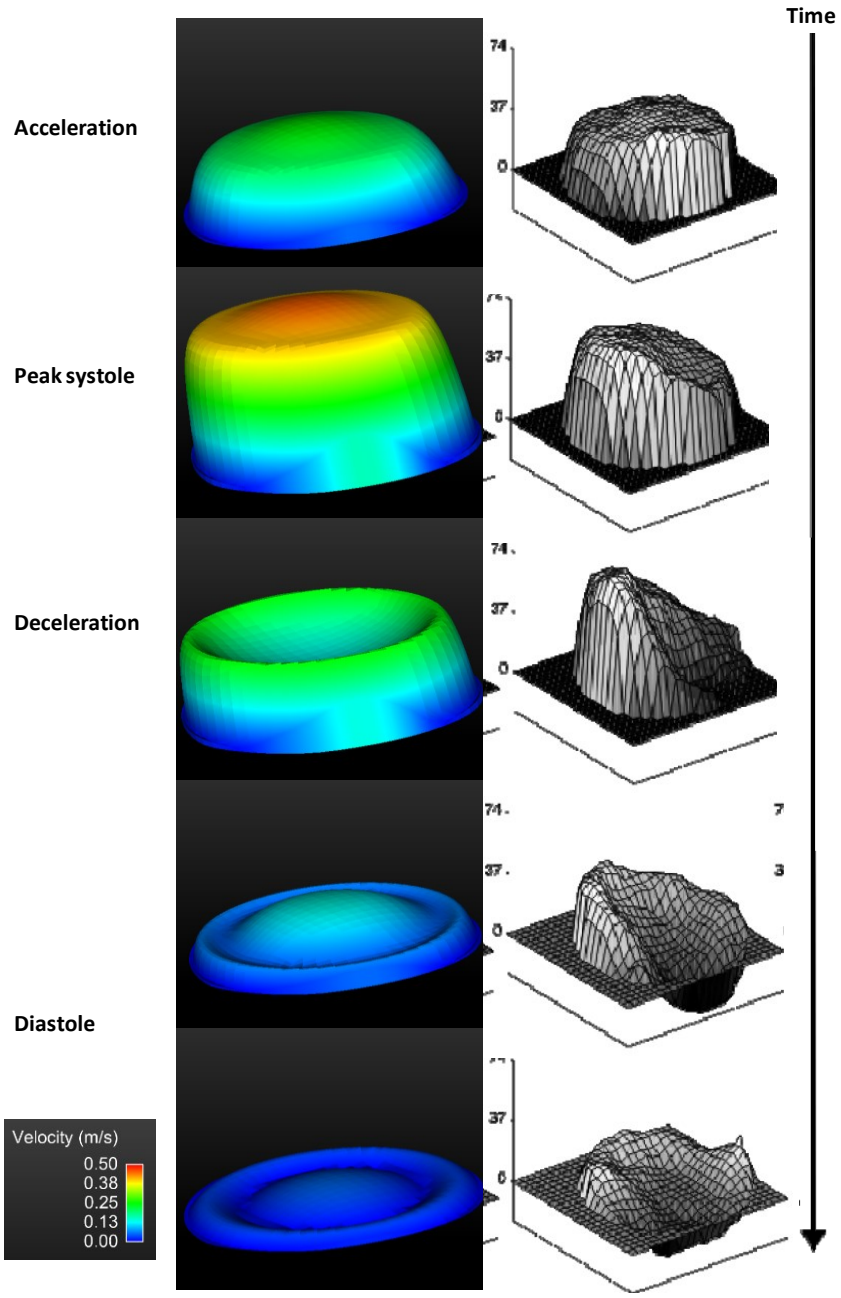

Figure 7-1 Theory vs. reality: Velocity through plane surface plot in the ascending aorta at different points in the cardiac cycle. The column on the left consists of a plot of the theoretical Womersley profile (Womersley, 1955), a common assumption for pulsatile CFD simulations. In the column on the right real patient data derived from phase contrast MRI in a similar location throughout the cardiac cycle are presented (Markl et al., 2012). It is clear that real velocity profiles look very different to what the best theoretical model can describe. This has serious implications in our ability to estimate and impose suitable volumetric flow rate boundary conditions.

7.1 Introduction

In the previous chapter the sensitivity of pressure drop to the volumetric flow rate was shown to be sufficiently high to have a marked effect on the CFD-derived pressure drops calculated in patient-specific applications. It was concluded that the uncertainty in the estimation of volumetric flow rate from invasively measured flow velocity data can potentially compromise the CFD results and is a bottleneck in the development of non-invasive CFD techniques for accurate prediction of pressure drop in individual patients.

In this chapter the results from a series of bench-top experiments conducted in order to assess the accuracy of estimating volumetric flow rate from invasive Doppler ultrasound flow velocity measurements are presented. A flow loop containing a pulsatile pump and flexible tubing was built and pressure and flow velocity measurements were made using a Combowire (same as the type used to provide the data in Chapter 4) on two different models, a simple plastic tube of known diameter and an idealised model of coronary artery stenosis. The Combowire-estimated flow rates were compared against the flow rate measured by a time-of-flight ultrasound flow probe (gold standard).

The chapter ends with a discussion of the most important limitations, and an assessment of the reliability of invasive Doppler ultrasound as a way of estimating volumetric flow rate for CFD simulations.

7.2 Methodology

7.2.1 Phantom models

Two phantom models were used in this study (see Figure 7-2). The first model was a 270mm long compliant plastic tube, 6 mm in diameter. The second model was a 52 mm long idealised phantom model of coronary geometry with a 75% area stenosis in the main branch. The model was created from a 3D CAD design using rapid prototyping. The material used is called TangoPlus (Sagi and Libermann, 2008) and has been shown to have similar distensibility to that of the human artery wall (Biglino et al., 2013). The idealised coronary artery phantom model is described in more detail in section 4.5 of Chapter 4. Both models

were required to have a degree of transparency that would allow visualisation of the wire during the invasive measurements.

The first model was used in order to test the accuracy of volumetric flow rate estimation in a simple geometry of known cross-sectional area. The second model is a more realistic geometry which contains large cross-sectional area longitudinal gradients, providing a more realistic challenge to the estimation of volumetric flow rate.

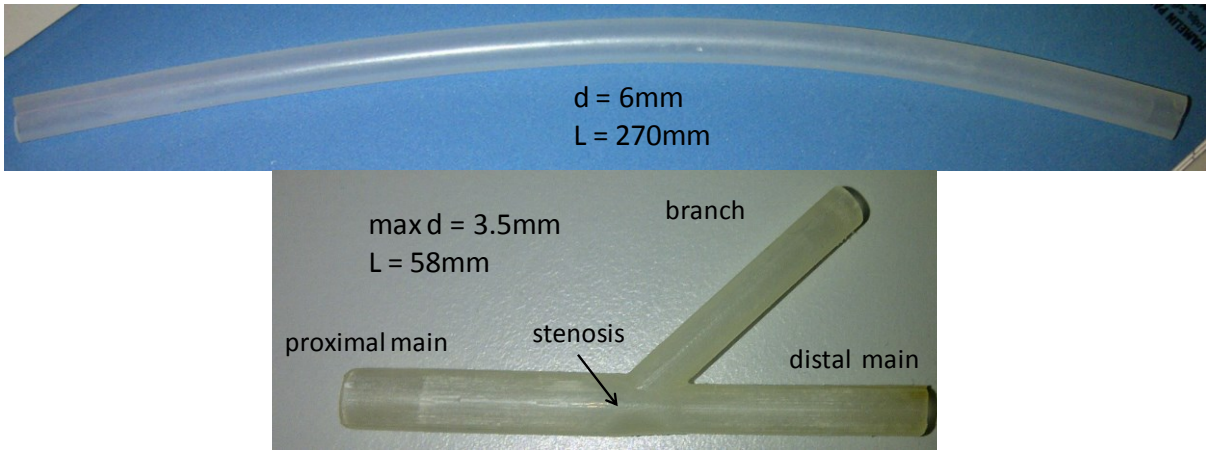

Figure 7-2. The two models used in the flow experiments. **Top.**A compliant tube of with no contriction**Bottom.**Idealised model of coronary anatomy, with stenosis on the level of the bifurcation. Flow to the distal main was occluded, so that flow only passed through the branch.

7.2.2 Experimental system

Experimental set-up

A schematic representation of the experimental set-up is shown in Figure 7-3. Each of the two phantom models was placed in a flow loop made of compliant tubing driven by a positive displacement pulsatile electric pump (pulsatile blood pump for rabbits, Harvard Apparatus, MA, USA). The pump is specifically designed to mimic the ventricular action of the heart, providing flow waveforms which are very similar to those observed in rabbits. The pump has controllable stroke volume and stroke rate, allowing for flexible control of the mean flow rate. In the rabbit pump model the stroke volume ranges from 0.5 ml to 10 ml, while the stroke rate can be set between 20 and 200 strokes per minute. For the purpose of this experiment, a stroke rate of 60 beats per minute was chosen and the stroke volume was

adjusted so that a target mean flow rate ranging from 3ml/s to 10ml/s was achieved. The pump output is controlled with an analog switch (Figure 7-4) meaning that the exact flow rate for all measurements was determined during post-processing.

An auxiliary flow loop was added to enable easier control and/or blocking of the flow in the main loop if desired. The Combowire Y-connector was placed in the main flow loop proximal to the phantom, an approach similar to that used in patients, where the wire is inserted in the coronary artery from the ostia, proximal to the stenosis.

The focus of this study was to assess the estimation of volumetric flow rate from flow velocity measurements. For this reason it was possible to obtain clinically relevant results without matching the rheological properties (viscosity, density) of the fluid used exactly to those of blood; therefore, a 35%w/w glycerol solution in water was used. The solution is a Newtonian fluid that has a kinematic viscosity of 3.52e-06 m^2/s, which is close to that of blood (average value ~2.7e-06 m^2/s).

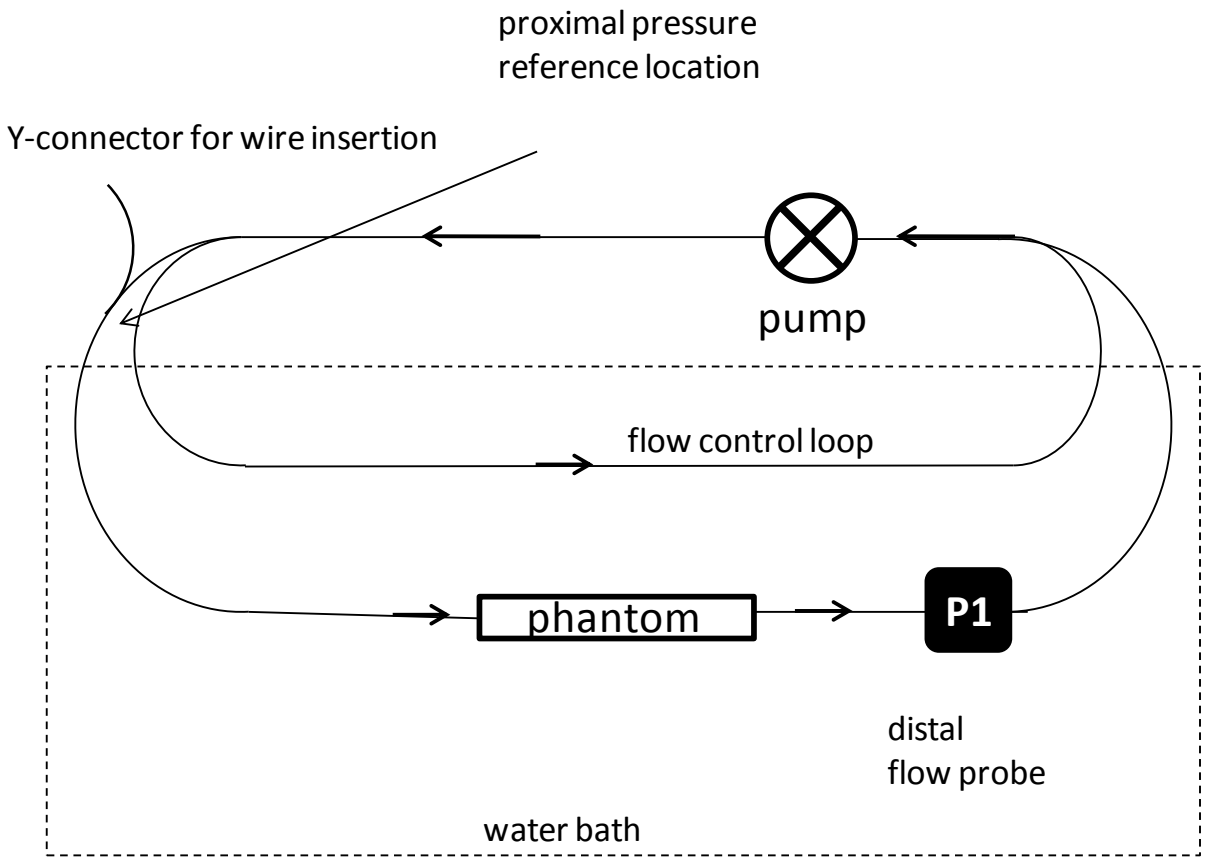

Figure 7-3 Schematic representation of the experimental system. The system (except the pump) was placed in a water bacth to ensure a robust signal from the flow probe P1.

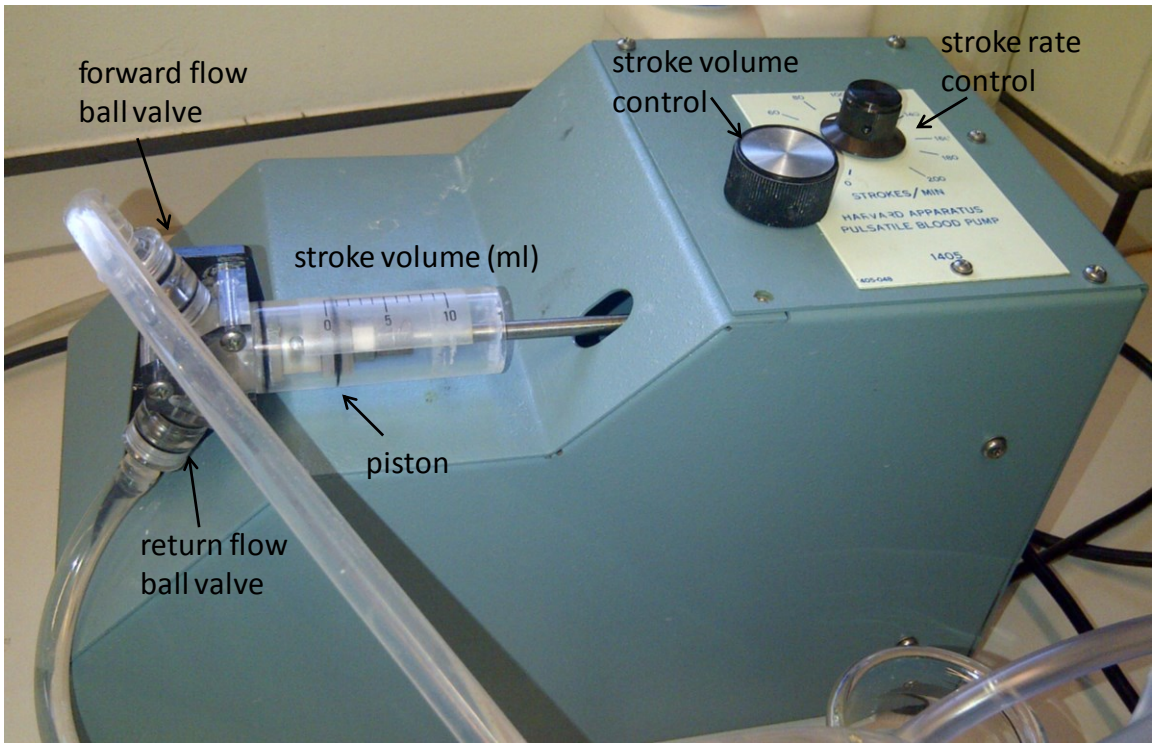

Figure 7-4 The pump used in the experiment (pulsatile blood pump for rabbits, Harvard Apparatus, MA, USA). The positive displacement pump can produce a realistic left ventricular flow waveform.

A small quantity of talcum powder was added to the reservoir to ensure a strong signal from the Doppler ultrasound, which measures the velocity of particles inside the fluid. Consequently, it is a valid assumption that the fluid used remained Newtonian and incompressible throughout the experiment. The flow rate through the phantom could be controlled by varying the stroke volume and stroke rate of the pump. Furthermore, a flow limiter distal to the phantom but proximal to the point where the two loops are reconnected was used to redirect part of the flow to the auxiliary loop. The peak Reynolds number was kept consistently below 700 to ensure laminar flow conditions.

A calibrated, time-of-flight perivascular ultrasonic flow-meter (T400 PS series, Transonic Systems Inc., NY, USA) was used to measure the instantaneous flow rate distal to the phantom. The probe consists of a cuff that loosely wraps around the tubing and position two transducers opposing a reflective plate to measure volumetric flow (Figure 7-5). This method is accepted as a reliable way to measure volumetric flow rate in clinical research, and in this study it was used as the gold standard volumetric flow rate measurement against which the flow rate estimations from the ultrasound flow velocity measurements would be compared. In order for the probe to work, air space between the probe and the measurement area must be filled, as air will not transmit the ultrasound signal. *In vivo* the use of acoustic

coupling gel to aid transmission is quite common, but in this bench-top experiment full immersion of the flow loop (except the pump) in a water bath was chosen as the most reliable way to ensure robust signal acquisition.

The flow probe was connected into a Transonic Systems T-402 instrumentation console fitted with a TS420 perivascular module as shown in Figure 7-5. This module, which is compatible with *in vivo* arterial/venous blood flow, was chosen for its ability to record both mean flow rate but also record instantaneous flow rate. The module is calibrated for the use with blood as circulating fluid, which has different acoustic properties to the fluid used. For this reason the numerical indications on the screen were not accurate for measurements in water, and the probe and module were calibrated before the experiment took place. The calibration curve for the probe is shown in Figure 7-5.

The Combowire XT wire was connected to a Combomap pressure and flow system (Volcano Corporation, San Diego USA), where it was possible to visualise pressure and flow velocity waveforms. The pressure signal had to be calibrated by placing the Combowire on a flat surface and zeroing the signal prior to the start of acquisition. The Combomap system can record data at specified times, and a log of the signal acquisition data can be saved and exported into purpose-built software Study Manager (Academic Medical Center, University of Amsterdam, The Netherlands) for analysis.

A 3.5 F pressure sensor wire (Millar Instruments, Houston, TX, USA) was inserted through the Y-connector and placed at the proximal end of the main loop where it recorded proximal pressure (Pa) for the duration of the experiment. The pressure sensor was calibrated just prior by recording measurements at known depths of water, and then converting from mmH_2O to mmHg. The signal from the Millar pressure sensor was passed through a PM-1000 transducer amplifier (DATAQ Instruments, Inc. Akron, OH, USA) before being connected to a measurement module.

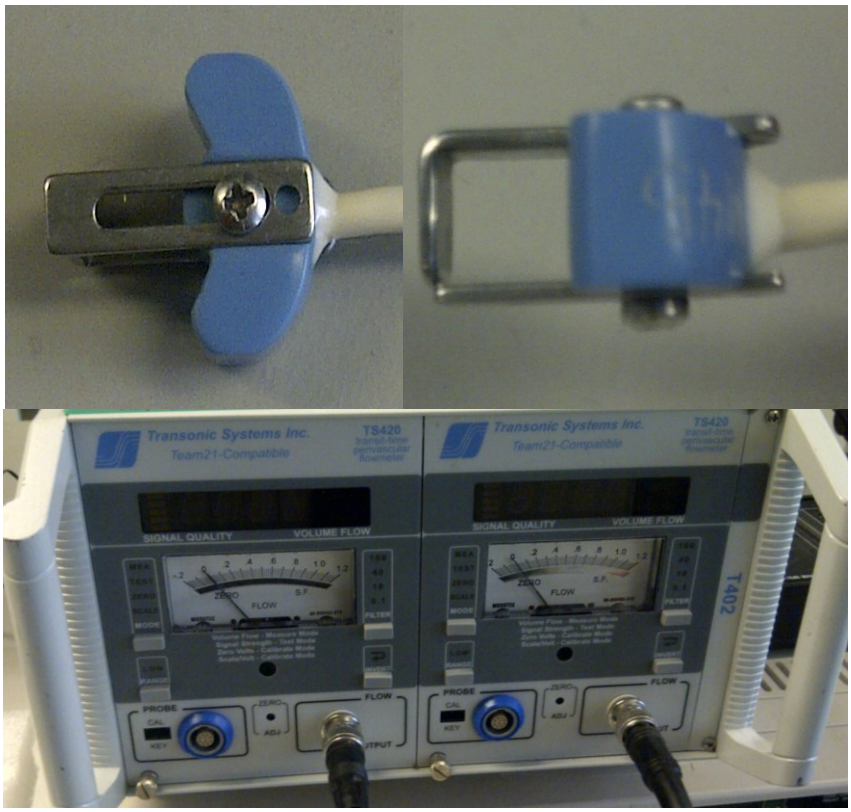

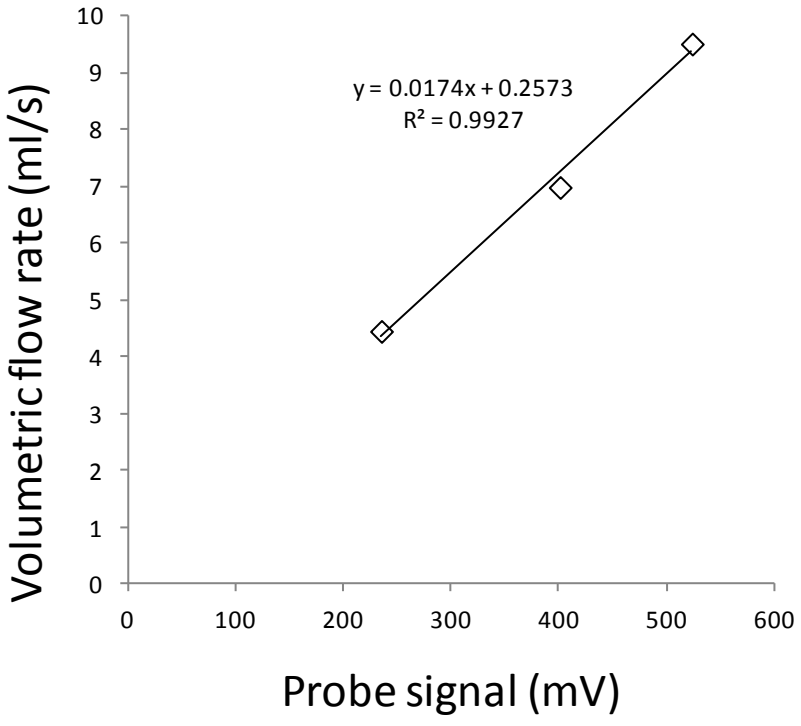

Figure 7-5 Top. Two views of the Transonics Systems T400 PS flow probe used in the experiment. **Middle.** The T-402 console fitted with two TS420 perivascular modules. This module is calibrated for blood, so manual calibration of the signal was required to obtain accurate measurements. **Bottom.** The calibration curve of the flow probe signal. Three measurements of the time it took to fill a 200 ml beaker were made for three different flow rate values. The calibration resulted in a linear equation which was used on all probe readings.

7.2.2 Data acquisition

The Transonic Systems console, the Combomap system and the Millar catheter transducer amplifier were connected to a DT9804-16SE-BNC USB measurement module (Data Translation GmbH, Bietigheim-Bissingen, Germany) to enable the transfer of the signal data to a PC for simultaneous signal recording (Figure 7-8). Notocord software (Notocord Systems, Croissy Sur Seine, France) was used to make simultaneous recordings of all four different signals (the flow probe, the Pa pressure measured by the Millar probe and the Combowire-measured Pd pressure and flow velocity data (Figure 7-6). The output of the DT9804 device provides electric signals which are then visualised in the Notocord system. These signals then need to be converted to pressure, velocity and flow rate measurements. Calibration for the flow probe and Millar catheter was performed manually, but the measurements of the Combowire pressure and velocity data were automatically calibrated by the Combomap system (Figure 7-7). To ensure the simultaneous recording of all signals from all sources, reference points were inserted into the Notocord live recording to denote the recording times in the Combomap system, thus eliminating potential time-lag errors.

Simultaneous measurements of pressure and Doppler flow velocity were performed using a Combowire XT (Volcano Corporation, San Diego USA). The procedure was performed by two cardiology registrars at Hammersmith Hospital (Drs Sukhjinder Nijjer and Ricardo Petraco) who were involved in the collection of the patient-specific imaging, pressure and flow velocity data presented and analysed in Chapter 4. The Combowire was inserted into the main flow loop proximal to the phantom, and was then manually guided to a location distal to the phantom, as close to the flow probe as possible without interfering with the probe signal, where three 30-second acquisition recordings were made. The flow rate was adjusted to a new value and, once the system had stabilised again, the data recordings were repeated for each flow rate. A total of fifteen recordings at four different flow rate levels were made for the straight tube phantom model.

In the case of the stenosis, measurements at the distal end of the model were made for three different flow rates, and five recordings were made before tears in the phantom model prevented further measurements.

The flow rate range tested is different between the two phantom models. For the straight tube experiment a wide flow rate range from ~ 4 - 12 ml/s was tested, in order to

better match the range tested by (Doucette et al., 1992). The flow rates used in the stenosis phantom experiments were lower than the flow rates used in the unobstructed tube experiment, aiming at a range from ~1-4 ml/s, covering the range of normal coronary and hyperaemic coronary flow, before the experiment was halted. The lower flow rates were achieved by reducing the resistance to the flow into the auxiliary loop, allowing for more flow to be diverted from the phantom model.

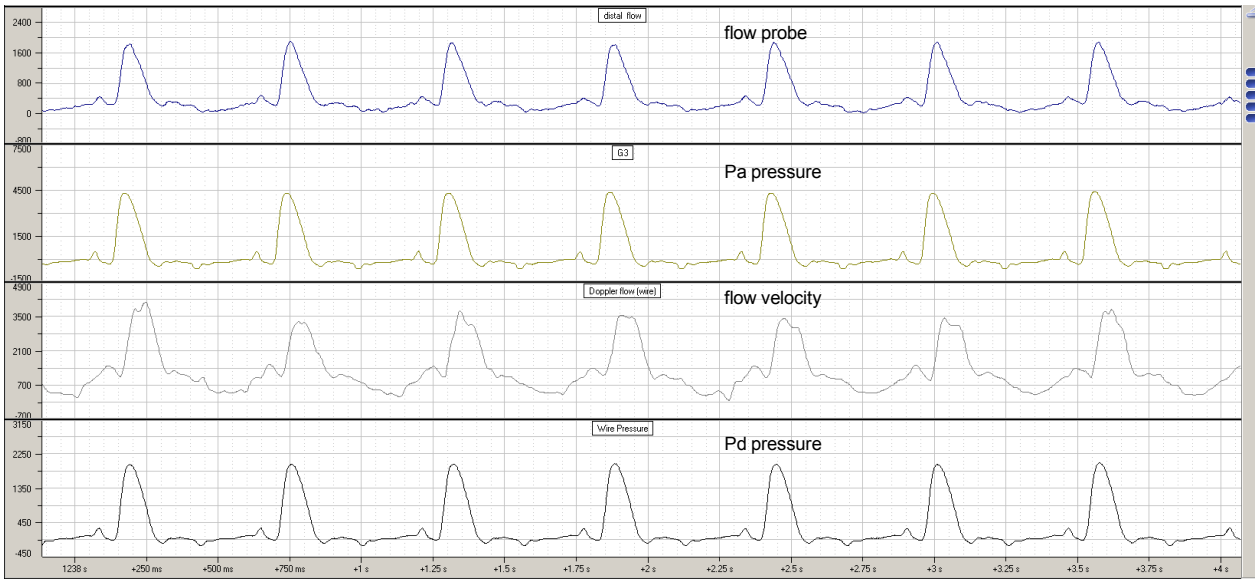

Figure 7-6 Example of the signal recordings made by the Notocord software. The four traces represent the signal from (top to bottom) the flow probe, the Millar catheter measuring proximal pressure, the Combowire flow velocity and pressure signals.

Figure 7-7. Left. The Volcano Combomap system console which allows for automatic calibration, visualisation and recording of the Combwiresignal.**Right**An example of a Combowire XT, which enables measurement of flow and pressure simultaneously (top) and the system of Y-connector, torque device and wire introducer used to insert and control the wire (bottom).

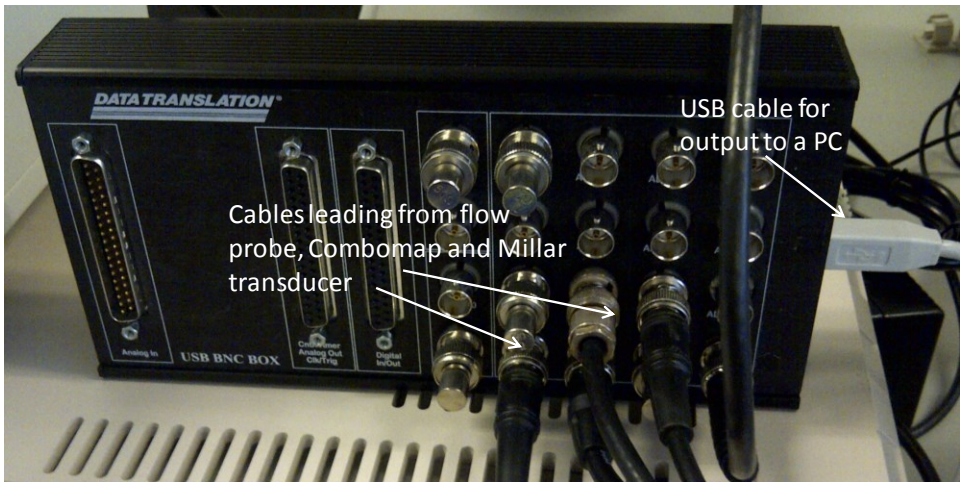

Figure 7-8 The USB measurement module (Data Translation GmbH, Bietigheim-Bissingen, Germany) used to transfer the signals to a PC for real-time recording of the data.

7.2.3 Data post-processing

The data collected was saved and exported to Microsoft Excel software, where they were sorted and analysed, based on the notes and markers placed during data acquisition.

Estimation of volumetric flow rate from Combowire Doppler wire

The Doppler ultrasound transducer embedded in the Combowire detects the particle moving at the maximum velocity at a given timepoint within the sample volume covered by the ultrasound beam, usually set at ±10 degrees from the centre (Doucette et al., 1992). The volumetric flow rate had to be estimated based on that velocity value, the cross-sectional area at the location of the measurement, and assumptions on the spatial distribution of velocity. Though in the literature it is suggested that the parabolic (Poiseuille) profile assumption is the closest to the realistic flow conditions (Figure 7-9), in this experiment it was found that the flat profile assumption gives the closest agreement with the flow rates measured by the flow probe, as shown in the Results section below.

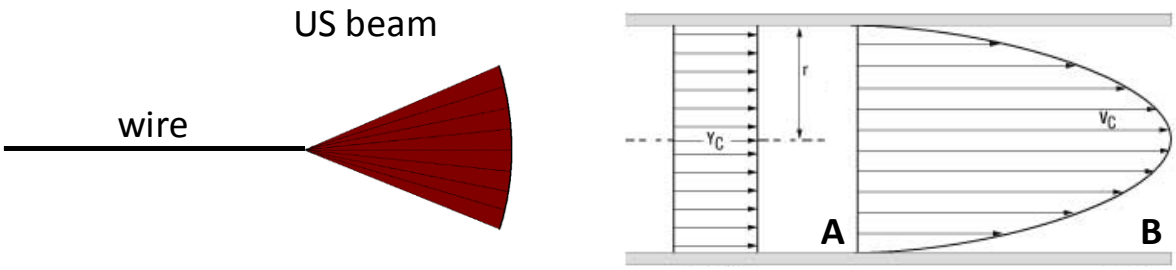

Figure 7-9 The difference between a flat and parabolic velocity profile. The ultrasound beam emitted by the wire detects the particle with the highest velocity within the sample volume. In the case of a flat profile (**A**) the maximum velocity on a cross-section is also the mean. In the case of parabolic flow (**B**) the mean spatial velocity is equal to half the maximum velocity. The flat and parabolic spatial velocity distributions allow for an analytical calculation of the volumetric flow rate.

7.3 Results

7.3.1 Unobstructed tube

A correlation plot between the Combowire-based flow rate estimates and the flow rates measured by the Transonics probe is shown in Figure 7-10. Even assuming a flat velocity spatial distribution, treating the velocity measured by the Combowire as the mean over the cross-section, there is a consistent underestimation of the flow rate, which is easily seen when comparing to the line of identity, and quantified in the Bland-Altman plot also shown in Figure 7-10. A negative bias of 0.70 ml/s was found across all measurements, with limits of agreement ranging from -3.11 to 1.71 ml/s. Agreement appears to be better at the lower flow rate level of approximately 4 ml/s, which is the level closest to coronary flow rate measurements.

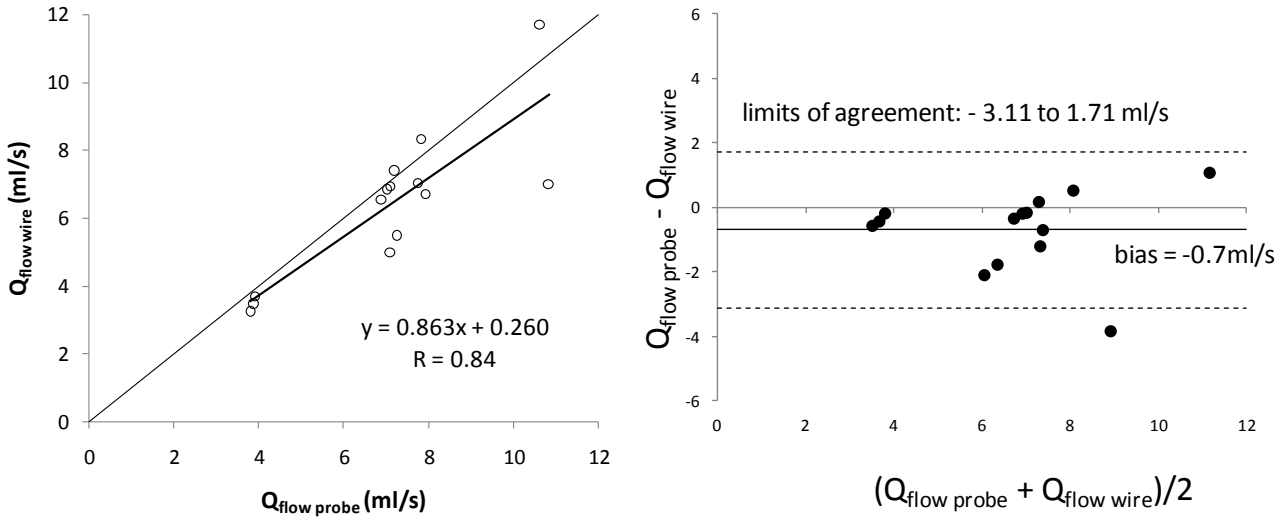

Figure 7-10 Left. Flow rate calculated from the Combowire measurements ($Q_{flow\ wire}$) vs. flow rate measured using a flow probe ($Q_{flow\ probe}$) and corresponding Bland-Altman plot (**right**) for the unobstructed tube (d = 6mm) at three different flow rate levels. A consistent underestimation of the flow rate was observed even when using the flat profile assumption.

7.3.2 Stenosis

The correlation plot of the Combowire-based flow rate estimates against the Transonics flow probe measurements distal to the stenosis in the phantom are shown in Figure 7-11. Again assuming a flat spatial distribution for the velocity, the Combowire-based estimates appear to be close to the line of identity.

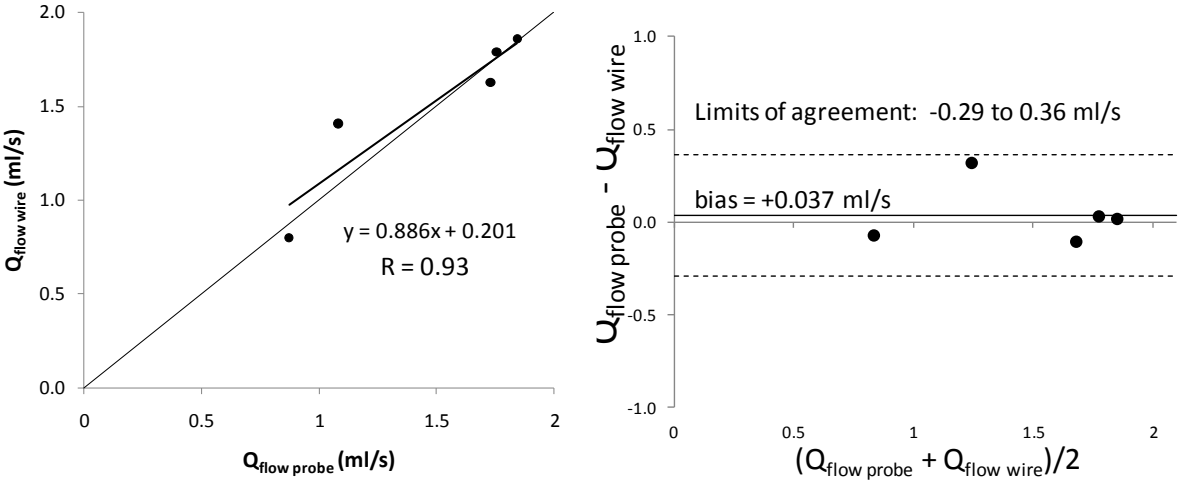

Figure 7-11 Top Left. Flow rate calculated from the Combowire measurements ($Q_{flow\ wire}$) vs. flow rate measured using a flow probe ($Q_{flow\ probe}$) at the distal end of a stenosis at three different flow rate levels, using the flat profile assumption. **Top right.** Respective Bland-Altman plot.

7.3.3 Doppler wire angle measurement

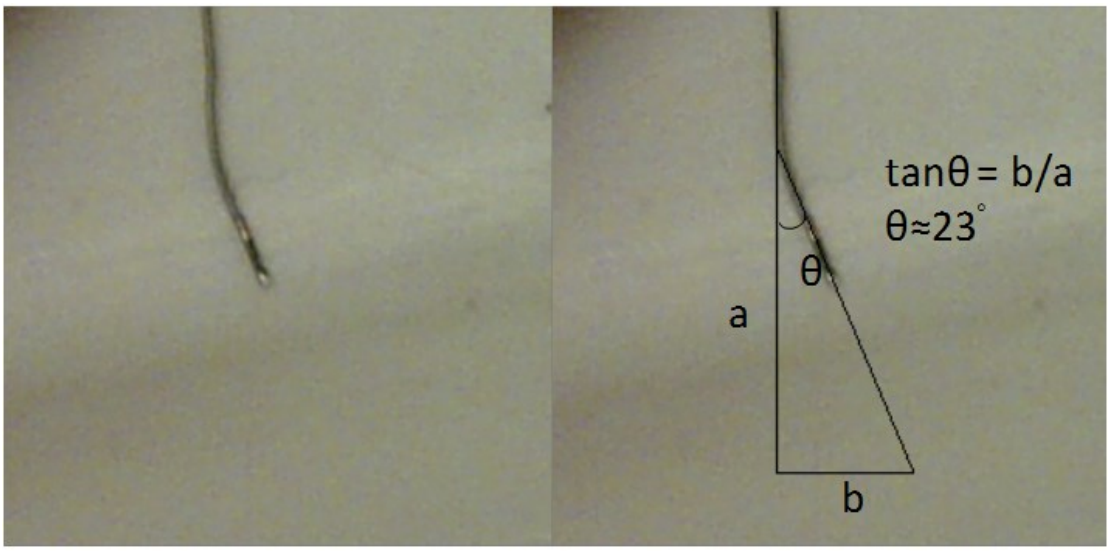

Figure 7-12 Left. Picture of the Combowire used in the experiments presented in this chapter. **Right**. Calculation of the wire angling used for easier manipulation using the tangent (ratio of side b over side a). The angle in this case was estimated to be ~23 degrees.

As discussed in Chapter 6, when a Combowire is used, interventional cardiologists tend to bend the tip of the Combowire in order to allow easier guiding and manoeuvring of the wire through the complicated coronary artery anatomy. There are no studies investigating

the effect that this wire angle can have on the measurements, and no measurement of this wire angle used in practice has been shown before. In Figure 7-12 the angle of the wire used in the experiment presented in this chapter is calculated at ~23 degrees using trigonometry. Given the fact that a Doppler wire has a beam angle of ~10 degrees, this measurement would suggest that the wire angle can have an effect on the measured velocity.

7.4 Discussion

7.4.1 The flat profile assumption gives the best agreement with measured results

As discussed extensively in Chapter 5, there are many uncertainties over the shape of the cross-sectional velocity profile measured inside a coronary artery, especially in the presence of stenosis (In Figure 7-11 an example of how the cross-sectional velocity profile can vary within one stenosed arterial segment can be seen). The Doppler flow wire studies presented so far assume a parabolic velocity spatial distribution over the cross-section, and their reported results (Gould et al., 1974c) show excellent agreement in cases of straight tubes *in vitro*. In the *in vivo* cases, however, the cross-sectional velocity distribution issue is bypassed by directly comparing flow velocity measurements to the gold standard flow rate, reporting good correlations. When flow wire-based flow rate estimates were compared with the gold standard flow rates the agreement results in consistent underestimation, with the deviation from the line of identity increasing at higher flow rates, a trend observed in the unobstructed tube experiments presented in Figure 7-10. Furthermore, when the *in vitro* experiments were repeated in a pullback through a tube with varying degrees of curvature, underestimations in velocity of more than 5 cm/s were observed in the highly curved areas at two different velocity levels, signifying that in realistic flow conditions flow underestimation is to be expected.

The relationship between the measured velocity V_{wire} and the cross-sectional mean velocity was revised from $0.5*V_{wire}$, as seen in (Gould et al., 1974c), to $0.47*V_{wire}$ by (Gould et al., 1974d), in a first indication that the parabolic profile assumption may not be suitable for *in vivo* flow rate estimation in the coronary arteries, though there are no more studies testing the validity of estimating flow rate from flow wire measurements.

One of the reasons for the lack of flow rate validation studies may be because in modern functional assessment methods for the severity of coronary artery disease such as coronary flow reserve (CFR) and hyperaemic stenosis resistance index (HSR), flow velocities measured using flow wires are used directly in the index calculations. This is done based on the argument that multiple velocity measurements are conducted in one vessel, the cross sectional area and spatial velocity distribution of which do not change from one instance of velocity measurement to the next; under these conditions a change in velocity (for example an increase during maximal vasodilation) can arguably be considered to reliably reflect the change in volumetric flow rate.

Though the use of Combowire or other combined pressure-flow probes are not commonly used to assess coronary lesions in clinical practice, the potential for estimation of the flow rate could prove useful in computational applications attempting to assess pressure gradient in a coronary vessel. In these cases, the volumetric flow rate is a necessary boundary condition in order to create a well-posed mathematical problem. As shown in Chapter 5, small errors in the volumetric flow rate estimation can result in great variation in the pressure gradients calculated by CFD for the same geometrical model, emphasizing the use of accurate estimates of flow rate as a necessary step towards achieving reliable CFD pressure gradient calculations. The errors reported in the studies referred to above and those shown in the experiment results presented in this chapter suggest that, even if a spatial velocity distribution profile could be used universally, great uncertainties remain over flow rate estimations. Based on the sensitivity analysis presented in Figure 7-9, underestimation of the mean volumetric flow rate by 0.70ml/s (the bias shown in the Bland-Altman plot of Figure 7-10) would result in a 10-15% change in pressure drop depending on stenosis severity. A change of this magnitude can potentially change the diagnosis of an intermediate lesion.

7.4.2 Better agreement is observed at lower flow rates

As in the validation studies by Doucette and Chou, the agreement between the Combowire-estimated and the measured volumetric flow rate becomes weaker at higher flow rates, where flow rate is more likely to be markedly underestimated in the Combowire-based estimates (Figure 7-10 and Figure 7-11). A possible explanation for this could be that, at higher flow rates, the velocity profile distribution further deviates from simple assumptions

(such as flat or parabolic), with the influence of geometry being potentially exacerbated by the increase in flow rate, resulting in the formation of jets and the presence of recirculating flow in parts of the cross section. Furthermore, because of the pulsatile nature of coronary flow (Womersley parameter in tubes the size of coronary arteries under physiological pulse conditions can range from 3-8) an increased peak Reynolds number which is still below the transition threshold can result in the increase of laminar disturbances caused by the reversal of the pressure gradients during the flow deceleration phase, also contributing to changes in the cross-sectional profile. The cross-sectional profile can be further modified by the presence of the catheter, as discussed in Chapter 6, leading to greater underestimation of the flow at higher flow rates (Torii et al., 2007).

The flow rates at which agreement with the measurements is best coincide with the flow rates observed most often in the coronary arteries at rest (1-3ml/s). In the unobstructed tube experiment, flow rate underestimation was present at the lowest flow rate, but the measurements were considerably closer to the line of identity at the two higher flow rate levels. In the stenosis experiment shown in Figure 7-11 (left), which was conducted at realistic resting flow rates of less than 2 ml/s, of the five measurements made there were two cases of underestimation and one of overestimation, while two measurements were lying very near the line of identity, resulting in an overall better correlation with the flow probe measurements.

7.4.3 Potential Limitations

The experiment presented in this chapter was small in scale, and resulted in limited number of data points. However, high correlations are observed and useful conclusions could be reached from the analysis of these results.

The circulating fluid chosen for the experiments was a solution of glycerol in water (35% w/w). This mixture was chosen over a blood substitute as it is simple to make and preserve but still matches the viscosity of blood fairly closely (kinematic viscosity of glycerol solution is 3.52e-06 m^2/s to an average value for blood of ~2.7e-06m^2/s), so that the flow conditions (Reynolds number and Womersley parameter) are as close as possible to those found in coronary flow. However, glycerol and water being Newtonian fluids, these

experiments cannot account for blood's non-Newtonian behaviour, though this is not expected to have a significant effect on the accuracy of the flow rate estimates at the shear rates observed in these experiments.

Compliant tubing was used in the experiments, but the two different phantoms used (the unobstructed tube and the stenosis phantom model) had different elastic properties, with the stenosis phantom being stiffer than the unobstructed tube. The changes in cross-sectional area due to wall compliance and flow pulsatility could not be evaluated for either model, and this is a limitation to the experiment. However, the arterial wall is compliant as well, and there are no known ways of measuring coronary arterial wall elasticity *in vivo*. Therefore, this is a limitation that any attempt at estimating volumetric flow rate from flow wire measurements *in vivo* will have to face, and incorporating the effect of compliance in the error may provide a more realistic assessment of the flow wire-based estimates than the rigid wall assumption.

A time-of-flight, perivascular ultrasonic flow-meter was used as the gold standard against which the Combowire-based flow rate estimates were compared. As discussed in previous chapters a gold standard comes with an error margin that must be taken into account when evaluating the results. The errors reported in validation studies for the ultrasonic flow meter against electromagnetic flow meters range from under 10% (Gorewit et al., 1989, Hartman et al., 1994) to 15% *in vivo* (Lundell et al., 1993), though the *in vitro* reported error in the latter study is again lower at ~11%. The variability reported is therefore consistently small, and the flow-meter can be relied on to provide accurate flow rate measurements.

7.5 Summary and Conclusion

In this chapter, the results from a series of bench-top experiments conducted to test the accuracy of volumetric flow rate estimates based on Doppler wire velocities are presented. A flow loop was set up using compliant tubing and a positive displacement pump to produce physiological pulsatile waveforms. A 35%w/w solution of glycerol in water with kinematic viscosity similar to blood was used as circulating fluid. Flow velocity measurements were made using a Volcano Combowire XT, commonly used in clinical practice for the functional assessment of coronary artery disease. Measurements were also

made using a calibrated, time-of-flight perivascular ultrasound flow-meter, which was used as the gold standard against which the Combowire measurements were compared. Two phantom models were tested: a long, unobstructed tube of known diameter, and an idealised model of a coronary artery bifurcation including a 75% area stenosis. Measurements were made at various flow rate levels, ranging from 1-2ml/s (physiological resting conditions) to 10ml/s.

The results from the experiments show that the assumption of a flat spatial velocity distribution when calculating volumetric flow rate from Combowire measurements provides the best agreement with the gold-standard probe measurements in all cases. Even though this goes against the results found by the two flow wire validation studies conducted in the 1990s, it does help explain the better performance of CFD in predicting pressure gradient when working under the flat profile assumption. A discussion as to why there is better agreement under the flat profile assumption is presented in Chapter 5. A good correlation was found between the Combowire-based flow rate estimates and the gold standard (0.84 for the unobstructed tube, 0.93 for the stenosis phantom). The correlation was better at smaller flow rates, while flow rate underestimation by the flow wire was more likely at higher flow rates.

In the case of the phantom stenosis model it was shown that individual flow measurements are equally likely to over- or underestimate the flow rate, resulting in very small average bias. This pattern is similar to that observed in the CFD-based pressure gradient calculations, where individual cases can be over- or underestimated in the CFD results compared to invasive measurements, but the overall bias is near zero. Given the fact that even small changes in volumetric flow rate can havea noticeable effect in the pressure drops observed (as presented in Chapter 6) the similar patterns in the flow rate and CFD-based pressure drop errors could provide a likely cause for the latter.

8. Conclusion and Recommendations

8.1 Main conclusions

One of the main objectives of this project was to investigate the pressure-flow relationship in models of the aortic root and the coronary arteries using computational fluid dynamics (CFD), with a focus on the phenomenon of pressure recovery in cases of aortic stenosis, and the ability of CFD to predict pressure drop in cases of coronary artery disease.

Making use of a mathematical model for laminar-turbulent transition which has been well-established as suitable for use in aortic flow, the potential for a device which maximises pressure recovery by minimising energy losses incurred by the presence of jet formation and separation and turbulence in cases of aortic stenosis was tested. The device has a Venturi-like geometry and was placed inside the aortic root/proximal ascending aorta, starting 10 mm above the valve orifice with a tapering section that captures the jet coming out of the narrowed valve orifice, then gently sloping out towards the aortic wall in an attempt to avoid flow separation and reduce energy lost as turbulence kinetic energy. It was shown that the pressure lost as turbulence kinetic energy in the aortic root can be almost eliminated with the use of the device, which can potentially result in the recovery of more than 50% of the lost pressure

Limitations to the device were, however, identified. Three different valve orifice shapes were investigated, an idealised, circular disk, a triangular shape with rounded angles and the orifice of a patient-specific, heavily calcified valve. In its original position 10 mm from the valve orifice, the efficiency of the device declined with the increasingly realistic valve shapes. Modification of the device to make it a perfectly fitting extension of the patient-specific valve orifice resulted in very high (>50%) levels of pressure recovery, creating a new set of challenges, such as finding ways to accommodate coronary flow.

Given the results presented in this proof-of-concept study, the conclusion was reached that a device taking advantage of pressure recovery to help develop a milder procedure of alleviating aortic stenosis symptoms can result in clinically useful levels of pressure recovery.

However, any potential device will have to either cross or become a continuation of the valve orifice, suggesting that modifications are required in the device to ensure energy lost on the orifice will be recovered too. This would add challenges to the device design, including provision for flow into the coronary arteries. Therefore, it was concluded that this device, with the modifications required to make it clinically applicable, would likely not present an advantage compared to existing procedures.

Fully patient-specific (including anatomical and pressure/flow data) studies of coronary arteries are very few, largely due to the smaller size of the coronary arteries, which can render non-invasive imaging resolution and pressure/flow measurement quality insufficient for use in CFD studies. As stated in the objectives of the thesis, a better understanding of the pressure/flow relationship in the coronary arteries would be useful given the recent studies suggesting that functional assessment of coronary artery disease is associated with better clinical outcomes than the standard anatomical assessment, and CFD could be a valuable tool for that purpose.

The first step towards that direction was to develop a new, quick, semi-automatic algorithm to create accurate 3D reconstructions of coronary anatomy by fusing angiography with optical coherence tomography (OCT). The OCT-derived lumen contours inherit the high image resolution of the state-of-the art intracoronary imaging method, while curvature and tortuosity information are provided by well-established techniques for angiograghy-based reconstruction. The accuracy of the reconstruction technique was tested by creating a virtual 3D model of a stenosis with bifurcation of known geometry and building a phantom model using rapid prototyping. Qualitatively it was found that the reconstructed model followed the shape of the original model accurately, capturing the stenosis position and bifurcation angle. Quantitatively, a small, consistent underestimation of the lumen contour area was found, which, however, is attributed to impurities causing roughness on the inner surface of the phantom model which are not present in the virtual model the reconstruction was compared against.

The next step was to use the reconstructed geometries in fully patient-specific, transient CFD simulations of 21 coronary vessels, in which pressure and flow velocity data acquired invasively in the catheterisation lab were used as boundary conditions. The complicated haemodynamics in the coronary arteries caused by the variable microvascular resistance were implicitly taken into account in the simulations by using pressure as inlet and

flow as outlet boundary conditions. The shape of the resulting distal pressure waveforms followed the measured distal pressure waveforms closely, with correlation coefficients higher than 0.88 in all cases, indicating the successful modelling of resistance in this study. Though the mean of differences between the measured and calculated distal pressure was negligible at ~4 mmHg (<4.5% of the mean distal pressure), the standard deviation was higher than expected at 8mmHg.

The 21 stenoses studied had a mean measured FFR of 0.85 and range from 0.69 to 0.96, with the majority (66.7%) of these falling in the clinically relevant intermediate lesion severity category (FFR = 0.70-0.90). The CFD-predicted FFR was found to have a significant, positive correlation with the measured FFR results ($r = 0.58$, $p = 0.003$). No bias was found between the virtual and actual FFR measurements, but the limits of agreement (±0.16) between the two suggest that uncertainties in the evaluation of an individual lesion's FFR remain. Despite this, there was an agreement of 77% between the severity diagnosis of the measured and predicted FFR, a number which is comparable to the accuracy results of the only existing relevant study (Zarins et al., 2013).

Another important objective of the project was to investigate the parameters which could negatively affect the accuracy of the CFD results in studies of coronary flow. Since the use of CFD in the study of coronary flow developed more recently than other applications of CFD in blood flow -and there are also fewer opportunities for validation of the results- it was considered useful to investigate the sensitivity of the CFD results to the anatomical accuracy of the reconstruction and the volumetric flow rate estimation errors.

For this reason, the anatomies of the 21 vessels originally studied were reconstructed using three different techniques: based on angiography imaging data only, based on OCT imaging data only and using the angiography and OCT fusion algorithm that was developed during this project. This was done in an attempt to evaluate which anatomical features (i.e. lumen shape or curvature/tortuosity) have a greater impact in the CFD FFR outcome. Using the correlation of CFD-predicted FFR to measured FFR, it was found that only the fusion of angiographic and OCT images can produce a virtual anatomy model that can successfully predict measured FFR ($r = 0.58$, $p = 0.003$). In the case of using angiography alone ($r = 0.048$, $p = 0.84$) or OCT alone ($r = 0.12$, $p = 0.6$) no significant correlation was found between the CFD and measured FFR results. This suggests that a highly accurate anatomical model is a requirement for CFD models that hope to be able to predict FFR. The only non-invasive

technique that can currently provide a satisfactory level of geometrical accuracy is 64-slice MD-CT.

The correlation between the CFD-predicted and measured FFR was positive when using the angiography/OCT fusion anatomical model, but it was still lower than expected. A sensitivity analysis to investigate the role that flow rate plays in the CFD-based calculation of FFR was conducted. Three patient-specific anatomies corresponding to a severe, mild and moderate lesion were chosen from the original 21 vessel group and reconstructed using the angiography/OCT fusion algorithm. Steady-state simulations using a 100mmHg fixed pressure at the inlet and varying the volumetric flow rate at the outlet within the physiological limits of flow rates observed in hyparaemic coronary flow were conducted. In all three cases it was shown that varying the flow rate within the physiological range can alter the FFR diagnosis, indicating that the CFD result is very sensitive to flow rate. This result has important implications in potential uses of CFD to predict pressure drop in coronary lesions, as it shows that reliable flow rate measurements are a requirement for accurate results.

This finding, of just how sensitive to flow rate variation the CFD results can be, led to the discussion of potential limitations posed to CFD studies by the fact that the most reliable coronary volumetric flow rate estimation can be made using intracoronary Doppler flow velocity measurements, which comes with a set of limitations and potential pitfalls. An experiment was designed to test the accuracy of flow rate estimated by a Doppler wire against a gold standard perivascular ultrasonic flow-meter in phantom models, an unobstructed tube and a model of idealised coronary anatomy, including a stenosis and bifurcation. Flow velocity measurements were made at various volumetric flow rate levels using a Combowire, a tool commonly used in research of coronary artery disease. It was found that, making use of the flat velocity distribution assumption (assuming that the measured velocity is close to the mean velocity over the cross-section) provides high correlation ($r>0.85$) and good agreement with the flow-meter measurements. Also, it was found that better agreement is observed at lower flow rates, comparable to the flow rates observed in resting coronary flow, whereas at higher flow rates a consistent underestimation was observed. It was also found that, at flow rates close to those observed in the coronary arteries Combowire-based flow estimates can be randomly over or under the measured value, resulting in minimal bias, but relatively wide limits of agreement.

The results from the bench-top experiments appear to indicate that the flat profile assumption will result in the most accurate estimate of the actual volumetric flow rate inside the coronary arteries. This result is consistent with the better performance of the CFD models observed when making the same assumption compared to the more commonly assumed parabolic (Poiseuille) flow spatial velocity distribution. This is contrary to previous validation studies on the subject, which found that the parabolic profile assumption gives the closest agreement with the gold standard measurements.

There are multiple possible reasons for this discrepancy. Looking into the spatial velocity profiles at various cross-sections of the CFD simulation results it is obvious that the relationship between the maximum and mean velocity on a cross-section varies greatly with location, proximity to a stenosis and overall vessel geometry. Furthermore, there are limitations in the flow wire itself, the two most important in this application being spectral broadening (accentuated by the bending of the wire tip by more than 20 degrees in clinical practice), and the potential to miss the maximum velocity if that lies very near the vessel wall and out of the sample volume, a common occurrence in curved vessels. The combination of the two could result in consistent underestimation of the maximum velocity such that the value recorded may be closer to the mean spatial velocity rather than the maximum. None of the previous flow wire validation studies made measurements in cases of stenosis either *in vivo* or *in vitro*, and reported velocity underestimations of ~14% when testing a flow wire in highly curved tubing *in vitro,* which could explain the discrepancy between the results of these experiments and the previous studies.

8.2 Assumptions and Limitations to the study

8.2.1 Assumptions in the CFD simulations

Assumptions on the rheology of blood

In all simulations performed, blood was modelled as Newtonian. As discussed in Chapter 2, blood is a suspension of particles (such as red blood cells and platelets) in plasma, and has complex rheological properties. At low shear rates it behaves as a non-Newtonian fluid, the viscosity of which declines with increasing shear rate. It has been experimentally found that at a shear rate of about 100 s^{-1} blood's viscosity stabilises. Though flow velocities

in the coronary arteries and the aorta exceed this shear rate threshold, it is possible that the Newtonian fluid assumption may not hold in parts of the flow field where there is stagnation, or very low, oscillating flow. However, studies have shown (Lee and Steinman, 2007) that the difference between modelling blood as Newtonian and non-Newtonian are negligible, and the Newtonian behaviour assumption is now standard in CFD simulations of large arteries.

Blood viscosity is a function of red blood cell concentration, or hematocrit, which varies from person to person. Due to lack of hematocrit information for the patients studied, a widely accepted average value of blood viscosity (0.00334 Pa.s) was used. Changes in blood viscosity within the normal hematocrit range are not expected to have a noticeable effect on pressure and flow characteristics.

The rigid wall assumption

Elasticity is a very important property of the arterial wall, and has been widely studied as arterial stiffness is associated with increased risks for cardiovascular diseases. Wall elasticity significantly affects the speed of wave propagation, with noticeable effects on the pressure and flow patterns observed. Coupling CFD with wall mechanics simulations to create fluid-structure interaction (FSI) models of flow in blood vessels is increasing in popularity. However, information on wall properties such as elasticity and thickness is required to realistically model fluid-structure interaction, and this information cannot be easily measured *in vivo*. Therefore, most FSI simulation use generic wall properties measured post-mortem, and not patient-specific ones, even though there is large variation from subject to subject. It has been shown (Torii et al., 2009c, Tan et al., 2009b) that FSI simulations contribute little to the accuracy of flow studies in larger arteries, and, with the increased computational cost of FSI, it is often considered unnecessary.

8.2.2 Limitations of the aortic stenosis study

The study on the aortic stenosis is a preliminary, proof-of-concept study. For this reason, an idealised geometry was used to represent the left ventricular outflow tract, aortic sinuses and proximal ascending aorta, while omitting important anatomical features such as the coronary ostia. The geometry consisted of circular, straight tubes, while the sinuses were assumed to have a symmetric, spherical shape. All simulations were steady-state. The

simplified, idealised design was chosen so that the study could better focus on the effect of the valve orifice shape on the efficiency of the device tested.

8.2.3 Limitations of the coronary artery study

A major limitation of the coronary artery study is the use of single vessel models, omitting flow lost to branches and collateral flow. This is a limitation inherited by the inability of OCT and other intracoronary imaging techniques to visualise more than one vessel at a time. Errors may also be introduced through the imaging methods used, including the use of serial monoplane angiography, and the assumption that the OCT-derived lumen contours are perpendicular to the vessel centreline and the application of a uniform in-plane rotation angle throughout the vessel. Moreover, there is a degree of uncertainty in determining the exact location of the FFR and flow velocity measurements used as boundary conditions. Because of this, it is possible that errors in the estimation of the volumetric flow rate from velocity measurements arising from uncertainty over the cross-sectional area of the measurement location are possible.

8.2.4 Limitations of the flow experiment study

The major limitation of the bench-top experiment study was its small size. Even though the high correlation coefficient observed helped achieve statistical significance in the unobstructed tube study, the fact remains that the number of experimental points ($n = 14$ for the unobstructed tube and $n = 5$ for the stenosis model) was low and all conclusions from this study can only be considered preliminary. However, they could provide incentive for larger scale studies investigating the accuracy of volumetric flow rate estimates based on flow wire velocity measurements, updated for the potential methodology pitfalls and limitations highlighted by these experiments.

8.3 Recommendations for future work

8.3.1 Pressure recovery in aortic stenosis

As demonstrated by the result presented in Chapter 3, a realistic application of a Venturi-shaped device promoting pressure recovery in cases of aortic valve stenosis would have to cross/remodel the valve. This presents a set of difficulties, however, because crossing the valve is a more invasive procedure than simply placing a device inside the ascending aorta.

The device design as presented in this thesis does not appear to present advantages over the currently available treatment options. It is, therefore, suggested that more detailed study into the design, potential benefits and application challenges of a pressure-recovering device should be conducted before revisiting this concept.

8.3.2 Coronary flow studies

Non-invasively assessing the functional severity of coronary artery disease using CFD is a very attractive idea which has been gaining in popularity in recent years. The concept of using patient-specific anatomical data and assumptions on flow and pressure as boundary conditions has the potential to result in useful clinical results (such as the FFR index) without the need for intracoronary pressure and flow velocity measurements. However an investigation into the potential pitfalls of the new method was necessary to establish the limits of reliability of using the CFD method.

The results of the CFD studies presented in Chapters 4 and 5 indicate that the quality of the anatomical and functional data used can have a significant effect on the accuracy of the CFD result. In particular, only with the use of anatomical reconstructions of high fidelity based on high resolution imaging data were CFD-derived values of FFR positively correlated with the measured values. Omitting vessel curvature and tortuosity, or using lower-resolution images which cannot well define lumen contours result in less than optimal results. Moreover, it was shown that the CFD-derived FFR result is sensitive to changes of volumetric flow rate which are within the hyparaemic physiological range, putting into

question the use of generic, or averaged, flow rate data as boundary conditions in CFD-based calculations of FFR.

There is currently no way of obtaining reliable flow velocity measurements in the coronary arteries non-invasively, and as it was shown in the experiments of Chapter 6 estimating volumetric flow rate from intracoronary Doppler flow velocity can result in errors too. Therefore, the need for reliable, patient-specific flow rate is an important limitation of CFD which may not be easily overcome in the near future. Recent studies have shown that the hyperaemic flow conditions stipulated as a requirement in the original experiments may not be necessary to assess coronary function, while it has also been shown that there is smaller variability in the flow rates observed in the wave-free diastolic period when peak flow occurs, which can be considered to be 20%-30% more than the mean baseline flow. Consequently, using the hyperaemia-free iFR index as the functional assessment test simulated with CFD may reduce the flow rate variability and may therefore help overcome the flow rate limitation of CFD coronary studies.

The limitations and challenges discussed in this thesis are not unique to the proposed methodology, but face all of the technologies and methodologies which try to address the problems of computational modelling of the coronary arteries. Almost all measures in clinical practice come with considerable variability. Common measures such as blood pressure vary by more than 15% when made in clinic, and FFR specifically has been shown to change classification 15% of the time when measured by world experts 10 minutes apart. Even clinical technologies with FDA approval make approximations which to the eyes of the CFD modeller may appear troublesome.

The question we face moving forward is not necessarily if we need to strive for engineering perfection, but rather whether it is possible to add significant benefit to clinical diagnostics in a cost-effective and timely manner. This may, on occasion, mean that simplifications in methodologies may be made that will result in less accurate models, but which might provide a stepping stone to accelerate development.

References

AKERSTROM, F., BARDERAS, M. G. & RODRIGUEZ-PADIAL, L. 2013. Aortic stenosis: a general overview of clinical, pathophysiological and therapeutic aspects. *Expert Rev Cardiovasc Ther,* 11**,** 239-50.

ALFONSI, G. 2009. Reynolds-Averaged Navier-Stokes Equations for Turbulence Modeling. *Applied Mechanics Reviews,* 62.

ALTMAN, D. G. & BLAND, J. M. 1983. Measurement in Medicine - the Analysis of Method Comparison Studies. *Statistician,* 32**,** 307-317.

ATHANASIOU, L. S., BOURANTAS, C. V., SIOGKAS, P. K., SAKELLARIOS, A. I., EXARCHOS, T. P., NAKA, K. K., PAPAFAKLIS, M. I., MICHALIS, L. K., PRATI, F. & FOTIADIS, D. I. 2012. 3D reconstruction of coronary arteries using Frequency Domain Optical Coherence Tomography images and biplane angiography. *Conf Proc IEEE Eng Med Biol Soc,* 2012**,** 2647-50.

BANERJEE, R. K., BACK, L. H., BACK, M. R. & CHO, Y. I. 1999. Catheter obstruction effect on pulsatile flow rate--pressure drop during coronary angioplasty. *J Biomech Eng,* 121**,** 281-9.

BANERJEE, R. K., BACK, L. H., BACK, M. R. & CHO, Y. I. 2000. Physiological flow simulation in residual human stenoses after coronary angioplasty. *J Biomech Eng,* 122**,** 310-20.

BARK, D. L., JR. & KU, D. N. 2010. Wall shear over high degree stenoses pertinent to atherothrombosis. *J Biomech,* 43**,** 2970-7.

BAUMGARTNER, H., HUNG, J., BERMEJO, J., CHAMBERS, J. B., EVANGELISTA, A., GRIFFIN, B. P., IUNG, B., OTTO, C. M., PELLIKKA, P. A., QUINONES, M. & EAE/ASE 2009. Echocardiographic assessment of valve stenosis: EAE/ASE recommendations for clinical practice. *Eur J Echocardiogr,* 10**,** 1-25.

BERDAJS, D., LAJOS, P. & TURINA, M. 2002. The anatomy of the aortic root. *Cardiovasc Surg,* 10**,** 320-7.

BIGLINO, G., VERSCHUEREN, P., ZEGELS, R., TAYLOR, A. M. & SCHIEVANO, S. 2013. Rapid prototyping compliant arterial phantoms for in-vitro studies and device testing. *Journal of Cardiovascular Magnetic Resonance,* 15.

BILEN, E., SARI, C., DURMAZ, T., KELES, T., BAYRAM, N. A., AKCAY, M., AYHAN, H. M. & BOZKURT, E. 2014. The importance of echocardiography in transcatheter aortic valve implantation. *Echocardiography,* 31**,** 101-10.

BLOOMFIELD, R. A., LAUSON, H. D. & ET AL. 1946. Recording of right heart pressures in normal subjects and in patients with chronic pulmonary disease and various types of cardio-circulatory disease. *J Clin Invest,* 25**,** 639-64.

BOGREN, H. G. & BUONOCORE, M. H. 1999. 4D magnetic resonance velocity mapping of blood flow patterns in the aorta in young vs. elderly normal subjects. *J Magn Reson Imaging,* 10**,** 861-9.

BONOW, R. O., CARABELLO, B. A., KANU, C., DE LEON, A. C., JR., FAXON, D. P., FREED, M. D., GAASCH, W. H., LYTLE, B. W., NISHIMURA, R. A., O'GARA, P. T., O'ROURKE, R. A., OTTO, C. M., SHAH, P. M., SHANEWISE, J. S., SMITH, S. C., JR., JACOBS, A. K., ADAMS, C. D., ANDERSON, J. L., ANTMAN, E. M., FUSTER, V., HALPERIN, J. L., HIRATZKA, L. F., HUNT, S. A., NISHIMURA, R., PAGE, R. L. & RIEGEL, B. 2006. ACC/AHA 2006 guidelines for the management of patients with valvular heart disease: a report of the American College of Cardiology/American Heart Association Task Force on Practice Guidelines (writing committee to revise the 1998 Guidelines for the Management of Patients With Valvular Heart Disease): developed in collaboration with the Society of Cardiovascular Anesthesiologists: endorsed by the Society

for Cardiovascular Angiography and Interventions and the Society of Thoracic Surgeons. *Circulation,* 114**,** e84-231.

BORYCZKO, K., DZWINEL, W. & YUEN, D. A. 2003. Dynamical clustering of red blood cells in capillary vessels. *Journal of Molecular Modeling,* 9**,** 16-33.

BOURANTAS, C. V., PAPAFAKLIS, M. I., LAKKAS, L., SAKELLARIOS, A., ONUMA, Y., ZHANG, Y. J., MURAMATSU, T., DILETTI, R., BIZOPOULOS, P., KALATZIS, F., NAKA, K. K., FOTIADIS, D. I., WANG, J., GARCIA GARCIA, H. M., KIMURA, T., MICHALIS, L. K. & SERRUYS, P. W. 2014. Fusion of optical coherence tomographic and angiographic data for more accurate evaluation of the endothelial shear stress patterns and neointimal distribution after bioresorbable scaffold implantation: comparison with intravascular ultrasound-derived reconstructions. *Int J Cardiovasc Imaging,* 30**,** 485-94.

BOURANTAS, C. V., PAPAFAKLIS, M. I., NAKA, K. K., TSAKANIKAS, V. D., LYSITSAS, D. N., ALAMGIR, F. M., FOTIADIS, D. I. & MICHALIS, L. K. 2012a. Fusion of optical coherence tomography and coronary angiography - In vivo assessment of shear stress in plaque rupture. *International Journal of Cardiology,* 155**,** E24-E26.

BOURANTAS, C. V., PAPAFAKLIS, M. I., NAKA, K. K., TSAKANIKAS, V. D., LYSITSAS, D. N., ALAMGIR, F. M., FOTIADIS, D. I. & MICHALIS, L. K. 2012b. Fusion of optical coherence tomography and coronary angiography - in vivo assessment of shear stress in plaque rupture. *Int J Cardiol,* 155**,** e24-6.

BOUVIER, E., LOGEART, D., SABLAYROLLES, J. L., FEIGNOUX, J., SCHEUBLE, C., TOUCHE, T., THABUT, G. & COHEN-SOLAL, A. 2006. Diagnosis of aortic valvular stenosis by multislice cardiac computed tomography. *Eur Heart J,* 27**,** 3033-8.

BROYD, C. J., SEN, S., MIKHAIL, G. W., FRANCIS, D. P., MAYET, J. & DAVIES, J. E. 2013. Myocardial ischemia in aortic stenosis: insights from arterial pulse-wave dynamics after percutaneous aortic valve replacement. *Trends Cardiovasc Med,* 23**,** 185-91.

CAMUGLIA, A. C., SYED, J., GARG, P., KIAII, B., CHU, M. W., JONES, P. M., BAINBRIDGE, D. & TEEFY, P. J. 2013. Invasively assessed coronary flow dynamics improve following relief of aortic stenosis with transcatheter aortic valve implantation. *J Am Coll Cardiol*.

CARDENES, R. 2012. 3D Reconstruction of coronary arteries from rotational X-ray angiography. 9th IEEE International Symposium on Biomedical Imaging, 2-5 May 2012 2012 Barcelona. 618 - 621

CARDENES, R., DIEZ, J. L., LARRABIDE, I., BOGUNOVIC, H. & FRANGI, A. F. 2011. 3D Modeling of Coronary Artery Bifurcations from CTA and Conventional Coronary Angiography. *Medical Image Computing and Computer-Assisted Intervention, Miccai 2011, Pt Iii,* 6893**,** 395-402.

CARO, C. G., FITZ-GERALD, J. M. & SCHROTER, R. C. 1969. Arterial wall shear and distribution of early atheroma in man. *Nature,* 223**,** 1159-60.

CASE, J. A. & BATEMAN, T. M. 2013. Taking the perfect nuclear image: quality control, acquisition, and processing techniques for cardiac SPECT, PET, and hybrid imaging. *J Nucl Cardiol,* 20**,** 891-907.

CASSAR, A., MATSUO, Y., HERRMANN, J., LI, J., LENNON, R. J., GULATI, R., LERMAN, L. O., KUSHWAHA, S. S. & LERMAN, A. 2013. Coronary atherosclerosis with vulnerable plaque and complicated lesions in transplant recipients: new insight into cardiac allograft vasculopathy by optical coherence tomography. *Eur Heart J,* 34**,** 2610-7.

CHAMULEAU, S. A. J., SIEBES, M., MEUWISSEN, M., KOCH, K. T., SPAAN, J. A. E. & PIEK, J. J. 2003. Association between coronary lesion severity and distal microvascular resistance in patients with coronary artery disease. *American Journal of Physiology-Heart and Circulatory Physiology,* 285**,** H2194-H2200.

CHOMA, M., SARUNIC, M., YANG, C. & IZATT, J. 2003. Sensitivity advantage of swept source and Fourier domain optical coherence tomography. *Opt Express,* 11**,** 2183-9.

CHOU, T. M., SUDHIR, K., IWANAGA, S., CHATTERJEE, K. & YOCK, P. G. 1994. Measurement of volumetric coronary blood flow by simultaneous intravascular two-dimensional and Doppler ultrasound: validation in an animal model. *American Heart Journal,* 128**,** 237-43.

CHRISTOU, M. A., SIONTIS, G. C., KATRITSIS, D. G. & IOANNIDIS, J. P. 2007. Meta-analysis of fractional flow reserve versus quantitative coronary angiography and noninvasive imaging for evaluation of myocardial ischemia. *Am J Cardiol,* 99**,** 450-6.

CHUA, C. K., GAN, J. G. K. & TONG, M. 1997. Interface between CAD and Rapid Prototyping systems .1. A study of existing interfaces. *International Journal of Advanced Manufacturing Technology,* 13**,** 566-570.

CILINGIROGLU, M., HAKEEM, A., FELDMAN, M. & WHOLEY, M. 2012. Optical coherence tomography imaging in asymptomatic patients with carotid artery stenosis. *Cardiovasc Revasc Med*.

CLAESSENS, T. E., VAN HERCK, P. L., MATTHYS, K. S., SEGERS, P., VRINTS, C. J. & VERDONCK, P. R. 2004. Influence of zero flow pressure on fractional flow reserve. *Biomech Model Mechanobiol,* 3**,** 48-55.

CLARK, C. 1976a. The fluid mechanics of aortic stenosis--I. Theory and steady flow experiments. *J Biomech,* 9**,** 521-8.

CLARK, C. 1976b. The fluid mechanics of aortic stenosis - II. Unsteady flow experiments. *J Biomech,* 9**,** 567-73.

CLARK, C. 1976c. Turbulent velocity measurements in a model of aortic stenosis. *J Biomech,* 9**,** 677-87.

COWELL, S. J., NEWBY, D. E., PRESCOTT, R. J., BLOOMFIELD, P., REID, J., NORTHRIDGE, D. B. & BOON, N. A. 2005. A randomized trial of intensive lipid-lowering therapy in calcific aortic stenosis. *N Engl J Med,* 352**,** 2389-97.

CRIBIER, A., ELTCHANINOFF, H., BASH, A., BORENSTEIN, N., TRON, C., BAUER, F., DERUMEAUX, G., ANSELME, F., LABORDE, F. & LEON, M. B. 2002. Percutaneous transcatheter implantation of an aortic valve prosthesis for calcific aortic stenosis: first human case description. *Circulation,* 106**,** 3006-8.

DASH, R. K., JAYARAMAN, G. & MEHTA, K. N. 1999. Flow in a catheterized curved artery with stenosis. *J Biomech,* 32**,** 49-61.

DAVIES, J. E., PARKER, K. H., FRANCIS, D. P., HUGHES, A. D. & MAYET, J. 2008. What is the role of the aorta in directing coronary blood flow? *Heart,* 94**,** 1545-7.

DAVIES, J. E., SEN, S., BROYD, C., HADJILOIZOU, N., BAKSI, J., FRANCIS, D. P., FOALE, R. A., PARKER, K. H., HUGHES, A. D., CHUKWUEMEKA, A., CASULA, R., MALIK, I. S., MIKHAIL, G. W. & MAYET, J. 2011. Arterial pulse wave dynamics after percutaneous aortic valve replacement: fall in coronary diastolic suction with increasing heart rate as a basis for angina symptoms in aortic stenosis. *Circulation,* 124**,** 1565-72.

DAVIES, J. E., WHINNETT, Z. I., FRANCIS, D. P., MANISTY, C. H., AGUADO-SIERRA, J., WILLSON, K., FOALE, R. A., MALIK, I. S., HUGHES, A. D., PARKER, K. H. & MAYET, J. 2006. Evidence of a dominant backward-propagating "suction" wave responsible for diastolic coronary filling in humans, attenuated in left ventricular hypertrophy. *Circulation,* 113**,** 1768-78.

DAVIES, P. F. 2009. Hemodynamic shear stress and the endothelium in cardiovascular pathophysiology. *Nat Clin Pract Cardiovasc Med,* 6**,** 16-26.

DE BRUYNE, B., BARTUNEK, J., SYS, S. U., PIJLS, N. H., HEYNDRICKX, G. R. & WIJNS, W. 1996. Simultaneous coronary pressure and flow velocity measurements in humans. Feasibility, reproducibility, and hemodynamic dependence of coronary flow velocity reserve, hyperemic flow versus pressure slope index, and fractional flow reserve. *Circulation,* 94**,** 1842-9.

DE BRUYNE, B., BAUDHUIN, T., MELIN, J. A., PIJLS, N. H., SYS, S. U., BOL, A., PAULUS, W. J., HEYNDRICKX, G. R. & WIJNS, W. 1994a. Coronary flow reserve calculated from pressure measurements in humans. Validation with positron emission tomography. *Circulation,* 89**,** 1013-22.

DE BRUYNE, B., FEARON, W. F., PIJLS, N. H., BARBATO, E., TONINO, P., PIROTH, Z., JAGIC, N., MOBIUS-WINCKLER, S., RIOUFOL, G., WITT, N., KALA, P., MACCARTHY, P., ENGSTROM, T., OLDROYD, K., MAVROMATIS, K., MANOHARAN, G., VERLEE, P., FROBERT, O., CURZEN, N., JOHNSON, J. B., LIMACHER, A., NUESCH, E., JUNI, P. & INVESTIGATORS, F. T. 2014. Fractional flow reserve-guided PCI for stable coronary artery disease. *N Engl J Med,* 371**,** 1208-17.

DE BRUYNE, B., PAULUS, W. J. & PIJLS, N. H. 1994b. Rationale and application of coronary transstenotic pressure gradient measurements. *Cathet Cardiovasc Diagn,* 33**,** 250-61.

DE BRUYNE, B., PIJLS, N. H., KALESAN, B., BARBATO, E., TONINO, P. A., PIROTH, Z., JAGIC, N., MOBIUS-WINKLER, S., RIOUFOL, G., WITT, N., KALA, P., MACCARTHY, P., ENGSTROM, T., OLDROYD, K. G., MAVROMATIS, K., MANOHARAN, G., VERLEE, P., FROBERT, O., CURZEN, N., JOHNSON, J. B., JUNI, P., FEARON, W. F. & INVESTIGATORS, F. T. 2012. Fractional flow reserve-guided PCI versus medical therapy in stable coronary disease. *N Engl J Med,* 367**,** 991-1001.

DE BRUYNE, B., PIJLS, N. H., SMITH, L., WIEVEGG, M. & HEYNDRICKX, G. R. 2001. Coronary thermodilution to assess flow reserve: experimental validation. *Circulation,* 104**,** 2003-6.

DE CESARE, N. B., ELLIS, S. G., WILLIAMSON, P. R., DEBOE, S. F., PITT, B. & MANCINI, G. B. 1993. Early reocclusion after successful thrombolysis is related to lesion length and roughness. *Coron Artery Dis,* 4**,** 159-66.

DEBAKEY, M. E., LAWRIE, G. M. & GLAESER, D. H. 1985. Patterns of atherosclerosis and their surgical significance. *Ann Surg,* 201**,** 115-31.

DEGROFF, C. G., SHANDAS, R. & VALDES-CRUZ, L. 1998. Analysis of the effect of flow rate on the Doppler continuity equation for stenotic orifice area calculations: a numerical study. *Circulation,* 97**,** 1597-605.

DEUSSEN, A., OHANYAN, V., JANNASCH, A., YIN, L. & CHILIAN, W. 2012. Mechanisms of metabolic coronary flow regulation. *J Mol Cell Cardiol,* 52**,** 794-801.

DEWAN, A. 2011. Tackling turbulent flows in engineering. Berlin ; Heidelberg: Springer,.

DEWEY, T. M., BROWN, D. L., HERBERT, M. A., CULICA, D., SMITH, C. R., LEON, M. B., SVENSSON, L. G., TUZCU, M., WEBB, J. G., CRIBIER, A. & MACK, M. J. 2010. Effect of concomitant coronary artery disease on procedural and late outcomes of transcatheter aortic valve implantation. *Ann Thorac Surg,* 89**,** 758-67; discussion 767.

DICARLI, M., CZERNIN, J., HOH, C. K., GERBAUDO, V. H., BRUNKEN, R. C., HUANG, S. C., PHELPS, M. E. & SCHELBERT, H. R. 1995. Relation among Stenosis Severity, Myocardial Blood-Flow, and Flow Reserve in Patients with Coronary-Artery Disease. *Circulation,* 91**,** 1944-1951.

DING, Z., ZHU, H. & FRIEDMAN, M. H. 2002. Coronary artery dynamics in vivo. *Ann Biomed Eng,* 30**,** 419-29.

DOH, J. H., KOO, B. K., NAM, C. W., KIM, J. H., MIN, J. K., NAKAZATO, R., SILALAHI, T., PRAWIRA, H., CHOI, H., LEE, S. Y., NAMGUNG, J., KWON, S. U., KWAK, J. J. & LEE, W. R. 2014. Diagnostic value of coronary CT angiography in comparison with invasive coronary angiography and intravascular ultrasound in patients with intermediate coronary artery stenosis: results from the prospective multicentre FIGURE-OUT (Functional Imaging criteria for GUiding REview of invasive coronary angiOgraphy, intravascular Ultrasound, and coronary computed Tomographic angiography) study. *Eur Heart J Cardiovasc Imaging,* 15**,** 870-7.

DOHI, T., MAEHARA, A., MORENO, P. R., BABER, U., KOVACIC, J. C., LIMAYE, A. M., ALI, Z. A., SWEENY, J. M., MEHRAN, R., DANGAS, G. D., XU, K., SHARMA, S. K., MINTZ, G. S. & KINI, A. S. 2014. The relationship among extent of lipid-rich plaque, lesion characteristics, and plaque progression/regression in patients with coronary artery disease: a serial near-infrared spectroscopy and intravascular ultrasound study. *Eur Heart J Cardiovasc Imaging*.

DOLAN, J. M., KOLEGA, J. & MENG, H. 2013. High wall shear stress and spatial gradients in vascular pathology: a review. *Ann Biomed Eng,* 41**,** 1411-27.

DOTTER, C. T., JUDKINS, M. P. & ROSCH, J. 1967. Nonoperative treatment of arterial occlusive disease: a radiologically facilitated technique. *Radiol Clin North Am,* 5**,** 531-42.

DOUCETTE, J. W., CORL, P. D., PAYNE, H. M., FLYNN, A. E., GOTO, M., NASSI, M. & SEGAL, J. 1992. Validation of a Doppler guide wire for intravascular measurement of coronary artery flow velocity. *Circulation,* 85**,** 1899-911.

DOWD, C. F., PHATOUROS, C. C., MALEK, A. M., LEMPERT, T. E., MEYERS, P. M., HALBACH, V. V. & HIGASHIDA, R. T. 1999. Embolization of non-ruptured aneurysms. *Interv Neuroradiol,* 5 Suppl 1**,** 93-6.

DURHAM, M. 2003. Rapid prototyping - Stereolithography, selective laser sintering, and polyjet. *Advanced Materials & Processes,* 161**,** 40-42.

FALK, E. 2006. Pathogenesis of atherosclerosis. *J Am Coll Cardiol,* 47**,** C7-12.

FALLEN, E. L., ELLIOTT, W. C. & GORLIN, R. 1967. Mechanisms of angina in aortic stenosis. *Circulation,* 36**,** 480-8.

FARD, A. M., VACAS-JACQUES, P., HAMIDI, E., WANG, H., CARRUTH, R. W., GARDECKI, J. A. & TEARNEY, G. J. 2013. Optical coherence tomography--near infrared spectroscopy system and catheter for intravascular imaging. *Opt Express,* 21**,** 30849-58.

FEARON, W. F., TONINO, P. A., DE BRUYNE, B., SIEBERT, U. & PIJLS, N. H. 2007a. Rationale and design of the Fractional Flow Reserve versus Angiography for Multivessel Evaluation (FAME) study. *American Heart Journal,* 154**,** 632-6.

FEARON, W. F., TONINO, P. A. L., DE BRUYNE, B., SIEBERT, U. & PIJLS, N. H. J. 2007b. Rationale and design of the fractional flow reserve versus angiography for multivessel evaluation (FAME) study (vol 154, pg 632, 2007). *American Heart Journal,* 154**,** 1243-1243.

FEIGL, E. O. 1983. Coronary physiology. *Physiol Rev,* 63**,** 1-205.

FENG, T., YUNDAI, C., HONGBIN, L., LIAN, C., ZHIJUN, S., JUN, G., QINHUA, J. & TAO, Z. 2013. Evaluation neointimal coverage in patients with coronary artery aneurysm formation after drug-eluting stent implantation by optical coherence tomography. *Int J Cardiovasc Imaging,* 29**,** 1677-83.

FOIN, N., GUTIERREZ-CHICO, J. L., NAKATANI, S., TORII, R., BOURANTAS, C. V., SEN, S., NIJJER, S., PETRACO, R., KOUSERA, C., GHIONE, M., ONUMA, Y., GARCIA-GARCIA, H. M., FRANCIS, D. P., WONG, P., DI MARIO, C., DAVIES, J. E. & SERRUYS, P. W. 2014. Incomplete stent apposition causes high shear flow disturbances and delay in neointimal coverage as a function of strut to wall detachment distance: implications for the management of incomplete stent apposition. *Circ Cardiovasc Interv,* 7**,** 180-9.

FREEMAN, R. V. & OTTO, C. M. 2005. Spectrum of calcific aortic valve disease: pathogenesis, disease progression, and treatment strategies. *Circulation,* 111**,** 3316-26.

FUKUHARA, M., ARIMA, H., NINOMIYA, T., HATA, J., HIRAKAWA, Y., DOI, Y., YONEMOTO, K., MUKAI, N., NAGATA, M., IKEDA, F., MATSUMURA, K., KITAZONO, T. & KIYOHARA, Y. 2013. White-coat and masked hypertension are associated with carotid atherosclerosis in a general population: the Hisayama study. *Stroke,* 44**,** 1512-7.

GAO, S. & GENG, Y. J. 2013. LOX-1: A male hormone-regulated scavenger receptor for atherosclerosis. *Vascul Pharmacol,* 59**,** 138-43.

GE, L., JONES, S. C., SOTIROPOULOS, F., HEALY, T. M. & YOGANATHAN, A. P. 2003. Numerical simulation of flow in mechanical heart valves: grid resolution and the assumption of flow symmetry. *J Biomech Eng,* 125**,** 709-18.

GERDTS, M. T. L. A. E. 2011. *Contrast Echocardiographyin Coronary Artery Disease*, InTech.

GIBSON, C. M., CANNON, C. P., DALEY, W. L., DODGE, J. T., JR., ALEXANDER, B., JR., MARBLE, S. J., MCCABE, C. H., RAYMOND, L., FORTIN, T., POOLE, W. K. & BRAUNWALD, E. 1996. TIMI frame count: a quantitative method of assessing coronary artery flow. *Circulation,* 93**,** 879-88.

GIJSEN, F. J., SCHUURBIERS, J. C., VAN DE GIESSEN, A. G., SCHAAP, M., VAN DER STEEN, A. F. & WENTZEL, J. J. 2014. 3D reconstruction techniques of human coronary bifurcations for shear stress computations. *J Biomech,* 47**,** 39-43.

GILON, D., CAPE, E. G., HANDSCHUMACHER, M. D., SONG, J. K., SOLHEIM, J., VANAUKER, M., KING, M. E. & LEVINE, R. A. 2002. Effect of three-dimensional valve shape on the hemodynamics of

aortic stenosis: three-dimensional echocardiographic stereolithography and patient studies. *J Am Coll Cardiol,* 40**,** 1479-86.
GIRASIS, C., SCHUURBIERS, J. C., ONUMA, Y., ABEN, J. P., WEIJERS, B., BOERSMA, E., WENTZEL, J. J. & SERRUYS, P. W. 2011. Two-dimensional quantitative coronary angiographic models for bifurcation segmental analysis: in vitro validation of CAAS against precision manufactured plexiglas phantoms. *Catheter Cardiovasc Interv,* 77**,** 830-9.
GIRASSOLLI, A., CARRIZO, S., JIMENEZ-VALERO, S., SANCHEZ RECALDE, A., RUIZ GARCIA, J., GALEOTTE, G. & MORENO, R. 2013. Utility of optical coherence tomography and intravascular ultrasound for the evaluation of coronary lesions. *Rev Port Cardiol,* 32**,** 925-9.
GLASS, C. K. & WITZTUM, J. L. 2001. Atherosclerosis. the road ahead. *Cell,* 104**,** 503-16.
GLOWINSKA, B., URBAN, M., KOPUT, A. & GALAR, M. 2003. New atherosclerosis risk factors in obese, hypertensive and diabetic children and adolescents. *Atherosclerosis,* 167**,** 275-86.
GOITEIN, O., BEIGEL, R., MATETZKY, S., KUPERSTEIN, R., BROSH, S., ESHET, Y., DI SEGNI, E. & KONEN, E. 2011. Prospectively gated coronary computed tomography angiography: uncompromised quality with markedly reduced radiation exposure in acute chest pain evaluation. *Isr Med Assoc J,* 13**,** 463-7.
GOLDSTEIN, J. A., MAINI, B., DIXON, S. R., BRILAKIS, E. S., GRINES, C. L., RIZIK, D. G., POWERS, E. R., STEINBERG, D. H., SHUNK, K. A., WEISZ, G., MORENO, P. R., KINI, A., SHARMA, S. K., HENDRICKS, M. J., SUM, S. T., MADDEN, S. P., MULLER, J. E., STONE, G. W. & KERN, M. J. 2011. Detection of lipid-core plaques by intracoronary near-infrared spectroscopy identifies high risk of periprocedural myocardial infarction. *Circ Cardiovasc Interv,* 4**,** 429-37.
GONZALO, N., GARCIA-GARCIA, H. M., SERRUYS, P. W., COMMISSARIS, K. H., BEZERRA, H., GOBBENS, P., COSTA, M. & REGAR, E. 2009. Reproducibility of quantitative optical coherence tomography for stent analysis. *EuroIntervention,* 5**,** 224-32.
GOREWIT, R. C., AROMANDO, M. C. & BRISTOL, D. G. 1989. Measuring Bovine Mammary-Gland Blood-Flow Using a Transit-Time Ultrasonic Flow Probe. *Journal of Dairy Science,* 72**,** 1918-1928.
GOUBERGRITS, L., WELLNHOFER, E., KERTZSCHER, U., AFFELD, K., PETZ, C. & HEGE, H. C. 2009. Coronary artery WSS profiling using a geometry reconstruction based on biplane angiography. *Ann Biomed Eng,* 37**,** 682-91.
GOULD, K. L. 1978a. Pressure-Flow Characteristics of Coronary Stenoses in Unsedated Dogs at Rest and during Coronary Vasodilation. *Circulation Research,* 43**,** 242-253.
GOULD, K. L. 1978b. Pressure-flow characteristics of coronary stenoses in unsedated dogs at rest and during coronary vasodilation. *Circ Res,* 43**,** 242-53.
GOULD, K. L. & KELLEY, K. O. 1982. Physiological significance of coronary flow velocity and changing stenosis geometry during coronary vasodilation in awake dogs. *Circ Res,* 50**,** 695-704.
GOULD, K. L. & LIPSCOMB, K. 1974a. Effects of coronary stenoses on coronary flow reserve and resistance. *Am J Cardiol,* 34**,** 48-55.
GOULD, K. L. & LIPSCOMB, K. 1974b. Effects of Coronary Stenoses on Coronary Flow Reserve and Resistance. *American Journal of Cardiology,* 34**,** 48-55.
GOULD, K. L., LIPSCOMB, K. & HAMILTON, G. W. 1974a. Physiologic Basis for Assessing Critical Coronary Stenosis - Instantaneous Flow Response and Regional Distribution during Coronary Hyperemia as Measures of Coronary Flow Reserve. *American Journal of Cardiology,* 33**,** 87-94.
GOULD, K. L., LIPSCOMB, K. & HAMILTON, G. W. 1974b. Physiologic basis for assessing critical coronary stenosis. Instantaneous flow response and regional distribution during coronary hyperemia as measures of coronary flow reserve. *Am J Cardiol,* 33**,** 87-94.
GOULD, L., REDDY, C. V., YACOB, U., TEICH, M., DEMARTINO, A., DEPALMA, D. & GOMPRECHT, R. F. 1974c. Perforation of the tricuspid valve by a transvenous pacemaker. *JAMA,* 230**,** 86-7.

GOULD, R. P., SELWOOD, L., DAY, A. & WOLPERT, L. 1974d. The mechanism of cellular orientation during early cartilage formation in the chick limb and regenerating amphibian limb. *Exp Cell Res,* 83**,** 287-96.

GRONENSCHILD, E., JANSSEN, J. & TIJDENS, F. 1994. CAAS. II: A second generation system for off-line and on-line quantitative coronary angiography. *Cathet Cardiovasc Diagn,* 33**,** 61-75.

GROVES, E. M., SETO, A. H. & KERN, M. J. 2014. Invasive testing for coronary artery disease: FFR, IVUS, OCT, NIRS. *Cardiol Clin,* 32**,** 405-17.

GRUENTZIG, A. R. & MEIER, B. 1983. Percutaneous transluminal coronary angioplasty. The first five years and the future. *Int J Cardiol,* 2**,** 319-23.

GUAGLIUMI, G., SIRBU, V., PETROFF, C., CAPODANNO, D., MUSUMECI, G., YAMAMOTO, H., ELBASIONY, A., BRUSHETT, C., MATIASHVILI, A., LORTKIPANIDZE, N., VALSECCHI, O., BEZERRA, H. G. & SCHMITT, J. M. 2013. Volumetric assessment of lesion severity with optical coherence tomography: relationship with fractional flow reserve. *EuroIntervention,* 8**,** 1172-1181.

HAJATI, O., ZARRABI, K., KARIMI, R. & HAJATI, A. 2012. CFD simulation of hemodynamics in sequential and individual coronary bypass grafts based on multislice CT scan datasets. *Conf Proc IEEE Eng Med Biol Soc,* 2012**,** 641-4.

HALON, D. A., RUBINSHTEIN, R., SHIRAN, A. & LEWIS, B. S. 2006. Resolution of an intra-coronary filling defect in the proximal left anterior descending coronary artery demonstrated by 64-slice multi-detector computed tomography. *Catheter Cardiovasc Interv,* 67**,** 246-9.

HARTMAN, J. C., OLSZANSKI, D. A., HULLINGER, T. G. & BRUNDEN, M. N. 1994. In vivo validation of a transit-time ultrasonic volume flow meter. *J Pharmacol Toxicol Methods,* 31**,** 153-60.

HAYASHI, H. & YAMAGUCHI, T. 2002. A simple computational model of the right coronary artery on the beating heart--effects of the temporal change of curvature and torsion on the blood flow. *Biorheology,* 39**,** 395-9.

HEINRICH, R. S., FONTAINE, A. A., GRIMES, R. Y., SIDHAYE, A., YANG, S., MOORE, K. E., LEVINE, R. A. & YOGANATHAN, A. P. 1996. Experimental analysis of fluid mechanical energy losses in aortic valve stenosis: importance of pressure recovery. *Ann Biomed Eng,* 24**,** 685-94.

HO, S. Y. 2009. Anatomy and myoarchitecture of the left ventricular wall in normal and in disease. *Eur J Echocardiogr,* 10**,** iii3-7.

HOFFMAN, J. I. 2000. Problems of coronary flow reserve. *Ann Biomed Eng,* 28**,** 884-96.

HOFFMANN, U., FERENCIK, M., CURY, R. C. & PENA, A. J. 2006. Coronary CT angiography. *J Nucl Med,* 47**,** 797-806.

HUANG, D., SWANSON, E. A., LIN, C. P., SCHUMAN, J. S., STINSON, W. G., CHANG, W., HEE, M. R., FLOTTE, T., GREGORY, K., PULIAFITO, C. A. & ET AL. 1991. Optical coherence tomography. *Science,* 254**,** 1178-81.

HUO, Y. & KASSAB, G. S. 2009. A scaling law of vascular volume. *Biophys J,* 96**,** 347-53.

HUO, Y., SVENDSEN, M., CHOY, J. S., ZHANG, Z. D. & KASSAB, G. S. 2012. A validated predictive model of coronary fractional flow reserve. *Journal of the Royal Society Interface,* 9**,** 1325-38.

IBRAHIM, D., BROILO, T. L., HEITZ, C., DE OLIVEIRA, M. G., DE OLIVEIRA, H. W., NOBRE, S. M., DOS SANTOS FILHO, J. H. & SILVA, D. N. 2009. Dimensional error of selective laser sintering, three-dimensional printing and PolyJet models in the reproduction of mandibular anatomy. *J Craniomaxillofac Surg,* 37**,** 167-73.

IDELSOHN, S. R., COSTA, L. E. & PONSO, R. 1985. A Comparative Computational Study of Blood-Flow through Prosthetic Heart-Valves Using the Finite-Element Method. *Journal of Biomechanics,* 18**,** 97-115.

INCALCATERRA, E., ACCARDI, G., BALISTRERI, C. R., CAIMI, G., CANDORE, G., CARUSO, M. & CARUSO, C. 2013. Pro-inflammatory genetic markers of atherosclerosis. *Curr Atheroscler Rep,* 15**,** 329.

IUNG, B., BARON, G., BUTCHART, E. G., DELAHAYE, F., GOHLKE-BARWOLF, C., LEVANG, O. W., TORNOS, P., VANOVERSCHELDE, J. L., VERMEER, F., BOERSMA, E., RAVAUD, P. & VAHANIAN,

A. 2003. A prospective survey of patients with valvular heart disease in Europe: The Euro Heart Survey on Valvular Heart Disease. *Eur Heart J,* 24**,** 1231-43.

IWATA, K. & OGASAWARA, K. 2013. Comparison of the cost-effectiveness of stress myocardial perfusion MRI and SPECT in patients with suspected coronary artery disease. *Radiol Phys Technol,* 6**,** 28-34.

JAGUSZEWSKI, M., KLINGENBERG, R. & LANDMESSER, U. 2013. Intracoronary Near-Infrared Spectroscopy (NIRS) Imaging for Detection of Lipid Content of Coronary Plaques: Current Experience and Future Perspectives. *Curr Cardiovasc Imaging Rep,* 6**,** 426-430.

JAVADZADEGAN, A., YONG, A. S., CHANG, M., NG, A. C., YIANNIKAS, J., NG, M. K., BEHNIA, M. & KRITHARIDES, L. 2013. Flow recirculation zone length and shear rate are differentially affected by stenosis severity in human coronary arteries. *Am J Physiol Heart Circ Physiol,* 304**,** H559-66.

JOHNSON, N. P., KIRKEEIDE, R. L., ASRRESS, K. N., FEARON, W. F., LOCKIE, T., MARQUES, K. M. J., PYXARAS, S. A., ROLANDI, M. C., VAN 'T VEER, M., DE BRUYNE, B., PIEK, J. J., PIJLS, N. H. J., REDWOOD, S., SIEBES, M., SPAAN, J. A. E. & GOULD, K. L. 2013. Does the Instantaneous Wave-Free Ratio Approximate the Fractional Flow Reserve? *Journal of the American College of Cardiology,* 61**,** 1428-1435.

JONES, W. P. & LAUNDER, B. E. 1972. Prediction of Laminarization with a 2-Equation Model of Turbulence. *International Journal of Heat and Mass Transfer,* 15**,** 301-&.

JUDKINS, M. P. 1967. Selective coronary arteriography. I. A percutaneous transfemoral technic. *Radiology,* 89**,** 815-24.

JUNG, J., LYCZKOWSKI, R. W., PANCHAL, C. B. & HASSANEIN, A. 2006. Multiphase hemodynamic simulation of pulsatile flow in a coronary artery. *J Biomech,* 39**,** 2064-73.

KAGADIS, G. C., SKOURAS, E. D., BOURANTAS, G. C., PARASKEVA, C. A., KATSANOS, K., KARNABATIDIS, D. & NIKIFORIDIS, G. C. 2008. Computational representation and hemodynamic characterization of in vivo acquired severe stenotic renal artery geometries using turbulence modeling. *Medical Engineering & Physics,* 30**,** 647-660.

KAJIYA, F. & GOTO, M. 1999. Integrative physiology of coronary microcirculation. *Jpn J Physiol,* 49**,** 229-41.

KEEGAN, J., GATEHOUSE, P. D., YANG, G. Z. & FIRMIN, D. N. 2004. Spiral phase velocity mapping of left and right coronary artery blood flow: correction for through-plane motion using selective fat-only excitation. *J Magn Reson Imaging,* 20**,** 953-60.

KERN, M. J., DE BRUYNE, B. & PIJLS, N. H. 1997. From research to clinical practice: current role of intracoronary physiologically based decision making in the cardiac catheterization laboratory. *J Am Coll Cardiol,* 30**,** 613-20.

KERN, M. J., LERMAN, A., BECH, J. W., DE BRUYNE, B., EECKHOUT, E., FEARON, W. F., HIGANO, S. T., LIM, M. J., MEUWISSEN, M., PIEK, J. J., PIJLS, N. H., SIEBES, M. & SPAAN, J. A. 2006. Physiological assessment of coronary artery disease in the cardiac catheterization laboratory: a scientific statement from the American Heart Association Committee on Diagnostic and Interventional Cardiac Catheterization, Council on Clinical Cardiology. *Circulation,* 114**,** 1321-41.

KILNER, P. J., HENEIN, M. Y. & GIBSON, D. G. 1997. Our tortuous heart in dynamic mode - an echocardiographic study of mitral flow and movement in exercising subjects. *Heart and Vessels,* 12**,** 103-110.

KIM, H. J., VIGNON-CLEMENTEL, I. E., COOGAN, J. S., FIGUEROA, C. A., JANSEN, K. E. & TAYLOR, C. A. 2010. Patient-specific modeling of blood flow and pressure in human coronary arteries. *Ann Biomed Eng,* 38**,** 3195-209.

KIM, H. T., KLINE, S. J. & REYNOLDS, W. C. 1971. Production of Turbulence near a Smooth Wall in a Turbulent Boundary Layer. *Journal of Fluid Mechanics,* 50**,** 133-&.

KIM, J. A., CHUN, E. J., LEE, M. S., KIM, K. J. & CHOI, S. I. 2013. Relationship between amount of cigarette smoking and coronary atherosclerosis on coronary CTA in asymptomatic individuals. *Int J Cardiovasc Imaging,* 29 Suppl 1**,** 21-8.

KLEIMAN, N. S. 2011. Bringing It All Together Integration of Physiology With Anatomy During Cardiac Catheterization. *Journal of the American College of Cardiology,* 58**,** 1219-1221.

KNOEBEL, S. B., MCHENRY, P. L., PHILLIPS, J. F. & PAULETTO, F. J. 1972. Coronary collateral circulation and myocardial blood flow reserve. *Circulation,* 46**,** 84-94.

KODALI, S. K., WILLIAMS, M. R., SMITH, C. R., SVENSSON, L. G., WEBB, J. G., MAKKAR, R. R., FONTANA, G. P., DEWEY, T. M., THOURANI, V. H., PICHARD, A. D., FISCHBEIN, M., SZETO, W. Y., LIM, S., GREASON, K. L., TEIRSTEIN, P. S., MALAISRIE, S. C., DOUGLAS, P. S., HAHN, R. T., WHISENANT, B., ZAJARIAS, A., WANG, D., AKIN, J. J., ANDERSON, W. N., LEON, M. B. & INVESTIGATORS, P. T. 2012. Two-year outcomes after transcatheter or surgical aortic-valve replacement. *N Engl J Med,* 366**,** 1686-95.

KOO, B. K., ERGLIS, A., DOH, J. H., DANIELS, D. V., JEGERE, S., KIM, H. S., DUNNING, A., DEFRANCE, T., LANSKY, A., LEIPSIC, J. & MIN, J. K. 2011. Diagnosis of ischemia-causing coronary stenoses by noninvasive fractional flow reserve computed from coronary computed tomographic angiograms. Results from the prospective multicenter DISCOVER-FLOW (Diagnosis of Ischemia-Causing Stenoses Obtained Via Noninvasive Fractional Flow Reserve) study. *J Am Coll Cardiol,* 58**,** 1989-97.

KOUSERA, C. A., WOOD, N. B., SEED, W. A., TORII, R., O'REGAN, D. & XU, X. Y. 2013. A numerical study of aortic flow stability and comparison with in vivo flow measurements. *J Biomech Eng,* 135**,** 011003.

KU, D. N., GIDDENS, D. P., ZARINS, C. K. & GLAGOV, S. 1985. Pulsatile Flow and Atherosclerosis in the Human Carotid Bifurcation - Positive Correlation between Plaque Location and Low and Oscillating Shear-Stress. *Arteriosclerosis,* 5**,** 293-302.

KUBO, T., AKASAKA, T., SHITE, J., SUZUKI, T., UEMURA, S., YU, B., KOZUMA, K., KITABATA, H., SHINKE, T., HABARA, M., SAITO, Y., HOU, J., SUZUKI, N. & ZHANG, S. 2013. OCT compared with IVUS in a coronary lesion assessment: the OPUS-CLASS study. *JACC Cardiovasc Imaging,* 6**,** 1095-104.

KUME, T., AKASAKA, T., KAWAMOTO, T., WATANABE, N., TOYOTA, E., NEISHI, Y., SUKMAWAN, R., SADAHIRA, Y. & YOSHIDA, K. 2006. Assessment of coronary arterial plaque by optical coherence tomography. *Am J Cardiol,* 97**,** 1172-5.

LABAN, M., OOMEN, J. A., SLAGER, C. J., WENTZEL, J. J., KRAMS, R., SCHUUBIERS, J. C. H., DENBOER, A., VONBIRGELEN, C., SERRUYS, P. W. & DEFEIJTER, P. J. 1995. ANGUS: A new approach to three-dimensional reconstruction of coronary vessels by combined use of angiography and intravascular ultrasound. *Computers in Cardiology 1995***,** 325-328.

LADISA, J. F., JR., OLSON, L. E., DOUGLAS, H. A., WARLTIER, D. C., KERSTEN, J. R. & PAGEL, P. S. 2006. Alterations in regional vascular geometry produced by theoretical stent implantation influence distributions of wall shear stress: analysis of a curved coronary artery using 3D computational fluid dynamics modeling. *Biomed Eng Online,* 5**,** 40.

LAMBRECHT, J. T., BERNDT, D. C., SCHUMACHER, R. & ZEHNDER, M. 2009. Generation of three-dimensional prototype models based on cone beam computed tomography. *Int J Comput Assist Radiol Surg,* 4**,** 175-80.

LANCELLOTTI, P. & MAGNE, J. 2013. Stress echocardiography in regurgitant valve disease. *Circ Cardiovasc Imaging,* 6**,** 840-9.

LANGTRY, R. B. & MENTER, F. R. 2009. Correlation-Based Transition Modeling for Unstructured Parallelized Computational Fluid Dynamics Codes. *Aiaa Journal,* 47**,** 2894-2906.

LEE, S. W. & STEINMAN, D. A. 2007. On the relative importance of rheology for image-based CFD models of the carotid bifurcation. *J Biomech Eng,* 129**,** 273-8.

LEE, Y. J., LIM, Y. S., LIM, H. W., YOO, W. J., CHOI, B. G. & KIM, B. S. 2013. Diagnostic accuracy of 64-slice multidetector CT angiography for detection of in-stent restenosis of vertebral artery ostium stents: comparison with conventional angiography. *Acta Radiol*.

LEITGEB, R., HITZENBERGER, C. & FERCHER, A. 2003. Performance of fourier domain vs. time domain optical coherence tomography. *Opt Express,* 11**,** 889-94.

LEON, M. B., SMITH, C. R., MACK, M., MILLER, D. C., MOSES, J. W., SVENSSON, L. G., TUZCU, E. M., WEBB, J. G., FONTANA, G. P., MAKKAR, R. R., BROWN, D. L., BLOCK, P. C., GUYTON, R. A., PICHARD, A. D., BAVARIA, J. E., HERRMANN, H. C., DOUGLAS, P. S., PETERSEN, J. L., AKIN, J. J., ANDERSON, W. N., WANG, D., POCOCK, S. & INVESTIGATORS, P. T. 2010. Transcatheter aortic-valve implantation for aortic stenosis in patients who cannot undergo surgery. *N Engl J Med,* 363**,** 1597-607.

LI, J. J. & CHEN, J. L. 2005. Inflammation may be a bridge connecting hypertension and atherosclerosis. *Med Hypotheses,* 64**,** 925-9.

LIPSCOMB, K. & GOULD, K. L. 1975. Mechanism of the effect of coronary artery stenosis on coronary flow in the dog. *American Heart Journal,* 89**,** 60-7.

LLOYD-JONES, D., ADAMS, R., CARNETHON, M., DE SIMONE, G., FERGUSON, T. B., FLEGAL, K., FORD, E., FURIE, K., GO, A., GREENLUND, K., HAASE, N., HAILPERN, S., HO, M., HOWARD, V., KISSELA, B., KITTNER, S., LACKLAND, D., LISABETH, L., MARELLI, A., MCDERMOTT, M., MEIGS, J., MOZAFFARIAN, D., NICHOL, G., O'DONNELL, C., ROGER, V., ROSAMOND, W., SACCO, R., SORLIE, P., STAFFORD, R., STEINBERGER, J., THOM, T., WASSERTHIEL-SMOLLER, S., WONG, N., WYLIE-ROSETT, J., HONG, Y., AMERICAN HEART ASSOCIATION STATISTICS, C. & STROKE STATISTICS, S. 2009. Heart disease and stroke statistics--2009 update: a report from the American Heart Association Statistics Committee and Stroke Statistics Subcommittee. *Circulation,* 119**,** e21-181.

LONG, Q., XU, X. Y., ARIFF, B., THOM, S. A., HUGHES, A. D. & STANTON, A. V. 2000. Reconstruction of blood flow patterns in a human carotid bifurcation: a combined CFD and MRI study. *J Magn Reson Imaging,* 11**,** 299-311.

LUNDELL, A., BERGQVIST, D., MATTSSON, E. & NILSSON, B. 1993. Volume blood flow measurements with a transit time flowmeter: an in vivo and in vitro variability and validation study. *Clin Physiol,* 13**,** 547-57.

LUSIS, A. J. 2000. Atherosclerosis. *Nature,* 407**,** 233-41.

MADDER, R. D., STEINBERG, D. H. & ANDERSON, R. D. 2013. Multimodality direct coronary imaging with combined near-infrared spectroscopy and intravascular ultrasound: initial US experience. *Catheter Cardiovasc Interv,* 81**,** 551-7.

MALEK, A. M., ALPER, S. L. & IZUMO, S. 1999. Hemodynamic shear stress and its role in atherosclerosis. *JAMA,* 282**,** 2035-42.

MALLAS, G., ROSENTHAL, A., CALFON, M. A., RAZANSKY, R. N., MAUSKAPF, A., JAFFER, F. A., BROOKS, D. H. & NTZIACHRISTOS, V. 2011. Progress on multimodal molecular / anatomical intravascular imaging of coronary vessels combining near infrared fluorescence and ultrasound. *Conf Proc IEEE Eng Med Biol Soc,* 2011**,** 1117-20.

MANBACHI, A., HOI, Y., WASSERMAN, B. A., LAKATTA, E. G. & STEINMAN, D. A. 2011. On the shape of the common carotid artery with implications for blood velocity profiles. *Physiol Meas,* 32**,** 1885-97.

MARKL, M., FRYDRYCHOWICZ, A., KOZERKE, S., HOPE, M. & WIEBEN, O. 2012. 4D flow MRI. *J Magn Reson Imaging,* 36**,** 1015-36.

MARKL, M., HARLOFF, A., BLEY, T. A., ZAITSEV, M., JUNG, B., WEIGANG, E., LANGER, M., HENNIG, J. & FRYDRYCHOWICZ, A. 2007. Time-resolved 3D MR velocity mapping at 3T: Improved navigator-gated assessment of vascular anatomy and blood flow. *Journal of Magnetic Resonance Imaging,* 25**,** 824-831.

MARTINI, F. H. 2004. *Fundamentals of Anatomy and Physiology,* San Francisco, Pearson-Benjamin Cummings.

MATSUMOTO, D., SHINKE, T., NAKAMURA, T., SHITE, J., LI, J., HOU, D. & CHRONOS, N. 2013. Optical coherence tomography and histopathological assessment of delayed arterial healing after drug-eluting stent implant in a pig coronary model. *Int J Cardiol,* 170**,** 152-9.

MEAKHAIL, T. A., ZIEN, Y., ELSALLAK, M. & ABDELHADY, S. 2008. Experimental study of the effect of some geometric variables and number of nozzles on the performance of a subsonic air-air ejector. *Proceedings of the Institution of Mechanical Engineers Part a-Journal of Power and Energy,* 222**,** 809-818.

MEERKIN, D., MAROM, H., COHEN-BITON, O. & EINAV, S. 2010a. Three-Dimensional Vessel Analyses Provide More Accurate Length Estimations than the Gold Standard QCA. *Journal of Interventional Cardiology,* 23**,** 152-159.

MEERKIN, D., MAROM, H., COHEN-BITON, O. & EINAV, S. 2010b. Three-dimensional vessel analyses provide more accurate length estimations than the gold standard QCA. *J Interv Cardiol,* 23**,** 152-9.

MENTER, F. 1994a. Two-Equation Eddy-Viscosity Turbulence Models for Engineering Applications. *AIAA Journal,* 32.

MENTER, F. R. 1994b. 2-Equation Eddy-Viscosity Turbulence Models for Engineering Applications. *Aiaa Journal,* 32**,** 1598-1605.

MENTER, F. R., LANGTRY, R. & VOLKER, S. 2006. Transition modelling for general purpose CFD codes. *Flow Turbulence and Combustion,* 77**,** 277-303.

MERRILL, E. W., GILLILAND, E. R., COKELET, G., SHIN, H., BRITTEN, A. & WELLS, R. E., JR. 1963. Rheology of blood and flow in the microcirculation. *J Appl Physiol,* 18**,** 255-60.

MEUWISSEN, M., SIEBES, M., CHAMULEAU, S. A., VAN ECK-SMIT, B. L., KOCH, K. T., DE WINTER, R. J., TIJSSEN, J. G., SPAAN, J. A. & PIEK, J. J. 2002a. Hyperemic stenosis resistance index for evaluation of functional coronary lesion severity. *Circulation,* 106**,** 441-6.

MEUWISSEN, M., SIEBES, M., SPAAN, J. A. & PIEK, J. J. 2002b. Rationale of combined intracoronary pressure and flow velocity measurements. *Z Kardiol,* 91 Suppl 3**,** 108-12.

MILNER, J. S., MOORE, J. A., RUTT, B. K. & STEINMAN, D. A. 1998. Hemodynamics of human carotid artery bifurcations: computational studies with models reconstructed from magnetic resonance imaging of normal subjects. *J Vasc Surg,* 28**,** 143-56.

MIN, J. K. & KOCHAR, M. 2012. Diagnostic accuracy of coronary computed tomography angiography in patients post-coronary artery bypass grafting. *Indian Heart J,* 64**,** 261-2.

MIN, J. K., KOO, B. K., ERGLIS, A., DOH, J. H., DANIELS, D. V., JEGERE, S., KIM, H. S., DUNNING, A. M., DEFRANCE, T., LANSKY, A. & LEIPSIC, J. 2012a. Usefulness of noninvasive fractional flow reserve computed from coronary computed tomographic angiograms for intermediate stenoses confirmed by quantitative coronary angiography. *Am J Cardiol,* 110**,** 971-6.

MIN, J. K., LEIPSIC, J., PENCINA, M. J., BERMAN, D. S., KOO, B. K., VAN MIEGHEM, C., ERGLIS, A., LIN, F. Y., DUNNING, A. M., APRUZZESE, P., BUDOFF, M. J., COLE, J. H., JAFFER, F. A., LEON, M. B., MALPESO, J., MANCINI, G. B., PARK, S. J., SCHWARTZ, R. S., SHAW, L. J. & MAURI, L. 2012b. Diagnostic accuracy of fractional flow reserve from anatomic CT angiography. *JAMA,* 308**,** 1237-45.

MINOR, R. K., BAUR, J. A., GOMES, A. P., WARD, T. M., CSISZAR, A., MERCKEN, E. M., ABDELMOHSEN, K., SHIN, Y. K., CANTO, C., SCHEIBYE-KNUDSEN, M., KRAWCZYK, M., IRUSTA, P. M., MARTIN-MONTALVO, A., HUBBARD, B. P., ZHANG, Y. Q., LEHRMANN, E., WHITE, A. A., PRICE, N. L., SWINDELL, W. R., PEARSON, K. J., BECKER, K. G., BOHR, V. A., GOROSPE, M., EGAN, J. M., TALAN, M. I., AUWERX, J., WESTPHAL, C. H., ELLIS, J. L., UNGVARI, Z., VLASUK, G. P., ELLIOTT, P. J., SINCLAIR, D. A. & DE CABO, R. 2013. SRT1720 improves survival and healthspan of obese mice (vol 1, 70, 2011). *Scientific Reports,* 3.

MONTALESCOT, G., SECHTEM, U., ACHENBACH, S., ANDREOTTI, F., ARDEN, C., BUDAJ, A., BUGIARDINI, R., CREA, F., CUISSET, T., DI MARIO, C., FERREIRA, J. R., GERSH, B. J., GITT, A. K., HULOT, J. S., MARX, N., OPIE, L. H., PFISTERER, M., PRESCOTT, E., RUSCHITZKA, F., SABATE, M., SENIOR, R., TAGGART, D. P., VAN DER WALL, E. E., VRINTS, C. J., ZAMORANO, J. L.,

BAUMGARTNER, H., BAX, J. J., BUENO, H., DEAN, V., DEATON, C., EROL, C., FAGARD, R., FERRARI, R., HASDAI, D., HOES, A. W., KIRCHHOF, P., KNUUTI, J., KOLH, P., LANCELLOTTI, P., LINHART, A., NIHOYANNOPOULOS, P., PIEPOLI, M. F., PONIKOWSKI, P., SIRNES, P. A., TAMARGO, J. L., TENDERA, M., TORBICKI, A., WIJNS, W., WINDECKER, S., VALGIMIGLI, M., CLAEYS, M. J., DONNER-BANZHOFF, N., FRANK, H., FUNCK-BRENTANO, C., GAEMPERLI, O., GONZALEZ-JUANATEY, J. R., HAMILOS, M., HUSTED, S., JAMES, S. K., KERVINEN, K., KRISTENSEN, S. D., MAGGIONI, A. P., PRIES, A. R., ROMEO, F., RYDEN, L., SIMOONS, M. L., STEG, P. G., TIMMIS, A. & YILDIRIR, A. 2013. 2013 ESC guidelines on the management of stable coronary artery disease: the Task Force on the management of stable coronary artery disease of the European Society of Cardiology. *Eur Heart J,* 34**,** 2949-3003.

MOORE, J. A., STEINMAN, D. A., HOLDSWORTH, D. W. & ETHIER, C. R. 1999. Accuracy of computational hemodynamics in complex arterial geometries reconstructed from magnetic resonance imaging. *Ann Biomed Eng,* 27**,** 32-41.

MORRIS, P. D., RYAN, D., MORTON, A. C., LYCETT, R., LAWFORD, P. V., HOSE, D. R. & GUNN, J. P. 2013. Virtual fractional flow reserve from coronary angiography: modeling the significance of coronary lesions: results from the VIRTU-1 (VIRTUal Fractional Flow Reserve From Coronary Angiography) study. *JACC Cardiovasc Interv,* 6**,** 149-57.

MORRIS, P. D., RYAN, D. R., LYCETT, R., MORTON, A. C., LAWFORD, P. V., HOSE, D. R. & GUNN, J. 2012. Computer Modelled Coronary Physiology and "Virtual" Fractional Flow Reserve from Rotational Angiography. *Heart,* 98**,** A14-A14.

MUHLENBRUCH, G., SEYFARTH, T., SOO, C. S., PREGALATHAN, N. & MAHNKEN, A. H. 2007. Diagnostic value of 64-slice multi-detector row cardiac CTA in symptomatic patients. *European Radiology,* 17**,** 603-609.

MULLANI, N. A. & GOULD, K. L. 1984. Functional cardiac imaging: positron emission tomography. *Hosp Pract (Off Ed),* 19**,** 103-7, 113-8.

MULLER, O., PYXARAS, S. A., TRANA, C., MANGIACAPRA, F., BARBATO, E., WIJNS, W., TAYLOR, C. A. & DE BRUYNE, B. 2012. Pressure-diameter relationship in human coronary arteries. *Circ Cardiovasc Interv,* 5**,** 791-6.

MURRAY, C. D. 1926. The Physiological Principle of Minimum Work: I. The Vascular System and the Cost of Blood Volume. *Proc Natl Acad Sci U S A,* 12**,** 207-14.

MURUGESAN, K., ANANDAPANDIAN, P. A., SHARMA, S. K. & VASANTHA KUMAR, M. 2012. Comparative evaluation of dimension and surface detail accuracy of models produced by three different rapid prototype techniques. *J Indian Prosthodont Soc,* 12**,** 16-20.

MYNARD, J. P. & STEINMAN, D. A. 2013. Effect of velocity profile skewing on blood velocity and volume flow waveforms derived from maximum Doppler spectral velocity. *Ultrasound Med Biol,* 39**,** 870-81.

NAKAZATO, R., PARK, H. B., BERMAN, D. S., GRANSAR, H., KOO, B. K., ERGLIS, A., LIN, F. Y., DUNNING, A. M., BUDOFF, M. J., MALPESO, J., LEIPSIC, J. & MIN, J. K. 2013a. Non-invasive Fractional Flow Reserve Derived from CT Angiography (FFRCT) for Coronary Lesions of Intermediate Stenosis Severity: Results from the DeFACTO study. *Circ Cardiovasc Imaging*.

NAKAZATO, R., PARK, H. B., BERMAN, D. S., GRANSAR, H., KOO, B. K., ERGLIS, A., LIN, F. Y., DUNNING, A. M., BUDOFF, M. J., MALPESO, J., LEIPSIC, J. & MIN, J. K. 2013b. Noninvasive fractional flow reserve derived from computed tomography angiography for coronary lesions of intermediate stenosis severity: results from the DeFACTO study. *Circ Cardiovasc Imaging,* 6**,** 881-9.

NAM, C. W., MANGIACAPRA, F., ENTJES, R., CHUNG, I. S., SELS, J. W., TONINO, P. A., DE BRUYNE, B., PIJLS, N. H. & FEARON, W. F. 2011. Functional SYNTAX score for risk assessment in multivessel coronary artery disease. *J Am Coll Cardiol,* 58**,** 1211-8.

NAM, C. W., YOON, H. J., CHO, Y. K., PARK, H. S., KIM, H., HUR, S. H., KIM, Y. N., CHUNG, I. S., KOO, B. K., TAHK, S. J., FEARON, W. F. & KIM, K. B. 2010. Outcomes of Percutaneous Coronary

Intervention in Intermediate Coronary Artery Disease Fractional Flow Reserve-Guided Versus Intravascular Ultrasound Guided. *Jacc-Cardiovascular Interventions,* 3**,** 812-817.
NANTO, S., MASUYAMA, T., TAKANO, Y., HORI, M. & NAGATA, S. 2001. Determination of coronary zero flow pressure by analysis of the baseline pressure-flow relationship in humans. *Jpn Circ J,* 65**,** 793-6.
NEREM, R. M. & SEED, W. A. 1972. An in vivo study of aortic flow disturbances. *Cardiovasc Res,* 6**,** 1-14.
NOZUE, T., YAMAMOTO, S., TOHYAMA, S., FUKUI, K., UMEZAWA, S., ONISHI, Y., KUNISHIMA, T., SATO, A., NOZATO, T., MIYAKE, S., TAKEYAMA, Y., MORINO, Y., YAMAUCHI, T., MURAMATSU, T., HIRANO, T., HIBI, K., TERASHIMA, M. & MICHISHITA, I. 2013. Impacts of age on coronary atherosclerosis and vascular response to statin therapy. *Heart Vessels*.
OTTO, C. M., LIND, B. K., KITZMAN, D. W., GERSH, B. J. & SISCOVICK, D. S. 1999a. Association of aortic-valve sclerosis with cardiovascular mortality and morbidity in the elderly. *N Engl J Med,* 341**,** 142-7.
OTTO, C. M., LIND, B. K., KITZMAN, D. W., GERSH, B. J., SISCOVICK, D. S. & CARDIOVASCULAR HLTH, S. 1999b. Association of aortic-valve sclerosis with cardiovascular mortality and morbidity in the elderly. *New England Journal of Medicine,* 341**,** 142-147.
OZKAN, A. 2012. Low gradient "severe" aortic stenosis with preserved left ventricular ejection fraction. *Cardiovasc Diagn Ther,* 2**,** 19-27.
PAELINCK, B. P., VAN HERCK, P. L., RODRIGUS, I., CLAEYS, M. J., LABORDE, J. C., PARIZEL, P. M., VRINTS, C. J. & BOSMANS, J. M. 2011. Comparison of magnetic resonance imaging of aortic valve stenosis and aortic root to multimodality imaging for selection of transcatheter aortic valve implantation candidates. *Am J Cardiol,* 108**,** 92-8.
PAPAFAKLIS, M. I., MURAMATSU, T., ISHIBASHI, Y., LAKKAS, L. S., NAKATANI, S., BOURANTAS, C. V., LIGTHART, J., ONUMA, Y., ECHAVARRIA-PINTO, M., TSIRKA, G., KOTSIA, A., NIKAS, D. N., MOGABGAB, O., VAN GEUNS, R. J., NAKA, K. K., FOTIADIS, D. I., BRILAKIS, E. S., GARCIA-GARCIA, H. M., ESCANED, J., ZIJLSTRA, F., MICHALIS, L. K. & SERRUYS, P. W. 2014. Fast virtual functional assessment of intermediate coronary lesions using routine angiographic data and blood flow simulation in humans: comparison with pressure wire - fractional flow reserve. *EuroIntervention,* 10**,** 574-83.
PARK, S. J., KANG, S. J., AHN, J. M., SHIM, E. B., KIM, Y. T., YUN, S. C., SONG, H., LEE, J. Y., KIM, W. J., PARK, D. W., LEE, S. W., KIM, Y. H., LEE, C. W., MINTZ, G. S. & PARK, S. W. 2012. Visual-functional mismatch between coronary angiography and fractional flow reserve. *JACC Cardiovasc Interv,* 5**,** 1029-36.
PARKER, K. H. 2013. *Reservoir/excess pressure analysis of coronary haemodynamics (2)* [Online]. Available: http://www.bg.ic.ac.uk/research/k.parker/res_press_web/rp_coronary_2.html 2013].
PEDLEY, T. J. 1980. *The fluid mechanics of large blood vessels,* Cambridge, Cambridge University Press.
PEIFFER, V., SHERWIN, S. J. & WEINBERG, P. D. 2013. Computation in the rabbit aorta of a new metric - the transverse wall shear stress - to quantify the multidirectional character of disturbed blood flow. *J Biomech,* 46**,** 2651-8.
PETRACO, R., ESCANED, J., SEN, S., NIJJER, S., ASRRESS, K. N., ECHAVARRIA-PINTO, M., LOCKIE, T., KHAWAJA, M. Z., CUEVAS, C., FOIN, N., BROYD, C., FOALE, R. A., HADJILOIZOU, N., MALIK, I. S., MIKHAIL, G. W., SETHI, A., KAPRIELIAN, R., BAKER, C. S., LEFROY, D., BELLAMY, M., AL-BUSTAMI, M., KHAN, M. A., HUGHES, A. D., FRANCIS, D. P., MAYET, J., DI MARIO, C., REDWOOD, S. & DAVIES, J. E. 2013a. Classification performance of instantaneous wave-free ratio (iFR) and fractional flow reserve in a clinical population of intermediate coronary stenoses: results of the ADVISE registry. *EuroIntervention,* 9**,** 91-101.
PETRACO, R., PARK, J. J., SEN, S., NIJJER, S. S., MALIK, I. S., ECHAVARRIA-PINTO, M., ASRRESS, K. N., NAM, C. W., MACIAS, E., FOALE, R. A., SETHI, A., MIKHAIL, G. W., KAPRIELIAN, R., BAKER, C.

S., LEFROY, D., BELLAMY, M., AL-BUSTAMI, M., KHAN, M. A., GONZALO, N., HUGHES, A. D., FRANCIS, D. P., MAYET, J., DI MARIO, C., REDWOOD, S., ESCANED, J., KOO, B. K. & DAVIES, J. E. 2013b. Hybrid iFR-FFR decision-making strategy: implications for enhancing universal adoption of physiology-guided coronary revascularisation. *EuroIntervention,* 8**,** 1157-65.

PETRACO, R., SEN, S., NIJJER, S., ECHAVARRIA-PINTO, M., ESCANED, J., FRANCIS, D. P. & DAVIES, J. E. 2013c. Fractional flow reserve-guided revascularization: practical implications of a diagnostic gray zone and measurement variability on clinical decisions. *JACC Cardiovasc Interv,* 6**,** 222-5.

PIAZZA, N., GRUBE, E., GERCKENS, U., DEN HEIJER, P., LINKE, A., LUHA, O., RAMONDO, A., USSIA, G., WENAWESER, P., WINDECKER, S., LABORDE, J. C., DE JAEGERE, P. & SERRUYS, P. W. 2008. Procedural and 30-day outcomes following transcatheter aortic valve implantation using the third generation (18 Fr) corevalve revalving system: results from the multicentre, expanded evaluation registry 1-year following CE mark approval. *EuroIntervention,* 4**,** 242-9.

PICANO, E. 1992. Stress echocardiography. From pathophysiological toy to diagnostic tool. *Circulation,* 85**,** 1604-12.

PIJLS, N. H., AENGEVAEREN, W. R., UIJEN, G. J., HOEVELAKEN, A., PIJNENBURG, T., VAN LEEUWEN, K. & VAN DER WERF, T. 1991. Concept of maximal flow ratio for immediate evaluation of percutaneous transluminal coronary angioplasty result by videodensitometry. *Circulation,* 83**,** 854-65.

PIJLS, N. H., BECH, G. J., DE BRUYNE, B. & VAN STRATEN, A. 1997. Clinical assessment of functional stenosis severity: use of coronary pressure measurements for the decision to bypass a lesion. *Ann Thorac Surg,* 63**,** S6-11.

PIJLS, N. H., DE BRUYNE, B., PEELS, K., VAN DER VOORT, P. H., BONNIER, H. J., BARTUNEK, J. K. J. J. & KOOLEN, J. J. 1996. Measurement of fractional flow reserve to assess the functional severity of coronary-artery stenoses. *N Engl J Med,* 334**,** 1703-8.

PIJLS, N. H., DE BRUYNE, B., SMITH, L., AARNOUDSE, W., BARBATO, E., BARTUNEK, J., BECH, G. J. & VAN DE VOSSE, F. 2002. Coronary thermodilution to assess flow reserve: validation in humans. *Circulation,* 105**,** 2482-6.

PIJLS, N. H., FEARON, W. F., TONINO, P. A., SIEBERT, U., IKENO, F., BORNSCHEIN, B., VAN'T VEER, M., KLAUSS, V., MANOHARAN, G., ENGSTROM, T., OLDROYD, K. G., VER LEE, P. N., MACCARTHY, P. A. & DE BRUYNE, B. 2010. Fractional flow reserve versus angiography for guiding percutaneous coronary intervention in patients with multivessel coronary artery disease: 2-year follow-up of the FAME (Fractional Flow Reserve Versus Angiography for Multivessel Evaluation) study. *J Am Coll Cardiol,* 56**,** 177-84.

PIJLS, N. H., VAN 'T VEER, M., OLDROYD, K. G., BERRY, C., FEARON, W. F., KALA, P., BOCEK, O., WITT, N., DE BRUYNE, B. & PYXARAS, S. 2012. Instantaneous wave-free ratio or fractional flow reserve without hyperemia: novelty or nonsense? *J Am Coll Cardiol,* 59**,** 1916-7; author reply 1917-8.

PIJLS, N. H., VAN GELDER, B., VAN DER VOORT, P., PEELS, K., BRACKE, F. A., BONNIER, H. J. & EL GAMAL, M. I. 1995. Fractional flow reserve. A useful index to evaluate the influence of an epicardial coronary stenosis on myocardial blood flow. *Circulation,* 92**,** 3183-93.

PIJLS, N. H., VAN SCHAARDENBURGH, P., MANOHARAN, G., BOERSMA, E., BECH, J. W., VAN'T VEER, M., BAR, F., HOORNTJE, J., KOOLEN, J., WIJNS, W. & DE BRUYNE, B. 2007. Percutaneous coronary intervention of functionally nonsignificant stenosis: 5-year follow-up of the DEFER Study. *J Am Coll Cardiol,* 49**,** 2105-11.

PIJLS, N. H. J. & TONINO, P. A. L. 2011. The Crux of Maximum Hyperemia The Last Remaining Barrier for Routine Use of Fractional Flow Reserve. *Jacc-Cardiovascular Interventions,* 4**,** 1093-1095.

PIJLS, N. H. J., VANSON, J. A. M., KIRKEEIDE, R. L., DEBRUYNE, B. & GOULD, K. L. 1993. Experimental Basis of Determining Maximum Coronary, Myocardial, and Collateral Blood-Flow by Pressure Measurements for Assessing Functional Stenosis Severity before and after Percutaneous Transluminal Coronary Angioplasty. *Circulation,* 87**,** 1354-1367.

PILIPOVIC, A., RAOS, P. & SERCER, M. 2009. Experimental analysis of properties of materials for rapid prototyping. *International Journal of Advanced Manufacturing Technology,* 40**,** 105-115.
PRAUSE, G. P., DEJONG, S. C., MCKAY, C. R. & SONKA, M. 1997. Towards a geometrically correct 3-D reconstruction of tortuous coronary arteries based on biplane angiography and intravascular ultrasound. *Int J Card Imaging,* 13**,** 451-62.
PU, J., MINTZ, G. S., BRILAKIS, E. S., BANERJEE, S., ABDEL-KARIM, A. R., MAINI, B., BIRO, S., LEE, J. B., STONE, G. W., WEISZ, G. & MAEHARA, A. 2012. In vivo characterization of coronary plaques: novel findings from comparing greyscale and virtual histology intravascular ultrasound and near-infrared spectroscopy. *Eur Heart J,* 33**,** 372-83.
RABER, L. & WINDECKER, S. 2013. IVUS-Guided Percutaneous Coronary Interventions: An Ongoing Odyssey? *Circulation*.
RAHIMTOOLA, S. H. 2006. Valvular heart disease/cardiac surgery. *J Am Coll Cardiol,* 47**,** D37-40.
RAJABI-JAGHARGH, E., KOLLI, K. K., BACK, L. H. & BANERJEE, R. K. 2011. Effect of guidewire on contribution of loss due to momentum change and viscous loss to the translesional pressure drop across coronary artery stenosis: an analytical approach. *Biomed Eng Online,* 10**,** 51.
RAMCHARITAR, S., DAEMAN, J., PATTERSON, M., VAN GUENS, R. J., BOERSMA, E., SERRUYS, P. W. & VAN DER GIESSEN, W. J. 2008. First direct in vivo comparison of two commercially available three-dimensional quantitative coronary angiography systems. *Catheter Cardiovasc Interv,* 71**,** 44-50.
REGAR, E., GNANADESIGAN, M., VAN DER STEEN, A. F. & VAN SOEST, G. 2013. Quantitative optical coherence tomography tissue-type imaging for lipid-core plaque detection. *JACC Cardiovasc Interv,* 6**,** 891-2.
RODRIGUES, A. C., SOBRINO, B., GENVIGIR, F. D., WILLRICH, M. A., ARAZI, S. S., DOREA, E. L., BERNIK, M. M., BERTOLAMI, M., FALUDI, A. A., BRION, M. J., CARRACEDO, A., HIRATA, M. H. & HIRATA, R. D. 2013. Genetic variants in genes related to lipid metabolism and atherosclerosis, dyslipidemia and atorvastatin response. *Clin Chim Acta,* 417**,** 8-11.
RODRIGUEZ-PALOMARES, J. F., CUELLAR, H., MARTI, G., GARCIA, B., GONZALEZ-ALUJAS, M. T., MAHIA, P., EVANGELISTA, A., TORNOS, P. & GARCIA-DORADO, D. 2011. [Coronary angiography by 16-slice computed tomography prior to valvular surgery]. *Revista Espanola De Cardiologia,* 64**,** 269-76.
ROLEDER, T., KOVACIC, J. C., ALI, Z., SHARMA, R., CRISTEA, E., MORENO, P., SHARMA, S. K., NARULA, J. & KINI, A. S. 2014. Combined NIRS and IVUS imaging detects vulnerable plaque using a single catheter system: a head-to-head comparison with OCT. *EuroIntervention,* 10**,** 303-11.
ROSS, J., JR. & BRAUNWALD, E. 1968. Aortic stenosis. *Circulation,* 38**,** 61-7.
ROSS, R. 1993. Rous-Whipple Award Lecture. Atherosclerosis: a defense mechanism gone awry. *Am J Pathol,* 143**,** 987-1002.
RUBINSHTEIN, R., HALON, D. A., GASPAR, T., LEWIS, B. S. & PELED, N. 2014. Automatic assessment of coronary artery calcium score from contrast-enhanced 256-row coronary computed tomography angiography. *Am J Cardiol,* 113**,** 7-11.
RUDZINSKI, W., WALLER, A. H. & KALUSKI, E. 2012. Instantaneous wave-free ratio and fractional flow reserve: close, but not close enough! *J Am Coll Cardiol,* 59**,** 1915-6; author reply 1917-8.
SAGI, O. & LIBERMANN, A. 2008. Expanding applications and opportunities with Polyjet (TM) rapid prototyping technology. *Virtual and Rapid Manufacturing***,** 569-573.
SAKAMOTO, S., TAKAHASHI, S., COSKUN, A. U., PAPAFAKLIS, M. I., TAKAHASHI, A., SAITO, S., STONE, P. H. & FELDMAN, C. L. 2013. Relation of distribution of coronary blood flow volume to coronary artery dominance. *Am J Cardiol,* 111**,** 1420-4.
SALMI, M. 2013. Accuracy of medical models made by additive manufacturing. *Journal of Cranio-Maxillo-Facial Surgery***,** 603-609.
SALMI, M., PALOHEIMO, K. S., TUOMI, J., INGMAN, T. & MAKITIE, A. 2013a. A digital process for additive manufacturing of occlusal splints: a clinical pilot study. *Journal of the Royal Society Interface,* 10**,** 20130203.

SALMI, M., PALOHEIMO, K. S., TUOMI, J., WOLFF, J. & MAKITIE, A. 2013b. Accuracy of medical models made by additive manufacturing (rapid manufacturing). *J Craniomaxillofac Surg,* 41**,** 603-9.

SAMIN, M., JUTHIER, F., VAN BELLE, C., AGOSTONI, P., KLUIN, J., STELLA, P. R., RAMJANKHAN, F., BUDDE, R. P., SIESWERDA, G., ALGERI, E., ELKALIOUBIE, A., BELKACEMI, A., BERTRAND, M. E., DOEVENDANS, P. A. & VAN BELLE, E. 2014. Automated 3D analysis of multislice computed tomography to define the line of perpendicularity of the aortic annulus and of the implanted valve: Benefit on planning transcatheter aortic valve replacement. *Catheter Cardiovasc Interv,* 83**,** E119-27.

SANT'ANNA, F. M., DA SILVA, E. R., BATISTA, L. A., BRITO, M. B., VENTURA, F. M., FERRAZ, H. A., BUCZYNSKI, L., BARROZO, C. A. M. & PIJLS, N. 2008. What is the Angiography Error when Defining Myocardial Ischemia During Percutaneous Coronary Interventions? *Arquivos Brasileiros De Cardiologia,* 91**,** 179-184.

SANT'ANNA, F. M., SILVA, E. E., BATISTA, L. A., VENTURA, F. M., BARROZO, C. A. & PIJLS, N. H. 2007. Influence of routine assessment of fractional flow reserve on decision making during coronary interventions. *Am J Cardiol,* 99**,** 504-8.

SCHAAR, J. A., MASTIK, F., REGAR, E., DEN UIL, C. A., GIJSEN, F. J., WENTZEL, J. J., SERRUYS, P. W. & VAN DER STEHEN, A. F. 2007. Current diagnostic modalities for vulnerable plaque detection. *Curr Pharm Des,* 13**,** 995-1001.

SCHLOSSER, T., SCHEUERMANN, T., ULZHEIMER, S., MOHRS, O. K., KUHLING, M., ALBRECHT, P. E., VOIGTLANDER, T., BARKHAUSEN, J. & SCHMERMUND, A. 2008. In-vitro evaluation of coronary Stents and 64-detector-row computed tomography using a newly developed model of coronary artery stenosis. *Acta Radiologica,* 49**,** 56-64.

SCHOENHAGEN, P., HILL, A., KELLEY, T., POPOVIC, Z. & HALLIBURTON, S. S. 2011. In vivo imaging and computational analysis of the aortic root. Application in clinical research and design of transcatheter aortic valve systems. *J Cardiovasc Transl Res,* 4**,** 459-69.

SCHUHLEN, H., EIGLER, N. L. & WHITING, J. S. 1994. Grading the angiographic extent of collateral filling. Comparison with coronary flow, collateral flow, and regional coronary flow distribution measurements. *Int J Card Imaging,* 10**,** 25-33.

SCHULTZ, C. J., SERRUYS, P. W., VAN DER ENT, M., LIGTHART, J., MASTIK, F., GARG, S., MULLER, J. E., WILDER, M. A., VAN DE STEEN, A. F. & REGAR, E. 2010. First-in-man clinical use of combined near-infrared spectroscopy and intravascular ultrasound: a potential key to predict distal embolization and no-reflow? *J Am Coll Cardiol,* 56**,** 314.

SCHUURBIERS, J. C., LOPEZ, N. G., LIGTHART, J., GIJSEN, F. J., DIJKSTRA, J., SERRUYS, P. W., VAN DER STEEN, A. F. & WENTZEL, J. J. 2009. In vivo validation of CAAS QCA-3D coronary reconstruction using fusion of angiography and intravascular ultrasound (ANGUS). *Catheter Cardiovasc Interv,* 73**,** 620-6.

SEELEY, B. D. & YOUNG, D. F. 1976. Effect of geometry on pressure losses across models of arterial stenoses. *J Biomech,* 9**,** 439-48.

SEGERS, P., BRIMIOULLE, S., STERGIOPULOS, N., WESTERHOF, N., NAEIJE, R., MAGGIORINI, M. & VERDONCK, P. 1999. Pulmonary arterial compliance in dogs and pigs: the three-element windkessel model revisited. *Am J Physiol,* 277**,** H725-31.

SEHOVIC, S. 2013. Diagnostic Capabilities of 64 Slice CT Coronography Compared to Classic in Coronary Disease Detection. *Acta Inform Med,* 21**,** 208-10.

SEILER, C. 2011. Aiming at a disorder's concept by 3D QCA vs. FFR: a case of advanced ballistics. *Eur Heart J,* 32**,** 261-3.

SEN, S., ASRRESS, K. N., NIJJER, S., PETRACO, R., MALIK, I. S., FOALE, R. A., MIKHAIL, G. W., FOIN, N., BROYD, C., HADJILOIZOU, N., SETHI, A., AL-BUSTAMI, M., HACKETT, D., KHAN, M. A., KHAWAJA, M. Z., BAKER, C. S., BELLAMY, M., PARKER, K. H., HUGHES, A. D., FRANCIS, D. P., MAYET, J., DI MARIO, C., ESCANED, J., REDWOOD, S. & DAVIES, J. E. 2013a. Diagnostic classification of the instantaneous wave-free ratio is equivalent to fractional flow reserve

and is not improved with adenosine administration. Results of CLARIFY (Classification Accuracy of Pressure-Only Ratios Against Indices Using Flow Study). *J Am Coll Cardiol,* 61**,** 1409-20.

SEN, S., ESCANED, J., MALIK, I. S., MIKHAIL, G. W., FOALE, R. A., MILA, R., TARKIN, J., PETRACO, R., BROYD, C., JABBOUR, R., SETHI, A., BAKER, C. S., BELLAMY, M., AL-BUSTAMI, M., HACKETT, D., KHAN, M., LEFROY, D., PARKER, K. H., HUGHES, A. D., FRANCIS, D. P., DI MARIO, C., MAYET, J. & DAVIES, J. E. 2012. Development and validation of a new adenosine-independent index of stenosis severity from coronary wave-intensity analysis: results of the ADVISE (ADenosine Vasodilator Independent Stenosis Evaluation) study. *J Am Coll Cardiol,* 59**,** 1392-402.

SEN, S., PETRACO, R., MAYET, J. & DAVIES, J. 2013b. Wave Intensity Analysis in the Human Coronary Circulation in Health and Disease. *Curr Cardiol Rev*.

SHI, H., ASCHOFF, A. J., BRAMBS, H. J. & HOFFMANN, M. H. 2004. Multislice CT imaging of anomalous coronary arteries. *Eur Radiol,* 14**,** 2172-81.

SIEBERT, U., BORNSCHEIN, B., SCHNELL-INDERST, P., RIEBER, J., PIJLS, N., WASEM, J. & KLAUSS, V. 2008. Measurement of fractional flow reserve to guide decisions for percutaneous coronary intervention. *GMS Health Technol Assess,* 4**,** Doc07.

SINHA ROY, A., BACK, M. R., KHOURY, S. F., SCHNEEBERGER, E. W., BACK, L. H., VELURY, V. V., MILLARD, R. W. & BANERJEE, R. K. 2008. Functional and anatomical diagnosis of coronary artery stenoses. *J Surg Res,* 150**,** 24-33.

SIOGKAS, P. K., PAPAFAKLIS, M. I., SAKELLARIOS, A. I., STEFANOU, K. A., BOURANTAS, C. V., ATHANASIOU, L. M., BELLOS, C. V., EXARCHOS, T. P., NAKA, K. K., MICHALIS, L. K., PARODI, O. & FOTIADIS, D. I. 2013. Computational assessment of the fractional flow reserve from intravascular ultrasound and coronary angiography data: A pilot study. *Conf Proc IEEE Eng Med Biol Soc,* 2013**,** 3885-8.

SLAGER, C. J., WENTZEL, J. J., SCHUURBIERS, J. C., OOMEN, J. A., KLOET, J., KRAMS, R., VON BIRGELEN, C., VAN DER GIESSEN, W. J., SERRUYS, P. W. & DE FEYTER, P. J. 2000. True 3-dimensional reconstruction of coronary arteries in patients by fusion of angiography and IVUS (ANGUS) and its quantitative validation. *Circulation,* 102**,** 511-6.

SMITH, C. R., LEON, M. B., MACK, M. J., MILLER, D. C., MOSES, J. W., SVENSSON, L. G., TUZCU, E. M., WEBB, J. G., FONTANA, G. P., MAKKAR, R. R., WILLIAMS, M., DEWEY, T., KAPADIA, S., BABALIAROS, V., THOURANI, V. H., CORSO, P., PICHARD, A. D., BAVARIA, J. E., HERRMANN, H. C., AKIN, J. J., ANDERSON, W. N., WANG, D., POCOCK, S. J. & INVESTIGATORS, P. T. 2011. Transcatheter versus surgical aortic-valve replacement in high-risk patients. *N Engl J Med,* 364**,** 2187-98.

SMITH, K. M. & SQUIERS, J. 2013. Hypertrophic cardiomyopathy: an overview. *Crit Care Nurs Clin North Am,* 25**,** 263-72.

STEELANT, J. & DICK, E. 2001. Modeling of laminar-turbulent transition for high freestream turbulence. *Journal of Fluids Engineering-Transactions of the Asme,* 123**,** 22-30.

STEFANINI, G. G., STORTECKY, S., MEIER, B., WINDECKER, S. & WENAWESER, P. 2013. Severe aortic stenosis and coronary artery disease. *EuroIntervention,* 9 Suppl**,** S63-8.

STEIN, P. D. & SABBAH, H. N. 1976. Turbulent blood flow in the ascending aorta of humans with normal and diseased aortic valves. *Circ Res,* 39**,** 58-65.

STEVENSON, D. M. & YOGANATHAN, A. P. 1985. Numerical-Simulation of Steady Turbulent-Flow through Trileaflet Aortic Heart-Valves .1. Computational Scheme and Methodology. *Journal of Biomechanics,* 18**,** 899-907.

SUD, V. K. & SEKHON, G. S. 1990. Simulation of Steady Cardiovascular Flow in the Presence of Stenosis Using a Finite-Element Method. *Physics in Medicine and Biology,* 35**,** 947-959.

SUN, P., DWYER, K. M., MERZ, C. N., SUN, W., JOHNSON, C. A., SHIRCORE, A. M. & DWYER, J. H. 2000. Blood pressure, LDL cholesterol, and intima-media thickness: a test of the "response to injury" hypothesis of atherosclerosis. *Arterioscler Thromb Vasc Biol,* 20**,** 2005-10.

SUTER, M. J., NADKARNI, S. K., WEISZ, G., TANAKA, A., JAFFER, F. A., BOUMA, B. E. & TEARNEY, G. J. 2011. Intravascular optical imaging technology for investigating the coronary artery. *JACC Cardiovasc Imaging,* 4**,** 1022-39.

SVENSSON, L. G., BLACKSTONE, E. H., RAJESWARAN, J., BROZZI, N., LEON, M. B., SMITH, C. R., MACK, M., MILLER, D. C., MOSES, J. W., TUZCU, E. M., WEBB, J. G., KAPADIA, S., FONTANA, G. P., MAKKAR, R. R., BROWN, D. L., BLOCK, P. C., GUYTON, R. A., THOURANI, V. H., PICHARD, A. D., BAVARIA, J. E., HERRMANN, H. C., WILLIAMS, M. R., BABALIAROS, V., GENEREUX, P., AKIN, J. J. & INVESTIGATORS, P. T. 2014. Comprehensive analysis of mortality among patients undergoing TAVR: results of the PARTNER trial. *J Am Coll Cardiol,* 64**,** 158-68.

TAN, F. P. 2011. Comparison of aortic flow patterns before and after transcatheter aortic valve implantation. *Cardiovascular Engineering and Technology*.

TAN, F. P., SOLOPERTO, G., BASHFORD, S., WOOD, N. B., THOM, S., HUGHES, A. & XU, X. Y. 2008. Analysis of flow disturbance in a stenosed carotid artery bifurcation using two-equation transitional and turbulence models. *J Biomech Eng,* 130**,** 061008.

TAN, F. P., WOOD, N. B., TABOR, G. & XU, X. Y. 2011. Comparison of LES of steady transitional flow in an idealized stenosed axisymmetric artery model with a RANS transitional model. *J Biomech Eng,* 133**,** 051001.

TAN, F. P. P., BORGHI, A., MOHIADDIN, R. H., WOOD, N. B., THOM, S. & XU, X. Y. 2009a. Analysis of flow patterns in a patient-specific thoracic aortic aneurysm model. *Computers & Structures,* 87**,** 680-690.

TAN, F. P. P., TORII, R., BORGHI, A., MOHIADDIN, R. H., WOOD, N. B. & XU, X. Y. 2009b. Fluid-Structure Interaction Analysis of Wall Stress and Flow Patterns in a Thoracic Aortic Aneurysm. *International Journal of Applied Mechanics,* 1**,** 179-199.

TARKIN, J. M., NIJJER, S., SEN, S., PETRACO, R., ECHAVARRIA-PINTO, M., ASRESS, K. N., LOCKIE, T., KHAWAJA, M. Z., MAYET, J., HUGHES, A. D., MALIK, I. S., MIKHAIL, G. W., BAKER, C. S., FOALE, R. A., REDWOOD, S., FRANCIS, D. P., ESCANED, J. & DAVIES, J. E. 2013. Hemodynamic Response to Intravenous Adenosine and Its Effect on Fractional Flow Reserve Assessment: Results of the Adenosine for the Functional Evaluation of Coronary Stenosis Severity (AFFECTS) Study. *Circ Cardiovasc Interv,* 6**,** 654-61.

TAYLOR, C. A., FONTE, T. A. & MIN, J. K. 2013. Computational fluid dynamics applied to cardiac computed tomography for noninvasive quantification of fractional flow reserve: scientific basis. *J Am Coll Cardiol,* 61**,** 2233-41.

TAYLOR, C. A., HUGHES, T. J. & ZARINS, C. K. 1998. Finite element modeling of three-dimensional pulsatile flow in the abdominal aorta: relevance to atherosclerosis. *Ann Biomed Eng,* 26**,** 975-87.

TEARNEY, G. J., BREZINSKI, M. E., BOUMA, B. E., BOPPART, S. A., PITRIS, C., SOUTHERN, J. F. & FUJIMOTO, J. G. 1997. In vivo endoscopic optical biopsy with optical coherence tomography. *Science,* 276**,** 2037-9.

TEARNEY, G. J., REGAR, E., AKASAKA, T., ADRIAENSSENS, T., BARLIS, P., BEZERRA, H. G., BOUMA, B., BRUINING, N., CHO, J. M., CHOWDHARY, S., COSTA, M. A., DE SILVA, R., DIJKSTRA, J., DI MARIO, C., DUDEK, D., FALK, E., FELDMAN, M. D., FITZGERALD, P., GARCIA-GARCIA, H. M., GONZALO, N., GRANADA, J. F., GUAGLIUMI, G., HOLM, N. R., HONDA, Y., IKENO, F., KAWASAKI, M., KOCHMAN, J., KOLTOWSKI, L., KUBO, T., KUME, T., KYONO, H., LAM, C. C., LAMOUCHE, G., LEE, D. P., LEON, M. B., MAEHARA, A., MANFRINI, O., MINTZ, G. S., MIZUNO, K., MOREL, M. A., NADKARNI, S., OKURA, H., OTAKE, H., PIETRASIK, A., PRATI, F., RABER, L., RADU, M. D., RIEBER, J., RIGA, M., ROLLINS, A., ROSENBERG, M., SIRBU, V., SERRUYS, P. W., SHIMADA, K., SHINKE, T., SHITE, J., SIEGEL, E., SONODA, S., SUTER, M., TAKARADA, S., TANAKA, A., TERASHIMA, M., THIM, T., UEMURA, S., UGHI, G. J., VAN BEUSEKOM, H. M., VAN DER STEEN, A. F., VAN ES, G. A., VAN SOEST, G., VIRMANI, R., WAXMAN, S., WEISSMAN, N. J., WEISZ, G. & INTERNATIONAL WORKING GROUP FOR INTRAVASCULAR OPTICAL COHERENCE, T. 2012. Consensus standards for acquisition, measurement, and reporting of

intravascular optical coherence tomography studies: a report from the International Working Group for Intravascular Optical Coherence Tomography Standardization and Validation. *J Am Coll Cardiol,* 59**,** 1058-72.

TONINO, P. A., FEARON, W. F., DE BRUYNE, B., OLDROYD, K. G., LEESAR, M. A., VER LEE, P. N., MACCARTHY, P. A., VAN'T VEER, M. & PIJLS, N. H. 2010. Angiographic versus functional severity of coronary artery stenoses in the FAME study fractional flow reserve versus angiography in multivessel evaluation. *J Am Coll Cardiol,* 55**,** 2816-21.

TOPS, L. F., WOOD, D. A., DELGADO, V., SCHUIJF, J. D., MAYO, J. R., PASUPATI, S., LAMERS, F. P., VAN DER WALL, E. E., SCHALIJ, M. J., WEBB, J. G. & BAX, J. J. 2008. Noninvasive evaluation of the aortic root with multislice computed tomography implications for transcatheter aortic valve replacement. *JACC Cardiovasc Imaging,* 1**,** 321-30.

TORII, R., KEEGAN, J., WOOD, N. B., DOWSEY, A. W., HUGHES, A. D., YANG, G. Z., FIRMIN, D. N., MCG THOM, S. A. & XU, X. Y. 2009a. The effect of dynamic vessel motion on haemodynamic parameters in the right coronary artery: a combined MR and CFD study. *Br J Radiol,* 82 Spec No 1**,** S24-32.

TORII, R., KEEGAN, J., WOOD, N. B., DOWSEY, A. W., HUGHES, A. D., YANG, G. Z., FIRMIN, D. N., THOM, S. A. & XU, X. Y. 2010. MR image-based geometric and hemodynamic investigation of the right coronary artery with dynamic vessel motion. *Ann Biomed Eng,* 38**,** 2606-20.

TORII, R., WOOD, N. B., HADJILOIZOU, N., DOWSEY, A. W., WRIGHT, A. R., HUGHES, A. D., DAVIES, J., FRANCIS, D. P., MAYET, J., YANG, G. Z., THOM, S. A. & XU, X. Y. 2009b. Stress phase angle depicts differences in coronary artery hemodynamics due to changes in flow and geometry after percutaneous coronary intervention. *Am J Physiol Heart Circ Physiol,* 296**,** H765-76.

TORII, R., WOOD, N. B., HADJILOIZOU, N., DOWSEY, A. W., WRIGHT, A. R., HUGHES, A. D., DAVIES, J., FRANCIS, D. P., MAYET, J., YANG, G. Z., THOM, S. A. M. & XU, X. Y. 2009c. Fluid-structure interaction analysis of a patient-specific right coronary artery with physiological velocity and pressure waveforms. *Communications in Numerical Methods in Engineering,* 25**,** 565-580.

TORII, R., WOOD, N. B., HADJILOIZOU, N., DOWSEY, A. W., WRIGHT, A. R., HUGHES, A. D., DAVIES, J., FRANCIS, D. P., MAYET, J., YANG, G. Z., THOM, S. A. M. & XU, X. Y. 2009d. Stress phase angle depicts differences in coronary artery hemodynamics due to changes in flow and geometry after percutaneous coronary intervention. *American Journal of Physiology-Heart and Circulatory Physiology,* 296**,** H765-H776.

TORII, R., WOOD, N. B., HUGHES, A. D., THOM, S. A., AGUADO-SIERRA, J., DAVIES, J. E., FRANCIS, D. P., PARKER, K. H. & XU, X. Y. 2007. A computational study on the influence of catheter-delivered intravascular probes on blood flow in a coronary artery model. *J Biomech,* 40**,** 2501-9.

TRUELSEN, T., MAHONEN, M., TOLONEN, H., ASPLUND, K., BONITA, R. & VANUZZO, D. 2003. Trends in stroke and coronary heart disease in the WHO MONICA Project. *Stroke,* 34**,** 1346-52.

TSIMIKAS, S. & DEMARIA, A. N. 2012. The clinical emergence of optical coherence tomography: defining a role in intravascular imaging. *J Am Coll Cardiol,* 59**,** 1090-2.

TU, S., HOLM, N. R., KONING, G., HUANG, Z. & REIBER, J. H. 2011. Fusion of 3D QCA and IVUS/OCT. *Int J Cardiovasc Imaging,* 27**,** 197-207.

TYCZYNSKI, P., FERRANTE, G., MORENO-AMBROJ, C., KUKREJA, N., BARLIS, P., PIERI, E., DE SILVA, R., BEATT, K. & DI MARIO, C. 2010. Simple versus complex approaches to treating coronary bifurcation lesions: direct assessment of stent strut apposition by optical coherence tomography. *Rev Esp Cardiol (Engl Ed),* 63**,** 904-14.

UNDERWOOD, M. J., EL KHOURY, G., DERONCK, D., GLINEUR, D. & DION, R. 2000. The aortic root: structure, function, and surgical reconstruction. *Heart,* 83**,** 376-80.

VAHANIAN, A., ALFIERI, O., AL-ATTAR, N., ANTUNES, M., BAX, J., CORMIER, B., CRIBIER, A., DE JAEGERE, P., FOURNIAL, G., KAPPETEIN, A. P., KOVAC, J., LUDGATE, S., MAISANO, F., MOAT, N., MOHR, F., NATAF, P., PIERARD, L., POMAR, J. L., SCHOFER, J., TORNOS, P., TUZCU, M., VAN HOUT, B., VON SEGESSER, L. K. & WALTHER, T. 2008a. Transcatheter valve implantation

for patients with aortic stenosis: a position statement from the European association of cardio-thoracic surgery (EACTS) and the European Society of Cardiology (ESC), in collaboration with the European Association of Percutaneous Cardiovascular Interventions (EAPCI). *EuroIntervention,* 4**,** 193-9.

VAHANIAN, A., ALFIERI, O., AL-ATTAR, N., ANTUNES, M., BAX, J., CORMIER, B., CRIBIER, A., DE JAEGERE, P., FOURNIAL, G., KAPPETEIN, A. P., KOVAC, J., LUDGATE, S., MAISANO, F., MOAT, N., MOHR, F., NATAF, P., PIERARD, L., POMAR, J. L., SCHOFER, J., TORNOS, P., TUZCU, M., VAN HOUT, B., VON SEGESSER, L. K. & WALTHER, T. 2008b. Transcatheter valve implantation for patients with aortic stenosis: a position statement from the European Association of Cardio-Thoracic Surgery (EACTS) and the European Society of Cardiology (ESC), in collaboration with the European Association of Percutaneous Cardiovascular Interventions (EAPCI). *Eur Heart J,* 29**,** 1463-70.

VAHANIAN, A., ALFIERI, O., ANDREOTTI, F., ANTUNES, M. J., BARON-ESQUIVIAS, G., BAUMGARTNER, H., BORGER, M. A., CARREL, T. P., DE BONIS, M., EVANGELISTA, A., FALK, V., IUNG, B., LANCELLOTTI, P., PIERARD, L., PRICE, S., SCHAFERS, H. J., SCHULER, G., STEPINSKA, J., SWEDBERG, K., TAKKENBERG, J., VON OPPELL, U. O., WINDECKER, S., ZAMORANO, J. L., ZEMBALA, M., JOINT TASK FORCE ON THE MANAGEMENT OF VALVULAR HEART DISEASE OF THE EUROPEAN SOCIETY OF, C. & THE EUROPEAN ASSOCIATION FOR CARDIO-THORACIC, S. 2013. [Guidelines on the management of valvular heart disease (version 2012). The Joint Task Force on the Management of Valvular Heart Disease of the European Society of Cardiology (ESC) and the European Association for Cardio-Thoracic Surgery (EACTS)]. *G Ital Cardiol (Rome),* 14**,** 167-214.

VAHANIAN, A., ALFIERI, O., ANDREOTTI, F., ANTUNES, M. J., BARON-ESQUIVIAS, G., BAUMGARTNER, H., BORGER, M. A., CARREL, T. P., DE BONIS, M., EVANGELISTA, A., FALK, V., LUNG, B., LANCELLOTTI, P., PIERARD, L., PRICE, S., SCHAFERS, H. J., SCHULER, G., STEPINSKA, J., SWEDBERG, K., TAKKENBERG, J., VON OPPELL, U. O., WINDECKER, S., ZAMORANO, J. L., ZEMBALA, M., GUIDELINES, E. S. C. C. F. P., JOINT TASK FORCE ON THE MANAGEMENT OF VALVULAR HEART DISEASE OF THE EUROPEAN SOCIETY OF, C. & EUROPEAN ASSOCIATION FOR CARDIO-THORACIC, S. 2012. Guidelines on the management of valvular heart disease (version 2012): the Joint Task Force on the Management of Valvular Heart Disease of the European Society of Cardiology (ESC) and the European Association for Cardio-Thoracic Surgery (EACTS). *Eur J Cardiothorac Surg,* 42**,** S1-44.

VAN DE HOEF, T. P., BAX, M., DAMMAN, P., DELEWI, R., HASSELL, M. E. C. J., PIEK, M. A., CHAMULEAU, S. A. J., VOSKUIL, M., VAN ECK-SMIT, B. L. F., VERBERNE, H. J., HENRIQUES, J. P. S., KOCH, K. T., DE WINTER, R. J., TIJSSEN, J. G. P., PIEK, J. J. & MEUWISSEN, M. 2013. Impaired Coronary Autoregulation Is Associated With Long-term Fatal Events in Patients With Stable Coronary Artery Disease. *Circulation-Cardiovascular Interventions,* 6**,** 329-335.

VAN DE HOEF, T. P., NOLTE, F., DAMMAN, P., DELEWI, R., BAX, M., CHAMULEAU, S. A., VOSKUIL, M., SIEBES, M., TIJSSEN, J. G., SPAAN, J. A., PIEK, J. J. & MEUWISSEN, M. 2012a. Diagnostic accuracy of combined intracoronary pressure and flow velocity information during baseline conditions: adenosine-free assessment of functional coronary lesion severity. *Circ Cardiovasc Interv,* 5**,** 508-14.

VAN DE HOEF, T. P., NOLTE, F., ROLANDI, M. C., PIEK, J. J., VAN DEN WIJNGAARD, J. P. H. M., SPAAN, J. A. E. & SIEBES, M. 2012b. Coronary pressure-flow relations as basis for the understanding of coronary physiology. *Journal of Molecular and Cellular Cardiology,* 52**,** 786-793.

VAN DEN WIJNGAARD, J. P., SCHULTEN, H., VAN HORSSEN, P., TER WEE, R. D., SIEBES, M., POST, M. J. & SPAAN, J. A. 2011. Porcine coronary collateral formation in the absence of a pressure gradient remote of the ischemic border zone. *Am J Physiol Heart Circ Physiol,* 300**,** H1930-7.

VAN DER HOEVEN, B. L., SCHALIJ, M. J. & DELGADO, V. 2012. Multimodality imaging in interventional cardiology. *Nat Rev Cardiol,* 9**,** 333-46.

VERGALLO, R., PAPAFAKLIS, M. I., YONETSU, T., BOURANTAS, C. V., ANDREOU, I., WANG, Z., FUJIMOTO, J. G., MCNULTY, I., LEE, H., BIASUCCI, L. M., CREA, F., FELDMAN, C. L., MICHALIS, L. K., STONE, P. H. & JANG, I. K. 2014. Endothelial Shear Stress and Coronary Plaque Characteristics in Humans: A Combined Frequency-Domain Optical Coherence Tomography and Computational Fluid Dynamics Study. *Circ Cardiovasc Imaging*.

VIGNON-CLEMENTEL, I. E., FIGUEROA, C. A., JANSEN, K. E. & TAYLOR, C. A. 2010. Outflow boundary conditions for 3D simulations of non-periodic blood flow and pressure fields in deformable arteries. *Comput Methods Biomech Biomed Engin,* 13**,** 625-40.

VIOLARIS, A. G., OZAKI, Y. & SERRUYS, P. W. 1997. Endovascular stents: A 'break through technology', future challenges. *International Journal of Cardiac Imaging,* 13**,** 3-13.

WAXMAN, S., DIXON, S. R., L'ALLIER, P., MOSES, J. W., PETERSEN, J. L., CUTLIP, D., TARDIF, J. C., NESTO, R. W., MULLER, J. E., HENDRICKS, M. J., SUM, S. T., GARDNER, C. M., GOLDSTEIN, J. A., STONE, G. W. & KRUCOFF, M. W. 2009. In vivo validation of a catheter-based near-infrared spectroscopy system for detection of lipid core coronary plaques: initial results of the SPECTACL study. *JACC Cardiovasc Imaging,* 2**,** 858-68.

WELLNHOFER, E., OSMAN, J., KERTZSCHER, U., AFFELD, K., FLECK, E. & GOUBERGRITS, L. 2010. Flow simulation studies in coronary arteries--impact of side-branches. *Atherosclerosis,* 213**,** 475-81.

WENTZEL, J. J., AGUIAR, S. H. & FAYAD, Z. A. 2003a. Vascular MRI in the diagnosis and therapy of the high risk atherosclerotic plaque. *J Interv Cardiol,* 16**,** 129-42.

WENTZEL, J. J., GIJSEN, F. J., STERGIOPULOS, N., SERRUYS, P. W., SLAGER, C. J. & KRAMS, R. 2003b. Shear stress, vascular remodeling and neointimal formation. *J Biomech,* 36**,** 681-8.

WENTZEL, J. J., SCHUURBIERS, J. C. H., LOPEZ, N. G., GIJSEN, F. J. H., DIJKSTRA, J., SERRUYS, P. W. & VAN DER STEEN, A. F. W. 2008. In vivo validation of CAAS QCA-3D coronary reconstruction using fusion of angiography and intravascular ultrasound (ANGUS). *European Heart Journal,* 29**,** 849-849.

WENTZEL, J. J., VAN DER GIESSEN, A. G., GARG, S., SCHULTZ, C., MASTIK, F., GIJSEN, F. J., SERRUYS, P. W., VAN DER STEEN, A. F. & REGAR, E. 2010. In vivo 3D distribution of lipid-core plaque in human coronary artery as assessed by fusion of near infrared spectroscopy-intravascular ultrasound and multislice computed tomography scan. *Circ Cardiovasc Imaging,* 3**,** e6-7.

WESTON, S. J., WOOD, N. B., TABOR, G., GOSMAN, A. D. & FIRMIN, D. N. 1998. Combined MRI and CFD analysis of fully developed steady and pulsatile laminar flow through a bend. *Jmri-Journal of Magnetic Resonance Imaging,* 8**,** 1158-1171.

WILCOX, D. 1993. A two-equation turbulence model for wall-bounded and free-shear flows. *AIAA 24th Fluid Dynamics Conference*.

WINDECKER, S., KOLH, P., ALFONSO, F., COLLET, J. P., CREMER, J., FALK, V., FILIPPATOS, G., HAMM, C., HEAD, S. J., JUNI, P., KAPPETEIN, A. P., KASTRATI, A., KNUUTI, J., LANDMESSER, U., LAUFER, G., NEUMANN, F. J., RICHTER, D. J., SCHAUERTE, P., SOUSA UVA, M., STEFANINI, G. G., TAGGART, D. P., TORRACCA, L., VALGIMIGLI, M., WIJNS, W. & WITKOWSKI, A. 2014. 2014 ESC/EACTS Guidelines on myocardial revascularization: The Task Force on Myocardial Revascularization of the European Society of Cardiology (ESC) and the European Association for Cardio-Thoracic Surgery (EACTS) Developed with the special contribution of the European Association of Percutaneous Cardiovascular Interventions (EAPCI). *EuroIntervention*.

WOMERSLEY, J. R. 1955. Mathematical theory of oscillating flow in an elastic tube. *J Physiol,* 127**,** 37-8P.

WONG, C. Y., GREEN, P. & WILLIAMS, M. 2013. Decision-making in transcatheter aortic valve replacement: the impact of frailty in older adults with aortic stenosis. *Expert Rev Cardiovasc Ther,* 11**,** 761-72.

WONG, P. K. C., JOHNSTON, K. W., ETHIER, C. R. & COBBOLD, R. S. C. 1991. Computer-Simulation of Blood-Flow Patterns in Arteries of Various Geometries. *Journal of Vascular Surgery,* 14**,** 658-667.

WOOD, N. B. 1999. Aspects of fluid dynamics applied to the larger arteries. *J Theor Biol,* 199**,** 137-61.

WOOD, N. B. X., X.Y. 2006. Modelling of haemodynamics in the cardiovascular system by integrating medical imaging techniques and computer modelling tools. *Studies in Multidisciplinarity.* Elsevier.

WU, H. H., GURNEY, P. T., HU, B. S., NISHIMURA, D. G. & MCCONNELL, M. V. 2013. Free-Breathing Multiphase Whole-Heart Coronary MR Angiography Using Image-Based Navigators and Three-Dimensional Cones Imaging. *Magnetic Resonance in Medicine,* 69**,** 1083-1093.

XU, C. & HUANG, Y. 2011. Experimental Characteristics of Pneumatic Pulse Jet Pumping Systems with a Venturi-Like Reverse Flow Diverter. *International Journal of Chemical Reactor Engineering,* 9.

XU, C. Y. & PRINCE, J. L. 1997. Gradient vector flow: A new external force for snakes. *1997 Ieee Computer Society Conference on Computer Vision and Pattern Recognition, Proceedings***,** 66-71.

XU, C. Y. & PRINCE, J. L. 1998. Snakes, shapes, and gradient vector flow. *Ieee Transactions on Image Processing,* 7**,** 359-369.

YACOUB, M. H., KILNER, P. J., BIRKS, E. J. & MISFELD, M. 1999. The aortic outflow and root: a tale of dynamism and crosstalk. *Ann Thorac Surg,* 68**,** S37-43.

YAKHOT, A., GRINBERG, L. & NIKITIN, N. 2005. Modeling rough stenoses by an immersed-boundary method. *J Biomech,* 38**,** 1115-27.

YAMAGUCHI, T. 1993. A computational fluid mechanical study of blood flow in a variety of asymmetric arterial bifurcations. *Front Med Biol Eng,* 5**,** 135-41.

YAP, C. H., DASI, L. P. & YOGANATHAN, A. P. 2010. Dynamic hemodynamic energy loss in normal and stenosed aortic valves. *J Biomech Eng,* 132**,** 021005.

YAQOOB, Z., WU, J. & YANG, C. 2005. Spectral domain optical coherence tomography: a better OCT imaging strategy. *Biotechniques,* 39**,** S6-13.

YIN, W., SHANMUGAVELAYUDAM, S. K. & RUBENSTEIN, D. A. 2009. 3D numerical simulation of coronary blood flow and its effect on endothelial cell activation. *Conf Proc IEEE Eng Med Biol Soc,* 2009**,** 4003-6.

ZAFAR, H., ULLAH, I., DINNEEN, K., MATIULLAH, S., HANLEY, A., LEAHY, M. J. & SHARIF, F. 2013. Evaluation of hemodynamically severe coronary stenosis as determined by fractional flow reserve with frequency domain optical coherence tomography measured anatomical parameters. *J Cardiol*.

ZARINS, C. K., TAYLOR, C. A. & MIN, J. K. 2013. Computed fractional flow reserve (FFTCT) derived from coronary CT angiography. *J Cardiovasc Transl Res,* 6**,** 708-14.

List of Publications

A. Journal Publications

This section lists the journal papers submitted or published throughout the project:

1. Kousera C.A., Wood, N.B., Seed WA, Torii R, O'Regan D, Xu XY., 'A numerical study of aortic flow stability and comparison with in vivo flow measurements.', J Biomech Eng. 2013 Jan;135(1):011003.
2. Foin N, Sen S, Petraco R, Nijjer S, Torii R, Kousera C, Broyd C, Mehta V, Xu Y, Mayet J, Hughes A, Di Mario C, Krams R, Francis D, Davies J.,' Method for percutaneously introducing, and removing, anatomical stenosis of predetermined severity in vivo: the "stenotic stent".', J CardiovascTransl Res. 2013 Aug;6(4):640-8.
3. Kousera C.A., Nijjer S, Torri R., Petraco R, Sen S.,Fion N., Hughes A., Francis D., Xu X., Davies J., 'Patient-specific Coronary Stenoses Can Be Modelled Using a Combination of OCT and Flow Velocities to Accurately Predict Hyperaemic Pressure Gradients.', IEEE TBME, 2014 Jun; 61(6):1902-1913
4. Foin N, Gutierez-Chico J, Nakatani S., Torii R., Bourantas C., Sen S., Nijjer S., Petraco R., Kousera C., Ghione M., Onuma Y., Garcia-Garcia H., Francis D., Wong P., Di Mario C., Davies J., SerruysP.,'Incomplete stent apposition causes high shear flow disturbances and delay in neointimal coverage as a function of strut to wall detachment distance. Implications for the Management of Incomplete Stent Apposition', Circulation: Cardiovascular Interventions, 2014 (in press)

B. Conference Proceedings

This section lists the abstracts related to the research published in conferences for oral and poster presentations:

1. 3D Reconstruction of Coronary Anatomy using Optical Coherence Tomography (OCT) & Angiography: Comparison of simulated & measured Fractional Flow Reserve (FFR), (poster and oral presentation)*Conference on Patient-Specific Modelling*, Cardiff,UK, January 2013.
2. 3D Reconstruction of coronary anatomy using optical coherence tomography and angiography (poster presentation),*8th International Symposium of Biomechanics in Vascular Biology and Cardiovascular disease*, Rotterdam, the Netherlands, April 2013.

3. 3D Reconstruction of coronary anatomy using optical coherence tomography and angiography (oral presentation), *19th Congress of the European Society of Biomechanics*, Patras, Greece, August 2013.

4. 3D Reconstruction of Coronary Anatomy using Optical Coherence Tomography (OCT) & Angiography and its application in numerical (CFD) studies, (oral presentation), Bioengineering 2013, Glasgow, UK, September 2013.

5. TCT-640 Optical Coherence Tomography can be combined with angiography to create highly accurate patient-specific models of human coronary anatomy in a rapid automated manner (poster presentation), *J Am CollCardiol*. 2013;62(18_S1):B195-B195, *25thTranscatheter Cardiovascular Therapeutics*, San Francisco, USA, October 2013

6. TCT-614 Patient-specific Coronary Stenoses Can Be Modeled Using a Combination of Optical Coherence Tomography and Flow Velocities to Accurately Predict Hyperaemic Pressure Gradients (poster presentation), *J Am CollCardiol*.

2013;62(18_S1):B186-B186, *25th Transcatheter Cardiovascular Therapeutics*, San Francisco, USA, October 2013

7. TCT-595 Location of Side Branch Access Critically Affects Results in Bifurcation Stenting: Insights From In-vitro Modeling and Optical Coherence Tomography (poster presentation), *J Am CollCardiol*. 2013;62(18_S1):B180-B181, *25th Transcatheter Cardiovascular Therapeutics*, San Francisco, USA, October 2013

8. Comparison of computationally calculated FFR using three-dimensional anatomical models of coronary stenoses created with three different methods to demonstrate the importance of accurate anatomy reconstruction (poster presentation), *EuroPCR*, Toulouse, France, May 2014.